Seismic Body Wave Attenuation Tomography beneath the Australasian region

Agus Abdulah

A thesis submitted for the degree of
Doctor of Philosophy
of The Australian National University

Research School of Earth Sciences
2007

Except where otherwise indicated in the text, the research described in this thesis is my own original work.

Agus Abdulah

July, 2007

Acknowledgements

This thesis has benefited from the assistance of a number of people. First, and foremost, I owe the greatest intellectual and personal debt to Professor Brian L.N. Kennett, my supervisor. Professor Kennett provided excellent guidance and support throughout my doctoral research and his detailed comments on my thesis helped me to improve it in every aspect. He gave me a detailed advice as to how to design and develop my research. I received inestimable knowledge from Brian.

I would like to express my gratitude to my thesis advisors: Professor Ian Jackson, Dr. Anya M. Reading, Dr. Malcolm Sambridge and Dr. Nick Rawlinson for their invaluable guidance and generosity with time and energy. Discussion with Professor Ian Jackson on the attenuation and the frequency dependence of attenuation from the laboratory measurement point of view was very useful. Dr. Anya M. Reading introduced me to basic seismology and seismic tomography inversion. Assistance and permission from Dr. Nick Rawlinson and Dr. Malcolm Sambridge to use their Fast Marching Method code was really valuable on the development of the 3-D ray tracing presented in Chapter 5.

I have benefited from discussion with Professor Douglas A. Wiens and Dr. Eric Debayle during their visit to the ANU as well as discussion with Dr. Irina Artemieva in the European Geosciences Union meeting in Vienna 2006. I thank to Dr. Teddy Surya Gunawan from School of Electrical Engineering and Telecommunications, University of New South Wales who introduced me the Multitaper Method in Digital Signal Processing.

I am grateful to Dr. Cvetan Sinadinovski for his kind support and help to do *P*-Wave Tomography of Northwestern Australia which is presented in Appendix A. Also for his suggestion to introduce the Root-mean Square (equation A.1) in this tomographic inversion. An incredible support from Armando Arcidiaco to provide seismic data was highly appreciated.

My special thanks are due to staff at Institut Teknologi Bandung, particularly Prof. Djoko Santoso, Prof Tachyuddin Taib (*alm*), Dr. Sri Widiyantoro, Dr. Teuku Abdullah Sanny, Dr. Sigit Sukmono, Dr. Darharta Dahrin and many other staff for their support and encouragement to study at the Australian National University (ANU).

This work has been supported through an ANU (Australian National University) PhD Scholarship and ARC (Australian Research Council) Discovery Grant DP0342618. I would like to express my sincerest gratitude to the ANU and the ARC Grant program-the Australian Government.

Heartfelt thanks go to my beloved wife, Della Temenggung, for her support, excellent understanding and great encouragement, and my children: Azzam and Aaqil who missed a lot of my company especially after sunset which was my prime time to do computer programming and seismic data measurements. I wish to express my sincerest appreciation to members of my family: my parents (*alm*), Mami, Papi, kang Wawan, ceu Apong, Kiyai Fanny, Takunan, Ses Eza, Yani, Sony and many others who understood and tolerated me going overseas to undertake my PhD research.

A long period of study would not have been possible without warm and friendly environment. I greatly appreciate the kindness of all Research School of Earth Sciences staff and students, in particular my roommates: Erdinç Saygin, Ima Itikarai and Andreas Fichtner. Finally, I am very grateful to all Indonesian community in Australia, particularly colleagues and friends at the Indonesian Embassy, KMI-ANZ, PPIA, TPA CERIA, ANUMA, PERMATA and BBC (especially Dodi Darmadi).

Agus Abdulah

Canberra, winter 2007

Table of Contents

Abstract

Geological features in the lithosphere and the upper mantle beneath the Australasian region have been studied through the analysis of thousands of seismograms recorded by portable seismic stations installed across Australia. The seismic studies were designed to extract information on 1-D and 3-D physical properties such as compressional and shear seismic wavespeeds, seismic anisotropy and attenuation.

Previous seismic studies have mostly been directed to constraining the seismic wavespeed distribution. However, knowledge of the pattern of seismic attenuation is still limited. Seismic attenuation is important as it is sensitive to different physical properties than the wavespeed. Attenuation links to geological features of the earth such as lithology and is frequently used to probe the temperature distribution.

This study uses different classes of information to extract the seismic attenuation distribution beneath the Australasian region by exploiting thousands of seismograms recorded across Australia from 1993 to 2006. A tomographic technique is used to invert differential attenuations of phases on and between these seismograms, which were measured through a spectral ratio method.

The differential attenuation between S and P seismic waves $\left(\Delta t^*_{SP}\right)$, between S and $S\left(\Delta t^*_{SS}\right)$, and between P and P $\left(\Delta t^*_{PP}\right)$for nearly 6500 event-station pairs refracted back from the mantle have been used to produce 3D images of the attenuation of shear and compressional waves. The values of the differential attenuation are estimated in each case using a spectral ratio method exploiting the Multitaper technique. The

frequency band is limited to 0.10 and 1.00Hz with the assumption that attenuation is nearly independent of frequency. This assumption is supported by the linear behavior of the logarithmic spectral ratio as a function of frequency for most seismograms.

The attenuation images depend on knowledge of the propagation paths of the seismic waves, and so a first inversion was made for the *P* and *S* wave travel times picked from the same set of seismograms to produce seismic wavespeed images. The use of waves refracted back from the upper mantle leads to some vertical smearing since many of the paths cross the uppermost mantle at steep angles. However the major features of seismic wave speeds and attenuation beneath the Australasian can be reliably delineated down to 320 km depth.

The seismic wavespeeds and attenuation images are produced by two tomographic inversion approaches:

(i) The kernel matrix of the inversion is built by using 1-D ray tracing in 1-D initial models (*ak135* seismic speed model and 1-D attenuation model from previous attenuation study).

(ii) The kernel matrix is improved by introducing 3-D initial models derived from surface wave tomography for Australasian region. The Fast Marching Method is used as a powerful algorithm to trace seismic ray paths in this 3-D models.

The seismic wave speed and seismic attenuation images produced in this study suggest the presence of a deep seated horizontal contrast between central Australia and the eastern seaboard. The Archaean and the Proterozoic rocks in the west and in the middle of the continent are associated with a high seismic wave speed anomaly with low seismic attenuation, whereas the Phanerozoic rocks and the presence of recent volcanism and the region of high heat flow in the east are associated with a low seismic wavespeed anomaly with high seismic attenuation. Several areas which have previously been associated with the existence of hot spots such as around Bass Strait and the Coral Sea display high seismic attenuation anomalies. The attenuation images also suggest a contrast between lithospheric and the upper mantle structures. The lithosphere is

characterized by low attenuation for both compressional and shear waves with *Qp*=1600-3000; *Qs*=800-1250, while the upper mantle beneath displays high attenuation i.e. *Qp*=230-250; *Qs*=120-140.

Frequency dependence of attenuation beneath the Australasian region is also observed by measuring the differential attenuation between *S* and *P* seismic waves $\left(\Delta t^*_{SP}\right)$ in a wider frequency band (up to 2.5 Hz). For this purpose, the broad frequency band is divided into four sub frequency bands by using a Golden section division (0.10-1.00 Hz, 0.50-1.50Hz, 1.00-2.00Hz and 1.50-2.5Hz). Then by using the assumption of a simple power law dependence frequency, the $\left(\Delta t^*_{SP}\right)$ from each sub frequency band are used to produce frequency dependence parameter (γ) paths. The $\left(\Delta t^*_{SP}\right)$ from each sub-frequency band are also inverted to produce tomographic images of seismic attenuation. Using the same assumption, the tomographic images of frequency dependence of attenuation beneath Australasian region is presented.

The frequency dependence of the paths (γ) covering eastern part of Australia and the Coral Sea area shows larger γ so that the frequency dependence in those areas is relatively stronger. In the north-west part of the Australian continent shows a mixture of paths with small and larger γ suggesting complex frequency dependence. These features are also supported by the tomographic images of frequency dependence of attenuation beneath the Australasian region. The frequency dependence of attenuations (exponent γ) increases with frequency with $0.1 < \gamma < 0.3$ at 35-120km depth interval; $0.02 < \gamma < 0.21$ at 120-220km and $0.0006 < \gamma < 0.02$ at 220-320km for frequency 1.00 – 2.00Hz.

Estimates of shear attenuation have been made for both *SH* and *SV* components so that we are able to make an estimate of polarization anisotropy for shear attenuation in terms of the ratio ζ between *SH* and *SV* attenuation. There is little indication of shear anisotropy in the asthenosphere (0.98 to 1.02) but in the lithosphere, ζ varies from 0.8 to 1.2. In general, for most of the Australian continent the *SH* waves are less attenuative than *SV* waves.

Chapter 1

Introduction

1.1 Background

The strategic position of the Australian continent between the seismicity belt which extends from Indonesia to New Zealand through Tonga-Fiji and the mid-ocean ridge to the south of the continent provides a wealth of events at suitable distances to be used as probes into the seismic structure of the upper mantle. The extensive deployments of portable broadband seismic stations across the Australian Continent and Tasmania since 1993 offer robust seismological data, with over 120 portable stations that provide a relatively dense coverage at distances from 5° to 45°.

Over the last two decades, a wide range of studies have been used to gain information on 1-D and 3-D structure in the mantle that exploits different aspects of seismograms. Studies on seismic tomography which use thousands of seismic travel times picked from high quality body wave seismograms or use the seismic waveform of large amplitude surface waves in the later part of the seismogram that travel nearly horizontally, have been conducted and successfully to delineate the major features of the geological structure beneath the Australian Continent.

Seismic travel time tomography for the Australian region was pioneered by Widiyantoro & van der Hilst [1996] who produced tomographic images in a zone covering the southern Philippines, Malaysia, Indonesia, Papua New Guinea and northern Australia. Subsequently, Gorbatov and Kennett [2001] have implemented the travel time tomographic inversion with a parameterization that has smaller cells near the earth's surface and larger cells at the depth.

Efforts in exploring the features of geological structure beneath the Australian Continent and surrounding regions have exploited surface wave tomography with the abundance of seismic data recorded by temporary broadband seismometers which have been deployed in a numerous number of projects conducted by Research School of Earth Sciences, the Australian National University, such as: SKIPPY [continent-wide,1993-1996], KIMBA [Kimberley Block, 1997,1998], QUOLL [southeast Australia, 1999], WACRATON [Western Australia, 2000-2001, 2002-2003], TIGGER [Tasmania, 2001-2002], TASMAL experiment [Gulf of Carpentaria to the southern Australia, 2003-] and LINKAGE [Northwestern Australia, 2006-2007].

Zielhuis and van der Hilst [1996] implemented the "Partitioned Waveform Inversion" (PWI) for surface wave tomography, which has two stages of analysis. The first step generates a shear wavespeed model for each path and the second combines the path dependent information in to a 3-D model. A three-stage inversion technique for surface wave tomography has also been applied to the Australian region by Yoshizawa and Kennett [2004]. In the first stage, path-specific one-dimensional (1-D) shear velocity profiles are derived from multimode waveform inversion to provide dispersion information. The information from all paths is then combined to produce multimode phase speed maps as a function of frequency. In the second stage, the 2-D phase speed maps are updated by including ray tracing and finite frequency effects through the influence zone around the surface wave paths over which the phase is coherent. During the third stage, the 3-D shear wave speed distribution is reconstructed from the set of updated multimode phase speed maps. The reliability of the two-stage tomographic

method has been improved by the development of two new techniques [Fishwick, 2005]: multiple starting models are used in the waveform inversion procedure and introducing a multi-scale component, where the final model is damped towards the large scale features of the data rather than a global reference model. These new techniques have been implemented for seismic data from all Australian National University temporary deployments, and additional data from permanent stations and a temporary deployment in New Zealand.

Studies on seismic attenuation of the Australasian region were initiated by Gudmundsson *et al.* [1994]. They used the spectral ratio between *S* and *P* windows for the analysis of 22 seismograms from the WRA broadband instrument and a further four from portable broadband instruments deployed near Warramunga.

A more recent study of attenuation in the Australian region was carried out by Cheng [2000]. He studied Australian attenuation structure by estimating the spectral ratio between *P* and *S* waves for nearly 2000 three-component seismograms from SKIPPY project [1993-1996]. The spectra of the *P*, *SV*, and *SH* waves and their accompanying noise were estimated by using Fast Fourier Transform of a single real function. The differential attenuation of each ray path was then measured by estimating the slope of spectral ratio of *S* to *P* waves. The differential attenuation data were organized into azimuthal corridors and inverted by using the Neighbourhood Algorithm (NA) to produce a set of 1-D *Q* profiles. A 3-D *Q* model at fixed frequency was then constructed by combining these 1-D *Q* profiles weighted by ray density. The seismic studies in Australasian region, mentioned above, are explained in more detail in Chapter 3.

In this work, thousands of seismograms from previous and recent projects (from 1993 to 2006) are used to produce seismic wavespeeds and attenuation images beneath the Australasian region using a tomographic technique. Differential attenuation together with the *P* and *S* wave travel times for these seismograms are measured and carefully hand picked. The seismic wavespeed images are produced by inverting residuals

between the picked *P* and *S* waves travel times and the results for a reference model. Attenuation images are constructed by utilizing the seismic wavespeeds and the differential attenuation information. The attenuation measurement methods and attenuation inversion procedures used in this study are explained in detail in Chapter 2, 4 and 5. The resulting tomographic images are used to improve the understanding in the interpretation of complex structure and the temperature distribution beneath the Australian continent and its surrounding regions.

1.2 Thesis Structure

Chapter 2 Attenuation Theory and Measurements

In this chapter, the basic concept of the attenuation process at the microscopic scale is presented. Attenuation measurements from various laboratory experiments are discussed and used as a benchmark for understanding the attenuation principles in seismology. Furthermore, attenuation measurement techniques particularly the techniques which are used in this study and their implementation for several Australian seismic datasets are also demonstrated.

Chapter 3 Australasian Setting and Previous Seismic Studies of Australia

The geological and tectonic features of the Australian continent and surrounding regions are outlined. Previous seismic studies of the Australasian region are discussed in more detail, with emphasis on probing of the lithospheric and upper mantle structure particularly from surface wave and attenuation studies.

Chapter 4 Seismic Speeds and Attenuation Tomography-Part I

The main focus of this chapter is the production of seismic wavespeed and attenuation images in the lithosphere and the upper mantle beneath the Australasian region. The images are produced by a tomographic technique in which the seismic ray paths are traced in a 1-D reference model. The characteristic of the seismic datasets

incorporated in the tomography are discussed. Also, details of the tomography procedure, checkerboard tests, model parameterization and the system of equations are outlined.

Chapter 5 Seismic Speeds and Attenuation Tomography-Part II

The seismic wavespeed and attenuation images beneath the Australasian are improved by introducing 3-D ray tracing in 3-D initial models rather than a 1-D reference model. The initial models used in this study represent geological features of the Australasian region derived from surface wave tomography. In this way, the starting point should lie close to the desired solution. Besides the improvement of estimates of shear attenuations, the pattern of compressional attenuation is also presented.

Chapter 6 Frequency Dependence of Attenuation beneath Australasian

Work on the frequency dependence of attenuation beneath the Australasian region is presented in this Chapter. The frequency dependence of the attenuation measurement method, the frequency dependence of the properties of the propagation paths and frequency dependence tomography are also revealed.

Chapter 7 Discussion

The models derived in the previous chapters are discussed in Chapter 7. An overview of comparison with previous wavespeeds and attenuation studies is provided. Further, a discussion of the correlation between attenuation, seismic speed and temperature beneath the Australasian region along with the study of the frequency dependence of attenuation and attenuation anisotropy is given.

Appendix

Separate work on *P* wave seismic speed tomography for Western Australia is presented in Appendix A. The 1D seismic ray tracing algorithm used in Chapter 4 is

outlined in Appendix B. The spectral theory of the multi taper method used in chapter 2 is also described in Appendix C. Digital version of this thesis and computer program for attenuation measurement are enclosed in a compact disc with the instruction is shown in Appendix D.

Chapter 2

Attenuation Theory and Measurements

2.1 Attenuation Theory

If a seismic wave passes through a material that is not perfectly elastic, it loses energy to the material and the amplitude of the wave gradually diminishes. This amplitude decrease is called *attenuation*, and its due to anelastic *damping* of the vibration of the particles in the material [Lowrie, 2004]. The attenuation during the passage of a wave through the Earth's interior is usually considered to be a combination of two mechanisms, intrinsic absorption and scattering loss due to distributed heterogeneities. The most important evidence for the existence of small-scale random heterogeneities is the existence of "coda" such as the tail portion of the seismograms of local earthquakes [Sato *et al.*, 1998], or the extended wavetrains following the onset of the *P* and *S* waves for many Indonesian earthquake recorded in northern Australia. Thus measurements of the attenuation of direct seismic waves need to be carefully considered to see whether total or intrinsic attenuation is important.

The explanation of attenuation due to intrinsic absorption mechanisms can be found in papers reviewed by Knopoff [1964], Jackson and Anderson [1970], Mavko and Nur [1979] and Dziewonski [1979]. Several proposed mechanisms are based on the

observation that crustal rocks have microscopic cracks and pores which may contain fluids. Intrinsic absorption mechanisms are proposed through frictional sliding on dry surfaces of thin cracks [Walsh, 1966], viscous dissipation in a zone of partially molten rock such as the low velocity or high attenuation zone beneath the lithosphere [Nur, 1971], the effect of partial saturation of cracks on absorption: fluid movement within cracks is enhanced by the presence of gas bubbles [Mavko and Nur, 1979]. An increase of Q_S^{-1} with increasing content of volatile in dry rocks revealed by Tittmann *et al.*, [1980]. They found that the increase was due to an interaction between an adsorbed water film on the solid surfaces by thermally activated motions. The scattering loss mechanism due to heterogeneities distributed in the earth also causes attenuation [Aki, 1980]. Scattering loss mechanisms caused by distributed crack and cavities have been studied by Matsunami [1990] and Kawahara and Yamashita [1992].

The Quantity of the rate of energy dissipation at frequency ω is provided by the loss factor $Q^{-1}(\omega)$, which is defined as the ratio of the energy loss in a circle $\Delta E(\omega)$ to the elastic energy stored in the oscillation E_0 [Kennett, 2001]:

$$Q^{-1}(\omega) = -\Delta E(\omega)/(2\pi E_0(\omega)) \tag{2.1}$$

E_0 is the sum of the strain and kinetic energy calculated using the instantaneous elastic moduli, and the energy dissipation ΔE arises from the imaginary part of the elastic moduli. For purely dilatational disturbances

$$Q_\kappa^{-1}(\omega) = -\mathrm{Im}\{\kappa_1(\omega)\}/\kappa_0 \tag{2.2}$$

and for purely deviatoric effects

$$Q_\mu^{-1}(\omega) = -\mathrm{Im}\{\mu_1(\omega)\}/\mu_0 \tag{2.3}$$

For the earth it appears that loss in pure dilatation is much less significant than loss in shear, and so $Q_\kappa^{-1} << Q_\mu^{-1}$ [Kennett, 2001].

The condition of causality leads to relations between dissipation and the frequency dependence of seismic properties so that the real part of $\mu_1(\omega)$ can be written in terms of the loss factor with frequency,

$$\mathrm{Re}\{\mu_1(\omega)\} = -\frac{2\mu_0}{\pi} P\int_0^\infty d\omega' \frac{\omega' Q_\mu^{-1}(\omega')}{\omega'^2 - \omega^2} \tag{2.4}$$

where *P* denotes the Cauchy principal value.

Because of the difficulties in isolating all factors which effect amplitude of a recorded seismic wave, the distribution of the loss factor Q_μ^{-1} in the earth is still imperfectly known [Kennett, 2001]. Based on the previous studies on the earth attenuation, it is suggested that the loss factor in the crust is moderate (Q_μ^{-1}~0.004) with an increase in the uppermost mantle (Q_μ^{-1}~0.01) and decrease to crustal values, or lower, in the mantle below 1000km. Over the frequency band 0.001-1Hz the intrinsic loss factor Q_μ^{-1} appears to be approximately constant [Kennett, 2001].

2.2 Laboratory Measurement of Attenuation

Laboratory measurements have been conducted for many years in order to provide a better interpretation of the characteristics of seismic attenuation and dispersion in the earth. To achieve this objective, the measurements are carried out on synthetic materials such as Fo_{90} Olivine, $CaTiO_3$ Perovskite polycrystals that have physical properties similar to the real material i.e. formational high temperature and pressure, partially molten, grain size, etc.

Relevant laboratory experiments on seismic attenuation have extensively carried out by RSES, ANU such as a study on Titanate Perovskite $CaTiO_3$ and $SrTiO_3$ at high temperature [Webb *et al.*, 1999]. They revealed that both of these perovskites display viscoelastic behaviour in the seismic frequency regime; with the temperature of onset of this frequency-dependent behaviour being grainsize-dependent. Also they observed that the rheology of fine-grained $SrTiO_3$ and $CaTiO_3$ perovskites to 5 mm grainsize shows that a ~20% dispersion in wavespeed is expected for the period range 1–1000 s, with dissipation (Q^{-1}) ~10^{-2} for 1 s period waves at1300ºC.

The effect of grain size and partial melting on seismic attenuation can be found in the experiment of Jackson *et al.* [2002] and Faul *et al.* [2003]. They examine specimens of fine-grained polycrystalline of Fo_{90} olivine either melt-free or containing 0.5-4% basaltic melt. The torsional forced oscillation and complementary microcreep

methods are used to measure the shear modulus and associated strain energy dissipation Q^{-1} at high temperatures and seismic frequencies. The result suggest that for the nominally melt-free material (containing << 0.1 vol. % melt) a strain-energy absorption band is observed within which Q^{-1} varies consistently and monotonically with frequency (0.01-1 Hz), temperature (1270-1570 K) and grainsize (3-23 μm). However, at the temperature of 1470 K that represents the upper mantle condition, the value of Q^{-1} ranges between 0.009 at 10 s period and 10 mm grainsize and 0.034 at 100 s period and 1 mm grainsize. Furthermore, Faul *et al.* [2003] explored the influence of a small basaltic melt fraction (0.004-0.037) on the seismic properties of fine-grained synthetic polycrystals of Fo_{90} olivine with torsional forced oscillation/microcreep methods. They inferred that levels of attenuation for melt-free material are generally consistent with those observed seismologically suggesting that the same grain-boundary diffusional processes thought to dominate the behavior of the fine-grained materials tested in the laboratory might also account for much of the wave speed variability and attenuation in the mantle. Meanwhile, for melt-bearing olivine, the extrapolated attenuation is generally somewhat higher than the highest seismologically measured attenuation. The progress report by Jackson [2000] indicates that dissipation and associated shear modulus dispersion for low-carbon iron alloys and Fo_{90} Olivine, $CaTiO_3$ Perovskite polycrystals both increase monotonically with increasing temperature and decreasing frequency. The extent of the departure from elastic behavior in these generally fine-grained materials appears to be sensitive to both grain size and impurity content.

The effect of temperature on seismic attenuation is also revealed by several laboratory measurements [Gribb and Cooper, 1998]. They observed the high-temperature (1200-1285°C) torsional dynamic attenuation (10^{-3}-10^{0}Hz) and unidirectional creep behavior of a fine, uniform grain sized (d≈3μm) olivine (~Fo_{92}) aggregate. The attenuation behavior displayed a band in Q_G^{-1} that is moderately dependent on frequency ($Q_G^{-1} \approx f^{-0.35}$) and temperature with $-1.5 < \log(Q_G^{-1}) < 0.5$. The

correlation between attenuation and temperature, Jackson [1993] showed that at seismic frequencies attenuation, Q^{-1}, in the mantle rocks at subsoliditus temperatures follows the Arrhenius law and an exponentially dependence in inverse temperature *1/T*:

$$Q^{-1} = A\tau^{\alpha} \exp\left(-\alpha E^{*} / RT\right) \tag{2.5}$$

where E^{*} is the activation energy, *R* is the gas constant, τ is the oscillation period, *A* is a scaling constant and the exponent α is approximately 0.15-0.30 as determined from seismic studies and laboratory measurements on the upper mantle rocks.

In separate experiment, Tan *et al.* [1997] examined shear wave dispersion and attenuation in fine-grained synthetic olivine aggregates using low-frequency torsional forced oscillation tests. The sample has a uniform grainsize of about 50μm, <0.1 vol.% of melt and minor amount of hydroxyl (~100ppm). The tests were conducted under 200MPa hydrostatic pressure, low oscillation frequencies (0.01-1 Hz) and within the linear regime of strain (amplitude < $5\text{x}10^{-5}$). The sample was first heated at 1300ºC, and subsequently measured at a series of lower temperatures. The result at 1300ºC showed that the shear modulus G is relatively low and strongly frequency dependent and the attenuation Q^{-1} is high (G ~ 33 GPa, Q^{-1} ~ 0.14 for 1 Hz). Q^{-1} varies with temperature and frequency as $Q^{-1} = A_0\left[\omega e^{E/} RT\right]^{-n}$ with the activation energy for the relaxation rate $E = 420 \pm 30$ kJ/mol and exponent $n = 0.31 \pm 0.02$.

2.3 Attenuation Measurements

Seismic attenuation affects both the amplitude and phase of seismic waves. Algorithms to measure attenuation are divided into those that use amplitude information, or phase information and those that use a combination of both. In this research, a spectral ratio method which uses amplitude information is used to estimate differential attenuation from Australian seismic data sets. The basic concept of the spectral ratio method is that the natural logarithm of the ratio between two amplitude spectra is estimated as a function of frequency, and then the attenuation (Q^{-1}) is related to the best fit of the slope of the ratio.

Rickett [2007] argued that the spectral ratio method has several advantages, such as: any frequency-independent scaling between waveforms falls into the intercept term in the linear regression and does not affect the estimation of *Q*. Further, the spectral-ratio method uses the entire available amplitude spectrum, in this way it lead to more reliable estimates. For these reasons the spectral ratio methods i.e. the wave ratio method and the station ratio method are used to measure differential attenuation of our seismic datasets.

2.3.1 The Wave-Ratio Method

As in the work of Gudmundsson *et al.* [1994], the spectral ratio method to estimate differential attenuation is used. To understand the concept of this method, let us begin with the amplitude spectrum $A(\omega,r)$ of a recorded wave at an epicentral distance *r,* with azimuth θ from the source, for a shallow source - which can be expressed as:

$$A(\omega,r) = S(\omega)B(\theta)C_s(\omega)M(\omega,r)G(r)C_r(\omega,r)I(\omega) \quad (2.6)$$

where ω is the angular frequency, $S(\omega)$ is the source spectrum, $B(\theta)$ is the source radiation pattern $C_s(\omega)$ is the crustal contribution at the source, $M(\omega,r)$ is the mantle contribution, $G(r)$ is the amplitude function in propagation and $C_r(\omega,r)$ is the contribution from the receiver crust. The spectrum arriving from the source is modulated by the instrumental response $I(\omega)$.

If equation 2.6 is transformed into its amplitude form with an additive equation for phase, we have:

$$|A(\omega,r)| = |S(\omega)||B(\theta)||C_s(\omega)||M(\omega,r)||G(r)||C_r(\omega,r)||I(\omega)| \quad (2.7)$$

The equation 2.7 will be used as the basis for our procedures to suppress specific parts of the response.

The term $G(r)$ is a function of both the geometrical spreading along the path and the influence of attenuation:

$$G(r) = g(r)\exp\left[-\frac{\omega}{2}\int\frac{dr}{Q(\omega,r)V(r)}\right] \tag{2.8}$$

here $g(r)$ is the geometrical spreading and the exponential term includes the effect of attenuation.

I estimate the attenuation term from the amplitude ratio between the spectra two body waves i.e. *S* and *P* waves. The spectral ratio between the two arrivals from the same event recorded at the same receiver cancels most effects of the source and the instrument function. By assuming that the two waves have similar propagation behavior, the effect of geometrical spreading and radiation pattern can also be isolated as well. The spectral ratio between *S* and *P* wave at the same receiver can be extracted from equations (2.7) and (2.8) as:

$$\ln\frac{|A(\omega)_S|}{|A(\omega)_P|} = -\frac{\omega}{2}\left[\int_S\frac{dr}{Q_S V_S} - \int_P\frac{dr}{Q_P V_P}\right] + \ln g_S(r) - \ln g_P(r) \tag{2.9}$$

Since the geometrical spreading is independent of frequency the only remaining frequency-dependent contribution is the effect of attenuation. Equation (2.9) can therefore be expressed as:

$$\ln\frac{|A(\omega)_S|}{|A(\omega)_P|} = -\frac{\omega}{2}(t_S^* - t_P^*) + c = -\pi f(t_S^* - t_P^*) + c \tag{2.10}$$

We recognize that the spectral amplitude ratio has a linear dependence on frequency *f*, with slope $(t_S^* - t_P^*)$, where e.g.

$$t_S^* = \int_S\frac{dr}{Q_S V_S} \tag{2.11}$$

The *differential attenuation* between the *S* and *P* arrivals is defined by $\Delta t_{SP}^* = (t_S^* - t_P^*)$.

2.3.2 The Station-Ratio Method

The equation 2.9 could be further simplified by considering an average *Q* between two stations, so:

$$\ln\frac{|A(\omega)a|}{|A(\omega)b|} = \ln\frac{G_a}{G_b}\frac{|C_a(\omega)|}{|C_b(\omega)|} + \frac{\omega(t_b - t_a)}{2Q} = \ln\frac{G_a}{G_b}\frac{|C_a(\omega)|}{|C_b(\omega)|} + \frac{\omega(r_b - r_a)}{2QV} \tag{2.12}$$

If the amplitude of seismic wave is corrected for geometrical spreading and crustal effects:

$$\ln \frac{|A(\omega)|G_a|C_a(\omega)|}{|A(\omega)a|G|C(\omega)|} = \frac{\omega(r_a - r)}{2QV} \tag{2.13}$$

The equation 2.12 is suitable for application to only two stations, when the first term of the right-hand side is a constant. By using equation 2.12, I estimate the differential attenuation between two *P* waves and two *S* waves recorded at different stations. For this purpose, I plot $\ln|A(\omega)a|/|A(\omega)b|$ versus ω. Then, in the range of seismic frequency band, linear regression is applied to obtain a slope and yield a value of *Q*. In this method, I choose a single station as our reference, thus the estimated value of *Q* is relative to the reference.

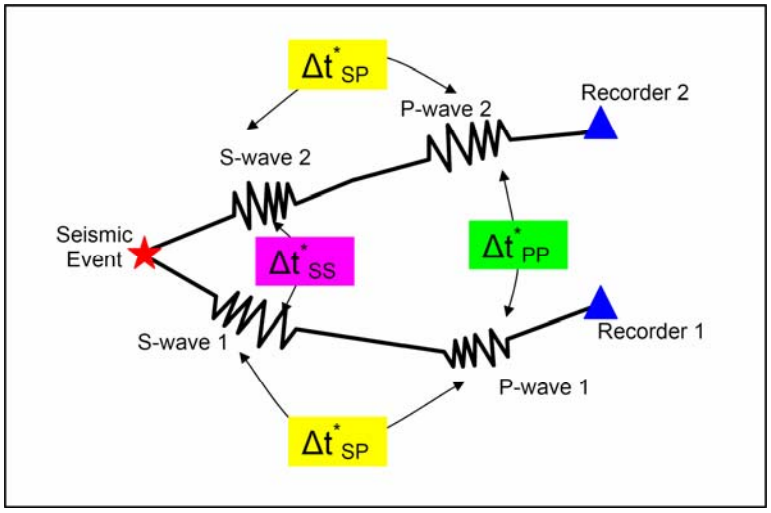

Figure 2.1: Schematic diagram of spectral ratio methods used in this study. Red star represents a seismic event, blue filled triangles represent recorders, exaggerated body waves are shown by wiggles, the Wave Ratio Method by Δt^*_{SP} and the Station Ratio Method by Δt^*_{PP} and Δt^*_{SS}.

A schematic diagram of the two spectral ratio methods used in this study is shown in Figure 2.1. Seismic waves from an event (red star) recorded by two recorders (blue triangles) is analyzed using The Wave Ratio method (Δt^*_{SP}) which is defined as spectral ratio between *S* wave and *P* waves recorded by each seismic station. The

seismic waves are also analyzed using the Station Ratio Method (Δt^*_{PP} and Δt^*_{SS}) which uses spectral ratio of *P* to *P* and *S* to *S* waves at different stations. In the measurements of the Δt^*_{PP} and Δt^*_{SS}, *P* and *S* waves recorded by recorder 1 are used as a reference. In the case when seismic waves from 1 event recorded by say 5 recorders, there will be 4 positive or negative values and 1 zero value of the Δt^*_{PP} and Δt^*_{SS}.

2.3.3 Test of Spectral Ratio Methods to Australian Data

In order to be able to measure attenuation easier and more interactive, a Graphical User Interfaces (GUI) has been developed. The GUI is built using the Matlab package based on the mathematical equation described in sections 2.3.1 and 2.3.2 above. The GUI has several features such as: ability to load up to 500 seismic datasets in SAC format and save in temporary memory, display, zoom in, zoom out, push button 'next' and 'previous' to analyze other data, display data information (julian day, date, station, delta, azimuth, depth and magnitude), traveltimes and frequency band picking button, estimate spectra using the Multitaper method [Percival & Walden, 1993], and save the result of estimation. Snapshots of the Graphical User Interface for the Wave Ratio Method (Δt^*_{SP}) and the Station Ratio Method (Δt^*_{PP} and Δt^*_{SS}) are shown in Figure 2.2 and 2.3.

Table 2.1: Seismic data information used in this test

Year	Julian Day	Origin Time	Lat [deg]	Lon [deg]	Depth [km]	*mb*
1994	145	16:36:53	138.8	-1.96	28	5.5
1994	153	18:17:34	112.83	-10.48	18	7.2
1994	156	05:56:45	113.49	-10.72	33	5.6
1994	158	18:31:42	104.44	-5.79	42	5.7
1994	164	22:48:27	113.62	-10.33	26	5.6
1994	165	21:01:55	126.31	1.52	33	5.7
1994	167	10:12:15	159.74	-9.76	109	6.0
1994	183	09:14:43	131.10	-5.76	88	5.9
1994	216	22:15:37	131.57	-6.34	33	6.2
1994	219	05:52:27	119.98	-10.27	26	5.7
1994	251	08:50:42	126.17	0.54	52	5.7
1994	253	04:54:10	126.6	7.55	79	5.6
1994	254	12:01:13	166.69	-16.05	33	5.6

To evaluate the reliability of the GUI being developed, tests for a set of Australian data were conducted. About 20 sets of three component seismic data for events recorded at stations SC02, SC04 and SC05 station from the SKIPPY experiment (1994) were employed. Information of this seismic data is shown in Table 2.1.

These three stations are selected because their geographical position is close to the Warramunga array, from which the seismic data of that have been analyzed by Gudmundsson *et al.* [1994] and Cheng [2000], thus our final result will be comparable with theirs.

For the calculation of the differential attenuation Δt^*_{SP}, the spectrum of the *P* wave is estimated from the vertical component (*Z*) and the *S* waves spectra from the rotated components i.e. transverse *(SH)* and radial *(SV)* relative to the great circle between the source and receiver. Besides these waves, I also consider *S* waves spectra from a combined horizontal term $H = \sqrt{(SH^2 + SV^2)}$.

The time window employed for the spectral estimation varies in length between 25s and 45s depending on the epicentral distance. Firstly *P* and *S* waves travel times are predicted by the *ttimes* software [Kennett and Engdahl, 1991] from which I compute *ak135* traveltimes [Kennett and Engdahl, 1995], then hand picking is used to obtain more accurate onsets. The spectral windows start at 1s before the *P* and 3s before the *S* arrivals.

I assume that the signal and the background noise are independent in phase, thus to minimize the effect of background noise, the signal spectrum is subtracted by the estimate of the noise spectrum. The Multitaper technique is also used to estimate the background noise spectrum with windows of the same length as for signal ending at the beginning of the signal window. Moreover, I only used amplitude spectra values which lie above the noise level and seismic data with high signal to noise ratio (see section 4.2). This assumption has been frequently used in earlier seismic attenuation inversions.

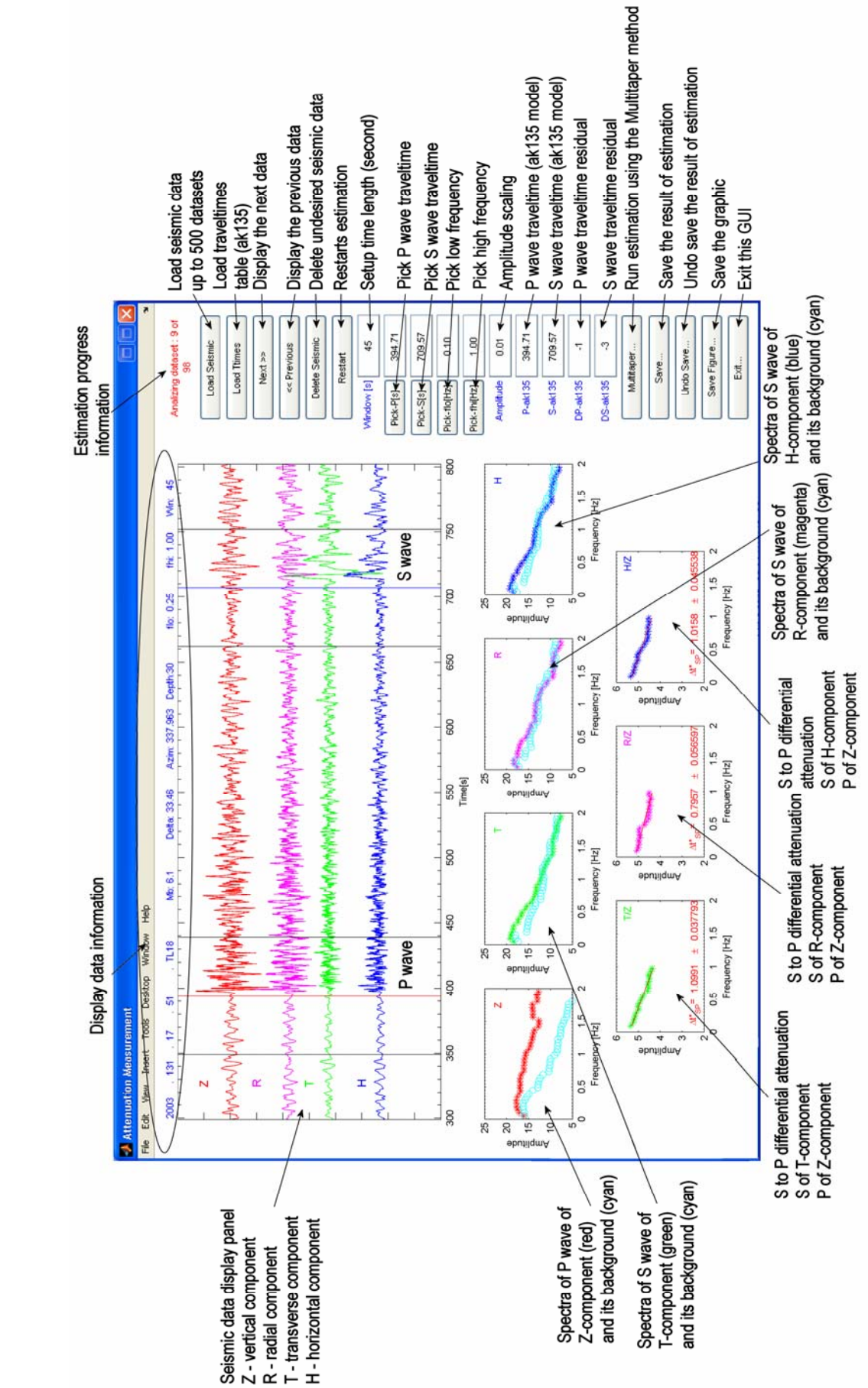

Figure 2.2 A snapshot of the Graphical User Interface for *S* to *P* differential attenuation estimation measurements.

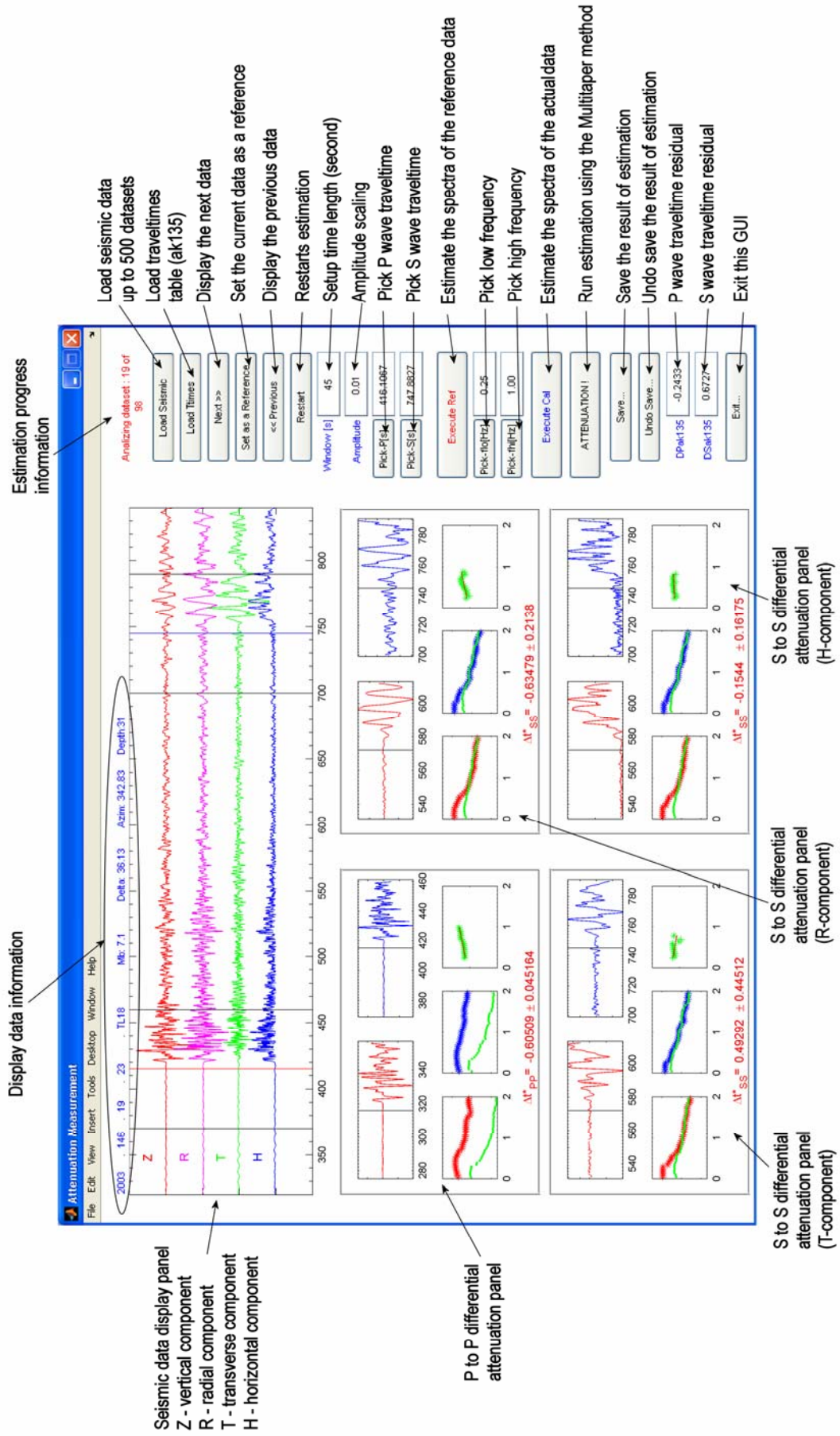

Figure 2.3 A snapshot of the Graphical User Interface for P to P and S to S differential attenuation measurements.

As can be seen from equation (2.10) the differential attenuation between *S* and *P* wave spectra can be obtained from the slope of the linear regression of the logarithm of the ratio of the amplitude spectra as a function of frequency. I use a frequency band of 0.10 to 1.0 Hz, and assume a weak dependence on frequency. In general the logarithmic spectral ratio is close to linear with frequency in this frequency band so that I can use a model in which attenuation is independent of frequency.

The penetration of the seismic ray path in depth increases as the epicentral distance increases. To see the behavior of average attenuation in the lithosphere, upper mantle and transition zone, examples of the Δt^*_{SP} estimation are shown at distances 12.4°, 19.9° and 26.1° in Figure 2.4(a), 2.4(b) and 2.4(c). Figure 2.4 (a) shows that at epicentral distance 12.4°, the frequency content of both *P* and *S* waves remain moderately high, suggesting that both seismic waves passed through low attenuation zone. Meanwhile, Figure 2.4 (b) shows a significant difference in the frequency content of *P* and *S*. The *P* waves remain moderately high frequency, but the *S* waves returned from the transition zone and below decay rapidly with increasing frequency. The features of frequency content of seismic waves in Figure 2.4 (c) are similar to that in Figure 2.4 (b).

A compilation of the Δt^*_{SP} measurement for all data used in this test is illustrated in Figure 2.5 (a). The figures show that, the frequency decay rates of *P* and *S* wave varies with the epicentral distance. It can be seen that the consistently low value of the Δt^*_{SP} out to a distance of 18°, followed by a sudden increase of the Δt^*_{SP} between distances of 18° and 21° and gradual decrease beyond the distance of 21°. The features show a good agreement with the previous study of the Δt^*_{SP} measurement of Warramunga data conducted by Cheng [2000] (Figure 2.5 (b) and Gudmundsson *et al.* [1994] (see Figure 3.9 (a)).

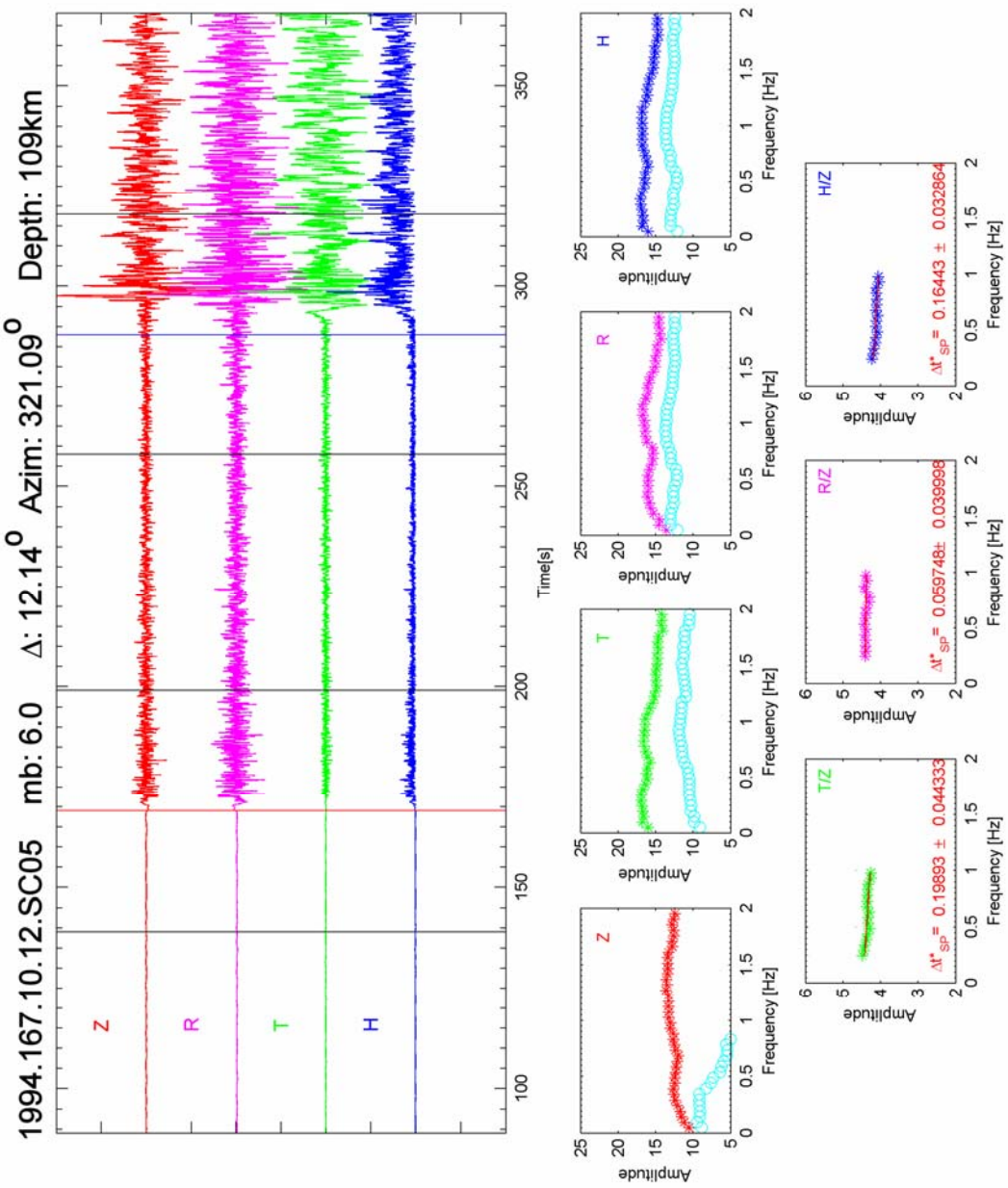
1994.167.10.12.SC05 mb: 6.0 Δ: 12.14° Azim: 321.09° Depth: 109km
Z
R
T
H
Time[s]
Amplitude
Frequency [Hz]
T/Z
R/Z
H/Z
Δt*SP= 0.19893 ± 0.044333
Δt*SP= 0.059748± 0.039998
Δt*SP= 0.16443 ± 0.032864

Figure 2.4(a)

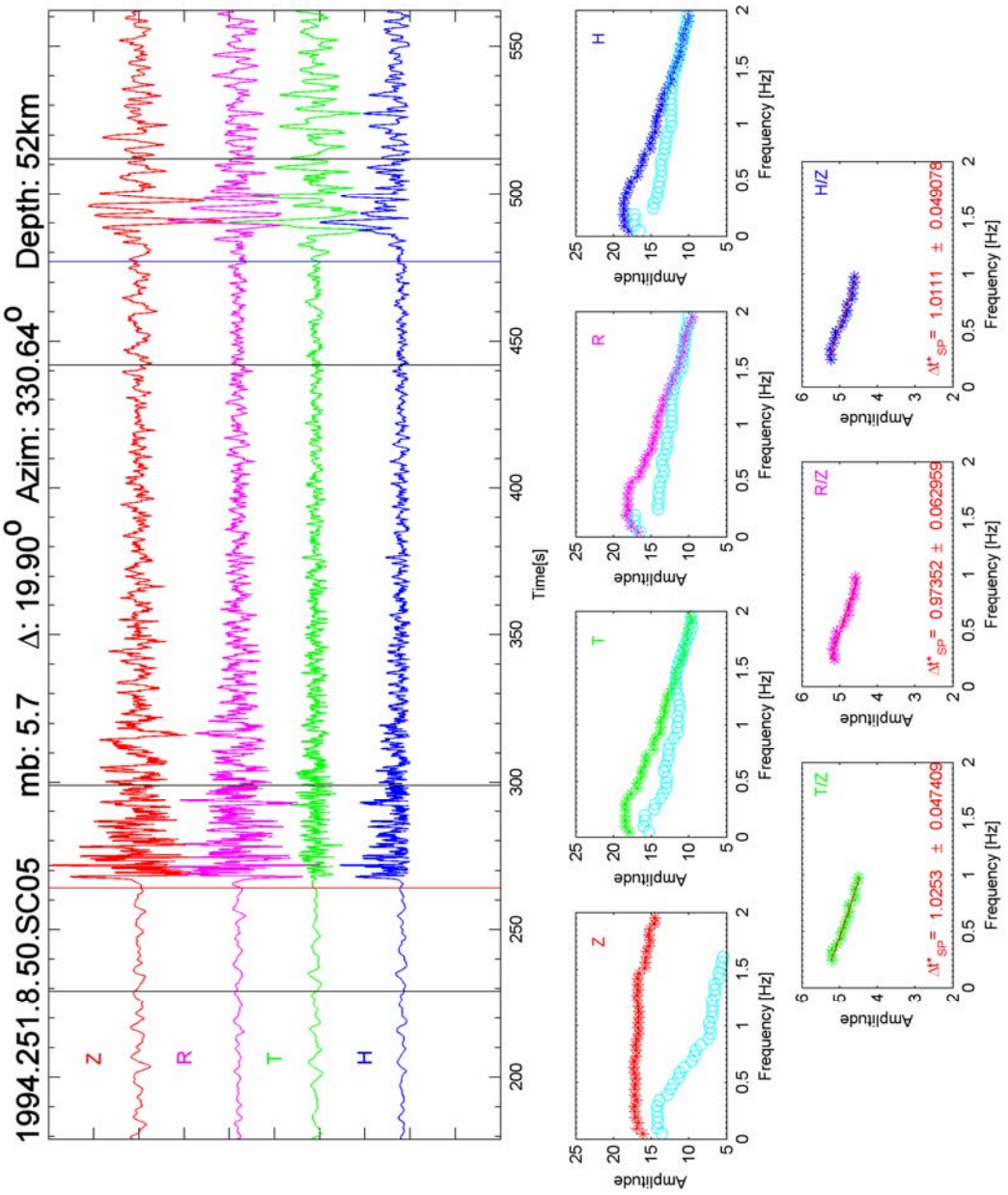
1994.251.8.50.SC05 mb: 5.7 Δ: 19.90° Azim: 330.64° Depth: 52km
Z
R
T
H
Time[s]
Amplitude
Frequency [Hz]
T/Z
R/Z
H/Z
Δt*SP = 1.0253 ± 0.047409
Δt*SP = 0.97352 ± 0.062959
Δt*SP = 1.0111 ± 0.049078

Figure 2.4(b)

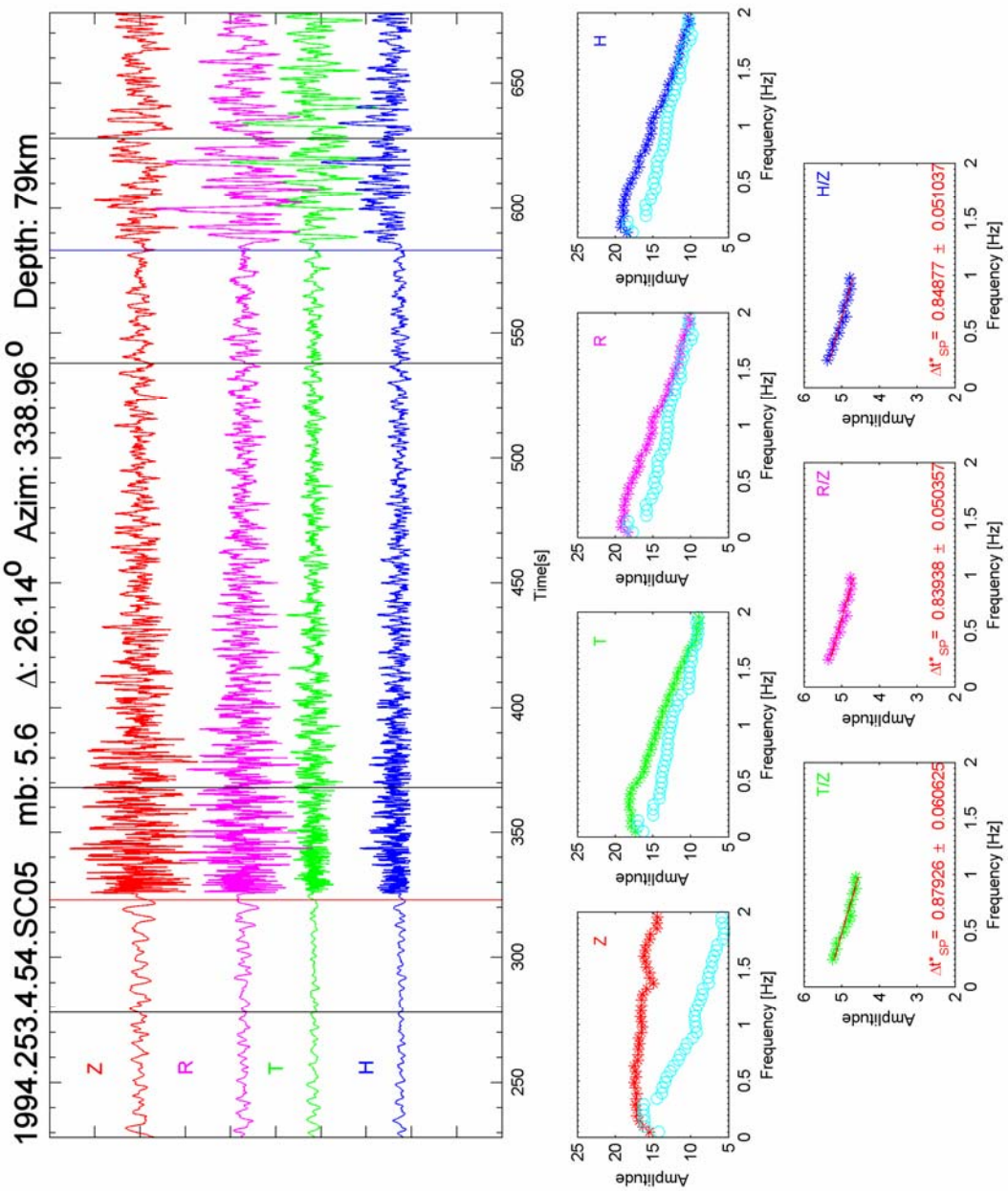

Figure 2.4: Examples of seismic signals recorded at the SC05 station with different epicentral distances and the vertical, radial, transverse and horizontal wave spectra and the spectral ratio measurements.

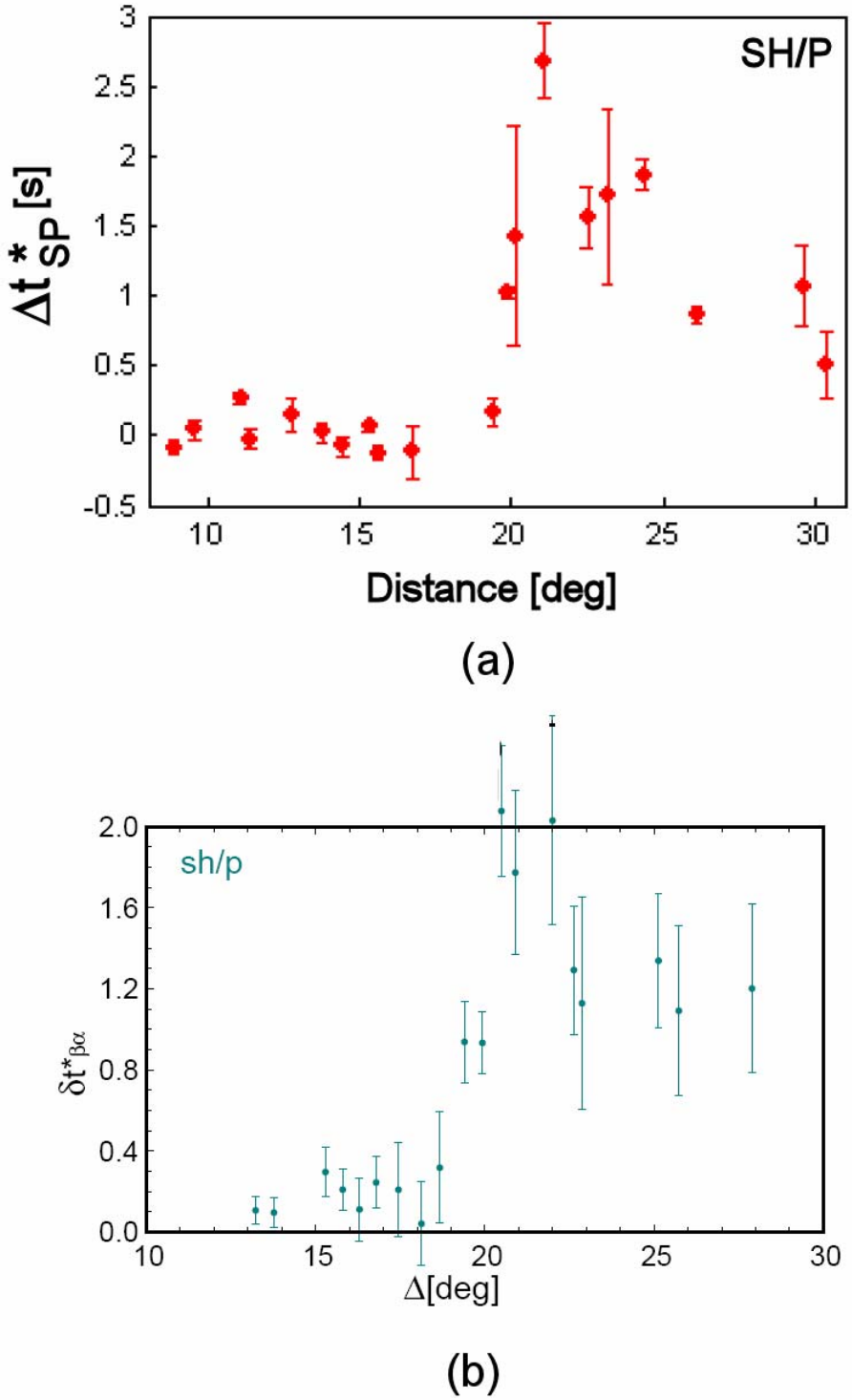

Figure 2.5: (a) Plot of measurements of logarithmic slope of spectral ratio as a function of epicentral distance in the frequency range from 0.1 to 1.00Hz for *SH* (top) component. Each dot represents a single datum with an error bar based on the quality of the linear fit to the spectral ratio. (b) The same plot of Cheng [2000].

The GUI is also applied to seismic datasets which are recorded from the recent project (TASMAL project, 2004). I choose 4 high quality datasets recorded by TL01 station. TL01 station is situated near the Tasman Line which is the line of separation of old Precambrian rocks in the central-west Australia from younger rocks in eastern part.

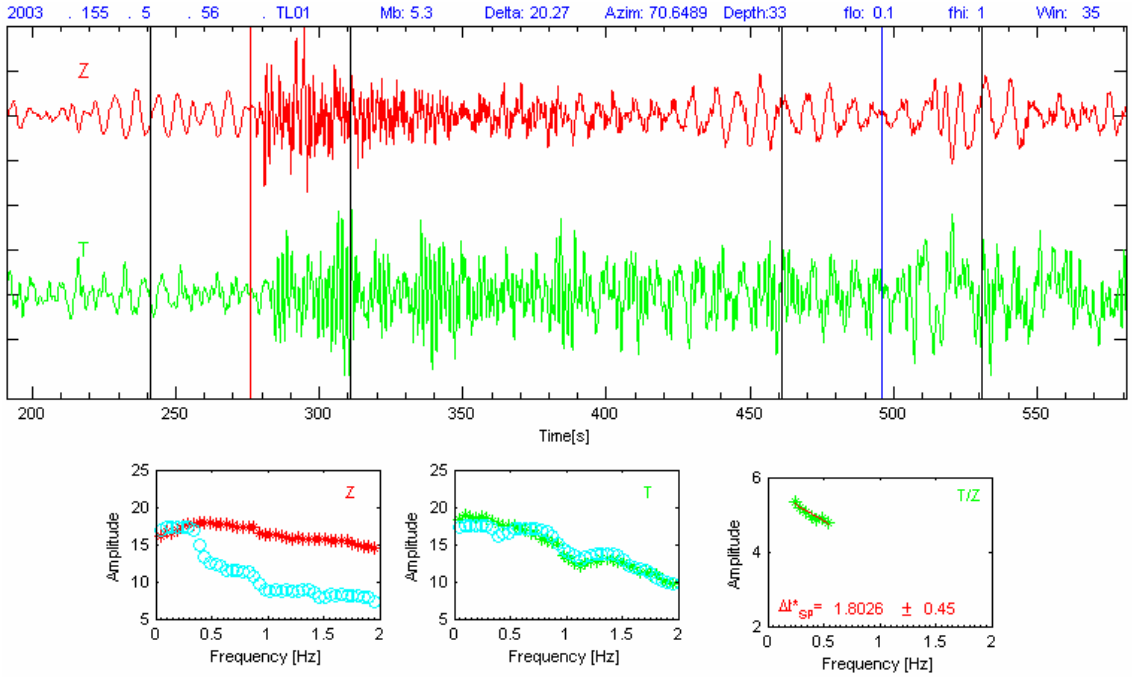

Figure 2.6 (a) azimuth: 70.65º; epicentral distance: 20.27º

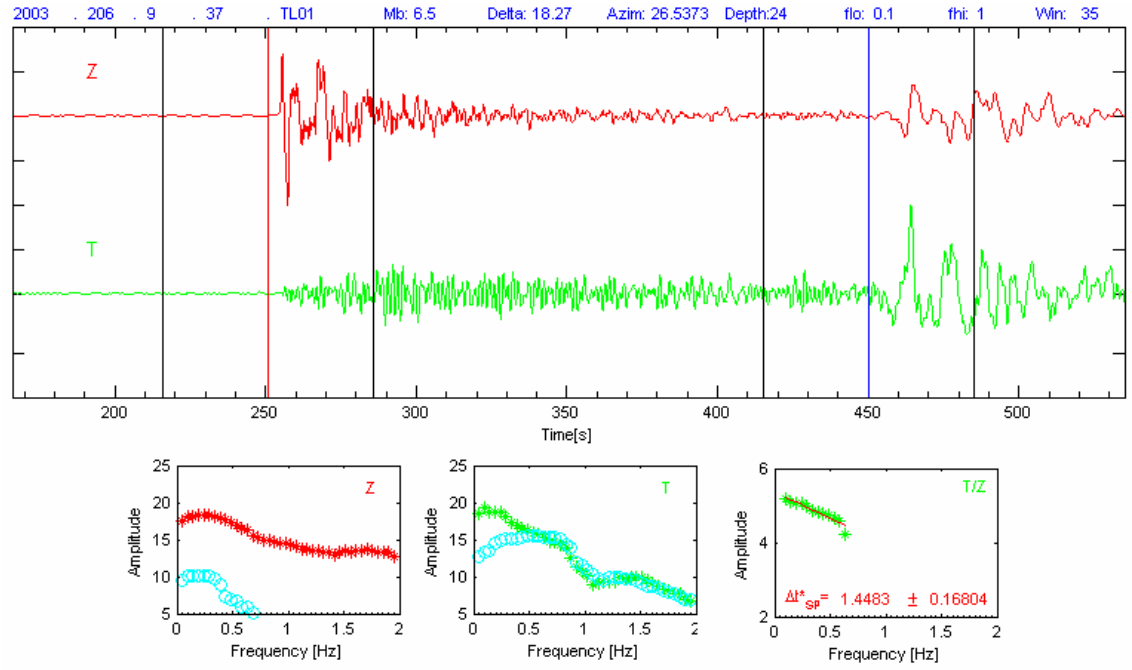

Figure 2.6 (b) azimuth: 26.54º; epicentral distance: 18.27º

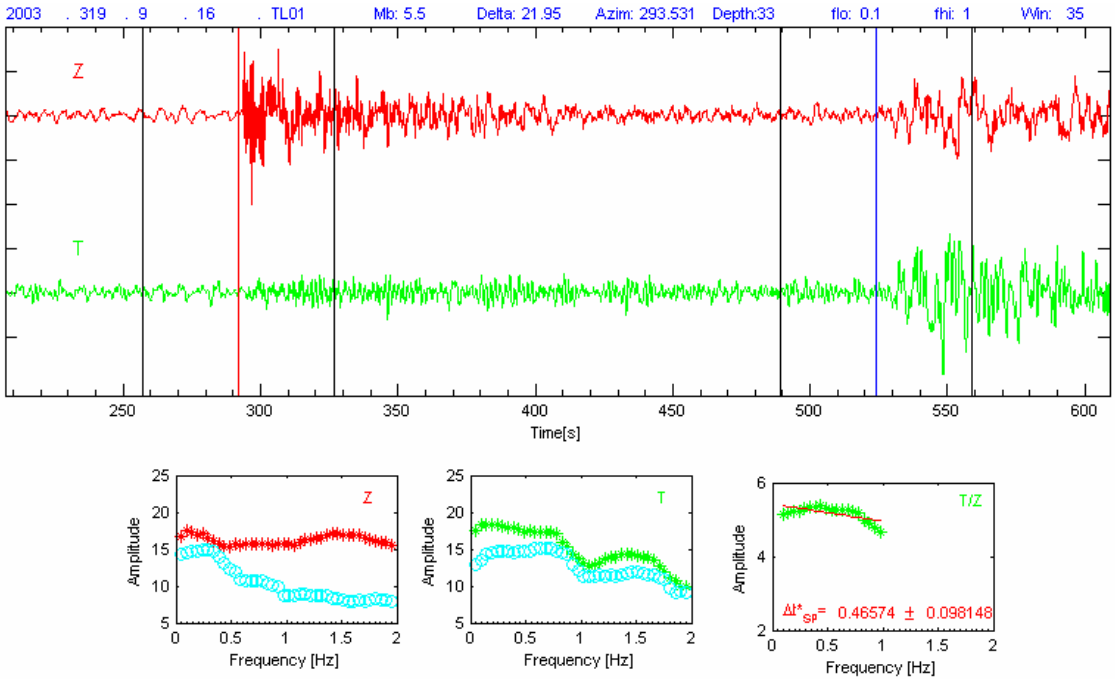

(c) azimuth: 293.53º; epicentral distance: 21.95º

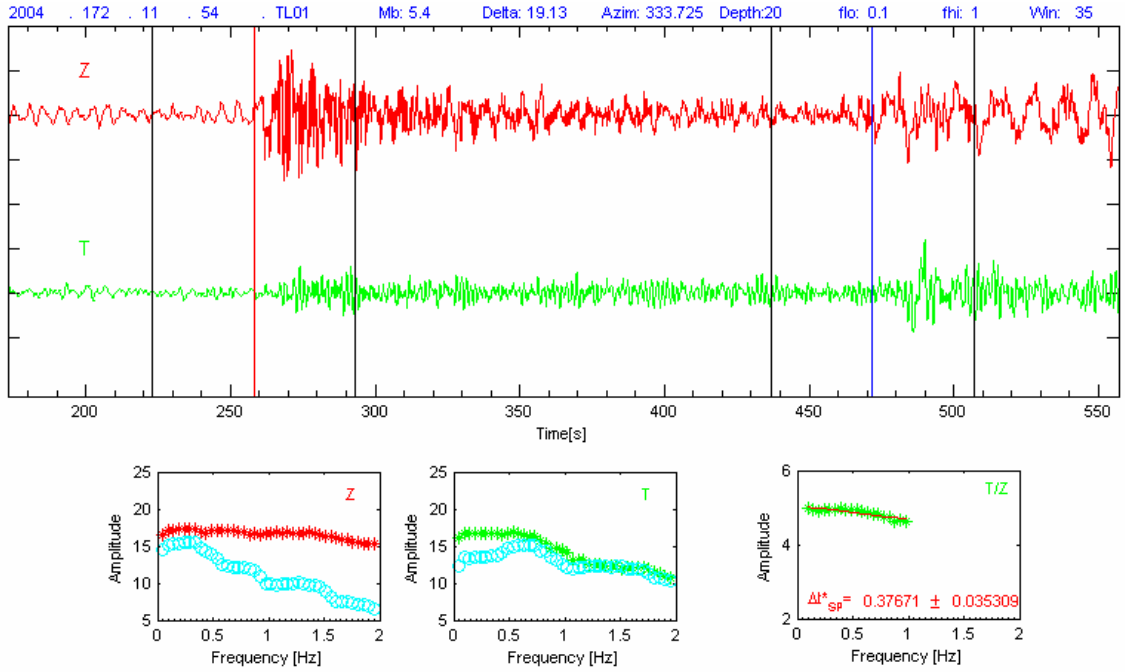

(d) azimuth: 333.73º; epicentral distance: 19.13º

Figure 2.6: The *S* to *P* differential attenuation (Δt^*_{SP}) estimation for TL01 station, *P* wave spectra is estimated from vertical component (red) and *S* wave spectra from transverse component (green). The signal spectrum is plotted as stars and the background noise is plotted as circles. (a) and (b) are paths from the east of Australia and (c) and (d) from the west.

(See Chapter 3 for more detail). The seismic events are taken for different azimuths relative to the station location. Figure 2.6 shows the Δt^*_{SP} estimation for TL01 station. The results of these measurements suggests that there is a correlation between values of the Δt^*_{SP} and lithological features. The Δt^*_{SP} results from the east (Figure 2.6 (a) and (b)) which are associated with young oceanic region, decay rapidly compare to paths from the west (Figure 2.6(c) and (d)) which are associated with the old cratonic region. All of these seismic paths are plotted in Figure 2.7.

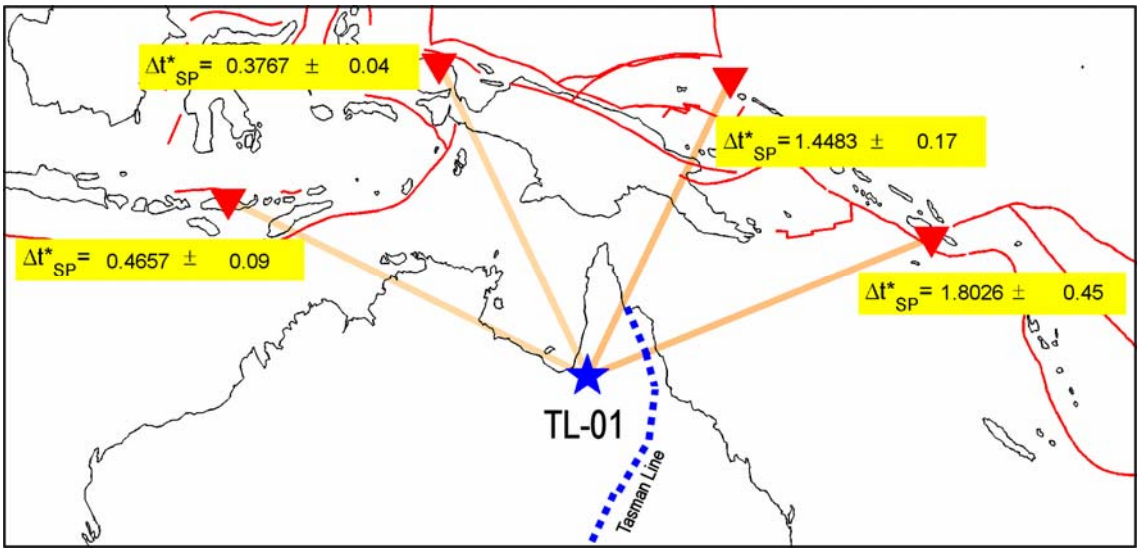

Figure 2.7: Seismic paths from four events (red triangles) discussed in Figure 2.6 above recorded at TL01 station (blue star) which is located around Tasman Line location (blue dotted line). The tectonic boundaries are illustrated in red lines. Note that the Δt^*_{SP} paths from the east are higher than those from the west.

The GUI which was developed based on the Station Ratio Method is also tested with 4 seismic datasets recorded by SKIPPY stations (SA04, SA05, SA06, and SA08). Again these four stations are located around the Tasman Line location for which, based on previous results, there is correlation between values of differential attenuation and geological features. The location of these stations, seismic event and propagation path can be seen in Figure 2.8. In this test, seismic data recorded by station SA04 station is

used as a reference. The values of Δt^*_{PP} and Δt^*_{SS} estimated from each station is also shown in the Figure.

Note that SA04 station which is located to the west of the Tasman Line has lower Δt^*_{PP} and Δt^*_{SS} than SA05 which is located to the east. This suggests that seismic waves traveling to SA04 are less attenuated than those traveling to SA05.

Representations of the application of the Station Ratio Method for each station are shown in Figure 2.9 (a), (b), (c) and (d) below. The top panel shows seismic data in time domain for vertical, radial, transverse and horizontal components. The left-bottom panel shows close up of *P* waves, its spectra and the Δt^*_{PP} estimation. The *P* waves and spectra of reference are drawn in red and the estimated data are in blue. The background noise spectra are drawn in green. The right-bottom panel shows Δt^*_{SS} estimation along with the value of each differential attenuation measurement and error in the estimation.

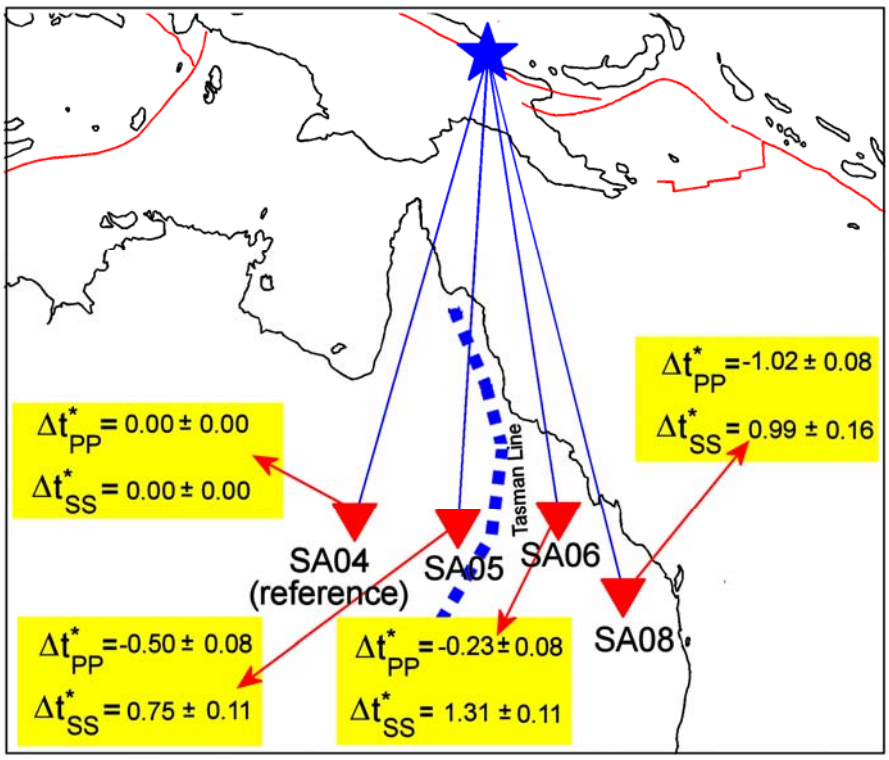

Figure 2.8: Seismic event and seismic station locations and great circle between the source and receiver path for seismic datasets used in the test of the Station Ratio Method. Blue triangle represents seismic events, red triangles represent seismic recorders. A blue dotted line is the geographical location of the Tasman Line. Red lines to the north of Australia show plate tectonic boundaries. In this measurement SA04 is used as a reference.

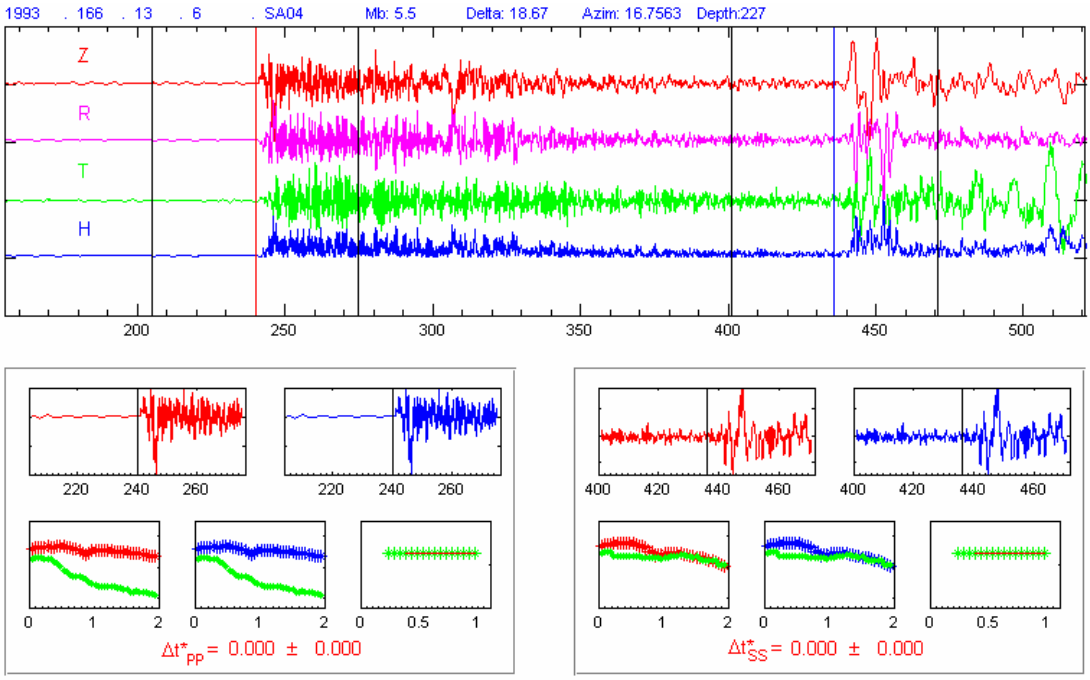

(a)

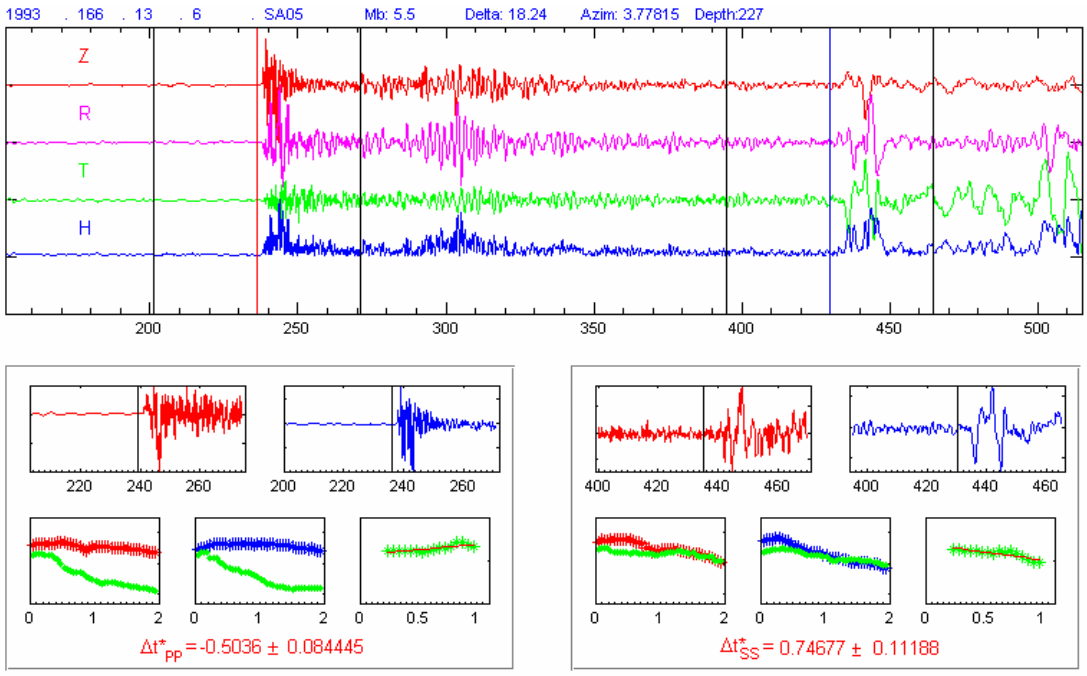

(b)

Figure 2.9: (continued)

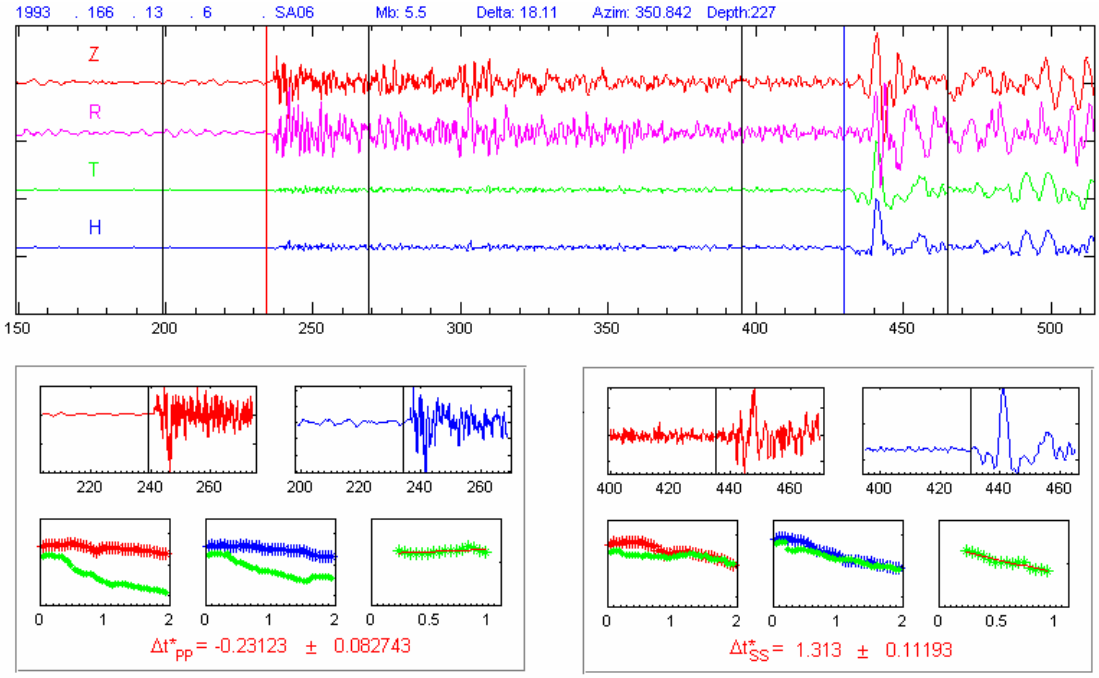

(c)

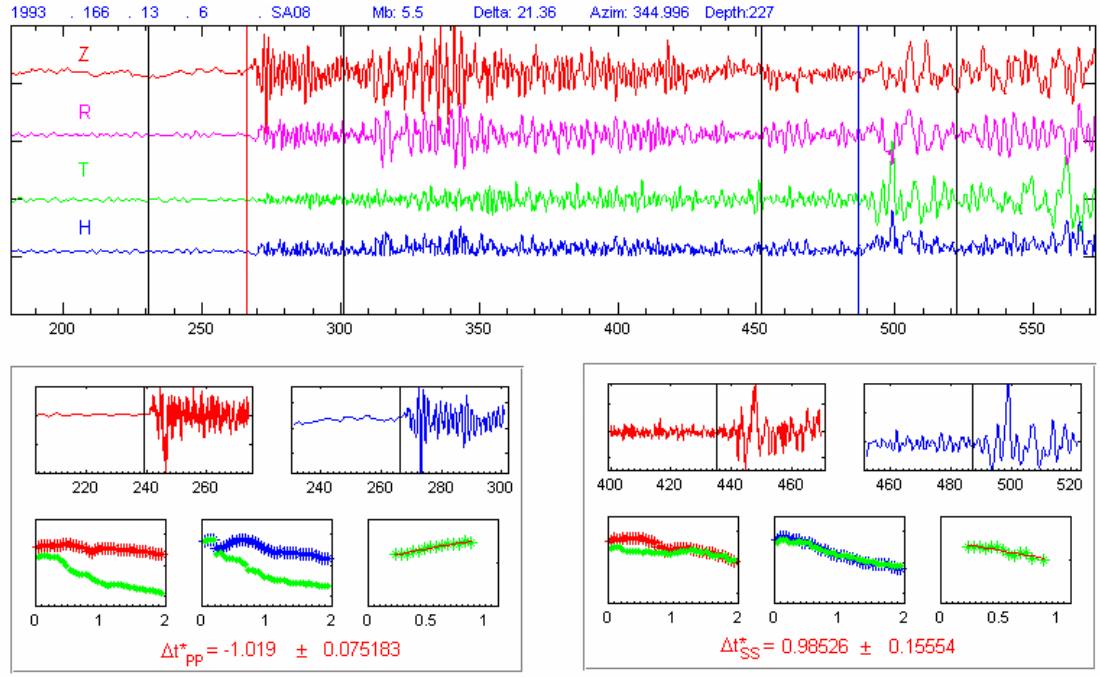

(d)

Figure 2.9: The *P* to *P* and *S* to *S* differential attenuation (Δt^*_{PP} and Δt^*_{SS}) estimation for the seismic data from an event in Irian Jaya recorded by SA04, SA05, SA06, and SA08 stations. (a) Estimation of the Δt^*_{PP} and Δt^*_{SS} for SA04 relative to itself (reference) resulting Δt^*_{PP} and Δt^*_{SS} equal to 0, (b), (c) and (d) the estimation of SA05, SA06 and SA08 respectively.

Chapter 3

Australasian Setting and Previous Seismic Studies of Australia

"Everyone is a product of their own experience. Hence geophysicists tend to favor geophysical methods and geologists tend to favor geological methods. It's only natural" [Brown, 2005].

The Seismologists observe seismic signals which have traveled through the earth. They analyze and manipulate this signal to understand geological features of the earth. Since correlation between the signal and earth features is not perfectly straight forward, a basic knowledge of geological features is needed to avoid misinterpretation.

In this Chapter, a broad outline of Australian geology and its tectonic setting is described. Also, geological interpretations from previous seismic studies are presented. This knowledge will be used as a platform for the interpretation of geological features of Australian regions from the attenuation images produced in this research.

3.1 Australian Setting

3.1.1 The Australian Continent

Based on studies of rocks at the surface, in general, the structure of the Australian continent is divided into three divisions which mark major stages in the evolution of the crust: the Archaean (older than 2500 Ma), the Proterozoic (2500-550 Ma) and the Phanerozoic (younger than 550 Ma). The Major Archaean outcrop lies in

the west and the Proterozoic rocks are found in the east of the continent (Figure 3.1). The Australian Continent is characterized by several cratons: Pilbara Craton, Yilgarn Craton, Gawler Craton, Curnamona Craton and Kimberley Craton. The Yilgarn Craton is characterized by granite-greenstone belts bounded by major strike-slip faults and shear zones, the south-western gneiss terranes and the gneissic Narryer terrane in the northwestern part of the craton. Based on seismic reflection data over the eastern Goldfields Province, it suggested that there is a three-layered crust [Drummond *et al.*, 2000]. The uppermost layer is formed by greenstone belts in the central and eastern parts of the section. The mid-crustal section (10-20km) consists of an east-dipping, west vergent duplex system, whereas the lower crust is characterized by shallowly dipping reflectors that are interpreted to represent ductile deformation [Drummond *et al.*, 2000]. The seismic reflection data also shows that the crustal thickness of the Yilgarn and Pilbara Cratons is between 30 and 35 km thick [Betts *et al.*, 2002].

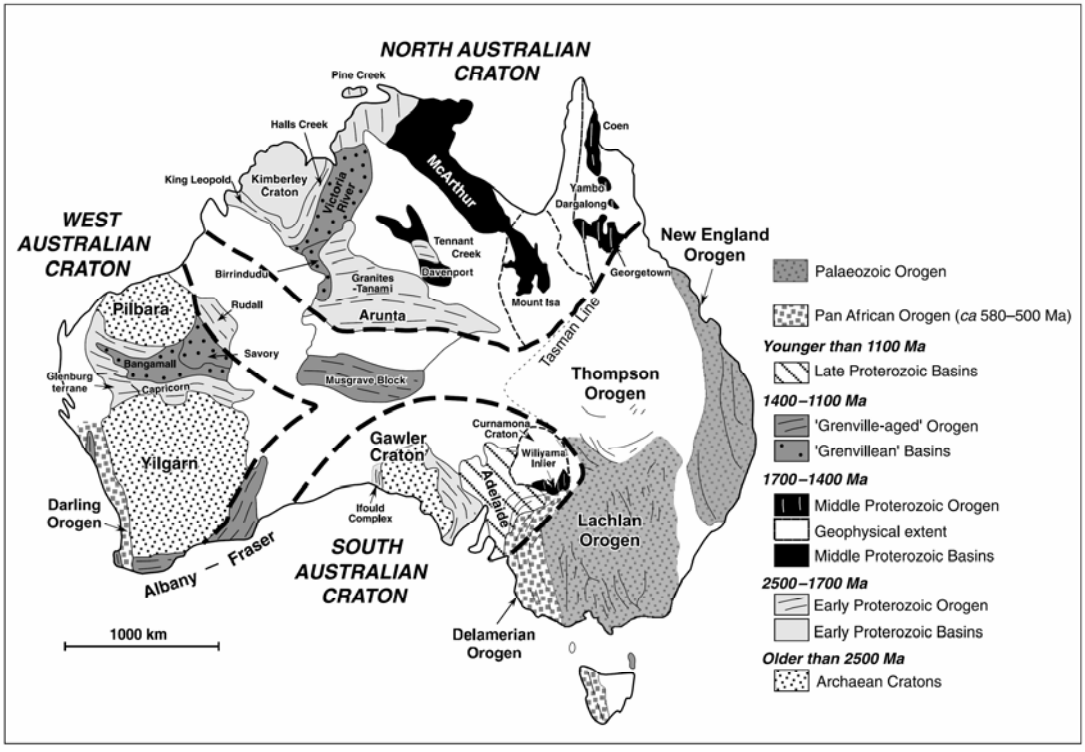

Figure 3.1: Geological map of the Australian plate showing major Archaean and Proterozoic terranes and Paleozoic Tasmanides. Note that central-western Australia is dominated by Archaean and Proterozoic while eastern part by Paleozoic [Betts *et al.*, 2002].

The Pilbara Craton is located to the north of the Yilgarn Craton comprises a central granite-greenstone belt characterized by a outcrop pattern dominated by 50-100 km diameter domal granitoid complexes, separated by synformal greenstones belts [Oliver & Cawood, 2001]. The Pilbara Craton consists of a series of early to mid-Archaean to Paleoproterozoic strata of the Hamersley Basin [Hickman, 1983].

Between the Pilbara and Yilgarn Cratons there is the Carpicorn Orogen which is characterized by regional metamorphism and plutonism with the main activity ending at 1840 Ma [Myers *et al.*, 1996]. According to the teleseismic receiver functions study of Reading & Kennett [2003] with three-component temporary stations were deployed in a line running southwards across Pilbara Craton, Capricorn and Yilgarn Craton, it is suggested that the crust-mantle boundary under the Pilbara Craton is shallow, at 30 km, with a sharp Moho and high-velocity crust beneath the exposed Pilbara granite-greenstone terrane. The Yilgarn Craton which extends beneath the basins exposed on the surface is deeper at 40 km. An anomalous region exists under the Southwest terrane which shows a thick high-velocity gradient zone at the base of the crust and a Moho dipping to the west. The character of the lateral heterogeneity in structure and its correspondence with terrane boundaries suggest that accretionary processes are significant in the evolution of the Yilgarn Craton.

In the south Australian region there is the Gawler Craton which is part of a complex collage of Archean to Mesoproterozoic metasedimentary and metaigneous terranes in southern Australia [Direen *et al.*, 2005]. The core of the Gawler Craton is comprised of Archean gneissic complexes, whose protoliths may be as old as 2.98 Ga [Dawson *et al.*, 2002].

The evolution of Tasmania region began as long ago as 800-750 Ma [Turner *et al.*, 1998], with prolific granite on King Island and deposition of thich turbidite sediment in North West Tasmania. Western Tasmania was formed in the Middle to Late Cambrian Tyennan Orogeny. The east of Tasmania contains no evidence of the Tyennan orogeny or Proterozoic outcrop [Elliot *et al.*, 1993]. The lithospheric structure

beneath Tasmania has been investigated using teleseismic tomography by Rawlinson *et al.* [2006]. They used 6520 relative *P* wave arrival time residuals from 101 distant earthquake recorded by 72 seismic recorders. Their images show marked transition from higher seismic speeds in the east to lower speeds in the west. Furthermore, the Tamar Fracture System does not overlie the narrow transition from relatively fast to slow speed. Farther in west region, an easterly deeping zone of relatively high velocity material beneath Rocky Cape Group and Arthur Lineament may be related to remnant subduction of oceanic lithosphere related with the mid-Cambrian Delamerian orogeny.

In the eastern part of Australian Continent, there are three major Orogens: the Lachlan, New England, and Thompson Orogens. The Lachlan Orogen is a turbidite-dominated orogen that forms the central part of the composite Palaeozoic Tasman Orogen [Coney *et al.*, 1990] along the eastern margin of Australia. Successive cratonisation from west to east included the Early Palaeozoic Delamerian Orogen (550-470 Ma), the Middle Palaeozoic Lachlan Orogen (450-340 Ma) and the Late Palaeozoic to Early Mesozoic New England Orogen (310–210 Ma), with their respective peak deformations of Late Cambrian - Early Ordovician, Late Ordovician - Silurian and Permian - Triassic age [Foster & Gray, 2000]. The Lachlan part is a Middle Palaeozoic orogen with a 200 million years history that occupies ~50% of the present outcrop of the Tasman Orogen [Gray & Foster, 2004]. The Lachlan and New England Orogens belong to an orogenic system that extended approximately 20,000 km along the eastern margin of Gondwana between the northern Andes and eastern Australia [Gray & Foster, 1998].

3.1.2 Surrounding Regions

In the surrounding regions of the Australian Continent there are several geological and tectonic features such as the Tasman Sea, the Coral Sea, the New Caledonia Basin, the Norfolk Ridge, the Australian Antarctic Discordance, the South

East Indian Ridge, the West Australian Basin, the Lord Howe Rise, the Macquarie Ridge, and the Indian-Antarctic Ridge (Figure 3.2).

The Tasman Sea is located to the east of the Australian Continent, it is an ocean basin which is bounded by the Lord Howe Rise and New Zealand to the east and to the south by major discordance that separates it from younger oceanic crust generated at the South East Indian Ridge and the extinct Macquarie Spreading center. In the northern part, it contains an elongated segment of continental crust, the Dampier Ridge which is separated from the Lord Howe Rise by two small basins: the Lord Howe and the Middleton basins. Based on tectonic lineaments visible in the gravity grid and interpreted as strike-slip faults, by magnetic anomaly, bathymetry, and seismic data, Gaina *et al.* [1998] identified 13 tectonic units. These 13 tectonic blocks and the Australian continent gradually separated due to either extensional or strike-slip movements, generating the Tasman Sea, the Lord Howe and the Middleton basins, and several failed rifts. The opening of the northern Tasman Sea is pretty well explained by the gradual stepwise separation of four Dampier Ridge tectonic fragments plus the Chesterfield Plateau and Australia in the frame work of a northward propagating rift.

Another major oceanic basin which borders the Australian margin to the east is the Coral Sea. The Coral Sea Basin is located northeast of Australia and is rimmed by several submarine plateaus such as the Queensland Plateau to the southwest, to the northwest by the Eastern Plateau, the Papuan Plateau to the North, the Louisiade Plateau to the northeast, and the Mellish Rise to the southeast. The Coral Sea basin is formed by Early Eocene oceanic crust [Gaina *et al.*, 1999].

According to magnetic anomaly interpretation and fracture zone data revealed from satellite-derived gravity anomalies, Gaina *et al.* [1999] derived finite rotations for the Coral Sea opening. These rotations are combined with the previous work of Gaina *et al.* [1998] in order to interpret the relative motion between the Louisiade Plateau, and the Mellish Rise. They revealed the existence of a triple junction between the Australian

Plate, Lousiade Plateau and several small plateaus attached to the northern Lord Howe Rise.

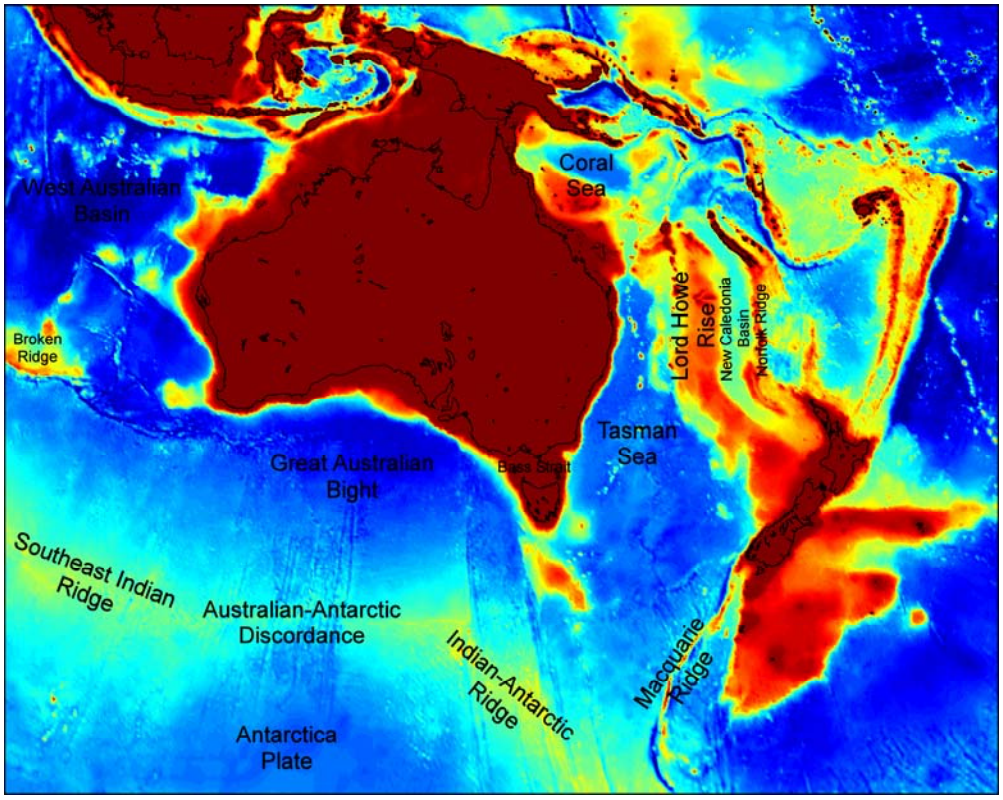

Figure 3.2: Geographic and Tectonic features in the surrounding regions of the Australian Continent [digital data courtesy of NOAA].

To the south of the Australian Continent, there is the Australian Antarctic Discordance which is a zone of subdued ridge morphology and a series of north-south trending fracture zones [Weissel & Hayes, 1974]. The Australian Antarctic Discordance is the deepest portion of the mid-ocean ridge system over a 600km long segment of the South East Indian Ridge. It is anomalous in terms of bathymetry and is characterized by unusual sea-floor morphology, isotope geochemistry, petrology, and seismic structure [Gurnis and Müller, 2003]. The Australian Antarctic Discordance has been associated with the location of former Mesozoic position of long-lived seduction on the Pacific margin of Australia. Seismic tomographic images suggest that beneath this former Mesozoic margin is a linear north-south high velocity seismic anomaly within the lower

mantle and a high velocity anomaly within the transition zone, as originally predicted by dynamic models [Gurnis and Müller, 2003].

To the west of Australia, there is the West Australian Basin. This basin is the oldest sea floor formed during the Jurassic (155 Ma). Based on surface wave study of Fishwick [2005], beneath the old West Australian Basin, fast shear velocity perturbations are determined.

To the north west of the continent, complex subduction zones exist between Australian and Eurasian plates. Tomographic images of Widiyantoro [1997] reveal the slab in the upper mantle resembles the present day Java trench, Timor trough, the curved Banda arc, and the Molucca Collision Zone. This study also indicated the presence of fast *P* wave speed beneath northern Australia.

3.2 Previous Seismic Tomography and Seismic Attenuation Studies of Australia

Studies on seismic tomography of the Australasian region have exploited the data availability from deployments of broadband instruments. In the SKIPPY experiment from 1993 to 1996 [van der Hilst *et al.*, 1994], recorders were deployed across the whole continent at approximately 400 km spacing. Subsequently in 1997 and 1998 a denser array of broadband instrument (KIMBA) were deployed in northwestern Australia. In 1999 additional recorders were installed in southeastern Australia (QUOLL). In 2000-2001, Western Australia was revisited with a broadly spread array to supplement the SKIPPY stations which had had technical problems. In less than a decade there has been a very thorough coverage of the Australian continent with broadband seismic stations. The high quality seismic data availability at a suitable distance from events in surrounding region with a dense stations spacing is ideal to explore the deep structure beneath the continent using seismic tomography technique.

3.2.1 Tomography Studies of Australia

Tomography studies of Australia have been conducted by using many types of seismic waves: surface waves, body waves, *Lg* coda, etc. Studies on surface wave tomography have been initiated by Zielhuis and van der Hilst [1996] by analyzing Rayleigh wave data from the stations in eastern Australia deployed in the SKIPPY experiment. Their model suggests the presence of a major contrast in the shear wavespeed in the mantle component of the lithosphere between central Australia and eastern Australia. The model revealed the presence of lowered shear wavespeeds beneath the east coast of Australia at depths around 140km which has a strong correlation with Neogene volcanism.

The Australian surface wave tomographic models have been improved as more data have been incorporated by van der Hilst *et al.* [1998] and Simons *et al.* [1999]. The shear wavespeed distribution for *SV* waves at 140, 200 and 300km depths derived from this inversion are presented in Figure 3.3 below.

Shear wave velocity contrasts between eastern Australia and central Australia (between 140ºE and 145ºE) is clearly pronounced at 140 and 200 depths and may be associated with the controversial Tasman line. The zones beneath the exposed Precambrian rocks in the west and central Australia are associated with high seismic wavespeeds. The Precambrian regions show the presence of significant internal structure with an indication of the separation of the major cratonic blocks, especially at shallower depths. The high seismic wavespeed anomaly at 300 km depth is concentrated in the central Australia. The seismic speed perturbation at this depth is less than the shallower structure, this anomaly could be associated with real geologic features in the upper mantle or might be correlated with the sampling pattern of lateral resolution.

Tomographic models from surface wave tomography was then improved by Yoshizawa and Kennett [2004] by using more seismic data and introducing a three-stage approach incorporating finite frequency effects.

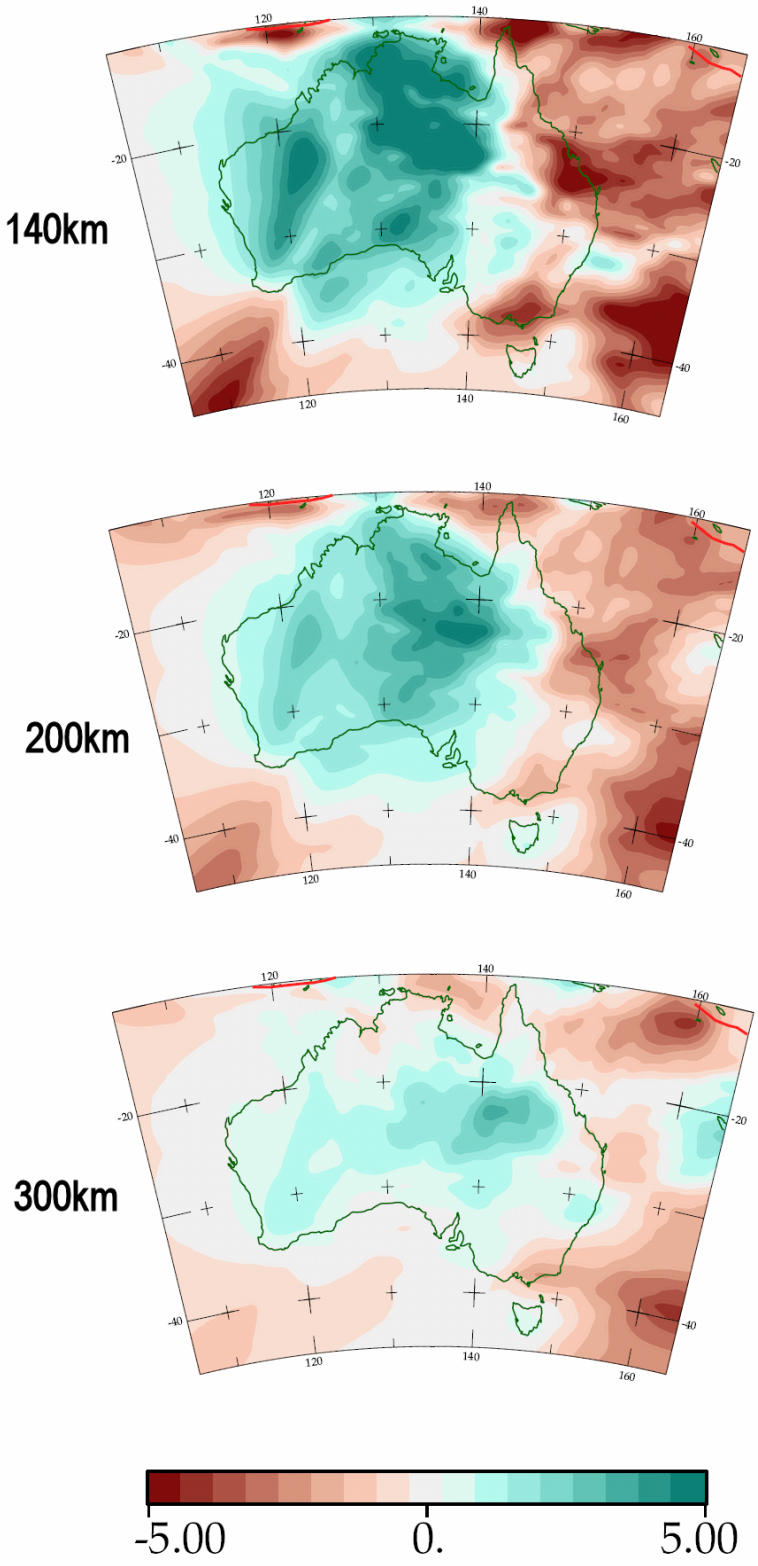

Figure 3.3: Three Dimensional shear wave speed model from 2000 Rayleigh waves using the Partitioned Waveform Inversion. Map views at 140 km, 200 km and 300 km depth [van der Hilst *et al.*, 1998].

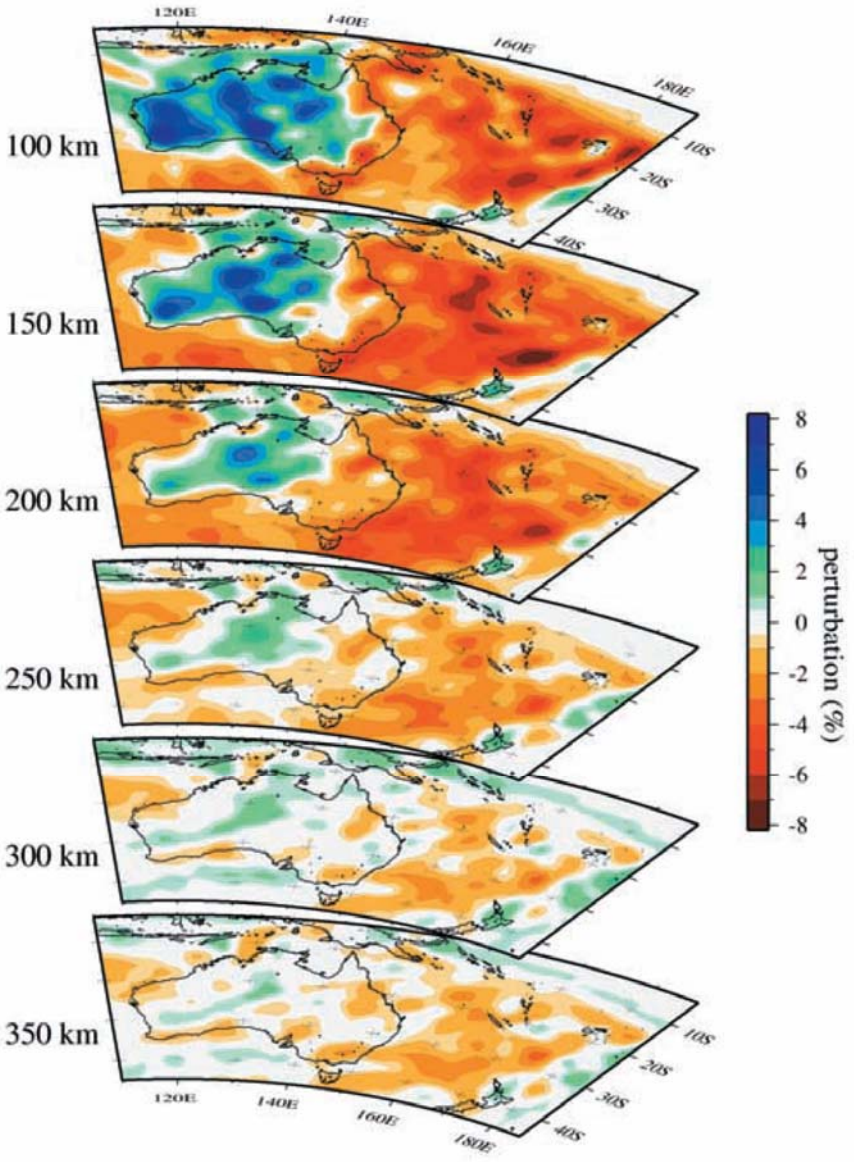

Figure 3.4: Shear wave speed model in the upper mantle. Reference velocities are 4.41 km/s at 100 km, 4.43 km/s at 150 km, 4.51 km/s at 200 km, 4.61 km/s at 250 km, 4.70 km/s at 300 km, and 4.75 km/s at 350 km [Yoshizawa and Kennett, 2004].

In general, the major features of Yoshizawa and Kennett's tomographic models are quite similar to those of the corresponding maps of van der Hilst *et al.* [1998]. Down to 200 km depth the cratonic slab in central and western Australia is characterize by high shear velocity and the oceanic crust in eastern seaboard is characterized by low shear velocity.

The availability of three-component seismic data allows the exploitation of polarization anisotropy beneath the Australian Continent. Debayle & Kennett [2003] presented radial anisotropy in term of the ratio between tangential (*SH*) waves velocity and radial (*SV*) velocity. Their result is presented in Figure 3.5. As can be seen from the figure, at slice 125km depth, in the continental region of Australia and in the subduction zones in the north, the value of the anisotropy is higher than 1 which is illustrated by green color scheme. In such regions the polarization anisotropy is such that *SH* is faster than *SV*. The vertical cross section of the anisotropy at -25ºS suggests that at central and eastern Australia *SH* is faster than *SV* down to 200-250km. The area where *SH* is faster than *SV* is the eastern region may be associated with the part where horizontal flow dominates in the upper mantle.

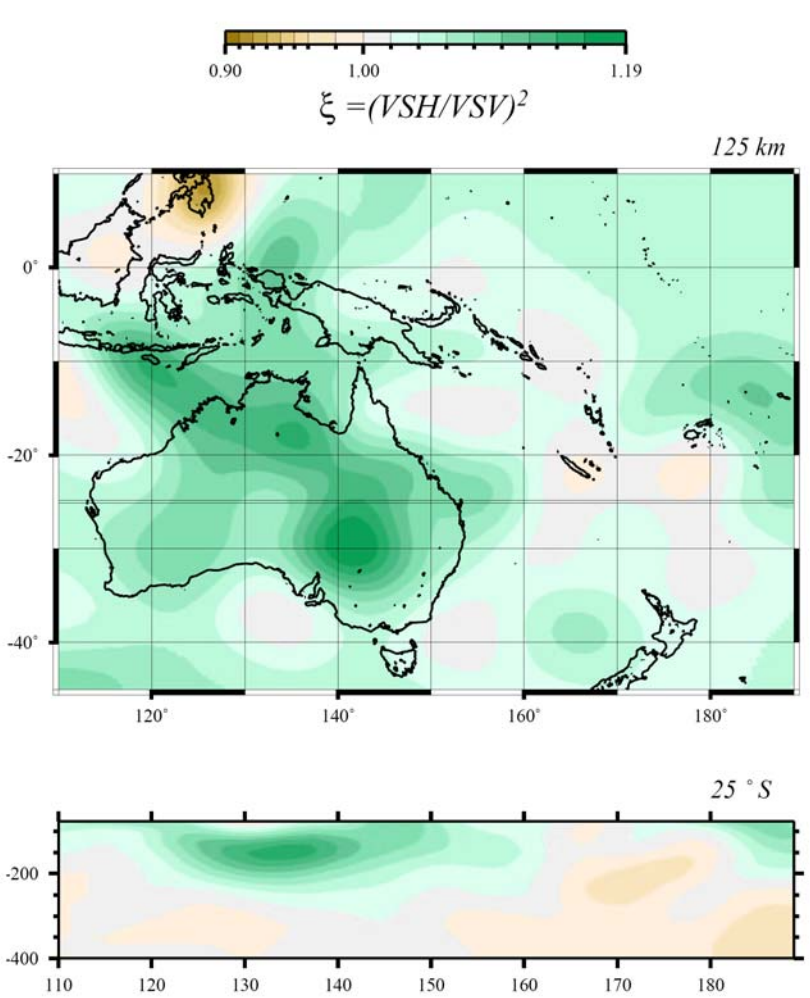

Figure 3.5: Distribution of polarization anisotropy model at slice 125km depth and vertical cross section at -25ºS [Debayle & Kennett, 2003]

The recent work on surface wave tomography has been conducted by Fishwick [2005] as more data from all Australian National University temporary deployments and additional data from permanent stations and temporary deployment in New Zealand are incorporated.

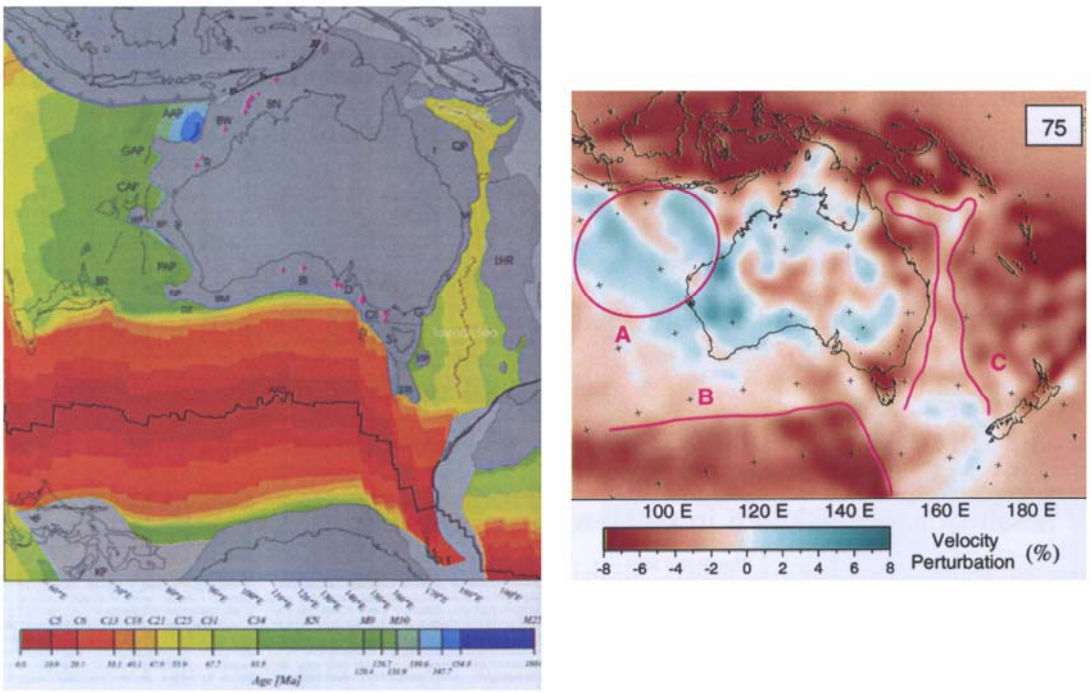

Figure 3.6: Correlations between age and shear wave speeds anomaly in Australasian [Fishwick, 2005].

Figure 3.6 above shows the shallowest layer of the tomographic model in a slice at 75km depth. The model suggests correlations between shear wavespeeds and geological structures in the oceans surrounding Australia. Evidence from the depth of the sea floor and the reduced heat flow away from mid-oceanic ridges suggests that the oceanic lithosphere cools with increasing age. The image suggests that shear wavespeeds increased with increasing age. Beneath the old West Australian Basin (A), fast shear velocity perturbations are observed, and beneath the young Southeast Indian, and Indian-Antarctic ridge system (B) much lower wavespeeds are imaged. To the east of Australia, the fastest wavespeeds are observed beneath the Tasman and Coral Sea and appear to be related to the coherent area of sea floor spreading (C).

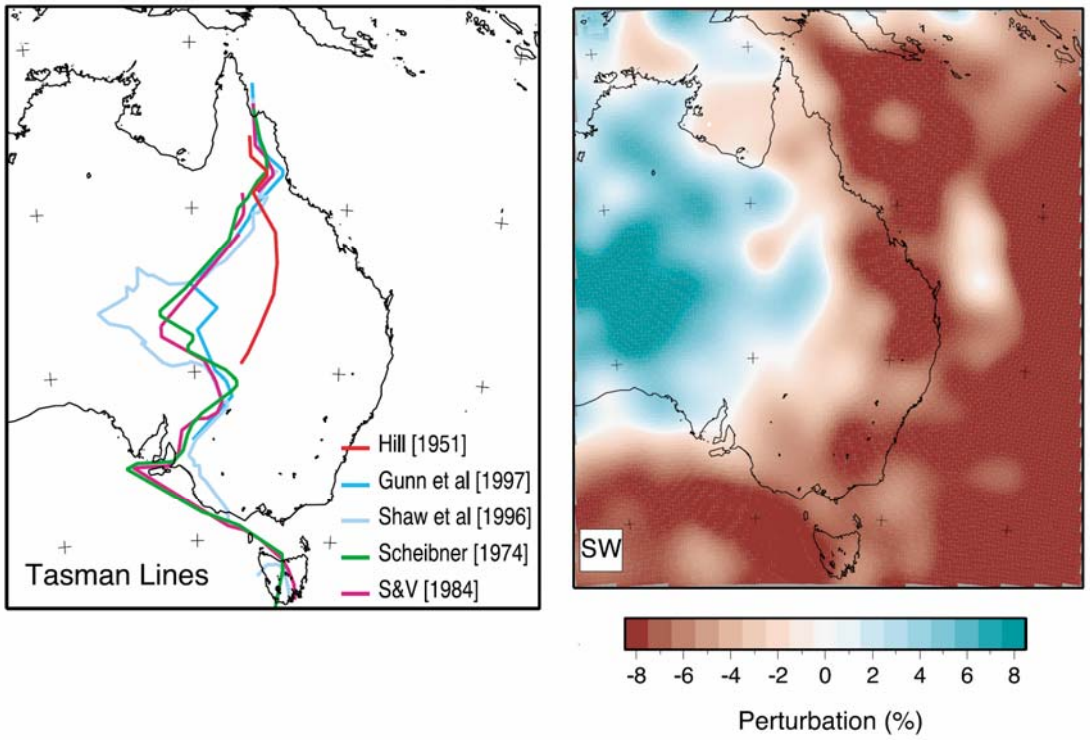

Figure 3.7: Correlations between Tasman Line concept and surface wave tomography at 150km depth [Fishwick, 2005].

The shear wavespeed slice at 150km depth derived from surface wave tomography is presented in Figure 3.7 along with locations of proposed Tasman Lines. At this depth the transition from slower to faster velocities is not a simple linear feature and appear to be a somewhat complex boundary between 138ºE and 143ºE [Fishwick, 2005].

The seismic structure beneath the Australasian regions also has been analyzed using seismic traveltimes tomography. Gorbatov and Kennett [2001] presented compressional (*P*) and shear (*S*) waves models derived from a data set contains 544690 *P*-wave and 393866 S-wave ray paths. All arrival times were selected from the catalog which have source or receiver located within the zone of study (95ºE to 190ºE; 50ºS to 10ºN). Since calculations of 3D ray paths for a large amount of data are very time consuming they combined the information from event clusters in a 2º x 2º x 50 km volume and station clusters in a 2º x 2º region into a single summary ray path for the region outside of the zone under study.

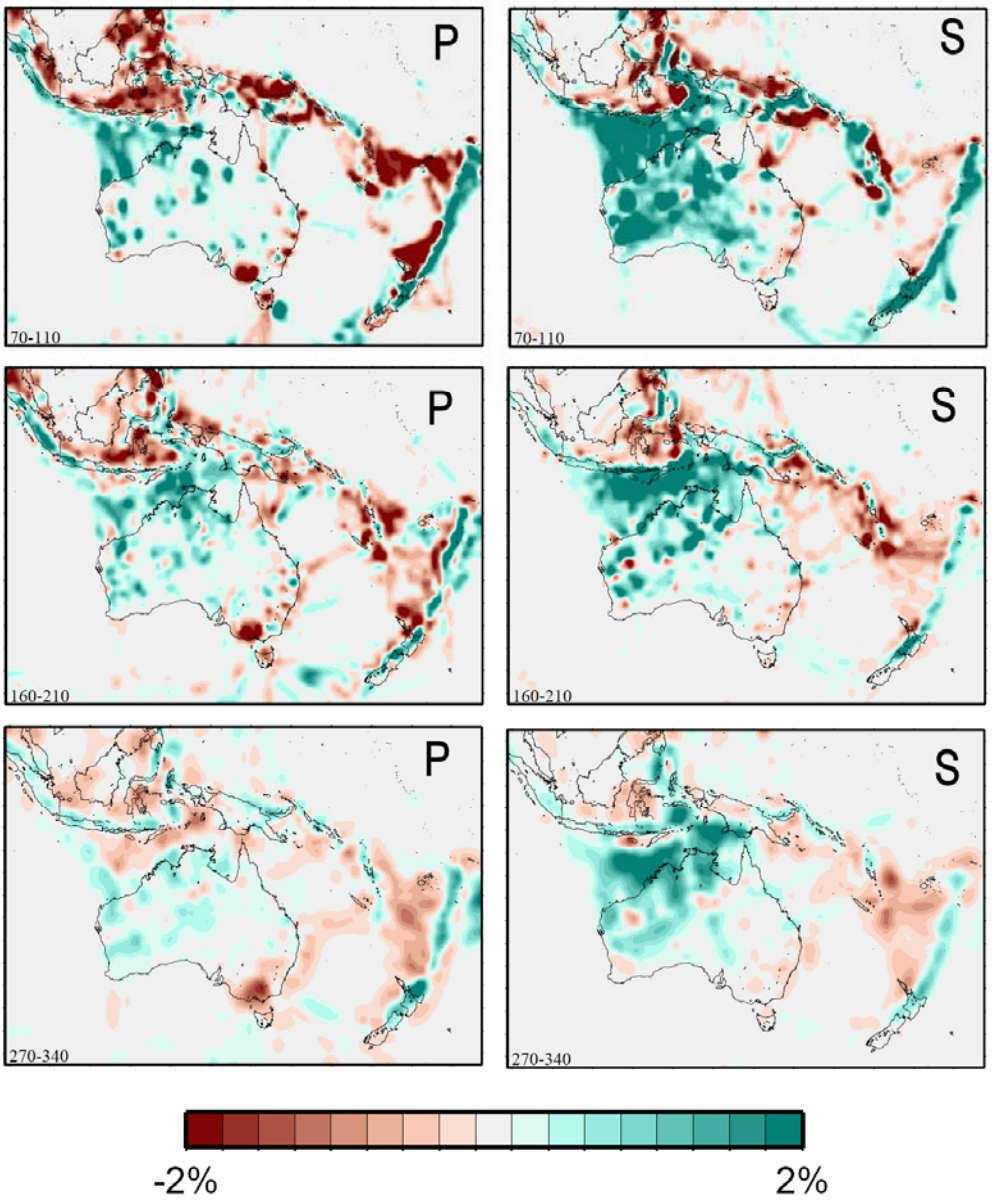

Figure 3.8: *P* (left) and *S* (right) wave tomographic models derived from traveltimes tomography at 70-110km, 160-210km and 270-340km depth. The colorbar is presented in percent relative to ak135 model [Gorbatov and Kennett, 2001]

The residual time assigned to the summary ray was the median of all the relevant data selected for summary ray path. Each summary ray was composed of at least three individual rays. The resulting data set contains 544690 *P*-wave and 393866 *S*-wave ray paths. The region of interest was parameterized by irregular cells from 0.5ºx0.5º to 1ºx1º and 19 layers down to the depth of 1600 km. The whole Earth mantle was parameterized by cells of 5ºx5º and 16 layers. The reference 1D Earth's velocity

model was *ak135* of Kennett *et al.* [1995]. The extended pseudobending ray tracing algorithm of Koketsu and Sekine [1998] is implemented in their tomographic code. The tomographic models for *P* and *S* waves at 70-110, 160-210, and 270-340km depth are presented in Figure 3.8. The *P* and *S* wave images are plotted using the same color scale of perturbation and so the high relative variations associated with *S* waves can be seen. The main subduction zones are clear in both the *P* and *S* images at around 135 km depth, and the fast wavespeeds in the Australian craton show up in patches reflecting the available path distribution.

3.2.2 Seismic Attenuation Studies of Australia

Seismic attenuation studies of the Australian continent have been conducted over the last two decades using different data sets and methodology. The studies before the deployment of broadband recorders (1992-presents) only used seismic signals recorded by short period recorders (1975-1993) from which attenuation profiles beneath a particular study area are determined.

Gudmundsson *et al.* [1994] presented an attenuation profile of the upper mantle beneath the north of the continent from the analysis of 22 broadband seismograms over the epicentral distance range from 12-30 degrees. They measured differential attenuation between *P* and *S* waves using the spectral ratio method. The attenuation profile produced from their modelling along with plot of behaviour of attenuation as a function of epicentral distance is presented in Figure 3.9. The measured slope of the S/P spectral ratio is consistently small out to 18º epicentral distance, where it increases dramatically. Their attenuation measurements are consistent with an average quality factor for *S* waves in the lithospheric lid of Q_S =1400 (Qp=2800) on the top of a highly attenuative asthenosphere of 200 km thickness with Q_S =100 (Qp=200), which is underlain by a transition zone with Q_S =600 (Qp=1200).

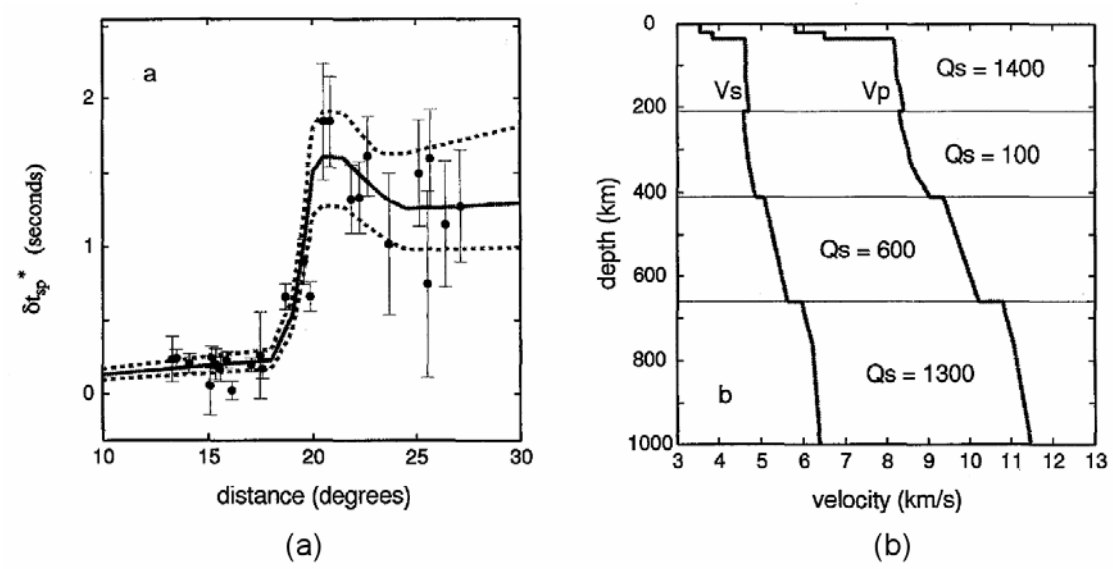

Figure 3.9: (a) Plot of differential attenuation as a function of epicentral distance. Each dot represents a single datum with a 1 SD error bar based on the quality of the linear fit to the spectral ratio. The solid curve represents the data fit produced by the Q model presented in (b). The dashed curves represent bounds on data predictions. (b) Plot of the velocity models used in the modeling as well as the Q model. [Gudmundsson *et al.* 1994]

Mitchell *et al.* [1998] have exploited *Lg* Coda Q (Q_{Lg}^{c}) from ground motion recorded by seven seismic stations across Australia. They presented tomographic image of Q_{Lg}^{c} and its frequency dependence at 1 Hz for almost the entire continent at low resolution. Their images suggest that Q_{Lg}^{c} at 1 Hz in Australia varies between about 330 and 600. The Tasman Fold Belt in eastern Australia is characterized by the lowest value of Q_{Lg}^{c} (330-400); they argued that this lowest value might be associated with fluids produced by orogenic activity which occurred during the Devonian and Carboniferous periods or by sedimentation that occurred in Jurassic and Triassic times. Meanwhile, the central and western Australia regions are also characterized by low Q_{Lg}^{c}. Smaller reduction of attenuation in these regions might be associated with sedimentation over the periods of Precambrian and Carboniferous or with deformation which occurred in the central Australian Mobile Belts during the carboniferous period.

The property of the frequency dependence of Q_{Lg}^{c} at 1 Hz (η) suggest that in the Tasman Fold Belt of eastern Australia the lowest values of for η correlate with low

values of attenuation. In the regions where resolution is poor and standard errors are high associated with low η. The frequency dependence η for the entire continent lies in the range 0.65 to 0.75, however there are two regions of very high η (nearly 1.0) in the northern part o Australia.

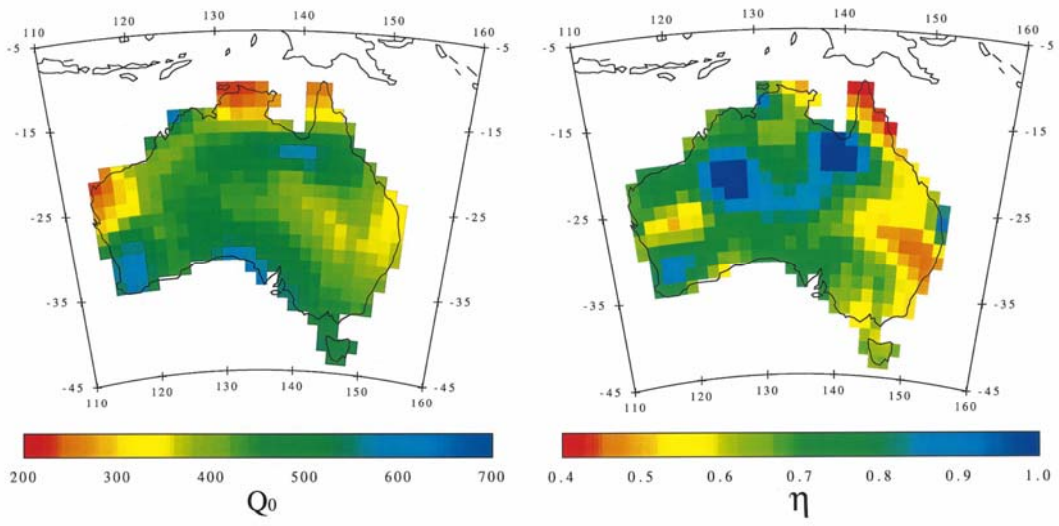

Figure 3.10: Tomographic image of *Lg* coda *Q* at 1 Hz for the entire Continent of Australia (left) and tomographic map of the frequency dependence of *Lg* coda *Q* at 1 Hz (right). [Mitchell *et al.*, 1998]

The low values derived for Q_{Lg}^{c} may be influenced by the assumptions made for geometrical spreading that are based on a sharp transition at the Moho. With a gradient at the base of the crust the Q_{Lg}^{c} is raised.

The most recent study of Attenuation was conducted by Cheng [2000]. He studied the Australian attenuation structure by estimating the spectral ratio of nearly 2000 seismograms recorded during the SKIPPY project with 73 temporary broadband three-component seismic stations and KIMBA project with 10 broadband stations in the Kimberly block. He again used the spectral ratio method of Gudmundsson *et al.* [1994] which is ratio of spectra between *P* and *S* waves. He predicted each spectrum using a single taper of Fast Fourier Transform (FFT) method. Over a narrow frequency band (< 1Hz) the slope of the logarithm of the spectral ratio is measured as the differential attenuation between *P* and *S* waves (Δt_{SP}^{*}).

Cheng organised the measured differential attenuation data into azimuthal corridors and then inverted the Δt^*_{SP} values using the Neighbourhood Algorithm (NA) of Sambridge [1999] to produce a set of 1-D Q profiles. A 3-D Q model at fixed frequency was then constructed by combining these 1-D Q profiles weighted by ray density.

Figure 3.11 below shows the pseudo 3-D Q model in the upper mantle beneath the Australia region using 2 x 2 degree cells (left panel). The Q model figure suggests that variation in attenuation is clearly pronounced in the Lithosphere (down to 210 km depth). The eastern part of the continent is characterized by high attenuation, while the central and western part is characterized by low attenuation. Below 210km depth there is no significant attenuation variation. This may be related with homogenous lithology.

Cheng also examined the seismic data up to 6.0 Hz to determine frequency dependence of attenuation (α) in the Australian region. The frequency dependency parameter is also estimated directly from the spectral ratio. It is assumed that there is a simple power law dependence of frequency, using this assumption the spectral ratio information is used. The frequency dependence parameter is extracted from the rate change of the logarithmic slope of the spectral ratio with frequency.

The geographical variation in frequency dependence of attenuation is shown in the right panel of the Figure 3.11. The raypaths covering the north-west part of the Australian continent show α close to zero with a small error in α; so that the frequency dependence of Q in this area is relatively weak. Meanwhile, in the eastern part of Australia and Coral Sea area, there is a mixture of paths with small and larger α so that the frequency dependence in those areas is more complex and depends on the depth of penetration of the waves.

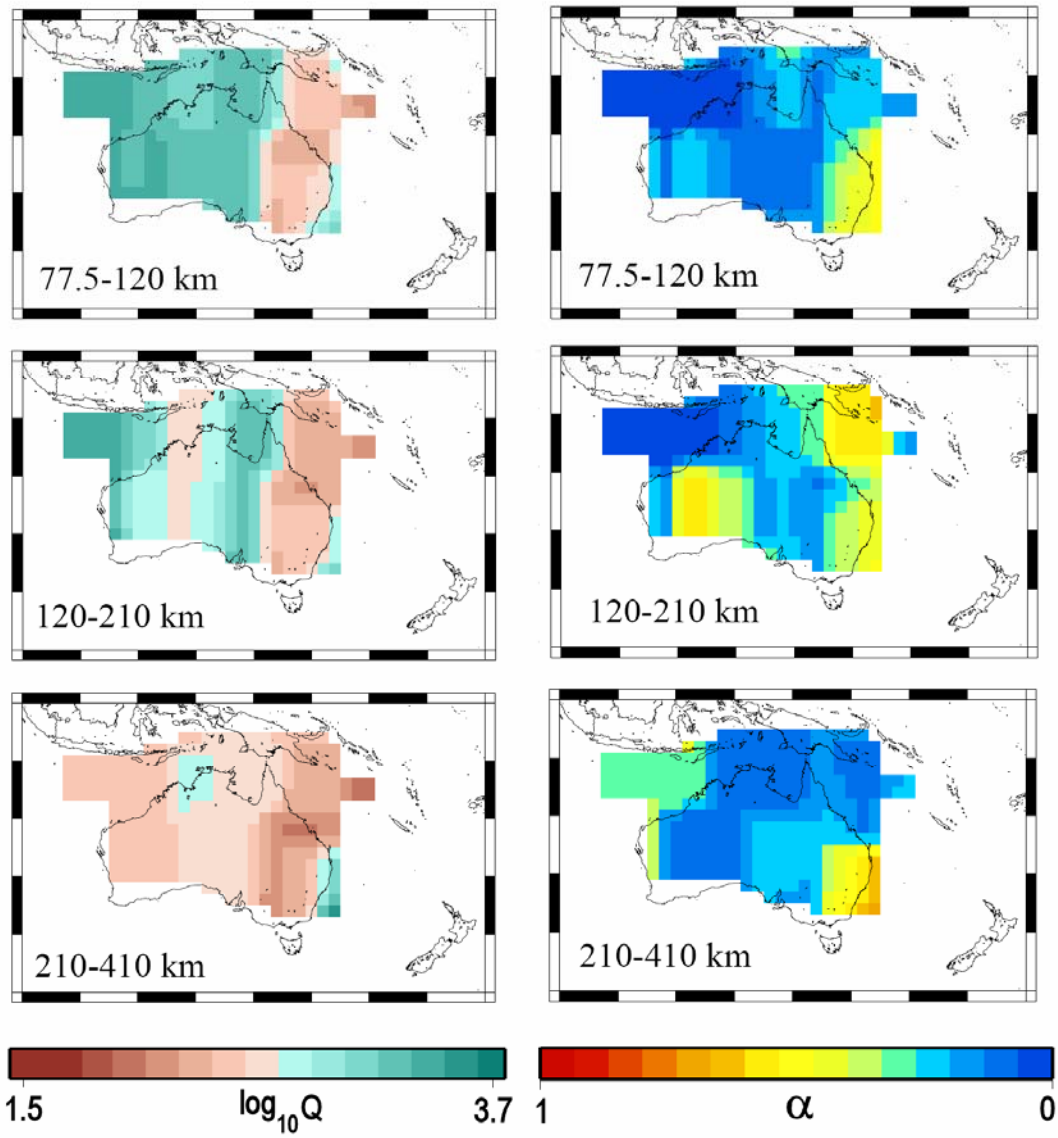

Figure 3.11: Pseudo three dimensional Q model in the upper mantle beneath the Australia region. The Q model was obtained by averaging the set of 1-D Q^{-1} profiles weighted by using three sets of ray density functions (left). Frequency dependence model of Australia α (right) [Cheng, 2000].

Chapter 4

Seismic Speeds and Attenuation Tomography-Part I[1]

4.1 Seismic Data

Thousands of seismic events from the region have been archived since 1992 by the Research School of Earth Sciences, Australian National University from a major program of deployment of portable broad-band seismic stations across Australia in experiments primarily designed to improve knowledge of the 3-D structure of the region. The SKIPPY experiment (1993-1996) with a sequence of 6 progressive deployments across the continent with an inter-station spacing of around 400km provided the first coverage of the whole of Australia and its surroundings. Subsequent experiments have been on a range of scales, including detailed studies of the Kimberley region, SE Australia and Tasmanian and broader scale coverage of Western Australia and the surroundings of the Tasman line marking the edge of Precambrian outcrop.

The recorders used in the SKIPPY and KIMBA projects are Refraction Technology units with 24-bit Analogue-to-Digital Conversion (ADC) and an internal Global Positioning System (GPS) corrected clock. Data were originally continuously recorded using a Digital Audio Tape (DAT) drive. The DAT drive was replaced by

[1] Part of this Chapter was presented for a poster session in the European Geosciences Union in Vienna 2006 and has been submitted to Earth and Planetary Science Letters 2007.

external disc drives for KIMBA and later projects. The sensors in the field are three-component broadband Güralp CMG-3ESP seismometers that are flat in velocity response from 30mHz to 30Hz. Four seismometers are flat to 0.016Hz (62.5s period) (type 1) while the remaining eight are flat to 0.033Hz (30 s period) (type 2).

Data is digitized at 25 samples per second and with the flat velocity response of the sensors and 24-bit ADC ensures very high data quality. Data are extracted for selected earthquakes (based on simple magnitude-distance criteria) from the Preliminary Determinations of Epicenters (PDE) catalogue, published by NEIC.

The equipment of Refraction Technology units with 24-bit Analogue-to-Digital Conversion (ADC) and an internal Global Positioning System (GPS) corrected clock is also used in QUOLL, WA, TIGGER, and TASMAL experiment. In QUOLL, WA and TIGGER experiment seismic data are collected in Orion and Reftek format, while in TASMAL project, seismic data are collected in Earth Data format (day files in miniseed).

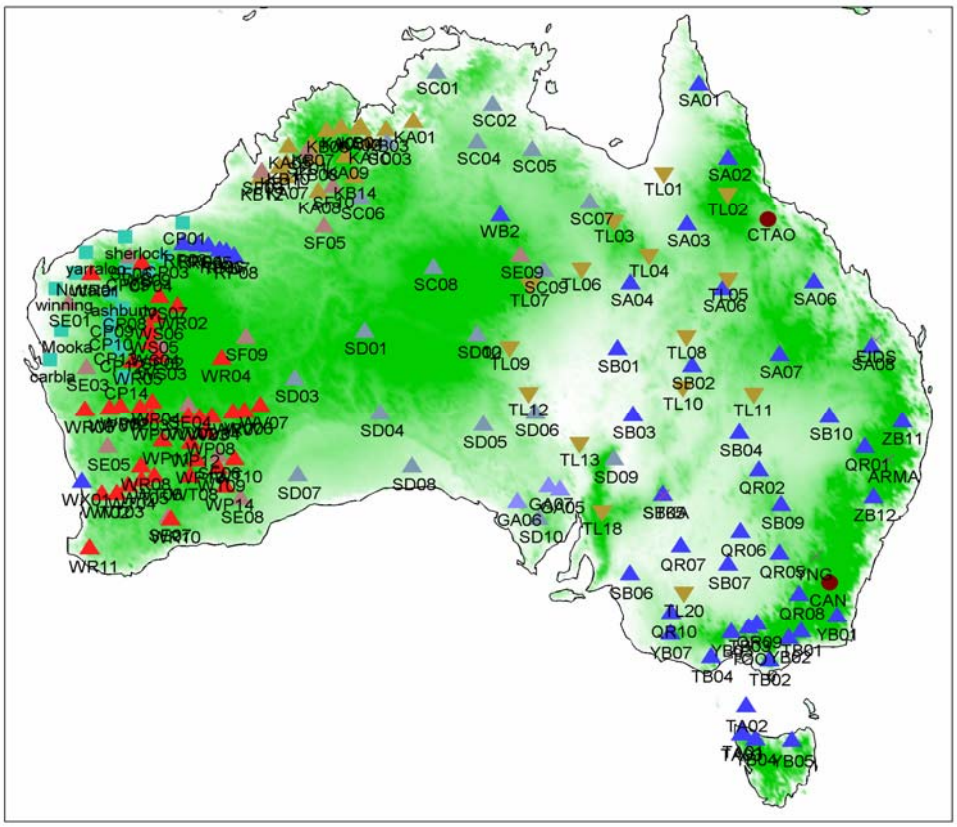

Figure 4.1: Portable broadband stations location used in this study. The background is the topography features of Australia.

Seismic data used in this study are selected firstly using the sacselect [2] program. The seismic data which are selected have magnitudes greater than 5.0 *mb* with epicental distances less than 40º to Australian stations to avoid too deep penetration of the refracted waves into the mantle. Moreover, broadband seismic data for events with magnitude bigger than 5.0*mb* have enough energy to bring useful information to seismic recorder. Secondly, the GUI described in sub chapter 2.3.3 is used to choose visually seismic data with a good quality. A good quality data is assessed if the data shows clear presence of *P* and *S* waves.

From the first selection, I collected about 16805 data sets, and then by using the GUI the number is reduced to 6368. A full list of seismic data included in this study is shown in Table 4.1.

Table 4.1: Total numbers of seismic data included in this study, and the numbers accepted for each deployment of seismometers.

PROJECTS	STATIONS	TOTAL	ACCEPTED
SKIPPY	SA, SB, ZB, SD, SC, ZC, YB	6684	2120
TASMAL	TL	4994	2519
WACRATON	SE,SF	248	105
	WS,WT,WV, WP	245	184
KIMBA	KA	331	45
	KB	23	12
QUOLL	QR,TB	110	75
LINKAGE	LP, CP, RP	2400	724
GAWLER	GA	831	210
IRIS	EIDS, ARMA, YNG, TOO	864	340
TIGGER	TA	75	34
ALL		**16805**	**6368**

[2] The sacselect is a computer program to select seismic data in SAC format. Seismic data can be selected based on: magnitude, epicentral distance, source depth, etc. This program was developed by Research School of Earth Sciences, Australian National University.

Detailed information on the distribution of source depth, epicentral distance, azimuth and event magnitude of seismic datasets used in this study is presented in Figure 4.2 below:

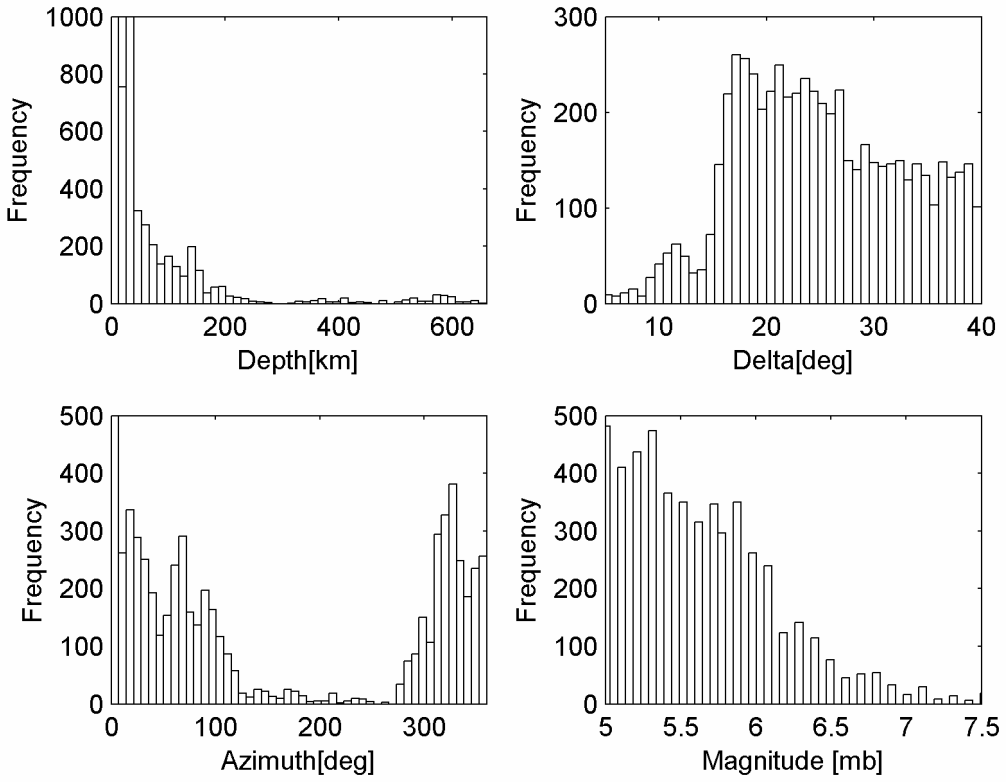

Figure 4.2: Seismic data behavior used in this study: source depth, epicentral distance, azimuth and magnitude.

The upper-left panel of histogram in Figure 4.2 shows that most of seismic data are generated by shallow events (0-70km depth) with 55% of population and intermediate events (70-300km depth) with 35%. Only 10% are generated from deep earthquakes. The distribution of epicentral distance is shown in the upper-right panel; the majority of the seismic data has epicentral distances greater than 17º. This situation will affect the clarity of our seismic dataset since most waves will have traveled through major earth discontinuities (410 and 660km depth). Fortunately, only seismic data with magnitude than 5.0*mb* are accepted (lower-right panel). In this way, seismic body waves (*P* and *S* waves) still have enough energy to reach seismic station. After the initial selection visual observation is conducted to assess the quality of seismic data. The

azimuth information in the lower-left panel is important to see how well the seismic data are crossing each other.

A geographical plot of the data is presented in Figure 4.3 below. The Figure shows the great-circle source-receiver paths, the events and the location of the receivers. The great-circle source-receiver paths are indicated in grey, the seismic events with magnitude between 5.0 and 7.0 which occurred between 1993 and 2006 are shown by color filled circles over the depth range from 3km to 700km indicated by color coding. The location of the portable broad-band stations are indicated by black filled triangles.

The majority of events are located to the north and to the east of Australia; there are only a limited number of events from the south, nevertheless, these still provide valuable information. From Figure 4.3, it can be seen that the Northern part of the continent has a good coverage of seismic data except for the Great Sandy Desert area where there is no seismic station since there are major difficulties in transportation access.

The three dimensional view of path coverage in the lower panel of Figure 4.3 shows that in the lithosphere (down to 220km) and the upper mantle (down to 320km), the majority of path will be traveling nearly vertically. Also, it can be seen from the figure, the majority of the earthquakes are shallow from the earthquake belt through Indonesia, New Guinea, New Caledonia and Vanuatu to Fiji. However, there are a few groups of events with depth greater than 400km, mostly in the Tonga-Kermadec subduction zone. The majority of the available events lie in the epicentral distances range between 20º and 30º, as a result the ray paths in the lithosphere and the asthenosphere pass through very steeply. In the northern part of Australia, about 60% of ray paths have azimuth 110º and 40% greater than 300º. In this way, the behavior of ray paths in the northern part of Australia provides a good pattern of crossings.

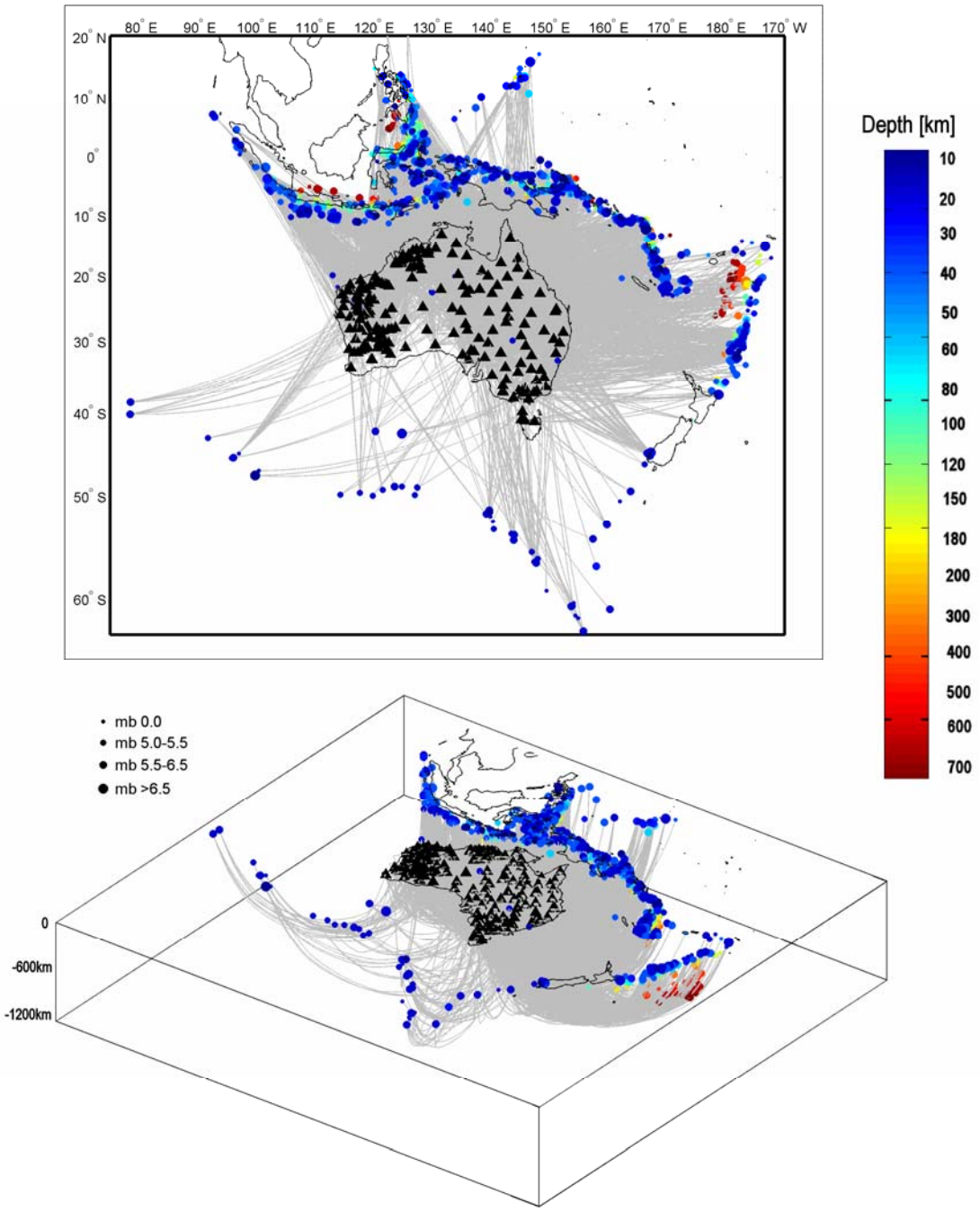

Figure 4.3: Seismic events locations (circles) with magnitude *mb* between 5.0 and 7.0 used in this study recorded by portable broadband stations across Australia. When magnitude is not provided, it is marked by *mb* 0.0. The portable broadband stations are shown by black filled triangles. Grey lines represent source-receiver paths which are traced in one-dimensional model of the ak135. Plain view (above), three dimensional view (below). The seismic events are colored scaled in depth.

4.2 Robust Seismic Travel times and Attenuation Measurements

By using the same procedure described in Sections 2.3.2 and 2.3.3, *P*, *S* wave arrival times, differential attenuation of *S* to *P* waves (Δt^*_{SP}), *P* to *P* (Δt^*_{SP}) and *S* to *S* (Δt^*_{SP}) for nearly 6500 high quality three-component seismic records discussed in Section 4.1 above have been carefully hand picked and measured.

The characteristics of the arrival time residuals, differential attenuation and corresponding error estimates for the seismic data are shown in Figure 4.4. Most of *P*-wave arrival times lie in the range from -5s to 5s relative to the *ak135* model, however the overall spread extends to -9 and 9s. The *S*-wavespeed anomalies extend to twice those for *P*, up to -18 and 18 s. The strong peak at negative times (-4 to -10s) arises from the fast paths into northern Australian stations. Furthermore, the Δt^*_{SP} values of transverse, radial and horizontal components lie in the range of -1.0s to 5s. Negative values can arise because the *P* wave path takes a more attenuative route (e.g. with asthenosphere penetration), but the *S* wave stays in the lithosphere. However, the majority of Δt^*_{SP} values are positive which means than *S* waves spectra decay more rapidly than those of *P* waves. Statistical error in the estimation of the Δt^*_{SP} shows how variable the spectral ratio is. A spectral ratio with high variance will produce a high error estimate and vice versa. The error estimates for the Δt^*_{SP} for the transverse, radial and horizontal components mainly fall below 0.2 which arises from the good clarity of both *P* and *S* waves for the selected events.

A geographical representation of the *P*, *S* travel times relative to ak135 and the differential attenuation (Δt^*_{SP}) are shown in Figure 4.5. The paths of *P* and *S* waves color coded by their travel time residuals and Δt^*_{SP} are presented in epicentral distance ranges from of 5-20º, 18-30º and 28-40º. The values show average between source and receiver pairs. The depth of the path propagation increases with epicentral distance. Roughly, in the *ak135* model, the path propagation depth is 1/3 of its epicentral distance (1º ≈ 111.19km).

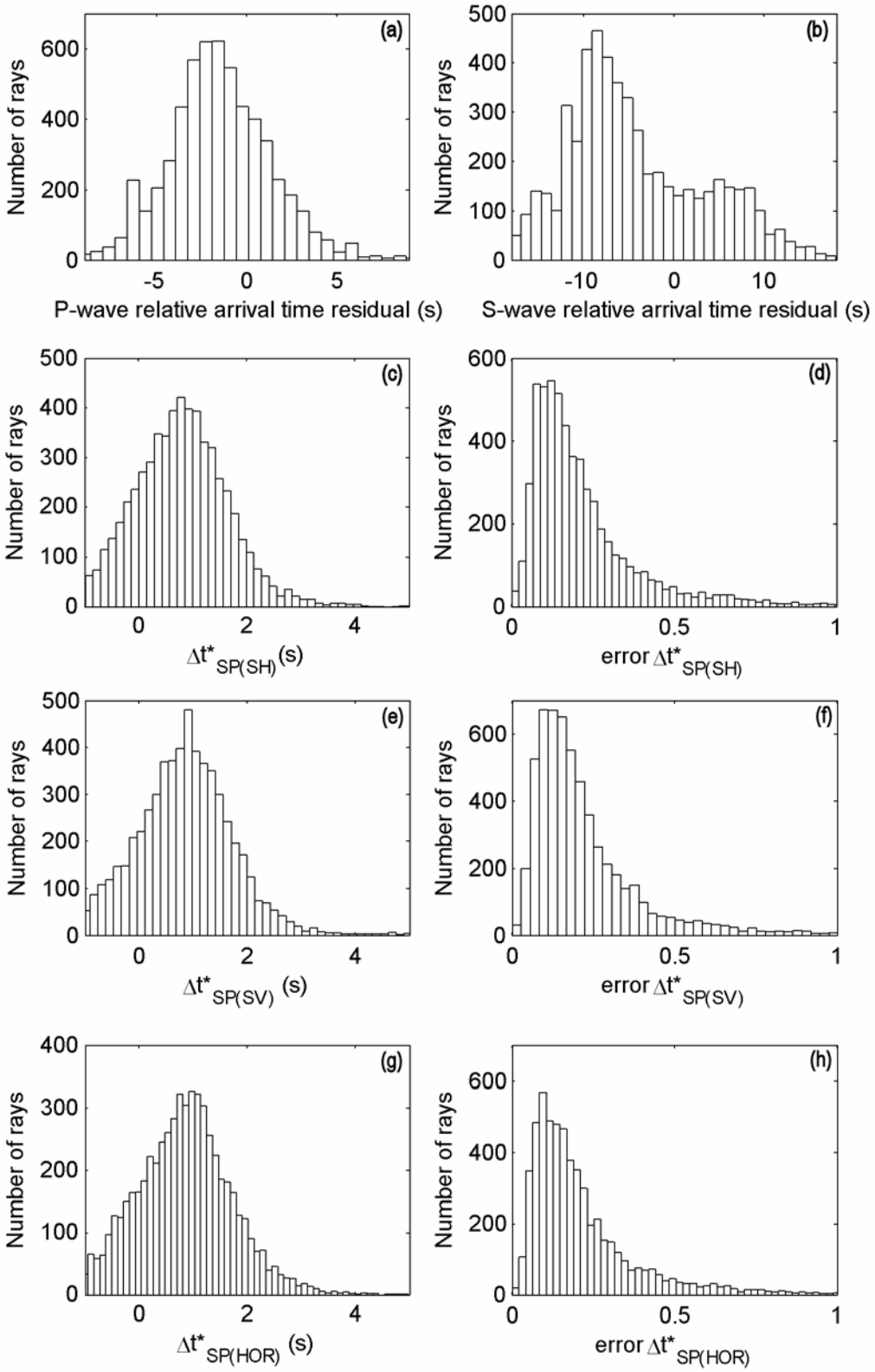

Figure 4.4: Characteristics of arrival time residuals, differential attenuation and error estimation of seismic data used in this study. (a-b) arrival time residuals relative to *ak135* model for *P* and *S* wave respectively. (c-h) Δt^{*}_{SP} distribution for transverse, radial and horizontal components and their error estimations.

For the whole set of epicentral ranges, most of the *P* and *S* waves traveltimes from the western events come in earlier (green and blue paths) than from the eastern ones (brown and red paths). Meanwhile, the behavior of the Δt^*_{SP} from eastern events suggest somewhat more attenuation. The Δt^*_{SP} from Indonesian events show variation between high and low attenuation and mostly tend to be less attenuative. There is less variability in the values of Δt^*_{SP} for the larger epicentral distance ranges.

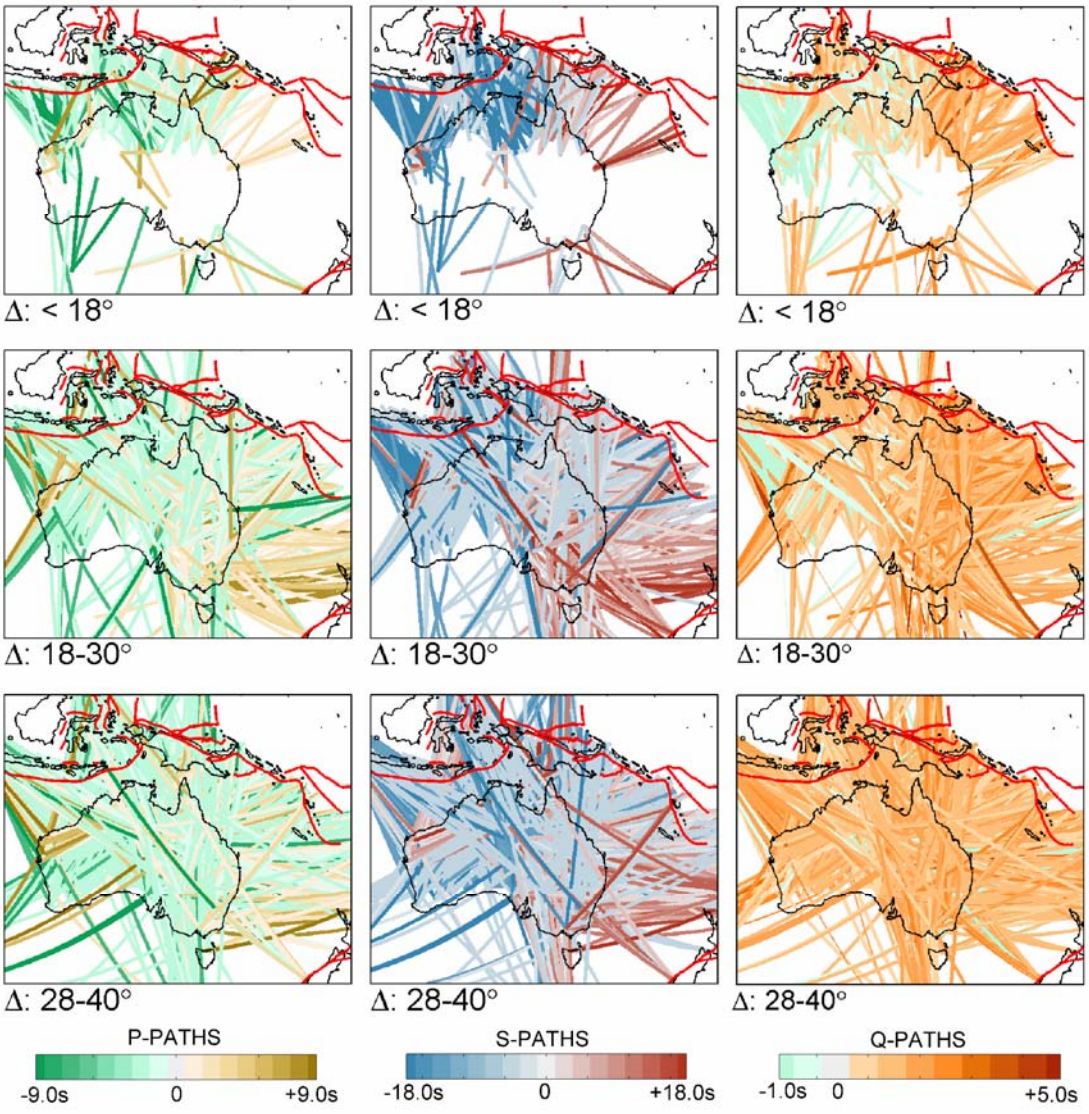

Figure 4.5: Summary of *P*, *S* waves travel times relative to the ak135 model and Δt^*_{SP} estimated from nearly 6500 dataset. The raypaths of Δt^*_{SP} are color scaled by the value of Δt^*_{SP} with line thickness inversely proportional to the inverse of the errors in the Δt^*_{SP} estimation. The red lines represent tectonic boundaries.

The distributions of the *P* to *P*-wave and the *S* to *S*-wave differential attenuation and their error estimates are presented in Figure 4.6. Values of the Δt^*_{PP} generally fall between -1s and 1s relative to each reference (see sub chapter 2.3.2 for the explanation), while the values of Δt^*_{SS} extend to twice as large as Δt^*_{PP}. The *S* waves are clearly attenuative than *P* waves.

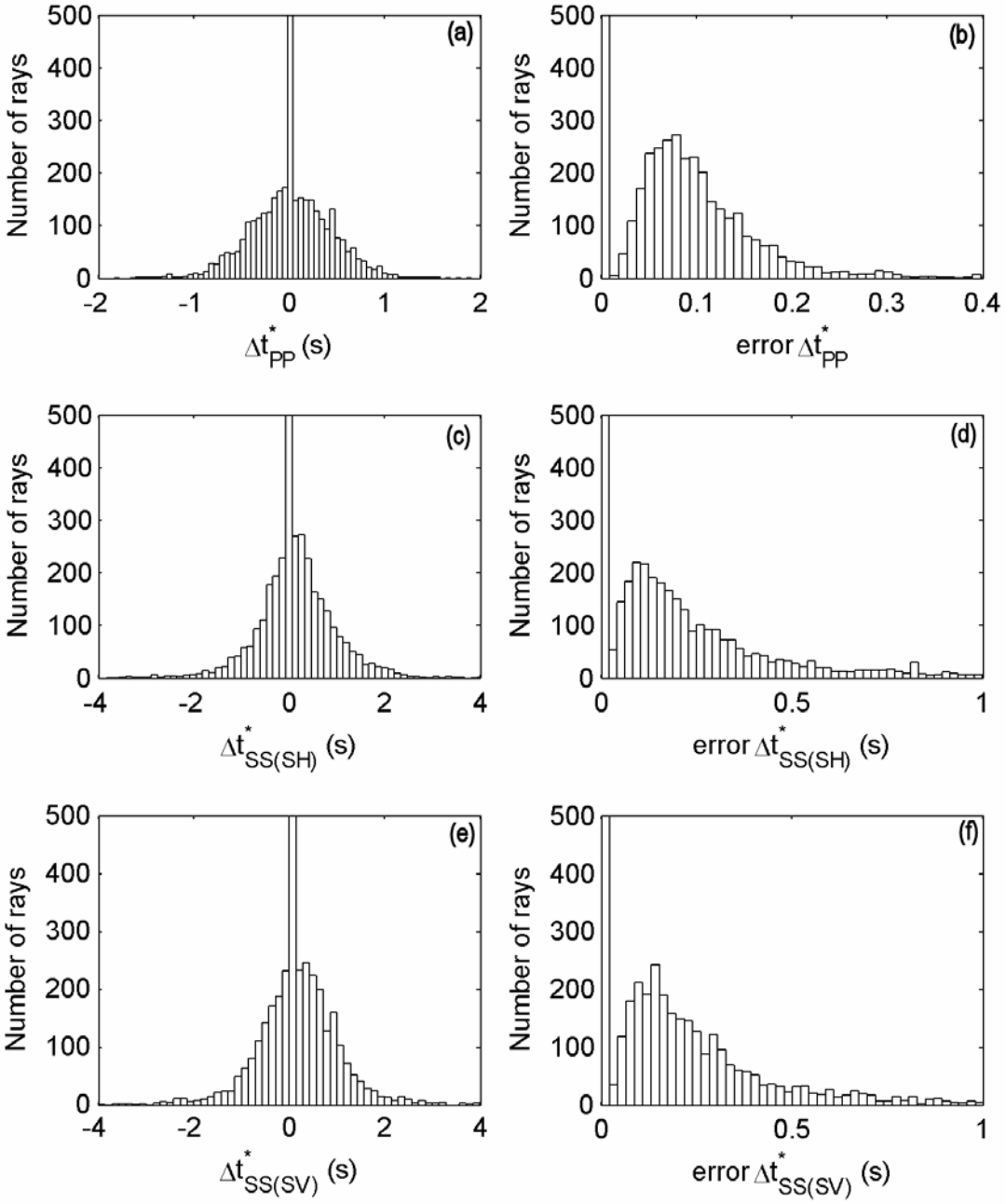

Figure 4.6: Distributions of *P* to *P*-wave and *S* to *S*-wave differential attenuation and its error estimation.

Since *P* waves come in earlier before the *S* waves, recording of *P* waves is relatively free of noise compared with *S* waves. Especially if epicentral distance is small, the *S* wave is frequently contaminated by the coda of the *P* wave. In this way, from the Figure 4.6, it can be seen that the error estimates for *S* waves are much higher than those of *P* waves.

Although the quality of the seismic data has been assessed using visual observation, to ensure the quality of earth attenuation determination, further data selection is conducted by employing estimates of the Signal to Noise (S/N) ratio. The Signal to noise ratio is defined as the power ratio between a signal and the background noise or *P* wave coda. Both signal and noise are measured within the same bandwidth. The mathematical expression for the S/N is shown in equation 4.1 below:

$$S/N = \left(\frac{\sqrt{\sum \left(A_{signal}(t) \right)^2 / N}}{\sqrt{\sum \left(A_{noise}(t) \right)^2 / N}} \right)^2 \tag{4.1}$$

Here S/N is the signal to noise ratio, $A_{signal}(t)$ and $A_{noise}(t)$ are the Amplitudes of signal and noise in time domain respectively and *N* is number of samples.

The behavior of the S/N of *P* and *S* waves is presented in Figure 4.7. Only the data with the S/N greater than 2.0 is used in the inversion, which leaves approximately 90% of the data selected from the visual process.

4.3 Tomography System of Equations

The Δt^*_{SP}, Δt^*_{PP} and Δt^*_{SS} differential attenuations and the arrival times of *P* and *S* which have been measured or hand picked are used in a tomographic inversion to construct three dimensional images beneath Australia. The images that will be constructed are *P* and *S* waves speed and its attenuation (Q_P and Q_S).

To understand the basic concept of seismic attenuation tomography, in this Section, the system of equations for attenuation tomography will be described.

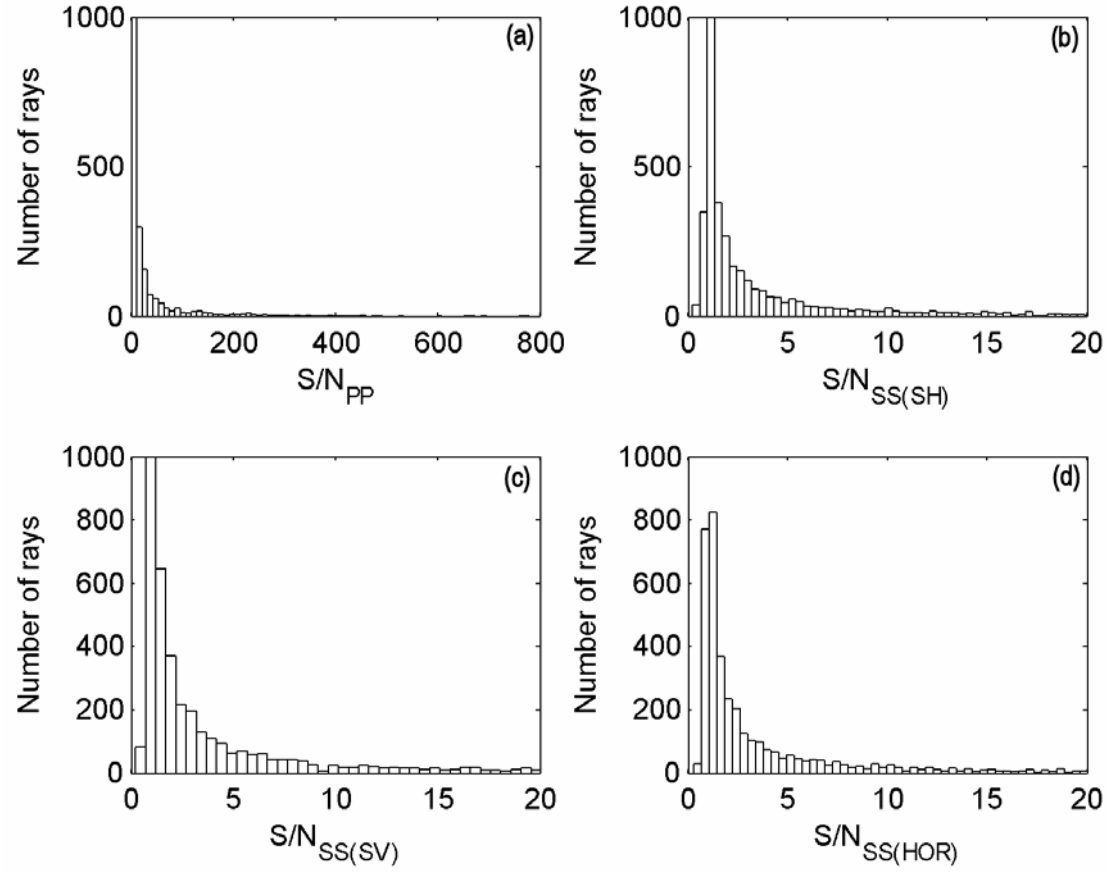

Figure 4.7: Signal to Noise Ratio (S/N) for *P* and *S* waves (transverse, radial and horizontal components)

Seismic attenuation t^* is defined as an integrated effect of attenuation along the path:

$$t^* = \int_{ray} \frac{dl}{VQ} \approx \sum_{cell} \frac{dl(cell)}{Q(cell)V(cell)} \tag{4.2}$$

The perturbation in attenuation t^* resulting from a perturbation to the attenuation Q is given by:

$$\frac{\partial t^*}{\partial Q^{-1}} = \frac{dl(cell)\delta Q^{-1}(cell)}{V(cell)} \tag{4.3}$$

For *S* to *P* differential measurement, we have:

$$\frac{\partial \Delta t^*_{SP}}{\partial Q_S^{-1}} = \frac{\partial t^*_S}{\partial Q_S^{-1}} - \frac{\partial t^*_P}{\partial Q_S^{-1}} \tag{4.4}$$

We assume that there is no loss in bulk compression so that seismic energy loss is confined to shear waves and so we have $Q_P \approx 2.3Q_S$.

We can rewrite the cellular kernels for attenuation from (4.2) and (4.3) as:

$$\frac{\partial \Delta t^*_{SP}}{\partial Q_S^{-1}} = \left(\frac{dl_S(cell)}{V_S(cell)} - \frac{dl_P(cell)}{2.3V_P(cell)} \right) \delta Q_S{}^{-1}(cell) \tag{4.5}$$

By using the same approach, for the *P* to *P* and *S* to *S* differential measurement, we have:

$$\frac{\partial \Delta t^*_{XX}}{\partial Q_X^{-1}} = \frac{\partial t^*_{X(stat1)}}{\partial Q_X^{-1}} - \frac{\partial t^*_{X(stat2)}}{\partial Q_X^{-1}} \tag{4.6}$$

Combining equation (4.3) and (4.6) we have:

$$\frac{\partial \Delta t^*_{XX}}{\partial Q_X^{-1}} = \frac{dl(cell-stat1)\delta Q_X{}^{-1}(cell)}{V_X\ (cell)} - \frac{dl(cell-stat2)\delta Q_X{}^{-1}(cell)}{V_X\ (cell)} \tag{4.7}$$

dl(*cell-stat*) indicates the path length in the cell associated with the ray to the particular station (which could be zero if the ray does not pass through the cell).

Rewrite equation (4.7):

$$\frac{\partial \Delta t^*_{XX}}{\partial Q_X^{-1}} = \frac{\left(dl(cell-stat1) - dl(cell-stat2)\right)}{V_X\ (cell)} \delta Q_X{}^{-1}(cell) \tag{4.8}$$

Where the term *'X'* corresponds to *P* or *S* wave.

We can represent (4.5) and (4.8) in the generalized form **d=G**{**m**}, [see e.g. the treatment by Rawlinson & Sambridge, 2003], where the data vector **d** is built from the differential attenuation for the different paths, **m** is a vector of attenuation model parameters and **G** is the kernel matrix. A similar form can be used with **d** containing the travel time residuals from a reference model, when **m** comprises the wavespeed variations**.** Comparison of $\mathbf{g}(\mathbf{m}_0)$ with the observations, travel times or differential attenuation, determines the initial level of fit. The next step is an iterative improvement of the model.

In the neighborhood of a model $\mathbf{m}_0$ we can make a linearization of the relationship $\mathbf{d}=\mathbf{G}\{\mathbf{m}\}$ to yield:

$$\mathbf{d}_{obs} \approx \mathbf{g}(\mathbf{m}_0) + \mathbf{G}(\mathbf{m}- \mathbf{m}_0) \tag{4.9}$$

which can be expressed as $\delta\mathbf{d} = \mathbf{G}\delta\mathbf{m}$ with $\delta\mathbf{d} = \mathbf{d}_{obs} - \mathbf{g}(\mathbf{m}_0)$ and $\delta\mathbf{m} = \mathbf{m}-\mathbf{m}_0$.

If equations (4.5 and 4.8) were exactly linear, then the Newton and quasi-Newton solutions would be the same because the second derivative terms in the Hessian matrix would vanish. To ensure stability the basic set of equations need to be supplemented by smoothness conditions and the objective function to be minimized can then be written as:

$$S(\mathbf{m})=\frac{1}{2}[(\mathbf{G}\delta\mathbf{m}-\delta\mathbf{d})^T \mathbf{C}_d^{-1}(\mathbf{G}\delta\mathbf{m}-\delta\mathbf{d}) + \varepsilon\delta\mathbf{m}^T\mathbf{C}_m^{-1}\delta\mathbf{m} + \eta\delta\mathbf{m}^T\mathbf{D}^T\mathbf{D}\delta\mathbf{m}] \tag{4.10}$$

where $\boldsymbol{D}$ is a second derivative operator, $\delta\mathbf{d}$ is the data deviations from the prediction from a reference model and T denotes a transpose. The parameter η controls the gradient smoothing and ε the deviations from the background model.

The solution of this class of minimization problem can be written as:

$$\delta\mathbf{m} = [\mathbf{G}^T \mathbf{C}_d^{-1}\mathbf{G} + \varepsilon\mathbf{C}_m^{-1} + \eta\, \mathbf{D}^T\mathbf{D}]^{-1} \mathbf{G}^T \mathbf{C}_d^{-1}\, \delta\mathbf{d} \tag{4.11}$$

where $\delta\mathbf{m}$ is the perturbation in the model vector, $\mathbf{G}$ is the matrix kernel containing the raypaths segments in each cell, $\mathbf{C}_d$ is the data covariance matrix and $\mathbf{C}_m$ an *a priori* model covariance matrix. The properties of the minimization are controlled by the *damping factor* ε and the smoothing parameter η, and inverse matrix operation.

In this chapter, the tomographic inversion will be focused on producing *P* and *S* wave speeds and *Qs* images from the Δt^*_{SP} measurements using one-dimensional initial models of seismic speed (ak135 model) and a 1-D model for *Qs*. The initial model of *Qs* used in this study has been developed by Cheng [2000] to represent the general features the Australian continent (Table 4.3).

The initial model for seismic velocity and attenuation is plotted as a function of depth in Figure 4.8 below. Both *P* and *S* wave speeds progressively increase with increasing depth. The *Qs* profile suggests low attenuation in the lithosphere (0-220km),

followed by very high attenuation in the upper mantle, then the attenuation is significantly decreased below the transition zones (410 and 660 km)

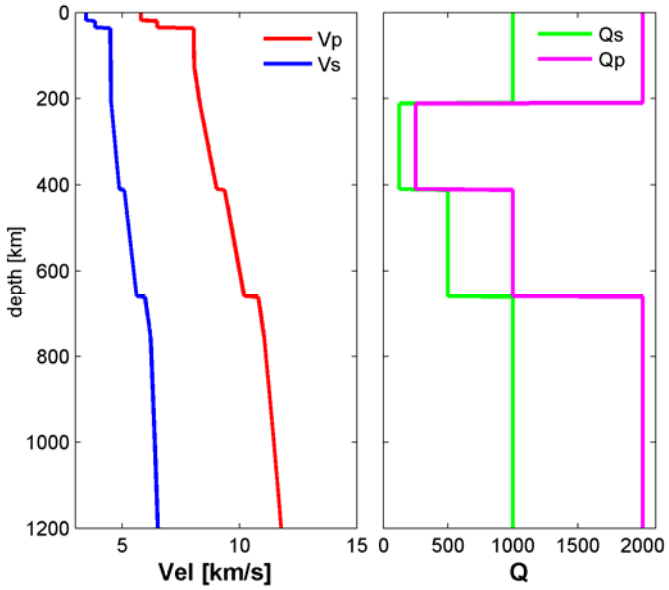

Figure 4.8: The representation *P* and *S* seismic velocity models of global reference model a*k135* [Kennett and Engdahl, 1995] and *Q* model [Cheng, 2000] used as initial model.

Table 4.1: Depth Interval and *P* and *S* waves speed used as initial model

Layer	Depth Interval (km)	*P*-Wave Speed (km/s)	*S*-Wave Speed (km/s)
1	0-35	6.1200	3.6383
2	35-120	8.0450	4.4899
3	120-220	8.1892	4.5112
4	220-320	8.5190	4.6266
5	320-410	8.8659	4.7918
6	410-535	9.5698	5.2124
7	535-660	9.9902	5.4776
8	660-860	11.0302	6.1655
9	860-1060	11.3910	6.3517
10	1060-1260	11.7070	6.4846

Table 4.2: The attenuation model used in this study

Earth Structure	Depth[km]	Q_S	Q_P
Lithosphere	0-210	1000	2000
Upper mantle	210-410	125	250
Transition zone	410-660	500	1000
Lower mantle	660-2,890	1000	2000

4.4 Model Parameterizations

We use a model volume encompassing the region of interest around Australia. The study area extends from latitude 22° N to 65°S, longitude 78° to 189° E and from 0-1240 km in depth.

The lithosphere and the upper mantle are divided into 10 layers with layer thickness ranging from 35km to 100km in the uppermost zone and from 100km to 200km in the deeper mantle (Table 4.1). This layer division represents the main features of earth structure which consists of lithosphere, upper mantle, transition zone and lower mantle. We use a uniform grid of constant velocity and attenuation cells with horizontal size 3°x3°. We examined several cell sizes [1°x1°, 2°x2° and 3°x3°] and found that the balance between resolution and ray sampling was at its best for 3°x3° cells. By using this model parameterization, the total number of unknowns to be solved for by the tomographic inversion is thus about 11100. I did not do any further relocation for each event location. I only used the event location which is embedded in each header of seismic data provided by Research School of Earth Sciences, Australian National University, which for most events is taken from the relocated catalogue of Engdhal, van der Hilst and Bulland [1998] and the later updates.

Because I use waves which are refracted back from the mantle the attainable resolution is at its best beneath the northern margin of Australia, as illustrated in the Figure 4.9 where we display both the path density and the distribution of the rosette diagrams of back azimuths for the set of cells in the three shallow layers for which we subsequently show tomographic results. The back azimuths are binned at every 10º. The gaps in the coverage on the continent can be mostly be related to the absence of stations in the most remote desert regions, or the configuration of events during the limited time over which a set of stations was operating. Although the quantity of seismic events from the western, southern and south eastern tectonic boundaries are limited, the figure shows that southern margin of the continent still has reasonable path density. This is

because of the extensive deployments of seismic stations during the QUOLL, TASMAL, WACRATON, and TIGGER experiments.

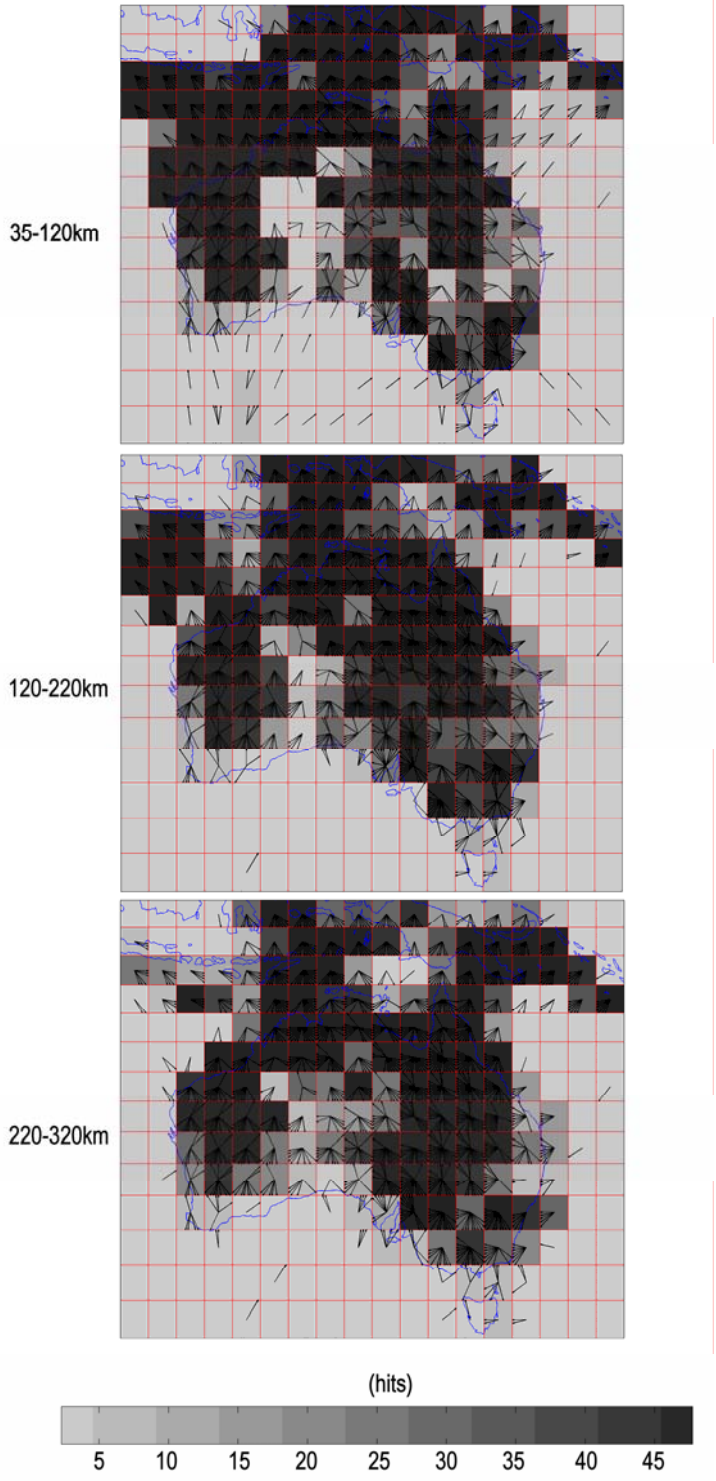

Figure 4.9: Rosette diagram of seismic ray path propagation is shown by black arrows. The rosette is defined by the back azimuth of path direction in tomographic cells. The gray background patches represents the paths density distribution.

4.5 Checkerboard Test

Before producing tomographic images from the inversion of the Australian data set, a set of checkerboard tests are carried out to evaluate the feasibility of the raytracing method being developed, the model parameterizations and the inversion method and to see how well wave-speed anomalies are recovered upon inversion.

Before the inversion is done, the kernel matrix needs to be constructed. The kernel is calculated from ray tracing using Snell's law in a 1-D earth model. Since we have exact information about receiver location, the ray tracing is started from the receiver to seismic event location. The shooting method is applied to reach seismic event location as closely as possible.

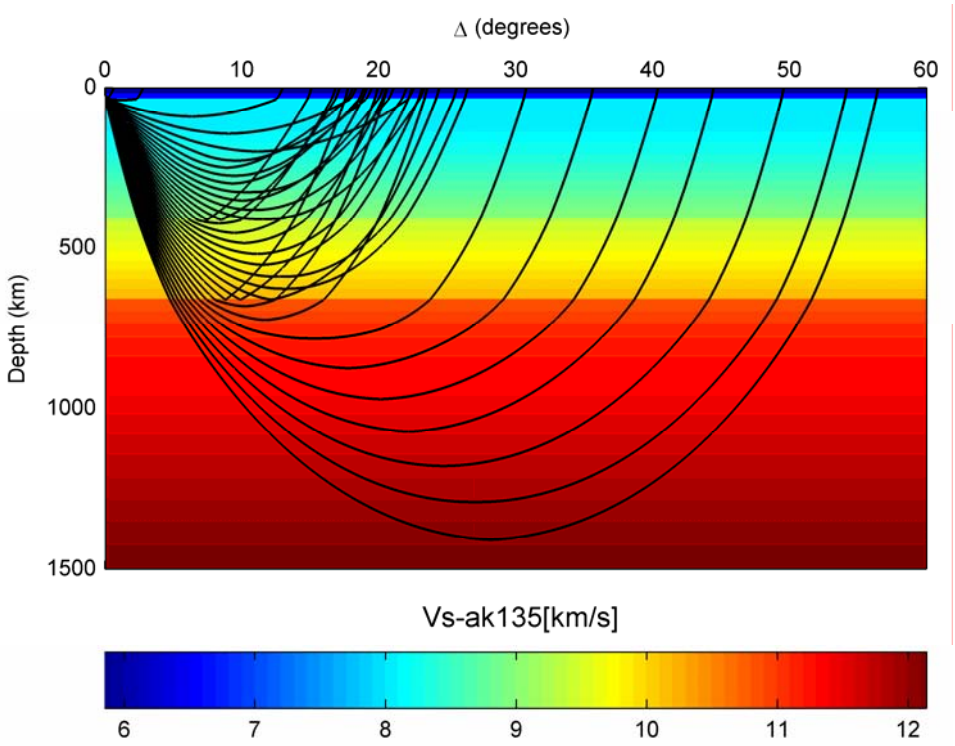

Figure 4.10: 1-D ray tracing of shear wave in the *ak135* velocity model; the depth of source is 33 km. The drastic change of direction at 410 and 660km represents two major earth discontinuities

Figure 4.10 shows seismic ray paths in *S* wave velocity model of the *ak135* model from an event with 33km depth. The two major earth discontinuities at 410km and 660km are shown as well as their characteristic effect on the refracted waves. The

seismic waves refracted back from these two discontinuities lead to the overlap of ray paths and the presence of caustics in the range of epicentral distance between 15° and 30°.Thus, in the real seismic measurements we will find the composite effect of several seismic phases. Meanwhile, the characteristics of raypaths for epicentral distances beyond 30° which are turned back by the velocity gradients in the lower mantle are somewhat simpler.

The next step, the distance between each pair of two successive points along the ray path is calculated to find ray-segment length in each cell.

In this checker board test, a set of synthetic models are divided into alternating regions of high and low velocity with cell sizes 9°x9 and 6°x6°. The input model is a simple structure of *S* wave perturbation with the anomalies having maximum perturbations of ± 2% relative to the ak135 model. Input and output models are calculated under the assumption that the seismic ray path is only influenced by 1-D structure.

The sparse matrix inversions in (4.10) are calculated using the LSQR algorithm of Paige and Saunders [1982] for the inversion of the seismic traveltimes produced from the forward modeling. For this inversion we use a diagonal data covariance matrix with elements 0.25s, the model covariance matrix with diagonal elements 0.0001, the damping factor ε is 10 and the smoothing parameter η is 5. Three iterations are employed, which is suitable for our data and produces reasonable results. I also examined the inversion by introducing a path density weighting. This weighting does not affect much to the final result of inversion.

Figure 4.11b-d and 4.10f-h are results from these checkerboard tests for particular depth slice. The checkerboard test shows that the recovered structure for Australian region is quite good especially for northern region where the raypaths density is high (see Figure 4.9). Although the southern margin of the continent has limited ray sampling, based on this checkerboard test, the recovered result in this region still shows a reasonable result.

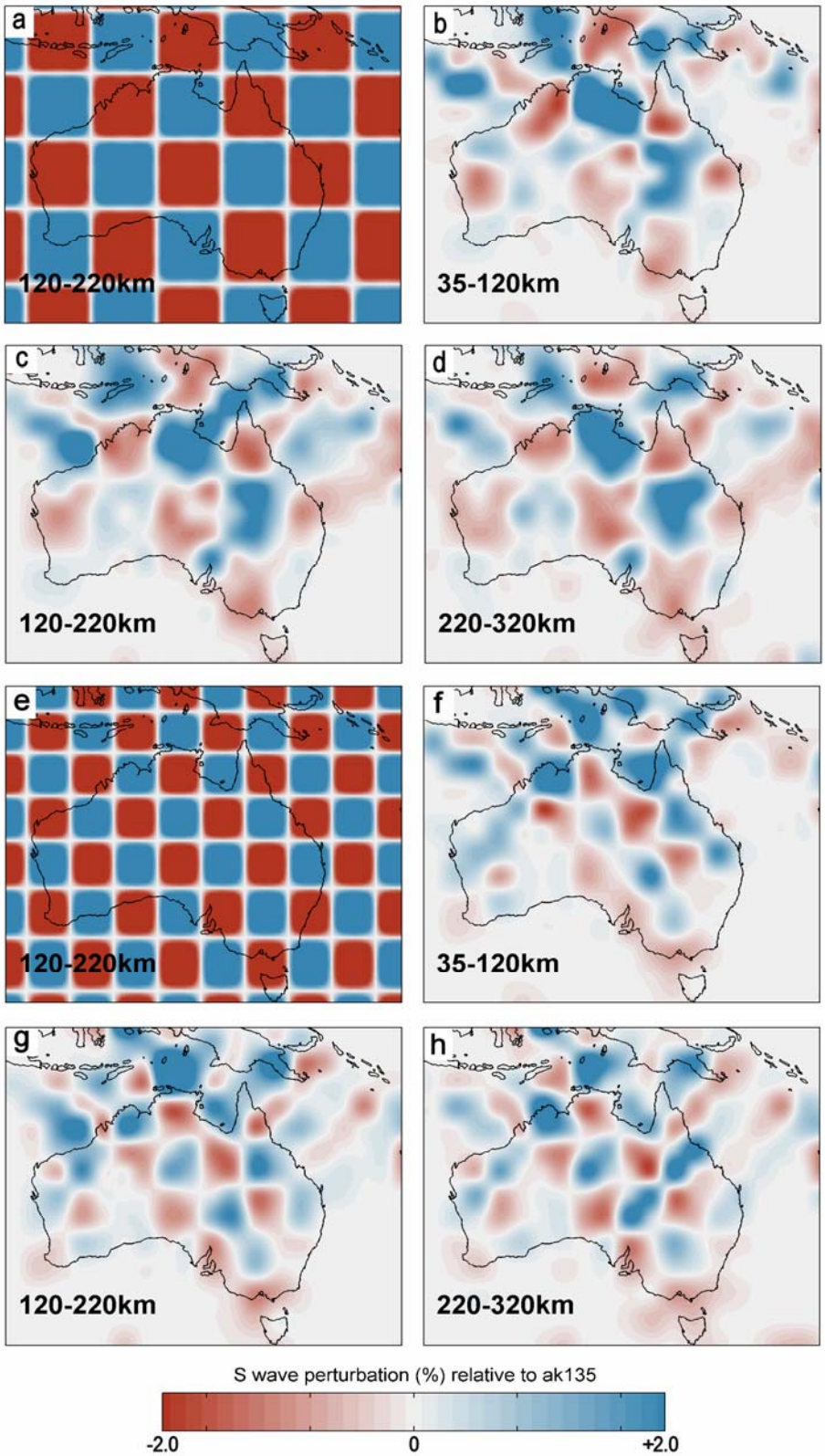

Figure 4.11: Checkerboard test at 35-120, 120-200 and 220-320km depth with different cell sizes: (a-d) 9º and (e-h) 6º. (b-d) and (f-h) are recovered structure for each tomographic inversion. (a) and (e) are input structure with the anomaly has maximum perturbations of ± 2% relative to the *ak135* model

In general the recovered seismic amplitude is reduced compared to the initial model; the seismic amplitude is gradually increased in the regions of higher seismic raypaths density. In the region where there is no ray sampling, the recovered structure has amplitude 0% relative to the initial model. In this way, the northern part of Australia has higher amplitude rather than southern part. Meanwhile, in the surrounding region of Australia such as Tasman Sea, Great Australian Bight, the oceanic ridges to the south of Australia, the recovered amplitude return to 0%.

4.6 Model Representations

The kernels for attenuation tomography depend on the wavespeeds distribution and so the first stage is to use the *P* and *S* wave picks made during the analysis of the seismic records to create 3-D wavespeeds distribution, which are then to be incorporated in the attenuation tomography.

4.6.1 Seismic Wave Speed Models

A total of 6368 relative arrival time residuals of *P* and *S* waves are used as input data to the inversion to produce 3-D models for both *P* and *S* wavespeeds. In order to solve the tomographic system of equation (equation 4.10), I define error estimates from the hand picking. The error estimates are set to be the same for all measured data i.e. 0.5 second to be used in the diagonal elements of $\boldsymbol{C}_d$. The *a priori* model uncertainty associated with each velocity cell, which is used to form the diagonal element of $\boldsymbol{C}_m$, is set to be 0.1 km/s. The damping factor ε is set to be 10 and the smoothing parameter η is 5. Since model parameterizations used in this study is based on constant velocity blocks, a smoothing parameter $\boldsymbol{D}$ is introduced. This parameter is necessary to simulate a continuously varying velocity field. However, if an implicitly smooth parameterization like cubic splines is used, then $\boldsymbol{D}$ parameter may be unnecessary [Rawlinson and Sambridge, 2003].

Several different numbers of iterations are employed i.e. 1, 2, 3, 5, 8, and 15. For each iteration, the objective function (equation 4.10) is minimized. As the number of iterations increases, the observed travel times are satisfied more closely. A useful parameter to measure data fit is the normalized misfit function χ^2 which is defined by Rawlinson and Sambridge [2003]:

$$\chi^2 = \frac{1}{N}\sum_{i=1}^{N}\left(\frac{d_m^i - d_{obs}^i}{\sigma_d^i}\right) \tag{4.11}$$

where $\{d_m^i\} = \mathbf{g}(\mathbf{m})$, $\{d_{obs}^i\}$ is the set of observed data, and $\{\sigma_d^i\}$ are travel time weighting.

The number of iteration as a function of misfit function along with *S* wave speed image at 120-220 depth is shown in the Figure 4.12. Between the number of iteration of 1 and 3, the misfit function is sharply decreases and above iteration 3, it is convergent and a satisfactory solution can be found. Since for iterations beyond 3 the misfit function is convergent, this number of iteration with $\chi 2 \approx 0.21$ is chosen.

Horizontal slices through the models of seismic wavespeed are shown in Figure 4.13 as perturbations from the *ak135* reference model [Kennett et al., 1995]. In northern Australia the *P* wave perturbation typically lies between -1% and 1% and between -2% and 2% for *S* waves. Despite the higher noise level in the observations of the *S* wave travel times, the shear wavespeed model is in good agreement with the images based on the *P* wave travel time data. The patterns of wavespeed variation are consistent with previous studies of body wave [Kennett, 2003] and surface wave tomography [Fishwick *et al.*, 2005] for Australia, with elevated wavespeeds in the centre and west of the continent and lower seismic wavespeeds towards the eastern seaboard. Since most of ray paths in southern Australia are very steep, there is some degree of vertical smearing in this region, but in the north where more lithospheric sampling is available the amplitude of variations is more reliable and smearing is reduced. The amplitude of the wavespeed anomalies can be enhanced somewhat by employing an inversion restricted to, say, the top 410 km but the geographic patterns are maintained (see Figure 4.14).

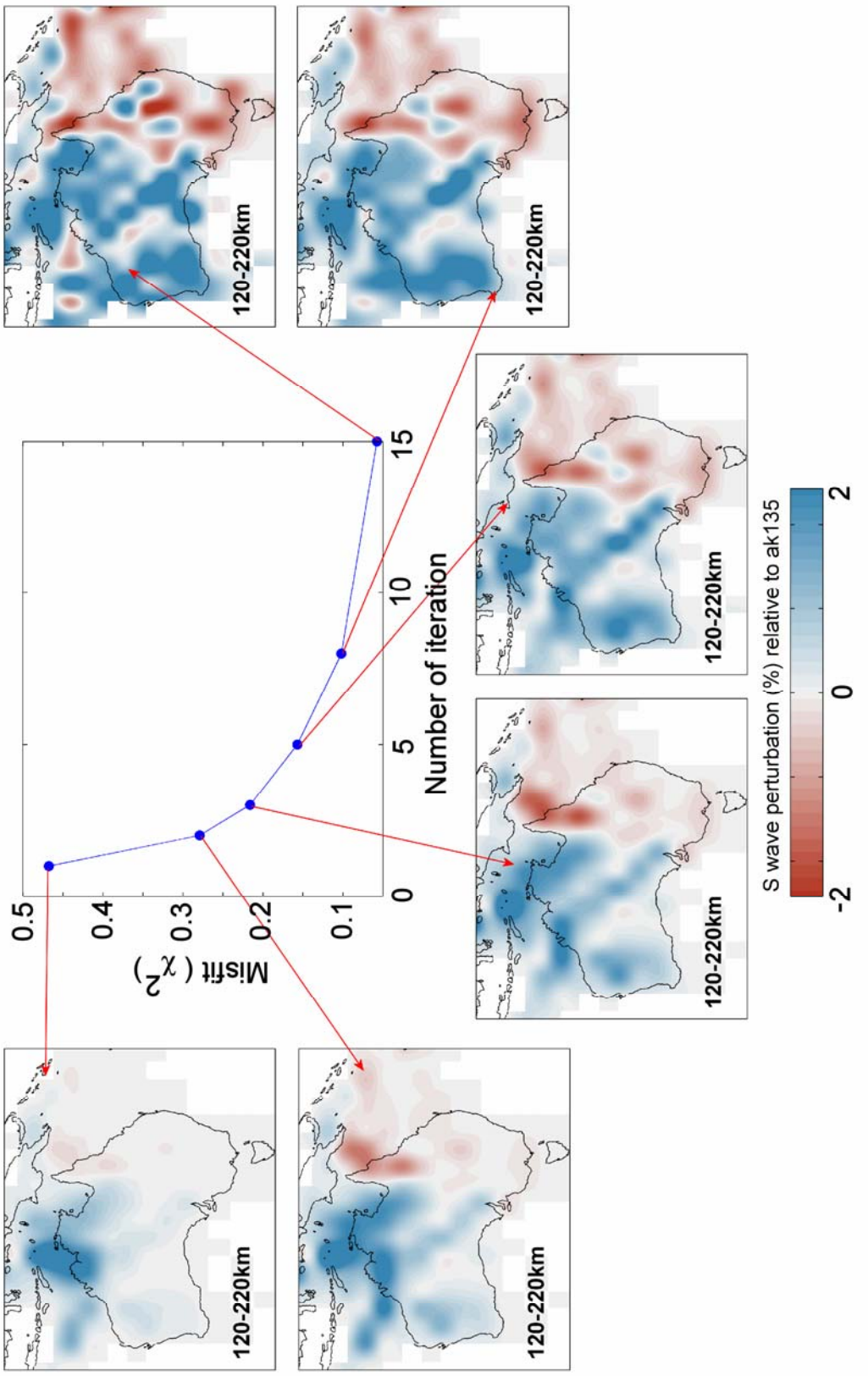

Figure 4.12: Number of iteration as a function of misfit function ($\chi 2$) along with S wavespeed perturbation image at 120-220 depth.

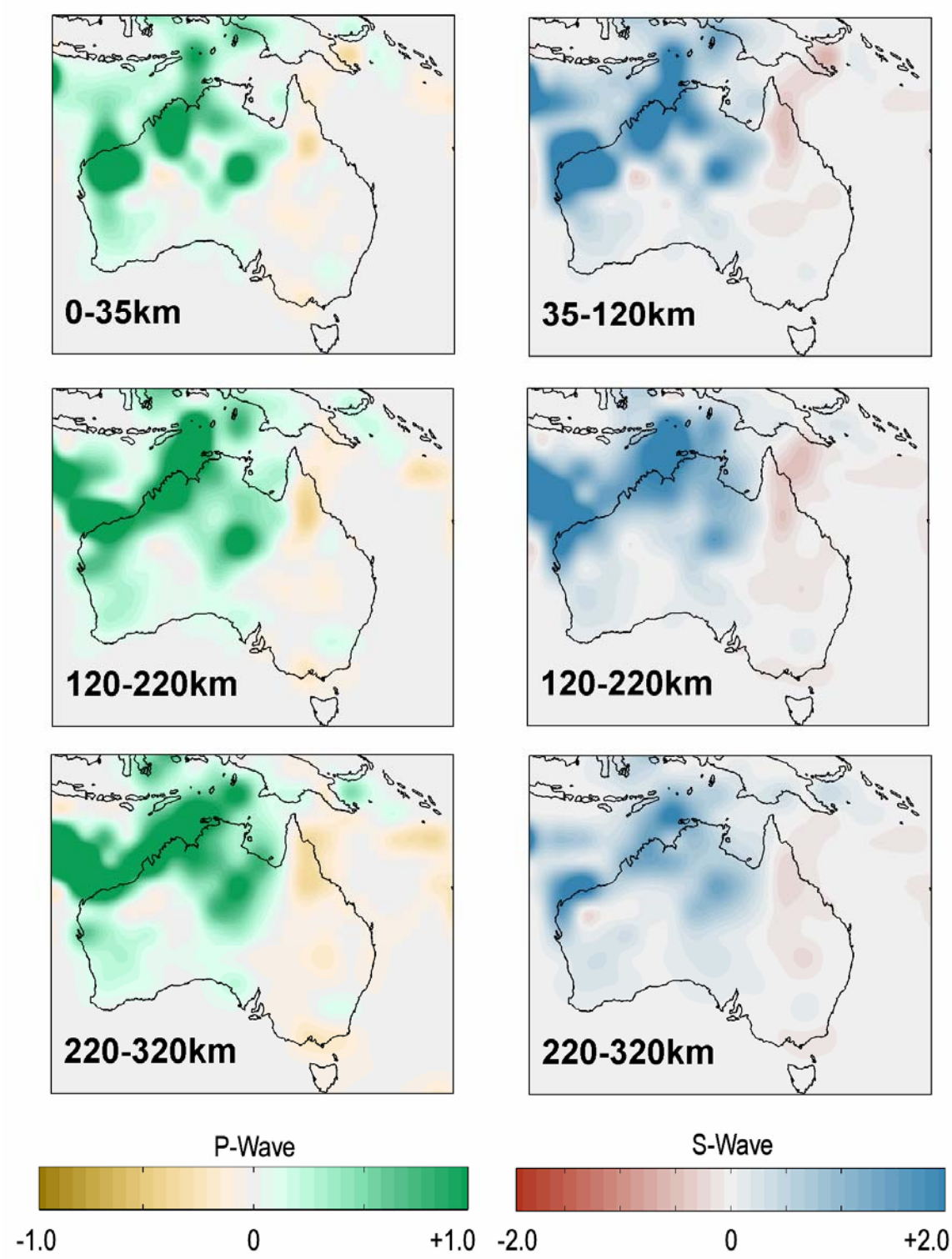

Figure 4.13: Horizontal slices of *P* and *S* wave speed perturbation at 35-120km, 120-220km and 220-320km through three-dimensional solution model obtained by inversion of nearly 6500 seismic travel times residuals. Speed perturbation is shown in percent relative to the *ak135* model. Zero hit of seismic path is presented as white blocks.

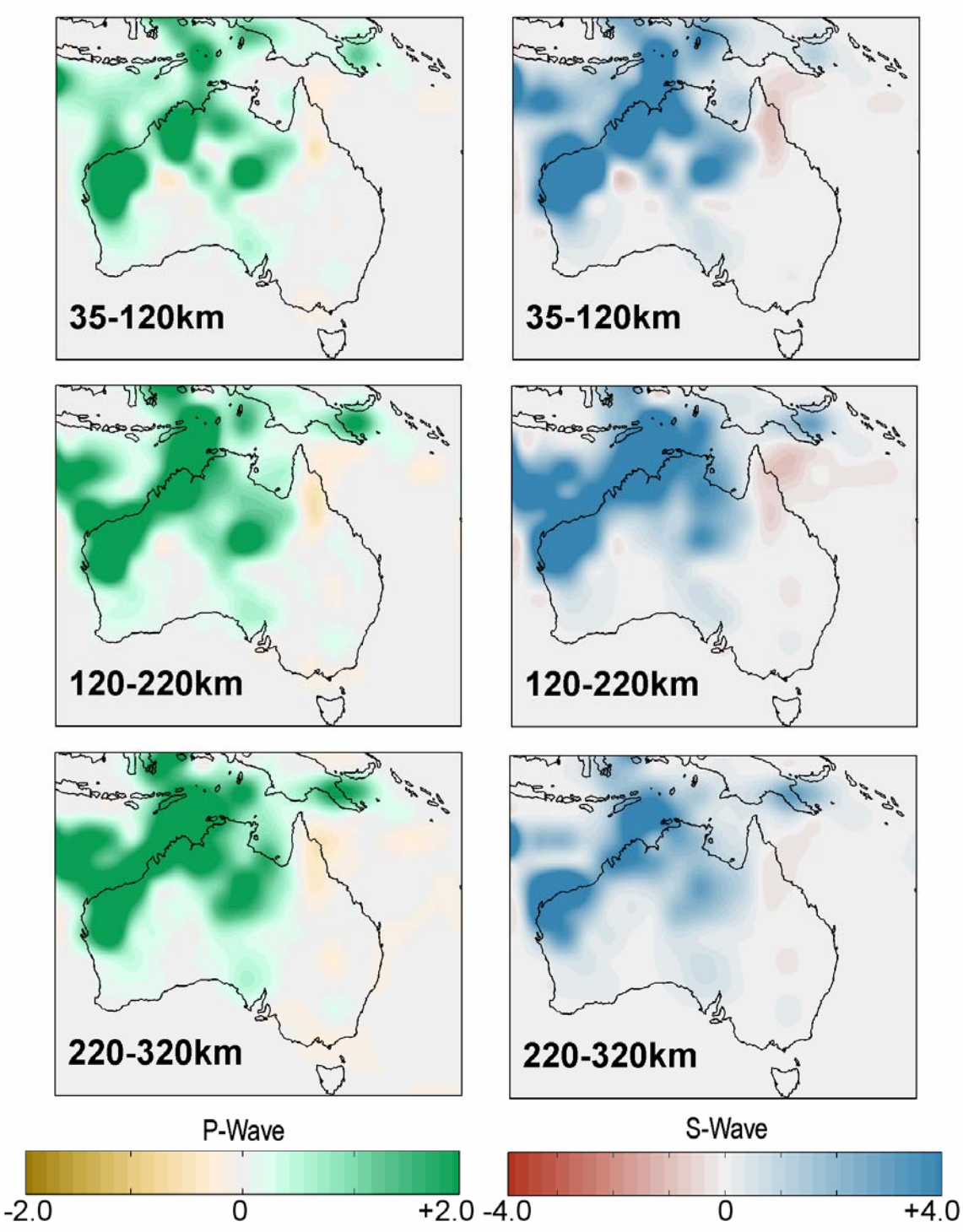

Figure 4.14: Horizontal slices of *P* and *S* waves speed at 35-120km, 120-220km and 220-320km produced from the inversion for just the top 410km.

4.6.2 Shear Attenuation Models

Both the *P* and *S* wavespeed models are then utilized for a tomographic inversion for *SH* and *SV* attenuation with the same cellular model representation as used in the seismic wavespeeds inversion. Besides the wavespeed information, in order to build kernel matrix for the attenuation inversion, one dimensional ray tracing for both *P* and *S* waves is conducted. The damping factor ε and smoothing parameter η are set to be the same as for seismic wavespeed inversion i.e. 10 and 5 respectively. The same procedure in choosing the best data fit as a function of the number of iteration is also employed.

Horizontal sections through the 3D model for transverse (*SH*) and radial (*SV*) wave attenuation (Q_{SH}^{-1} and Q_{SV}^{-1}) are shown in Figure 4.15. The models are plotted as perturbation relative to the initial model so that the results are comparable for both *P* and *S* wave speed structures. In this case, reference Q_S^{-1} are 1/1400 in the depth range 35-120km and between 120-220km, much higher Q_S^{-1}=1/100 in the range 220-320km.

The attenuation images suggest that there is a strong correlation between regions of high seismic wavespeed and minimum attenuation, particularly in the seismic lithosphere in the north where seismic sampling is at its best. There is little difference between the relative loss factor (Q_S^{-1}) patterns between the two shear wave polarizations in the low loss zone to 220km, but a little more variability in the higher loss zone beneath. In the lithosphere, above 220km depth, the level of variation of Q_S^{-1} varies from essentially zero to 0.002 in the centre and west with Archaean and Proterozoic rocks. The Phanerozoic rocks in the east show increased attenuation with a concentration near the relatively recent volcanism and region of high heat flow in the northern Queensland. In general the loss factors need to increase below 120 km in the east.

As previously suggested by Gudmundsson *et al.* [1994] from rather limited data, there is a need to invoke a very strong contrast in attenuation in depth. The loss factor for *SH* and *SV* waves must be much larger below 220 km, so that the third panel in

Figure 4.15 is presented at a different scale so the more subtle geographic variations can be seen.

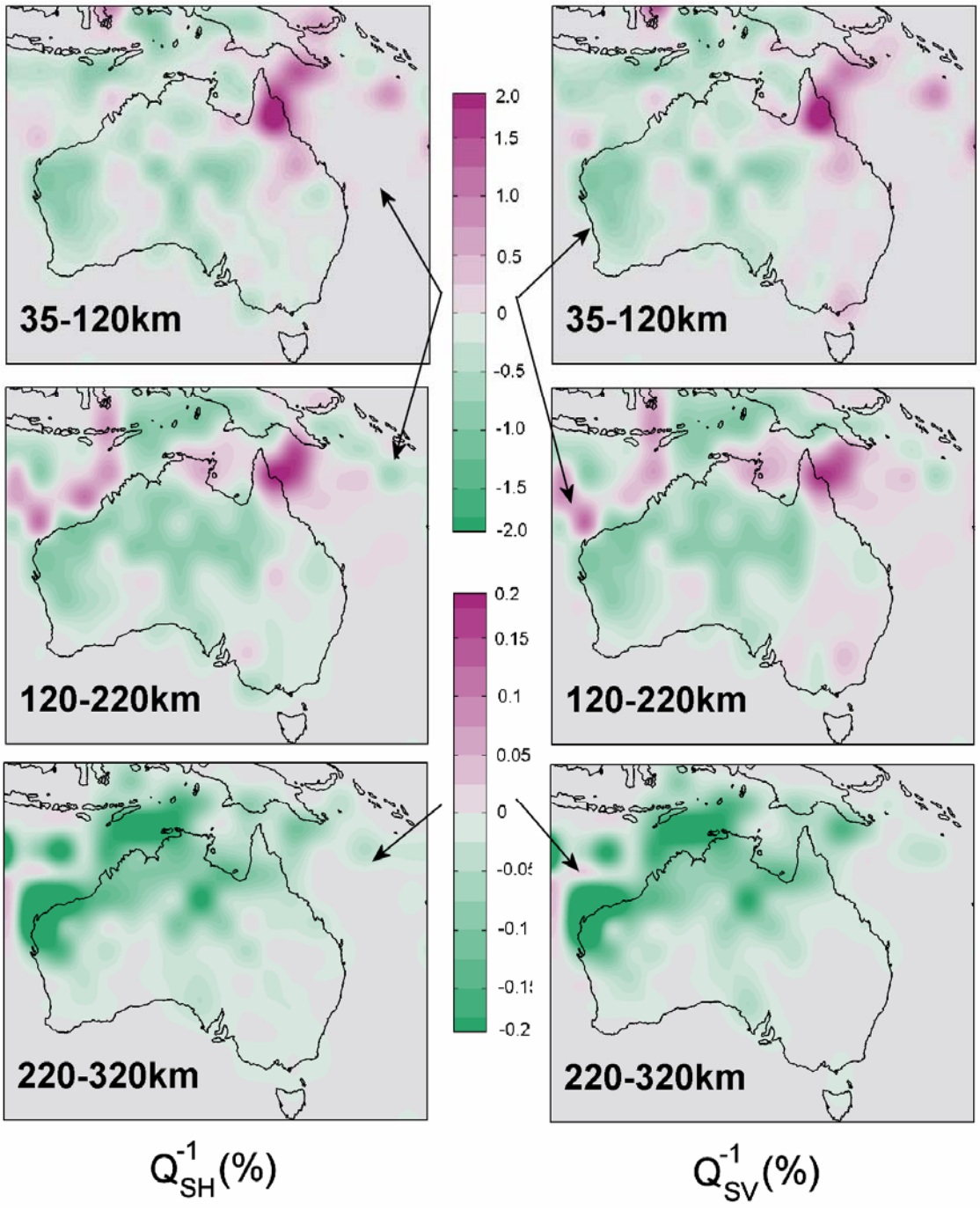

Figure 4.15: Tomographic images of *SH* and *SV* waves attenuation perturbation of the Australian continent produced by the inversion of nearly 6500 *S* to *P* differential attenuation (Δt^*_{SP}). Purplish color represents more attenuative and greenish is less attenuative. Reference Q_S^{-1} are 1/1400 at 35-120km and 120 and 220km, 1/100 at 220-320km

The values of Q_S^{-1} range from 0.005 to 0.01 in the asthenospheric upper mantle. These values represent the average over a 100 km thick zone so that it is possible that there could be localized zones of very strong loss.

The limited sampling with refracted waves in western Australia leads to a patchy pattern in the images that is directly related to the path density distribution rather than the character of the paths.

Vertical profiles of attenuation down to 320 km depth beneath central-western and eastern Australia are presented in Figure 4.16. The central-western Australia profile is average of 16 locations (blue filled circles in the first panel), while eastern is average of 12 locations (red filled circles). The Tasman Line is also presented on the figure. It is clear that down to 220km depth, eastern Australia region has higher attenuation than central-western. Below 220km depth, although the contrast is small, the eastern Australia still shows higher attenuation (close up pictures in the third panel).

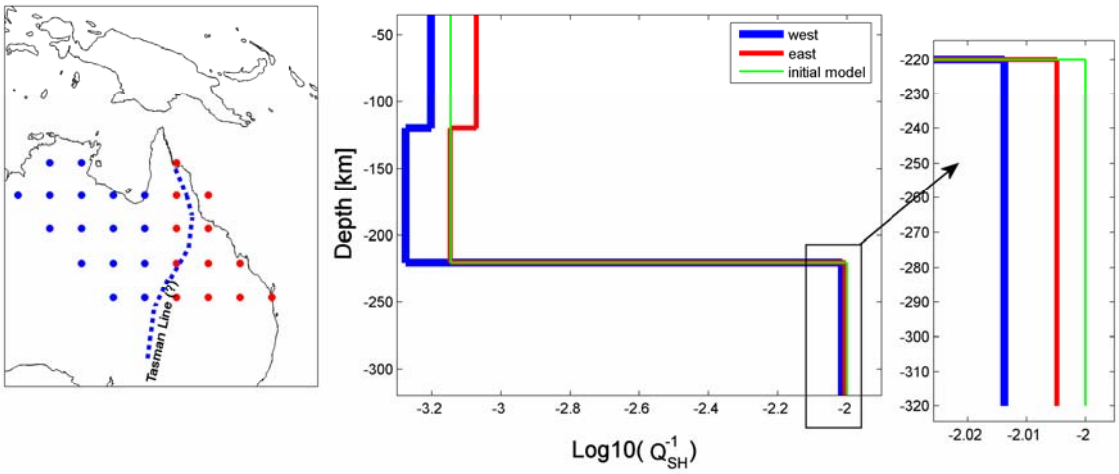

Figure 4.16: Vertical profiles of Q_{SH}^{-1} for western (blue) and eastern (red) Australia produced from their respective starting model (green). Each profile is average value from several locations (the first panel). Close up graphic deeper than 220km is shown in the third panel.

Chapter 5

Seismic Speeds and Attenuation Tomography-Part II

In this Chapter, our tomographic images have been improved by introducing a 3-D initial model and employing 3-D ray tracing rather than just using a 1-D model. The 3-D initial model is derived from a heavily smoothed surface wave inversion for shear wavespeed with conversion to *P* wave velocity and density by spatially varying scaling factors. The model includes the dominant contrast between central-western Australia and the east. The smoothness is very suitable for ray tracing. Separate tracing has to be undertaken for *P* and *S* waves since the variability of the *Vp/Vs* ratio means that the ray paths for the two wave types are different.

Application of the 3-D ray tracing to this model yields seismic ray paths that are positioned in a *'proper'* place. In this way, our inversion kernel behavior should be close to the actual situation.

5.1 3-D Ray Tracing

In order to trace the seismic ray path of each event-station pair of our seismic data set in the 3-D model, the Fast Marching Method (FMM) of Rawlinson *et al.* [2005] is applied. The theory of the FMM and its application in tomographic problem for either

synthetics or real data has been comprehensively described by Rawlinson & Sambridge [2003].

The FMM is a grid based numerical algorithm to trace the evolution of monotonically advancing interfaces using a finite difference solution of the Eikonal equation [Rawlinson and Sambridge, 2003]. Compared to the shooting method which is used in Chapter 4, the FMM is very robust, and is capable of tracing seismic paths even in very complex media [Rawlinson and Sambridge, 2004]. Whereas, the shooting method can fail to converge on the true two point paths.

In a three dimensional volume, the first-order upwind difference scheme for the eikonal equation can be described as:

$$\begin{bmatrix} \max\left(D_{ijk}^{-x}T,-D_{ijk}^{+x}T,0\right)^2 + \\ \max\left(D_{ijk}^{-y}T,-D_{ijk}^{+y}T,0\right)^2 + \\ \max\left(D_{ijk}^{-z}T,-D_{ijk}^{+z}T,0\right)^2 \end{bmatrix}^{\frac{1}{2}} = s_{ijk} \tag{5.1}$$

Here we have used the finite difference operator notation:

$$D^{+x}T = \frac{T(x+\delta x)-T(x)}{\delta x} \tag{5.2}$$

$$D^{-x}T = \frac{T(x)-T(x-\delta x)}{\delta x} \tag{5.3}$$

and s_{ijk} is slowness at the grid point (*i,j,k*), T is traveltime, δx is the grid spacing in x.

The FMM calculate traveltimes in a downwind fashion from known values upwind using a narrow band method. The narrow band basically represents the propagating wavefront, and grid points are marked as either *alive*, *close* or *far* [Rawlinson & Sambridge, 2003]. The concept of these grid points is shown in Figure 5.1.

Unlike the shooting method used in Chapter 4, the calculation of the FMM is started from a source point to a receiver. The traveltimes at neighboring grid points are calculated to make the first step of the narrow band. By using the Fermat's Principle i.e the ray follows the path of least time, the points with minimum traveltime are then accepted as *alive* points, and all neighboring points to this alive point are updated (if

close) or calculated for the first time if *far*. In the case they *close*, the narrow band progresses downwind.

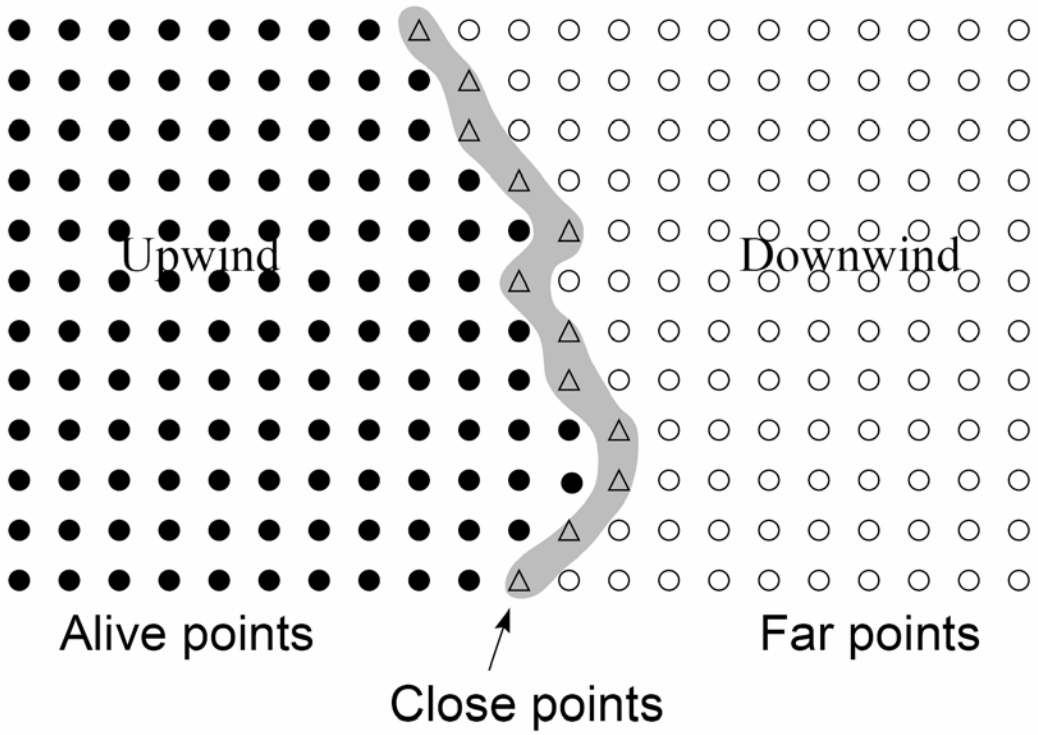

Figure 5.1: Concept of the narrow band method. *Alive* points have their traveltimes calculated. *Close* points is a transition and have trial values. *Far* points have no values calculated. *Alive* points lie upwind of the narrow band while *far* points lie downwind. [Rawlinson & Sambridge, 2003]

An example of the application of the FMM to a 2-D synthetic model is shown in Figure 5.2. In order to show the robustness of the algorithm, the model has been set with very complex structure in which velocity variations lie between 1 and 12.5 km/s. The source point is located at 20 km depth and 21 receivers are located on the earth surface. The calculated wavefronts are visualized by grey lines and source-receiver ray paths by black lines. It can be seen that the wavefronts and rays paths are well determined as they avoid low velocity anomalies and prefer to be located in high velocity zones. The wavefronts are plotted at 0.5 second intervals; the rays are always perpendicular to the wavefronts.

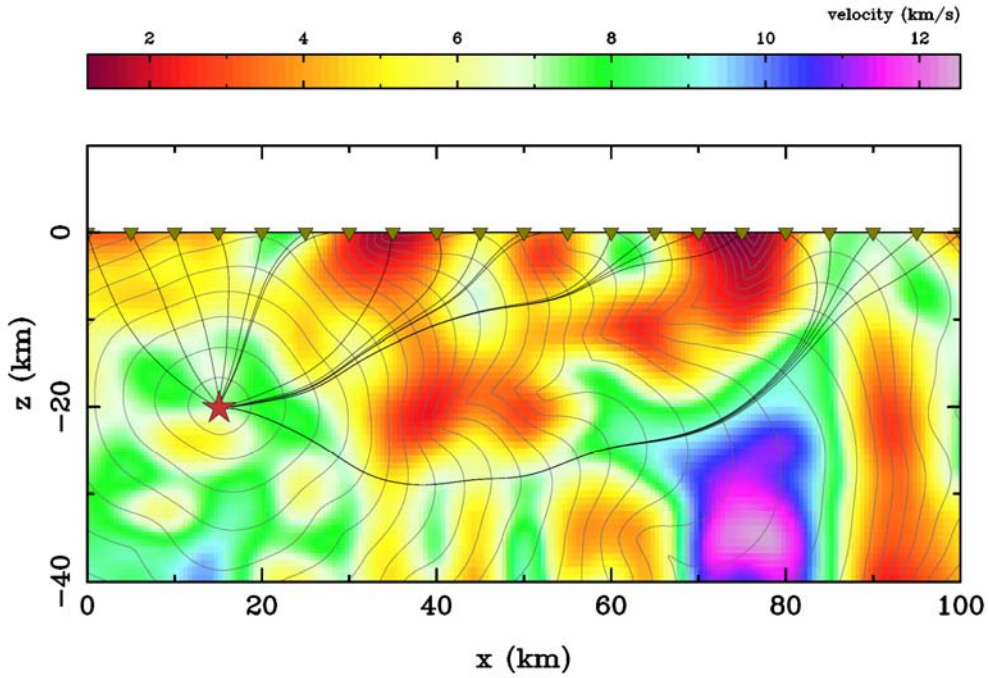

Figure 5.2: Application of the FMM in a synthetic complex 2D velocity medium. Wavefronts are drawn by thin grey lines; ray paths are denoted by black lines. The ray paths are always perpendicular to the wavefronts [Rawlinson & Sambridge, 2003].

Our seismic datasets which have been ray-traced in the 1-D model *ak135* (as shown in Figure 4.3) are retraced using the FMM scheme in the 3D initial model. Since our study area is wider and deeper than the initial model, the velocity model *ak135* is used to fill this gap (see Figure 5.3 for illustration).

Since the number of seismic event is greater than receivers, the seismic receivers are treated as sources and vice versa. In this way, data handling is much simpler.

In this ray tracing work, a grid of velocity nodes is used rather than a constant velocity block parameterization. The distance between the grid nodes is similar to the constant cell sizes used in Chapter 4, i.e., 3 x 3º.

Figure 5.4 shows a vertical cross section at -20ºS of *P* wavespeed of the initial model on which several rays between latitude -15ºS and -25ºS are overlain. Seismic recorders lying in between these latitudes are represented by grey filled triangles and seismic events by black filled circles. Although the initial model is not perfectly form stratification especially down to 400 km depth, the behavior of seismic ray paths seems

quite smooth (i.e. the ray paths are not look like those in Figure 5.2). This may be caused by 2-D projection and effect of coarse grid node distribution.

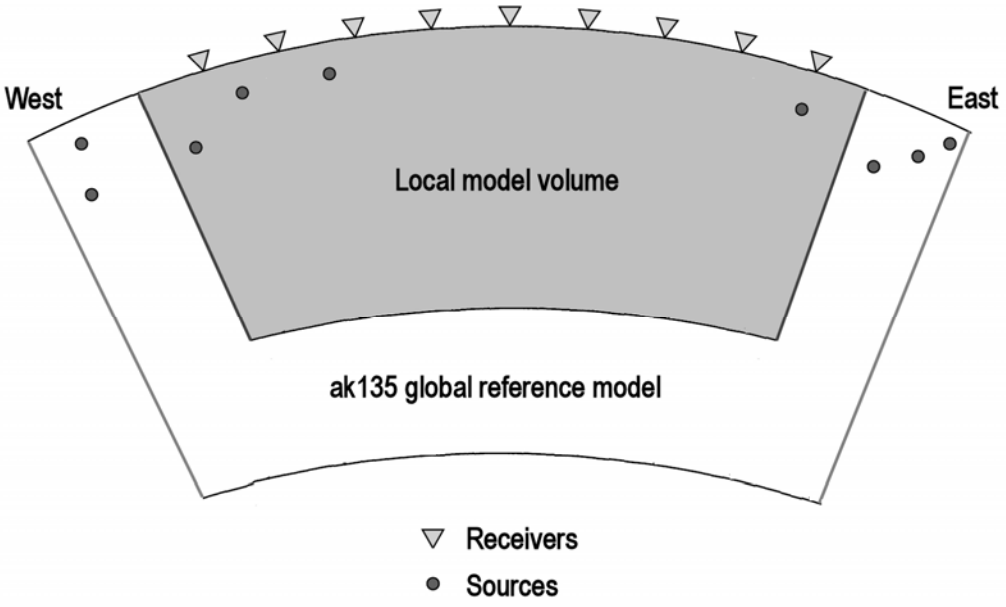

Figure 5.3: Cartoon of west-east cross section of initial model used in this study. The *ak135* global reference model is used to fill the gap of the area which is not covered by local model volume. All of seismic stations are located on the surface of the local model; while earthquakes are located in both areas.

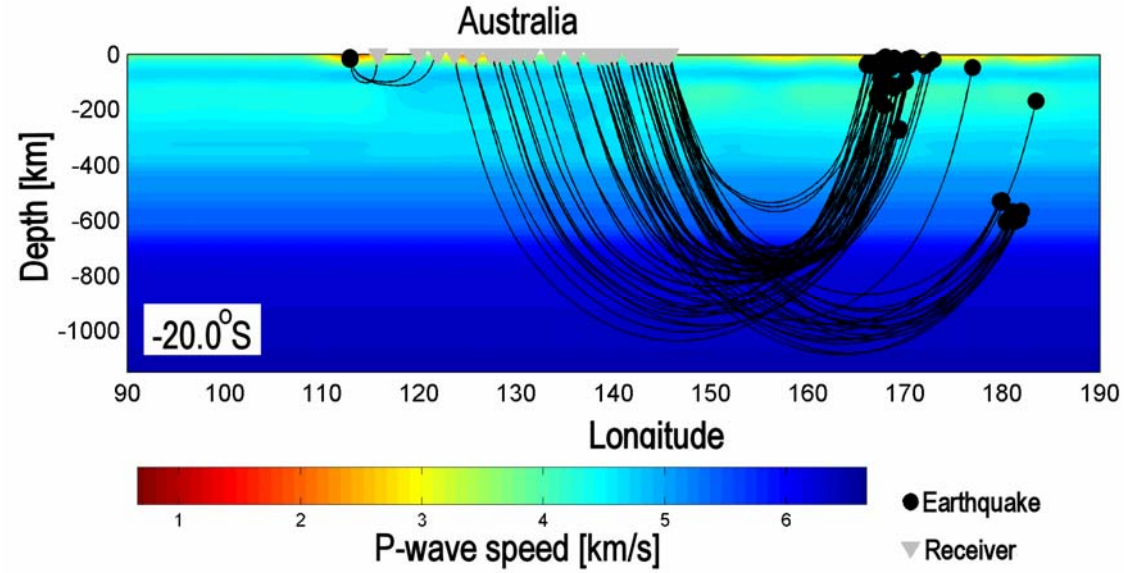

Figure 5.4: Vertical cross section of *P* wave speed initial model at -20ºS. Some seismic recorders are illustrated by grey filled triangles and seismic events by black filled circles. Source-receiver paths are drawn by black lines.

The 3-D initial model of *P* and *S* wavespeeds and *Qs* at slices 35-120km, 120-220km and 220-320km are shown in Figure 5.5. The wave speed images are plotted in perturbation relative to the *ak135* model. The color bar at 220-320 km for the *Qs* model is different from that for 35-120 and 120-220km since the variation of attenuation at this level is low.

Compared to the seismic wavespeed images produced from various seismic studies of Australasian regions, especially the surface wave studies as described in Chapter 3, the seismic wavespeeds of the initial model show some similarities. The major seismic contrast down to 220km depth between continental region of central-western Australia and eastern seaboard is well developed This seismic contrast extends down to 250km depth e.g. surface wave tomographic images of Yoshizawa and Kennett [2004]. While in our initial model such contrast does not appear as a result of averaging down to 320 km. Furthermore, variation in both *P* and *S* wave speeds of the model is very high compare to our body waves tomographic images (see Figure 4.12) i.e. ±1% *P* and ±2% *S* wave, relative to *ak135* model. Perturbations of initial model are ±4% and ±6% for *P* and *S* wave respectively.

Assuming that attenuation is a function of seismic wavespeed, the *Qs* model is generated from *S* wave speed model. This step is needed since availability of attenuation structure beneath Australasian region is still limited. The conversion is averaged so that the variation of attenuation is similar to the attenuation features beneath Australia produced from previous attenuation studies i.e. Gudmundsson *et al.* [1994] and Cheng [2000]. Our *Qs* model has variation between 850 and 1250 in the lithosphere (down to 220km) and 100 and 125 in the upper mantle (220-320km). The variation in attenuation of our *Qs* initial model is similar to Cheng [2000] and our previous study of attenuation in Chapter 4, i.e. contrasts in attenuation down to 220km between central-western Australia and eastern seaboard is clearly shown. Central-western Australia is characterized by low attenuation and the eastern seaboard is marked by high attenuation. In the upper mantle the attenuation is sharply increased despite its low

variability. Using the same approach as for the generation of the *Qs* model, a 3D initial model of *Qp* is also produced. The *Qp* model is generated from the *Qs* model by assuming that $Qp=2.25Qs$.

5.2 Seismic Speeds Models

The final model for seismic wavespeeds from the inversion using the 3-D initial models with the 3-D ray tracing of the FMM method are presented in Figure 5.6 below. Both models are shown as perturbations relative to the *ak135* model.

The perturbation for both *P* and *S* wavespeeds are larger than those obtained using rays in the 1-D reference model. This is a common property of using 3-D tracing and is most likely due to the improved positioning of velocity anomalies so that paths crossing these features are more consistent.

The images are inverted from the same dataset and model parameterization used for producing the seismic wavespeeds images shown in Figure 4.13. The LSQR algorithm is also used for inverting the kernel matrix. The inverted seismic wave speeds models are plotted with the same color scales as their initial models in order to see the change upon inversion. Since the features of the initial models are *'close'* to the characteristic of Australasian regions, the recovered seismic wave speeds are not much different from the initial models. In the regions where path densities are good, the recovered models tend to be higher in amplitude i.e. northern part of Australia. On the other hand, where the path densities are low or no paths, the behavior of recovered models are the same or similar to their initial state.

Again, the strong variation in the neighborhood of the Tasman Line is well demonstrated in both *P* and *S* wave speed models. The main wavespeed contrast lies more to the east at 35-120km depth compared with that at 120-220km. The models show that beneath central-western Australia, in contrast the lithosphere is dominated by a fast seismic speed anomaly, and the eastern sea board has a slow anomaly. Below

220km depth, variations in both *P* and *S* waves speed are low. This may be induced by the choice of a homogenous upper mantle.

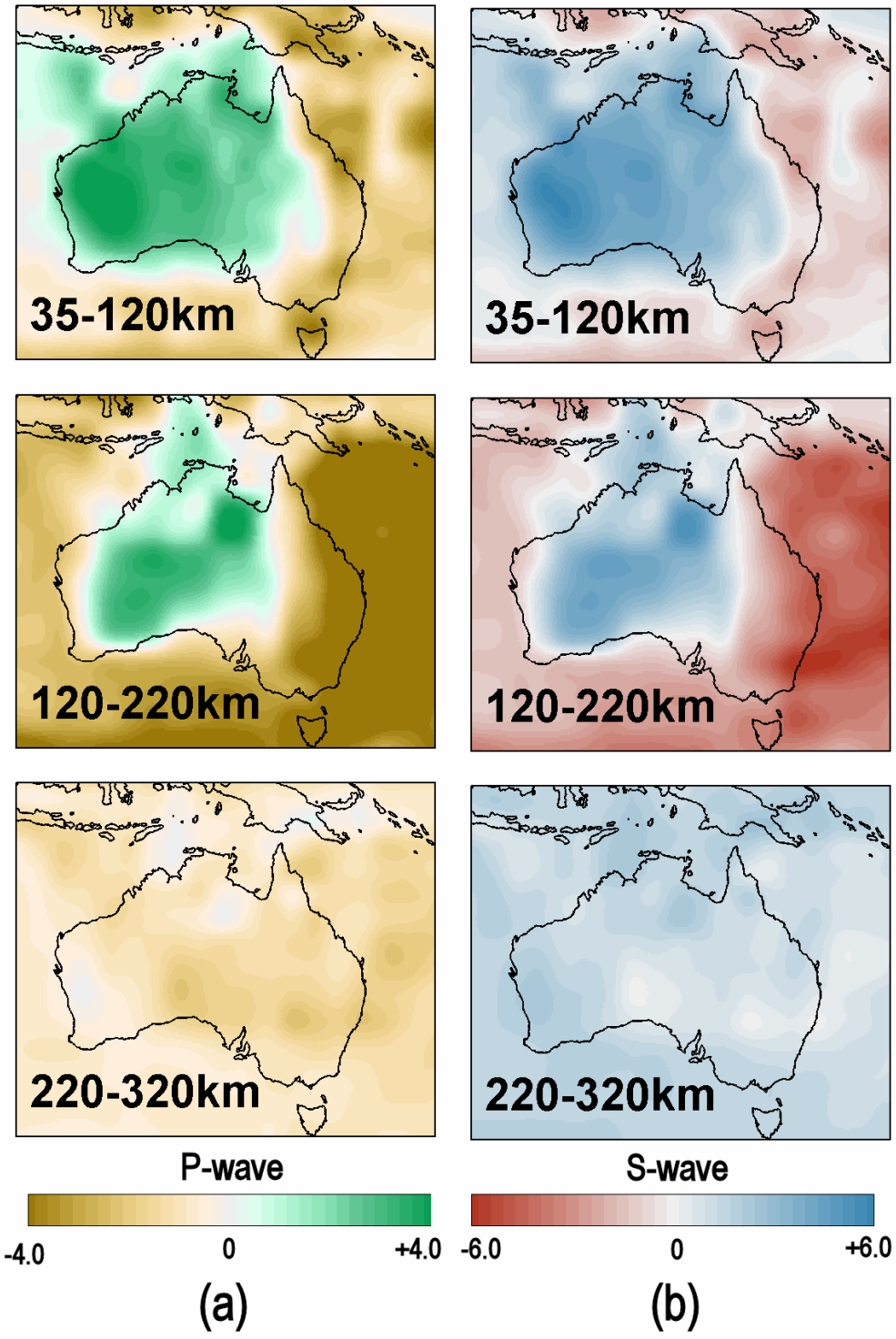

Figure 5.5: (continued)

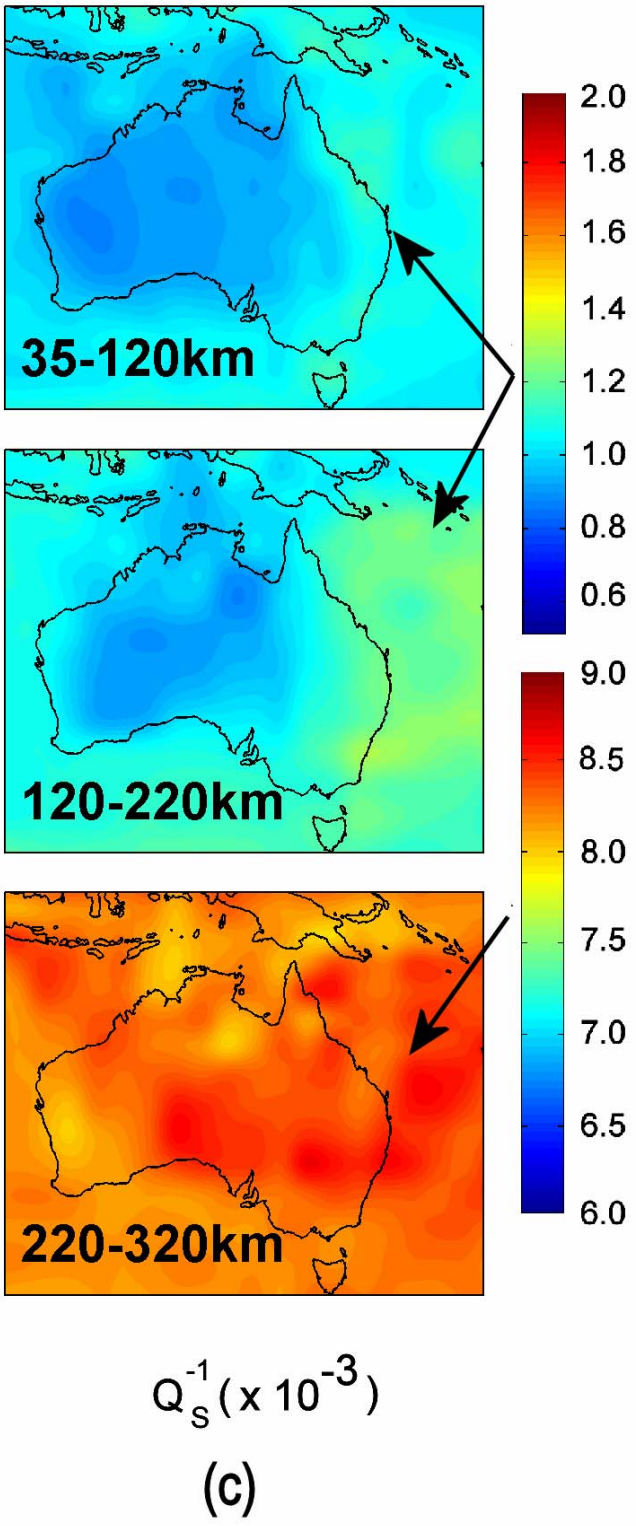

Figure 5.5: 3D initial model at 35-120, 120-220 and 220-320km used in this study: (a) *P* wave speed (b) *S* wave speed (c) Shear Attenuation (*Qs*). Both *P* and *S* wave speed are presented in percent relative to the *ak135* model. Color scale of *Qs* at 220-320km is different from that at 35-120 and 120-220km.

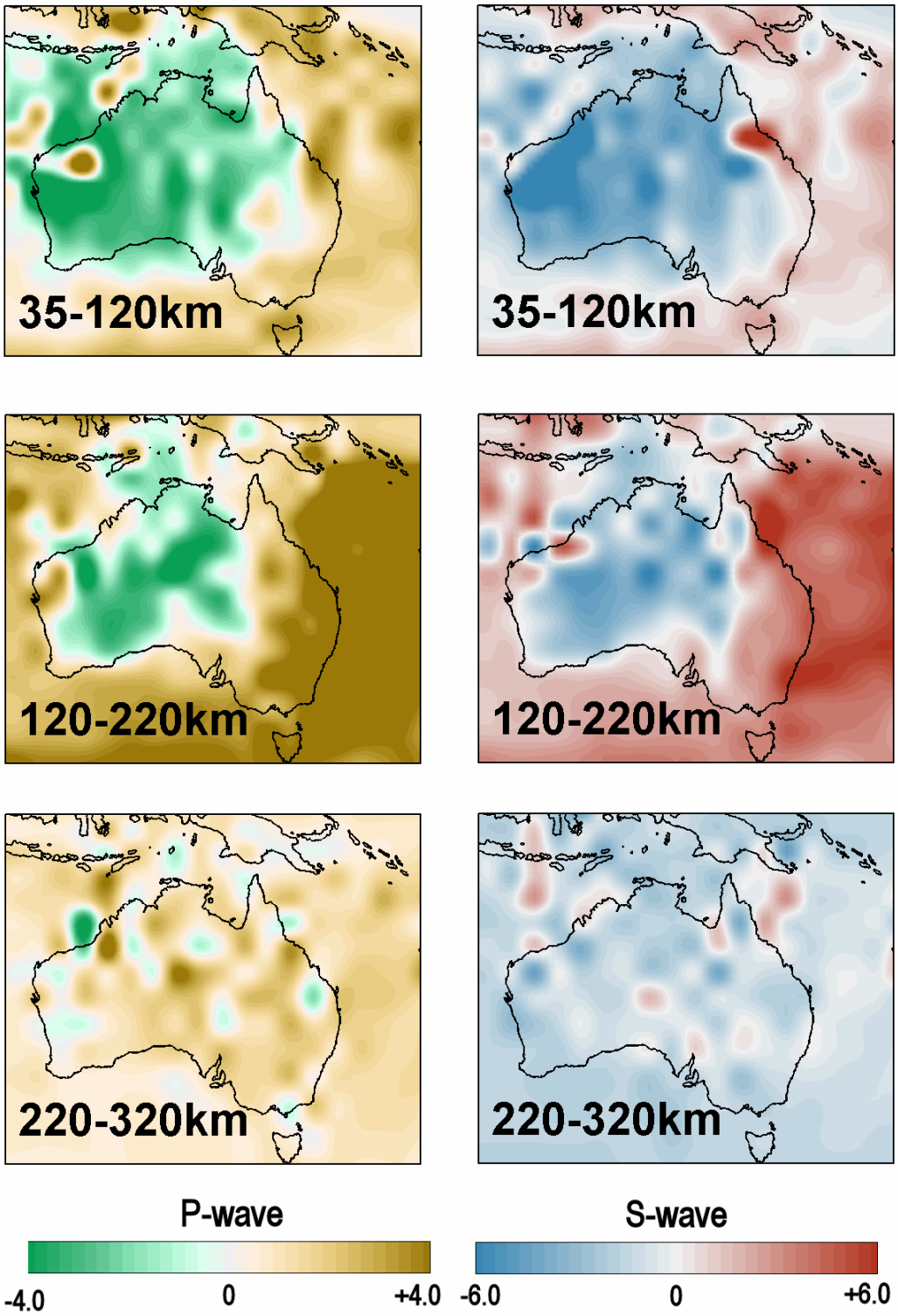

Figure 5.6: Results from the 3-D inversion procedure at 35-120, 120-220 and 220-320km using 3D initial models (left) *P* wave speed perturbation (right) *S* wave speed perturbation. Seismic speeds are plotted in percent relative to the *ak135* model.

The *P* wavespeed image suggests that the upper mantle is dominated by fast seismic wavespeed anomaly, while the *S* wave image shows a mixture between fast and slow wavespeed anomalies. The inversion results also reveals fast seismic wavespeeds to the north of Australia, which may correspond to the subduction zone between Australian and Eurasian plates. The oceanic lithosphere to the east, south and west of Australia is presented by low wavespeed anomalies.

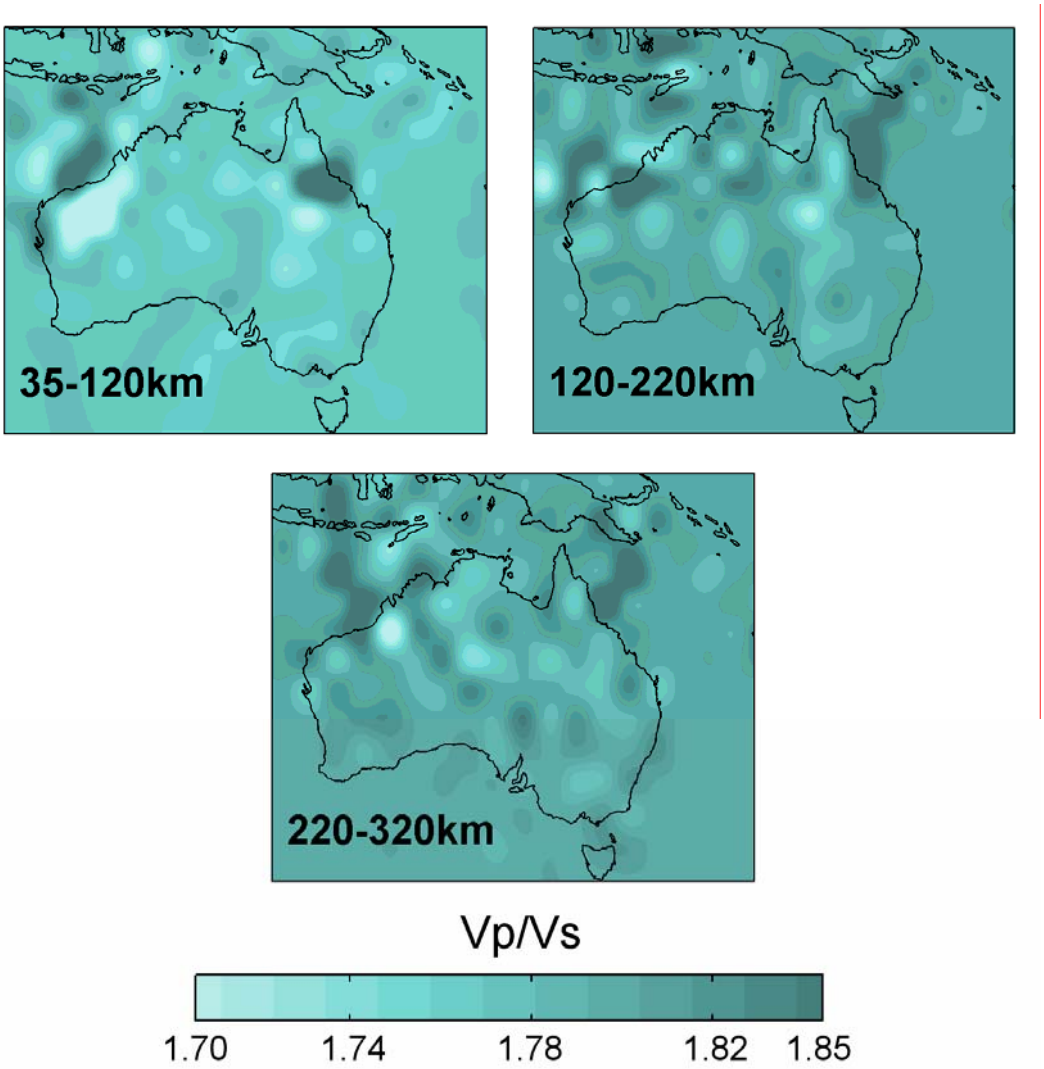

Figure 5.7: Ratio of *Vp/Vs* at 35-120, 120-220 and 220-320km obtained from Figure 5.6.

Figure 5.7 shows the *Vp/Vs* ratio images for depth intervals 35-120km, 120-220km and 220-320km. The images are produced from *Vp* and *Vs* images presented in Figure 5.6. The existence of complex *Vp/Vs* ratio variations beneath Australian is revealed for all presented depth intervals, with value of the ratio varies between 1.70 and 1.85. In term of the value of *Vp/Vs*, the *Vp/Vs* ratio at 120-220km is similar to that at 220-320km, meanwhile the value *Vp/Vs* in the interval 35-120km is somewhat smaller.

5.3 Attenuation Models

The inverted seismic wavespeeds models presented in Figure 5.6 are then used for the inversion of the differential attenuation data obtained from the wave ratio and the station ratio measurements (Δt^*_{SP}, Δt^*_{PP} and Δt^*_{SS}) to produce shear and compressional attenuation models (Q^{-1}_{SH}, Q^{-1}_{SV} and Q^{-1}_{P}). To distinguish the attenuation models produced from the inversion of the Δt^*_{SP}, Δt^*_{PP} and Δt^*_{SS} information, the following term are used: Q^{-1}_{SH-SP} and Q^{-1}_{SV-SP} for transverse and radial shear attenuation obtained from the Δt^*_{SP} method, Q^{-1}_{SH-SS} and Q^{-1}_{SV-SS} for transverse and radial shear attenuation obtained from the Δt^*_{SS} method and Q^{-1}_{P-PP} for compressional attenuation from the Δt^*_{PP} method. Both *P* and *S* waves ray paths in 3-D models are also used to build a kernel matrix along with the inverted seismic wavespeeds and initial models of attenuation ($Q^{-1}_{P\_init}$ and $Q^{-1}_{S\_init}$).

We use exactly the same model parameterizations and inversion procedure as the inversion of attenuation in Chapter 4. This approach is used in order to have a final model which will be comparable with the previous model. Again for the inversion of the Δt^*_{SP}, it is assumed that there are no losses in pure compression and $V_P = V_S\sqrt{3}$, in this way, we have $Q_{P\_init}/Q_{S\_init} = 2.25$. This ratio will decrease if there is any further loses in compression.

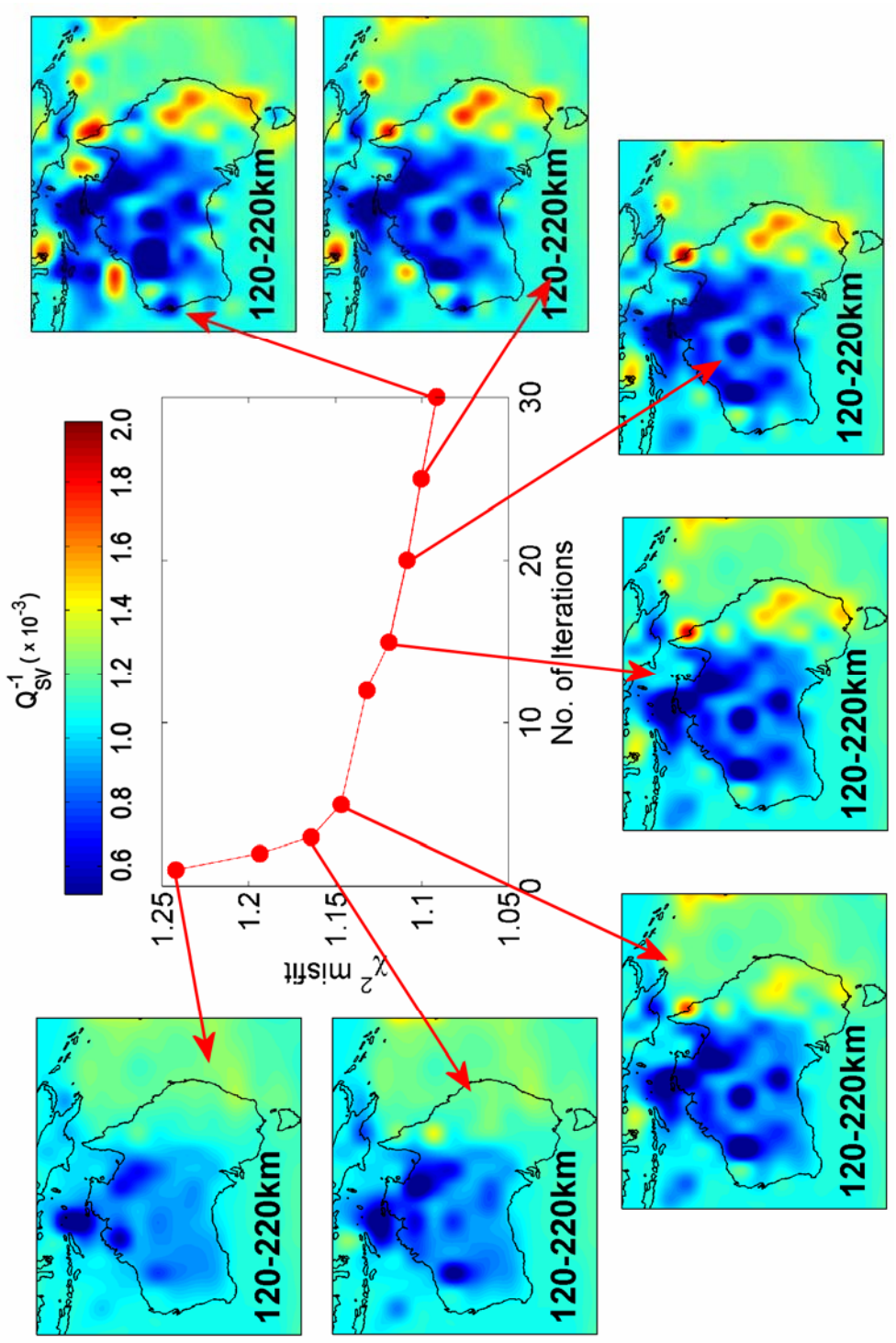

Figure 5.8: Number of iteration as a function of misfit function (χ^2) along with attenuation images at 120-220km depth interval. When the number of iterations is too high, our model is less damped. On the other hand, it is over damped.

Since our kernel is quite sensitive to the number of iterations, data and model covariance, the misfit χ^2 is used as our quality control. The cross plot of the misfit versus number of iterations with each corresponding tomographic images at 120-220km is shown in Figure 5.8. Our misfit parameter lies between 1.05 to 1.25 in the iteration number between 1 and 30. If the value of misfit is relatively small it means that there is no significance difference between observed data and its model. It can be seen that the value of the misfit is getting smaller as the number of iterations increases, from which it is suggested that our inversion is satisfying the model. We stop the iteration when once we have a reasonable result of misfit (i.e. the misfit function start to converge) and reasonable geological features. In this inversion we stop at the 5^{th} iteration.

The final 3-D models for Q_{SH-SP}^{-1} and Q_{SV-SP}^{-1} beneath Australasian region in the depth intervals 35-120, 120-220 and 220-320km are displayed in Figure 5.9. In order to see attenuation variation in the upper mantle (220-320km), attenuation images at this level are plotted with different color scale used to that for the lithosphere.

The attenuation images produced in this study are similar to the seismic velocity images produced by *P* and *S* waves tomography (see Figure 5.6), suggesting that velocity and attenuation anomalies are produced from similar physical processes, most probably affected by rock temperature, pressure, hot spots and partial melting.

The tomographic models clearly reveal most of the major geological features in the regions. The attenuation of cratonic Australia is distinguishable from the surrounding region especially to the south and west Australia. The lithosphere in general is dominated by low attenuation feature, while the upper mantle beneath has high attenuation. Again, the contrast in seismic speeds between the Precambrian central-western Australia and the Phanerozoic eastern seaboard is also well exhibited in both transverse and radial shear attenuation.

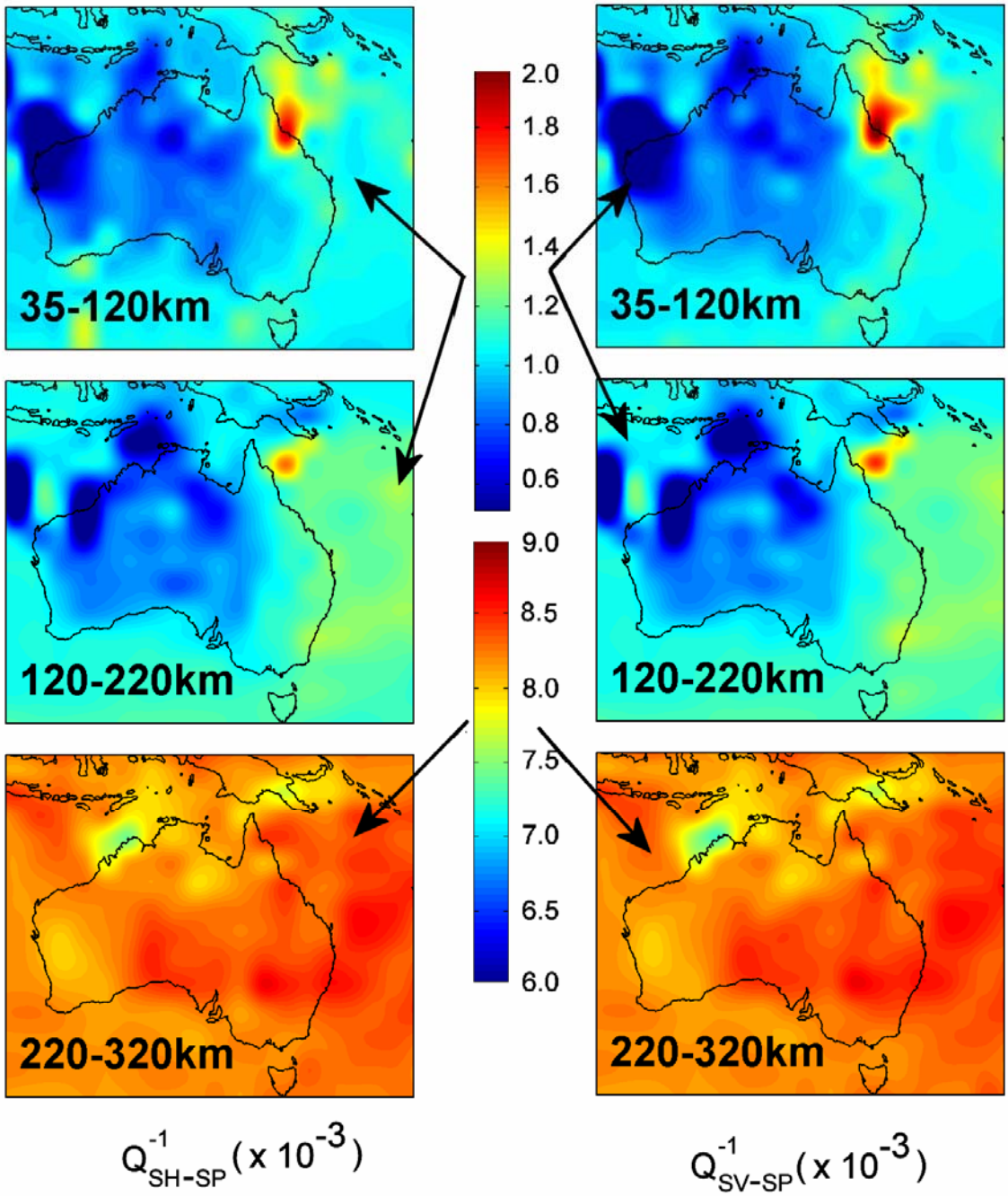

Figure 5.9: Transverse and radial shear attenuation (Q^{-1}_{SH-SP} and Q^{-1}_{SV-SP}) beneath Australasian region at 35-120, 120-220 and 220-320km. Note that the color scale for the lithosphere and the upper mantle are different. The images are produced from the inversion of nearly 6500 Δt^{*}_{SP} measured by the wave ratio method.

The Q_{SH-SP}^{-1} and Q_{SV-SP}^{-1} in the lithosphere beneath central-western region of Australia lie between 0.0008 and 0.001 ($Q_{S-SP} \approx 1000-1250$) while beneath eastern seaboard they rise to between 0.001 and 0.0012 ($Q_{S-SP} \approx 833-1000$). An extremely high attenuation region exists at shallower depth in and around the Coral Sea which is consistent with the attenuation images produced by 1D model but now better imaged and more localized. Several high attenuation anomalies also exist around Bass Strait and along eastern coast of Australia where the recent volcanic activities occur.

The Q_{SH-SP}^{-1} and Q_{SV-SP}^{-1} images in the upper mantle (220-320km) suggest very high attenuation compared to the lithosphere which varies between 0.0072 and 0.0085 ($Q_{S-SP} \approx 120-140$). In the northern part of Australia, where ray path density is higher, the image indicates low attenuation compare to southern part.

Representations of the Q_{SH-SS}^{-1} and Q_{SV-SS}^{-1} images give independent verification for the determination of lithospheric and upper mantle attenuation features beneath Australasian. The Q_{SH-SS}^{-1} and Q_{SV-SS}^{-1} images show similarities and consistency with the Q_{SH-SP}^{-1} and Q_{SV-SP}^{-1} images. The consistent features are low loss lithosphere beneath central-western Australia, high attenuation beneath eastern sea board and very high attenuation around Coral Sea and very high attenuation with low variation in the upper mantle.

The value of Q_{SH-SS}^{-1} and Q_{SV-SS}^{-1} in the lithosphere beneath central-western region of Australia lie between 0.0007 and 0.0009 ($Q_{S-SS} \approx 1100-1450$) while beneath eastern seaboard between 0.0012 and 0.0014 ($Q_{S-SS} \approx 715-833$).Very high attenuation which exceeds 0.0014 ($Q_{S-SS} \approx 715$) in the western lithosphere is situated around Great Sandy Desert where path density is low. This attenuation anomaly may be an artificial structure.

The Δt_{PP}^{*} data is inverted to yield determination of compressional attenuation structure beneath Australasian region. Compared to the Δt_{SS}^{*}, the Δt_{PP}^{*} data is relatively free of noise. In this way, the inverted Q_{P-PP}^{-1} structure is more trustworthy than Q_{S-SS}^{-1}. Despite this limitation, the Q_{SH-SS}^{-1} and Q_{SV-SS}^{-1} patterns still shows similarities with

the Q_{P-PP}^{-1}. This may be aided by the restriction to seismic data with Signal to Noise ratio greater than 2.0 that is employed in all inversions.

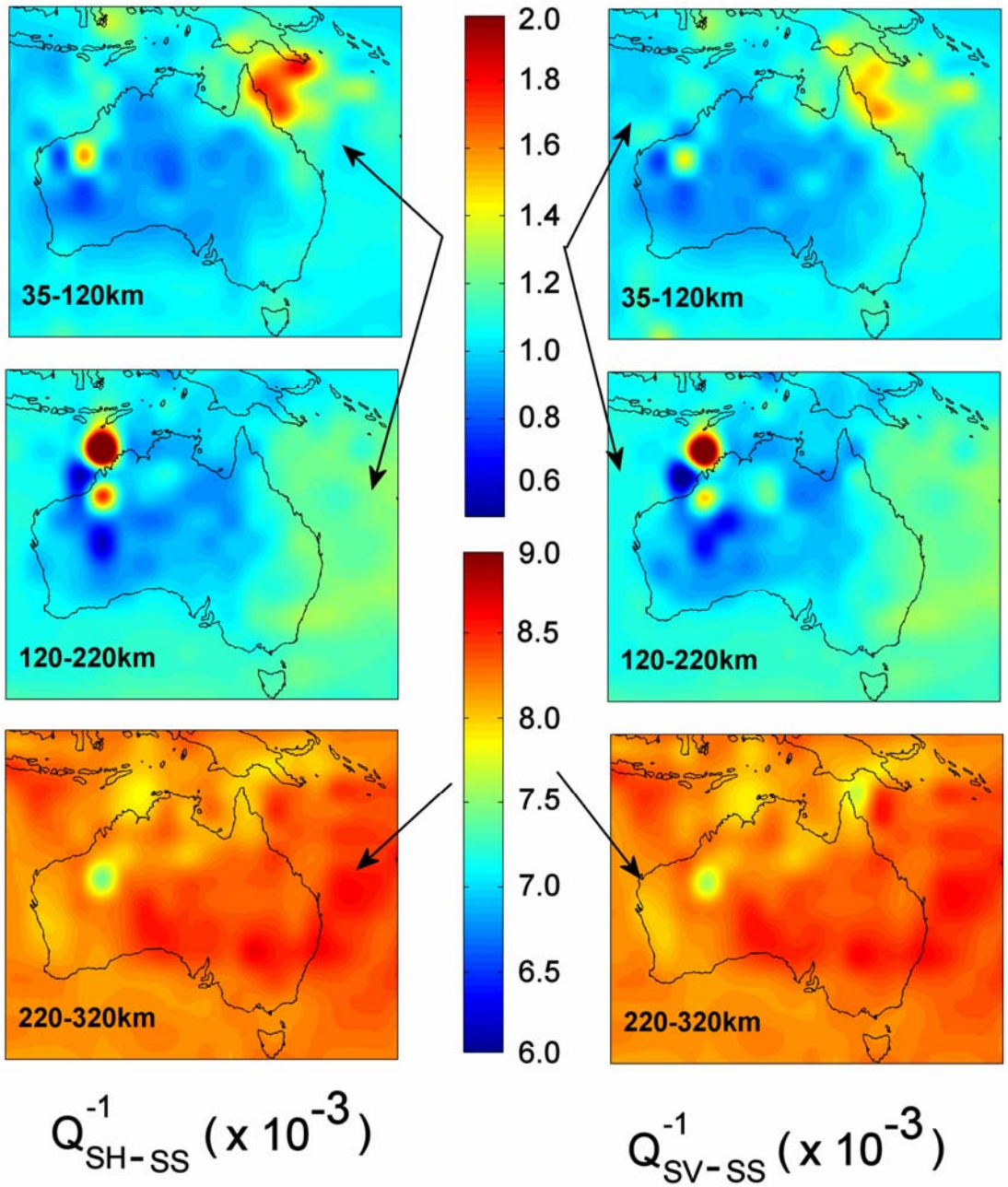

Figure 5.10: Transverse and radial shear attenuation (Q_{SH-SS}^{-1} and Q_{SV-SS}^{-1}) beneath Australasian region at 35-120, 120-220 and 220-320km. The images are produced from the inversion of Δt_{SS}^{*} data. Note that the color scale for the lithosphere and the upper mantle are different.

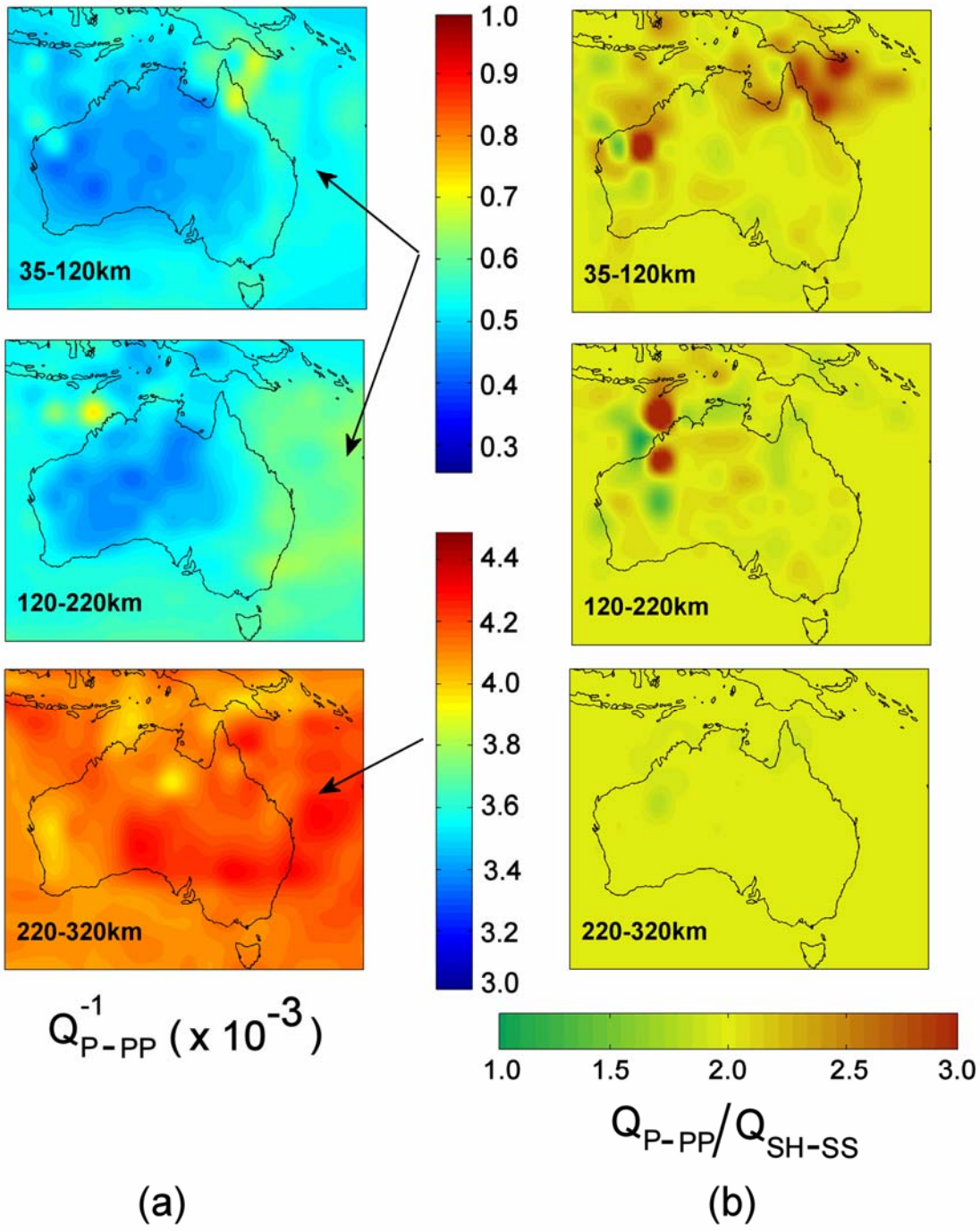

Figure 5.11: (a) Compressional attenuation (Q^{-1}_{P-PP}) beneath Australasian region at 35-120, 120-220 and 220-320km. The images are produced from the inversion of Δt^{*}_{PP} data. Note that the color scale for the lithosphere and the upper mantle are different. (b) Ratio of Q^{-1}_{P-PP} over Q^{-1}_{SH-SS}.

Figure 5.11 (a) shows the Q_{P-PP}^{-1} images of the Australasian region in the depth intervals 35-120, 120-220 and 220-320km. Note that the color scale of Q_{P-PP}^{-1} is half of that for Q_{S-SS}^{-1}. Again the images show several similarities with previous attenuation images. In the lithosphere beneath central-western Australia, the Q_{P-PP}^{-1} lie between 0.0003 and 0.0005 ($Q_{P-PP} \approx 2000-3300$). While in the eastern seaboard Q_{P-PP}^{-1} has values between 0.0005 and 0.0006 ($Q_{P-PP} \approx 1600-2000$). As demonstrated in the other attenuation images, the attenuation in the shallower structure around Coral Sea is quite high compared to its surroundings as much as 0.0007 ($Q_{P-PP} \approx 1500$). In the upper mantle the Q_{P-PP}^{-1} lie between 0.004 and 0.0043 ($Q_{P-PP} \approx 230-250$).

Figure 5.11 (b) shows the ratio of Q_{P-PP}^{-1} to Q_{SH-SS}^{-1} for entire region. In general the ratio varies between 1.5 and 2.75, suggesting that in this region attenuation is dominated by loss in shear. To some extent the variation of the ratio is influenced by geological features i.e. the main transition around the Tasman Line is suggested by the contrast in the ratio. To the east of the Tasman Line, shear wave seems more strongly attenuated than in western parts. In the upper mantle, the variation in the ratio is very low and it is suggested that shear wave is about twice more attenuating than compressional wave.

Chapter 6

Frequency Dependence of Attenuation beneath the Australasian region

Examination of the differential attenuation of *S* to *P* waves (Δt^*_{SP}), *P* to *P* (Δt^*_{SP}) and *S* to *S* (Δt^*_{SP}) in the frequency band between 0.10 and 1.00 Hz as discussed in the previous chapter revealed the lateral and vertical variation of seismic attenuation beneath the Australasian region. The measurements of the differential attenuation in the narrow frequency band between 0.10Hz and 1.00 Hz were conducted under the assumption that in this frequency band, attenuation is nearly independent of frequency. This assumption was supported by the linear behavior of the logarithmic spectral ratio as a function of frequency (over the band 0.1-1.00Hz) for most seismograms.

In this Chapter, the frequency dependence of attenuation beneath the Australasian region is investigated by measuring the differential attenuation of *S* to *P* waves (Δt^*_{SP}) of nearly 6500 seismic data in a broad frequency band of 0.10-2.5 Hz. This broad frequency band is chosen for three reasons. *The first reason*, is that the broad frequency band of 0.10 - 2.5Hz is in the band where, for events with *Ms* < 6.0, the spectrum is expected to be declining only slowly with frequency [Aki, 1967 –see Figure 6.1]. For higher frequencies a more rapid decline, $S(\omega) = S(0) \Big/ \left[1 + (\omega/\omega_0)^2\right]$, makes

measurement difficult. In Aki's model, the spectral amplitude increases with magnitude M_S for all frequencies which is in agreement with real seismic data. The ω-square asymptote represents the dominance of a stopping phase at high frequencies, and the number of stopping points (or the length of stopping loop) increases with the ruptured area. A ceiling for the ω-cube model is exists because the nucleation point is a single point for any earthquakes [Aki, K and P.G. Richards, 2002]. The spectral chart of Aki [1967] is also similar to the behavior of seismic spectra of Australian seismic data (Figure 6.2). Figure 6.2 shows characteristics of seismic spectra of *P* and *S* waves of several Australian seismic data recorded by eastern stations (Tasman Line Experiment, 2003-2006) and Linkage Project (2006-2007) in western Australia with magnitude *mb* 5.5 to 6.5, depth 25 to 60km and epicentral distance Δ: 25º to 40º.

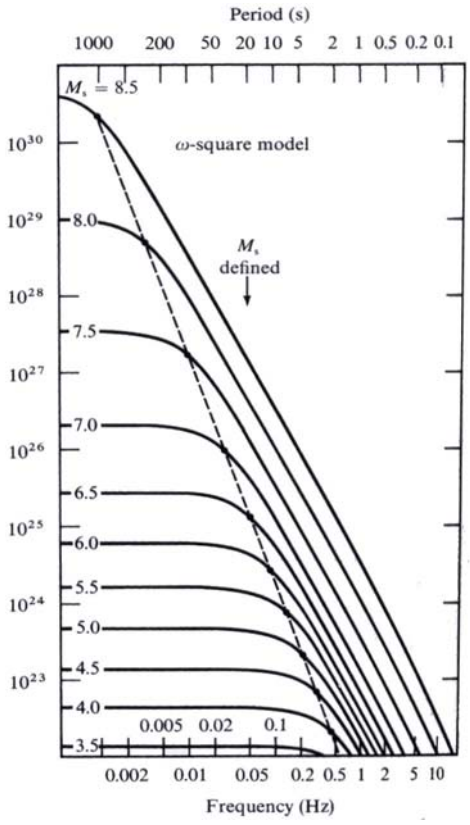

Figure 6.1: Characteristics of seismic body waves spectra observed at a certain distance from earthquakes with different M_S. The vertical coordinate shows the corresponding seismic moment. The broken dashed line is the locus of the corner frequency ω_0. [From Aki, 1967].

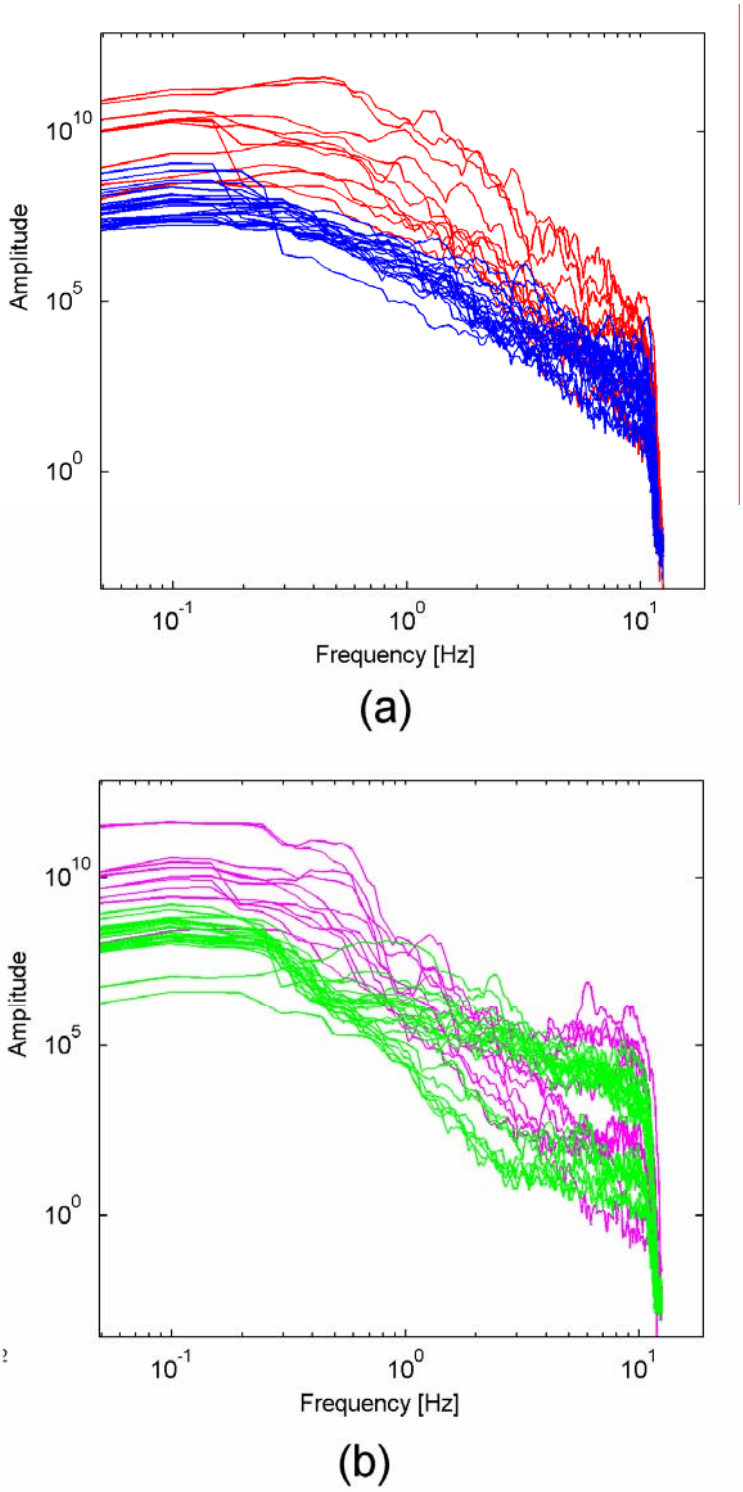

Figure 6.2: Behavior of (a) *P* and (b) *S* wave spectra spectra observed at eastern (red and magenta) and western (blue and green) Australian seismic stations with magnitude *mb* 5.5 to 6.5, depth 25 to 60km and epincentral distance Δ: 25º to 40º. Note that both amplitude and frequency axes are plotted with a logarithmic scale. The anti-alias filter cuts in near 10Hz, Nyquist Frequency is 12.5Hz for the 25 sample/s recording at the portable stations.

The second reason, between 0.1 and 2.5 Hz, the spectrum of Australian seismic data mainly lie above the noise spectrum, while above 2.5Hz the data spectrum tends to lie below noise spectrum. In other words, beyond this frequency the seismic signals are heavily contaminated by unneeded noise (i.e. *P* wave coda). *The third reason,* based on visual observation to the logarithmic spectral ratio as a function of frequency of Australian seismic data, in the frequency band of 0.10-2.5Hz some seismogram show linear behavior and a few show a *'kink'* behavior. The *'kink'* behavior of the logarithmic spectral ratio as a function of frequency suggests a significant effect from higher frequency on the attenuation properties.

6.1 Differential Attenuation Measurements in 0.10 - 2.5 Hz

In the examination of the differential attenuation of *S* to *P* waves (Δt^*_{SP}) as a function of frequency, the broad frequency band 0.10 - 2.5Hz is divided into a set of four sub-frequency bands using the Golden section. The technique for estimating the differential attenuation of *S* to *P* waves (Δt^*_{SP}) that was employed in Chapter 4 is now used to measure the Δt^*_{SP} for each sub frequency band. The four frequency bands are displayed in Table 6.1.

Table 6.1: the frequency bands use to estimate attenuation dependence on frequency in a broad frequency band between 0.10 and 2.5Hz

Frequency band symbol	Frequency band (Hz)	Center frequency (Hz)
f1	0.10 – 1.00	0.55
f2	0.50 – 1.50	1.00
f3	1.00 – 2.00	1.50
f4	1.50 – 2.50	2.00

Figure 6.3 shows an example of seismic spectra between 0 and 2.5 Hz for *P* and *S* waves and their background spectra along with the differential attenuation measurement from *S* to *P* wave spectral ratio for transverse (*T*), radial (*R*) and horizontal (*H*) components. The seismic event is situated around the Solomon Islands and was recorded by Tasman Line Experiment Station, TL02. The values of the Δt^*_{SP}

from each of the sub-frequency bands are shown. It can be seen that, the curvatures of the spectral ratios of all components show a *'kink'* behavior at around 0.85Hz and 1.30Hz possibly due to enhanced noise, but the change in slope indicates clear frequency dependence. This behavior yields variation of the Δt^*_{SP} values for each sub-frequency band, which suggest an existence of a frequency dependence of attenuation.

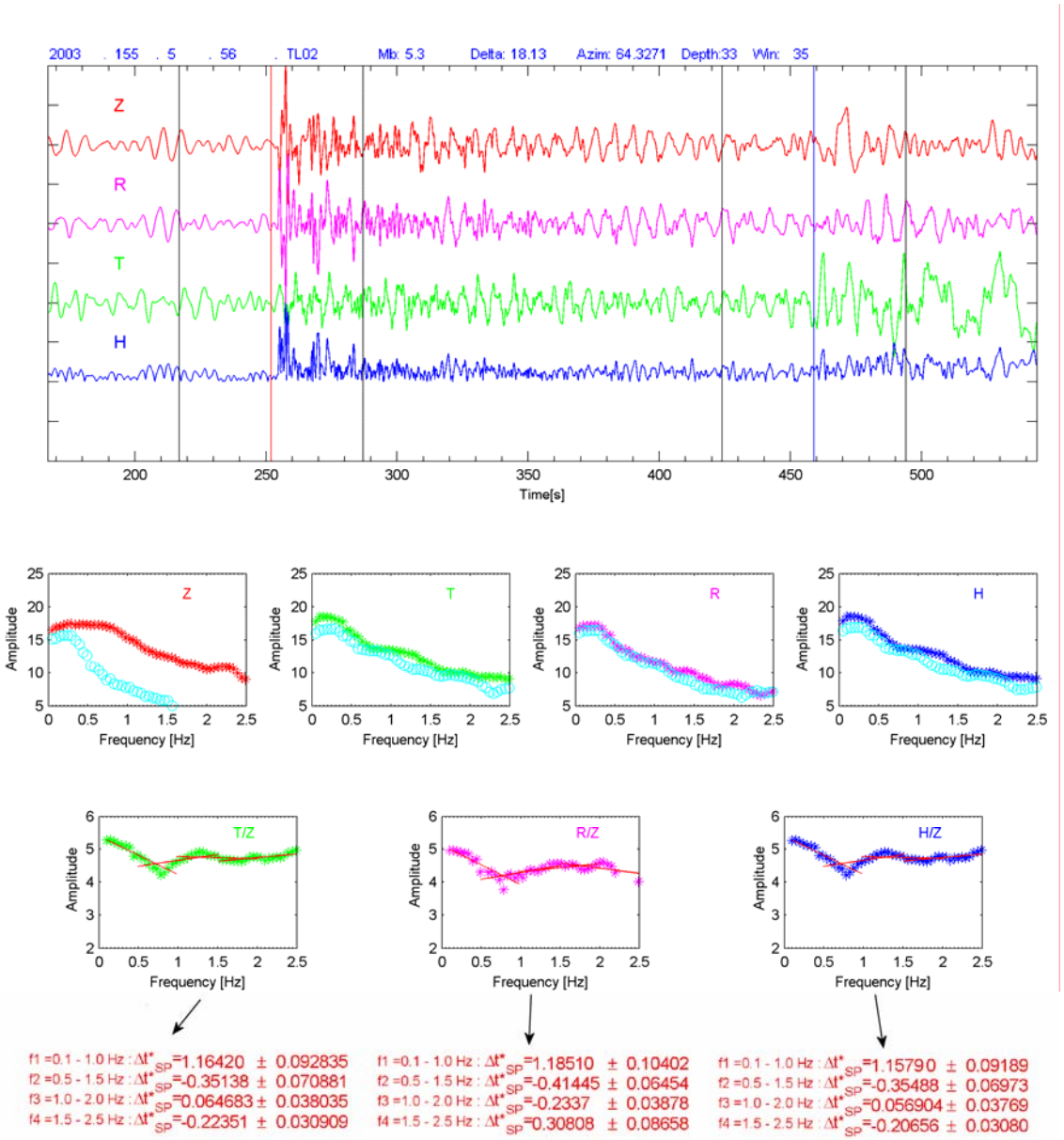

Figure 6.3: *Upper panel*, unfiltered seismic seismogram from an event around Solomon Islands that was recorded by TL02 station. *Middle panel*, spectra of *P* wave (vertical component) and *S* waves (transverse, radial and horizontal components) and their backgrounds. Logarithmic slope of the spectral ratio at sub frequencies 0.1-1.0, 0.5-1.5, 1.0-2.0, 1.5-2.5Hz are shown in lower panel.

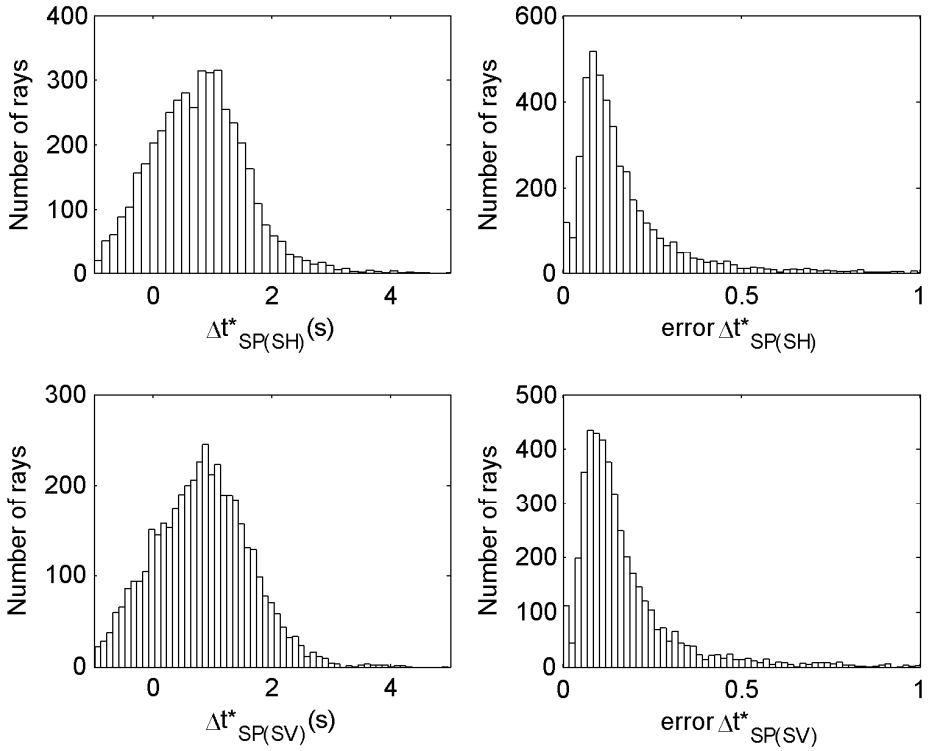

Figure 6.4 (a) f1: 0.1-1.0Hz

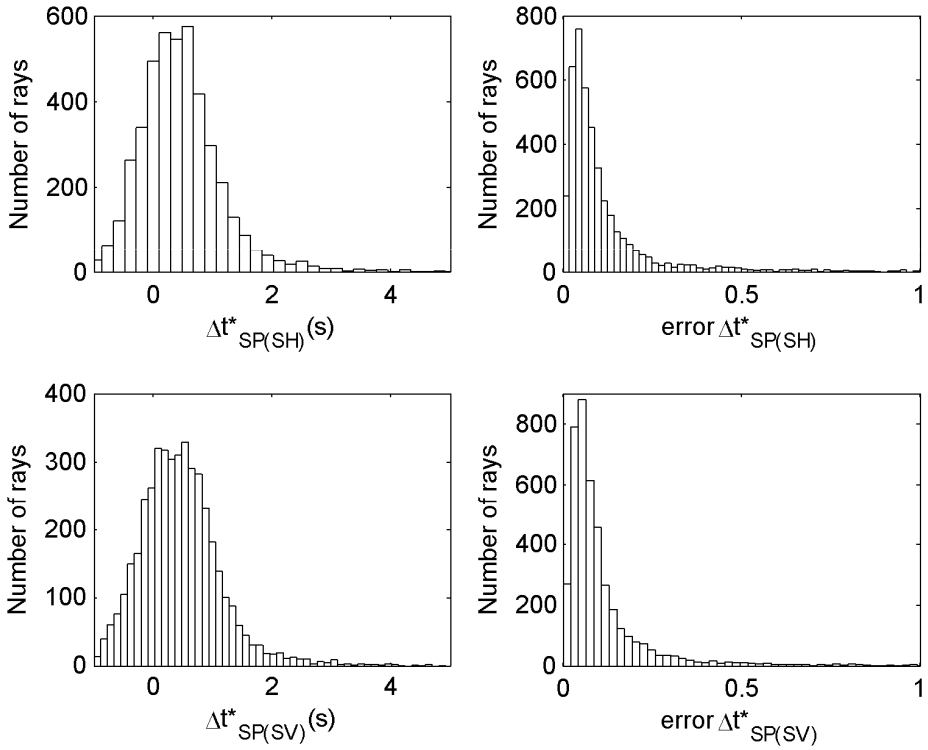

Figure 6.4 (b) f2: 0.5-1.5Hz (continued)

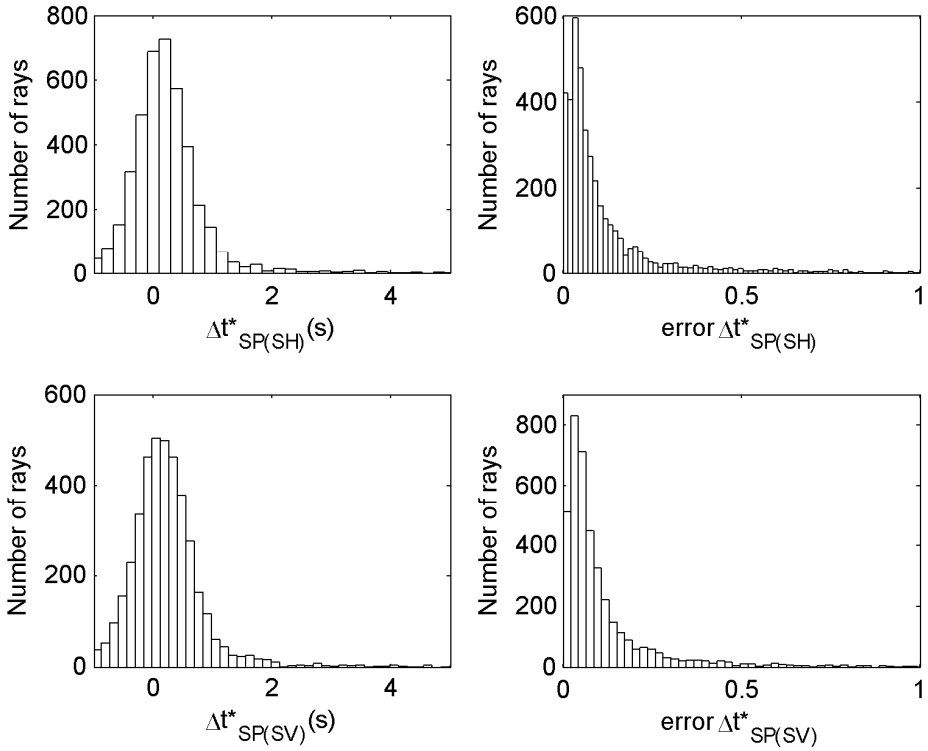

Figure 6.4 (c) f3: 1.0-2.0Hz

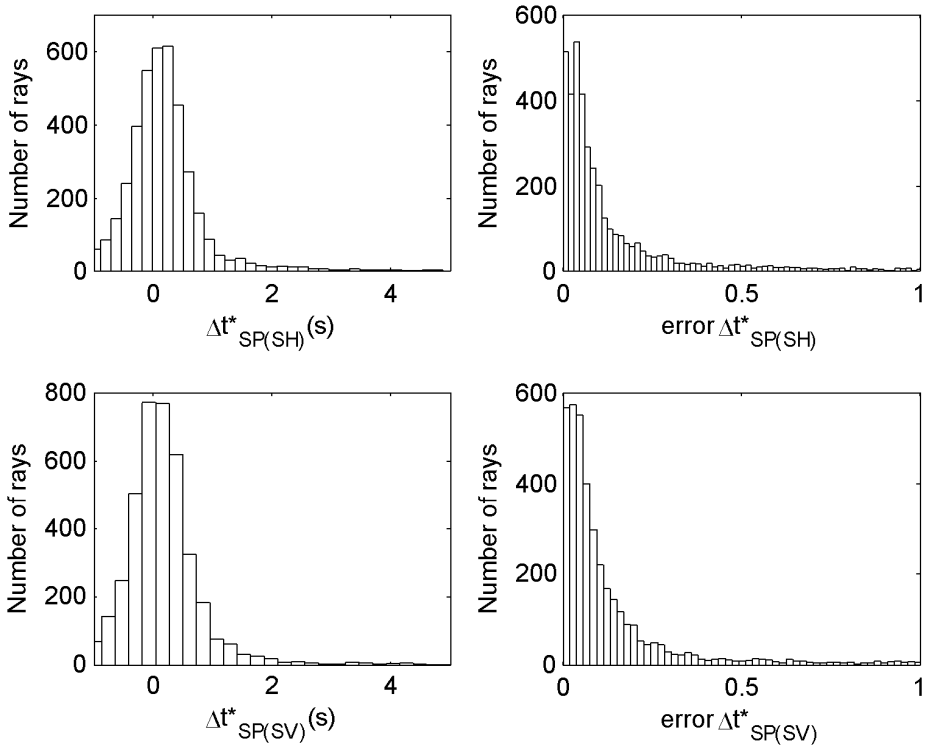

Figure 6.4 (d) f4: 1.5-2.5Hz

Figure 6.4: Distribution of the Δt^*_{SP} values and error estimates for nearly 6500 Australian seismic dataset at sub frequency band (a) 0.1-1.0Hz (b)0.5-1.5Hz (c)1.0-2.0Hz and (d) 1.5-2.5Hz.

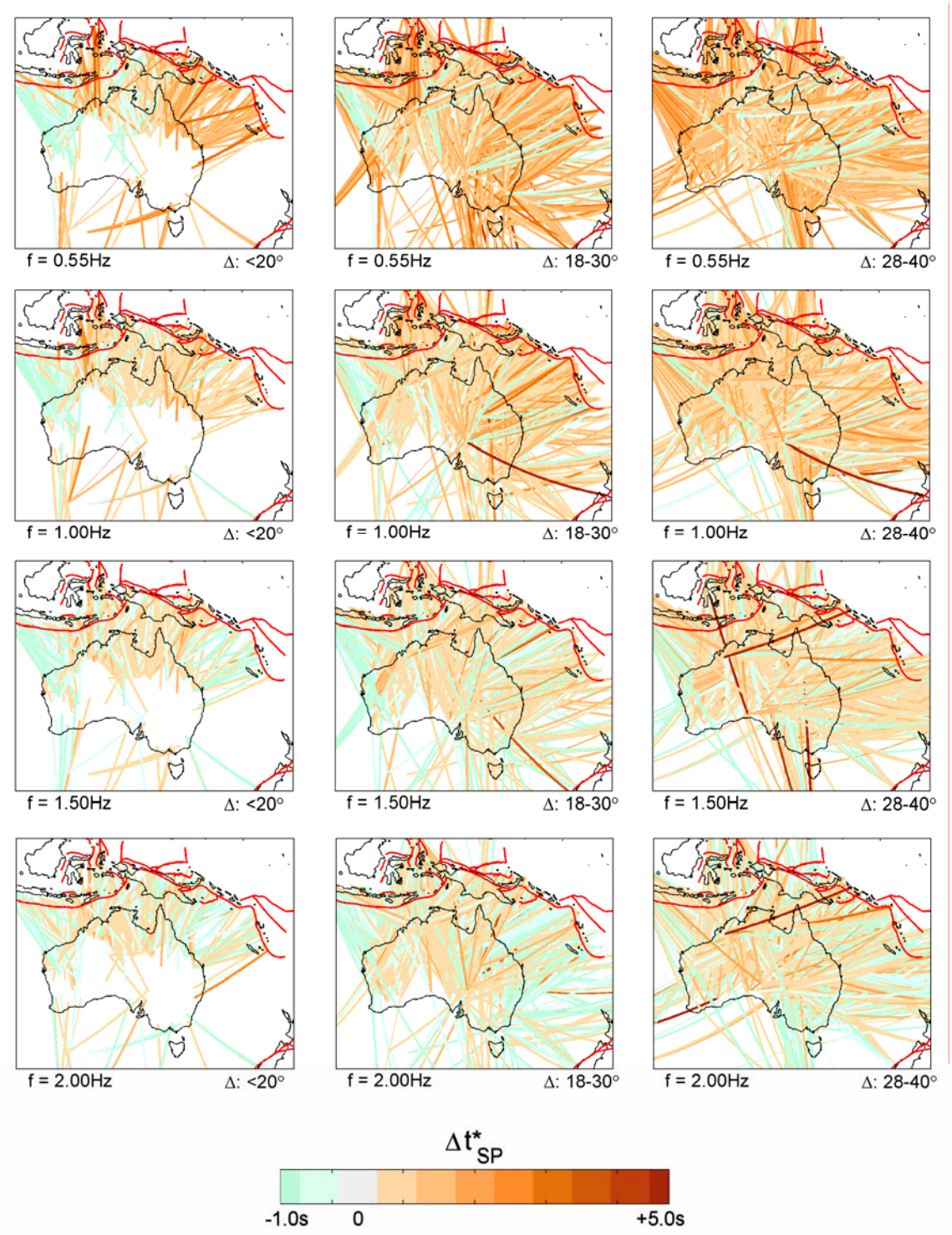

Figure 6.5: Summary of *S* to *P* waves differential attenuation (Δt^*_{SP}) estimated from nearly 6500 Australian seismic dataset at center frequencies 0.55Hz, 1.00Hz, 1.50Hz and 2.00Hz. The raypaths of Δt^*_{SP} are color scaled by the value of Δt^*_{SP} with line thickness inversely proportional to the inverse of the errors in the Δt^*_{SP} estimation with epicentral distance ranges from of 5-20º, 18-30º and 28-40º. The red lines represent tectonic boundaries.

The Δt^*_{SP} values and error estimate distributions for nearly 6500 Australian seismic dataset at each sub-frequency band are presented in Figure 6.4. The Figure shows that at center frequencies 0.55 and 1.00 Hz the Δt^*_{SP} values are mainly distributed between -1.0s and 3.0s, while at center frequencies 1.50 and 2.00Hz are distributed between -1.0 and 2.0s for both transverse and radial components. In other words, the differential attenuation (Δt^*_{SP}) decreases with increasing frequency. In addition, for all center frequencies most of the error estimate distribution lies below 0.5s.

A geographical representation of the differential attenuation (Δt^*_{SP}) at all center frequencies is shown in Figure 6.5. The ray paths of Δt^*_{SP} are color coded by the value of Δt^*_{SP} with line thickness inversely proportional to the inverse of the errors in the Δt^*_{SP} estimation and presented in epicentral distance ranges from 5-20º, 18-30º and 28-40º. The values of Δt^*_{SP} represent the average between source and receiver pairs. The depth of the path propagation increases with epicentral distance.

Figure 6.5 shows the general patterns of the differential attenuation (Δt^*_{SP}) are different from one center frequency to another for all epicentral distances. The lithospheric paths (i.e. $\Delta < 20º$) from eastern Australia (from seismic events around Irian Jaya, Papua New Guinea, Solomon Islands, New Caledonia and New Zealand) that are associated with high attenuation zones show a dramatic change from high attenuation at center frequencies 0.55 and 1.00Hz to a mixed pattern between low and high attenuation at center frequencies 1.50 and 2.00Hz. The paths from western Australia particularly from seismic events around Java and Bali that are associated with a low attenuation zone, show a low attenuation pattern for all center frequencies. The pattern of the Δt^*_{SP} for the lithospheric paths is also similar to that for deeper paths (i.e. Δ: 18-30º). It can be seen that at center frequencies 0.55 and 1.00Hz, the paths from eastern Australia show high attenuation, while at center frequencies 1.50 and 2.00Hz show a mixture between high and low attenuation. For epicentral distances Δ: 28-40º, the attenuation paths at center frequencies 0.55 and 1.00Hz are dominated by high attenuation. This may be affected by high attenuation zone of the upper mantle (below

220km). At central frequencies 1.50 and 2.00Hz, the pattern is still dominated by high attenuation paths in spite of the emergence of some low attenuation paths. The difference of attenuation patterns between the first two central frequencies (0.55 and 1.00Hz) and the last two (1.50 and 2.00Hz) suggest the existence of frequency dependent of attenuation.

6.2 Frequency Dependence of Attenuation Paths

The exponent of the frequency dependence of attenuation is estimated based on equation:

$$\Delta t^*_{SP(f2)} = \Delta t^*_{SP(f1)} \left(\frac{f2}{f1} \right)^{-\gamma} \tag{6.1}$$

Here $\Delta t^*_{SP(f2)}$ and $\Delta t^*_{SP(f1)}$ are *S* to *P* differential attenuation at center frequency $f2$ and $f1$ respectively and γ is the frequency dependence of attenuation at $f2$ with $f1$ treated as a reference. Taking natural logarithm of the equation 6.1, the frequency dependence of attenuation is defined by:

$$\gamma = -\ln\left(\frac{\Delta t^*_{SP(f2)}}{\Delta t^*_{SP(f1)}} \right) \Big/ \ln\left(\frac{f2}{f1} \right) \tag{6.2}$$

The frequency dependence of attenuation also can be treated from the power law relationship between *Q* and frequency:

$$Q_{f2} = Q_{f1} \left(\frac{f2}{f1} \right)^{\gamma} \tag{6.3}$$

Here Q_{f2} and Q_{f1} are attenuation at center frequency $f2$ and $f1$ respectively. When the value of $\gamma \approx 0$, the ratio of $f2$ over $f1$ will be close to 1 which yields $Q_{f2} = Q_{f1}$. In other words when $\gamma \approx 0$ the attenuation is not depend on frequency. On the other hand, when $\gamma \approx 1$ the dominant dependence is with frequency.

The estimation of frequency dependence of attenuation from the power law relationship between *Q* and frequency has been implemented by a numerous of authors such as Ulug and Berckhemer [1984], Flanagan and Wiens [1998] and Cheng [2000].

A study of frequency dependence of attenuation in the Australian continent was conducted by Cheng [2000] by utilizing 2000 seismograms from the SKIPPY experiment [1993-1996]. To estimate the frequency dependence of attenuation from individual data, he divided a broad frequency band into six sub frequency bands with center frequencies: 0.44Hz, 0.71Hz, 1.15Hz, 1.85Hz, 3.00Hz and 4.85Hz. He obtained a set of 1-D profiles of Q^{-1} and γ inverted from the estimation of frequency dependent Δt^*_{SP} by using Neighborhood Algorithm inversion method of Sambridge [1999]. Then by combining the 1-D Q^{-1} and γ profiles weighted by the ray path density, Cheng constructed a pseudo 3-D Q^{-1} and γ structure beneath the Australian continent. An example of his 1-D Q and γ profiles inverted from the SKIPPY data is shown in Figure 6.6. Figure 6.6 suggests that there is high attenuation and strong frequency dependence of attenuation in the upper mantle beneath the Coral Sea.

In my study, the frequency dependence of attenuation (γ) paths were derived by using equation 6.2 with the differential attenuation paths (Δt^*_{SP}) information as shown in Figure 6.5. The differential attenuation results (Δt^*_{SP}) at center frequency 0.55Hz is selected as the reference to estimate the γ for paths at center frequencies 1.00, 1.50 and 2.00Hz.

Figure 6.7 shows summary of the geographical variation of the exponent γ with propagation path. The ray paths are color scaled by the γ values for different epicentral distance groups, < 20º, 18-30º and 28-40º at center frequencies 1.0, 1.5, 2.0, average of 1 and 1.5Hz and average of 1.0, 1.5 and 2.0 Hz. The value of the exponent γ is between 0.0 and 1.0. Smaller values of γ represent less frequency dependence of attenuation and high values mean a high frequency dependence of attenuation. Figure 6.7 clearly shows a significant geographical variation in γ. The behavior of γ paths within short epicentral distances (i.e. Δ < 20º) represents the characteristic of the frequency dependence of attenuation in the lithospheric layer.

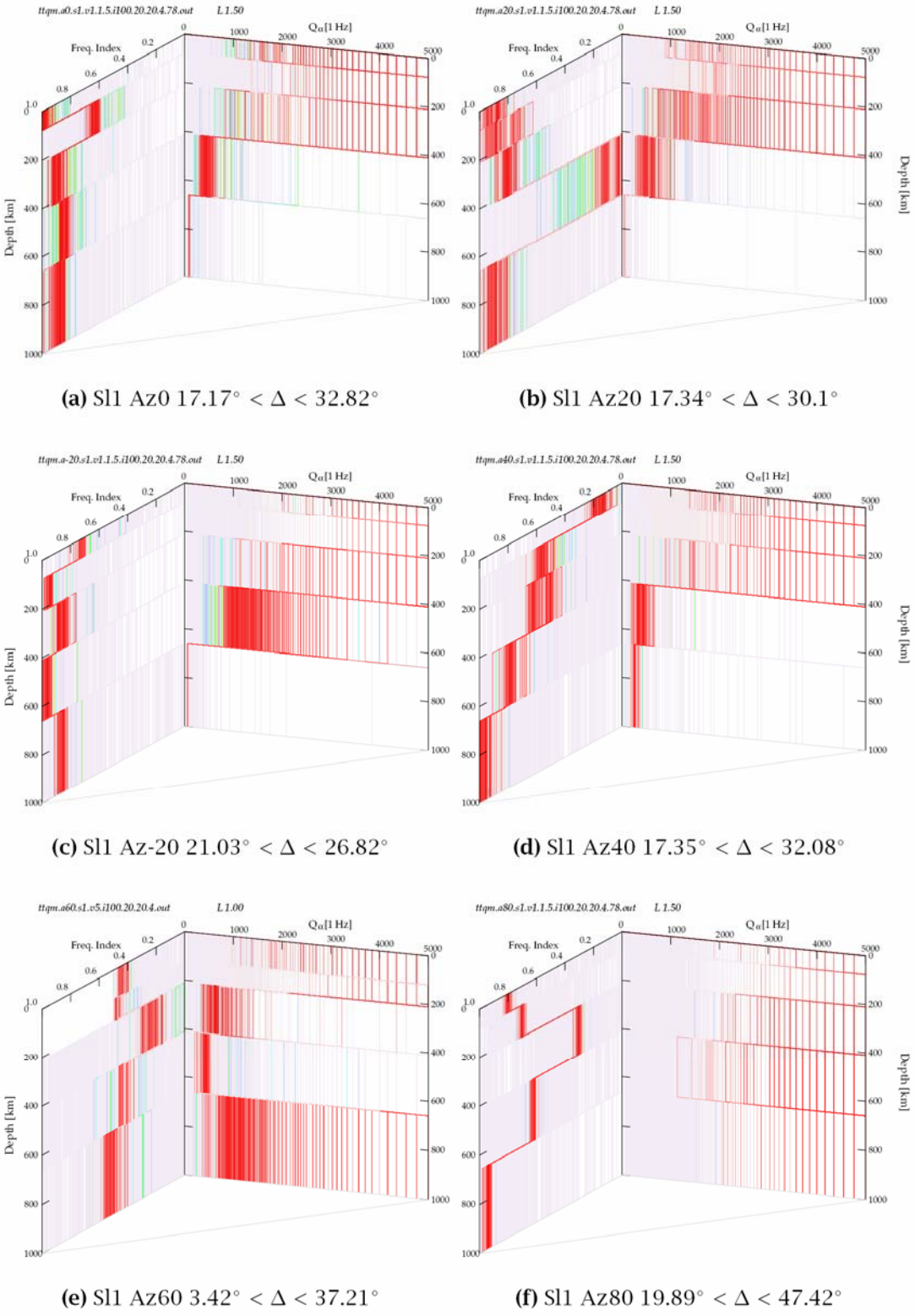

(a) Sl1 Az0 17.17° < Δ < 32.82°

(b) Sl1 Az20 17.34° < Δ < 30.1°

(c) Sl1 Az-20 21.03° < Δ < 26.82°

(d) Sl1 Az40 17.35° < Δ < 32.08°

(e) Sl1 Az60 3.42° < Δ < 37.21°

(f) Sl1 Az80 19.89° < Δ < 47.42°

Figure 6.6: An example of 1-D Q and γ profiles inverted from seismic data covering the Coral Sea. Epicentral distance range and azimuth corridor are shown in the caption of each sub Figure [From Cheng, 2000].

The frequency dependence of attenuation paths covering the north-west part of the Australian continent (from seismic events around Java) have values of γ close to zero. This suggests the frequency dependence of attenuation in this area is relatively weak. Most of paths crossing beneath the Coral Sea, eastern part and southern margin of the Australian Continent have relatively large γ. This indicates the effect of high attenuation zone around Coral Sea with a high frequency dependence of attenuation. Ray paths covering northern part of Australia show a mixture of small and large γ so that the frequency dependence of attenuation in this area is more complex.

The variation of γ for the intermediate distance range (i.e. Δ: 18-30º), where the turning point of those group of ray paths are roughly in the transition zone, suggest a mixture of small and large γ for any locations. The mixture between small and large γ may be caused by the difference of depth penetration of seismic ray paths. A mixture between small and large γ also exists for the epicentral distance Δ: 28-40º, however high frequency dependence of attenuation paths seem to dominate. Particularly, most paths from around Java show large γ.

6.3 Frequency Dependence of Attenuation Tomography

In this Section, 3-D images of the frequency dependence of attenuation beneath the Australasian region are presented. The approach is rather different from the pseudo 3-D images of Cheng [2000] which were produced by combining 1-D profiles of γ. In my work, 3-D images of the frequency dependence of attenuation are derived from a set of 3-D tomography images of Q_s at center frequencies 0.55, 1.00, 1.50 and 2.00Hz by using power law relationship of equation 6.3.

The Q_s tomography images are produced using the same technique and model parameterizations used to produce the results in section 5.3. Besides, seismic dataset, raypaths coverage and tomographic resolution are the same too. The result of the tomographic inversion for 35-120km, 120-220km and 220-320km for different center frequency can be seen in Figure 6.8. Figure 6.8 (a) is the tomographic images of Q_s for

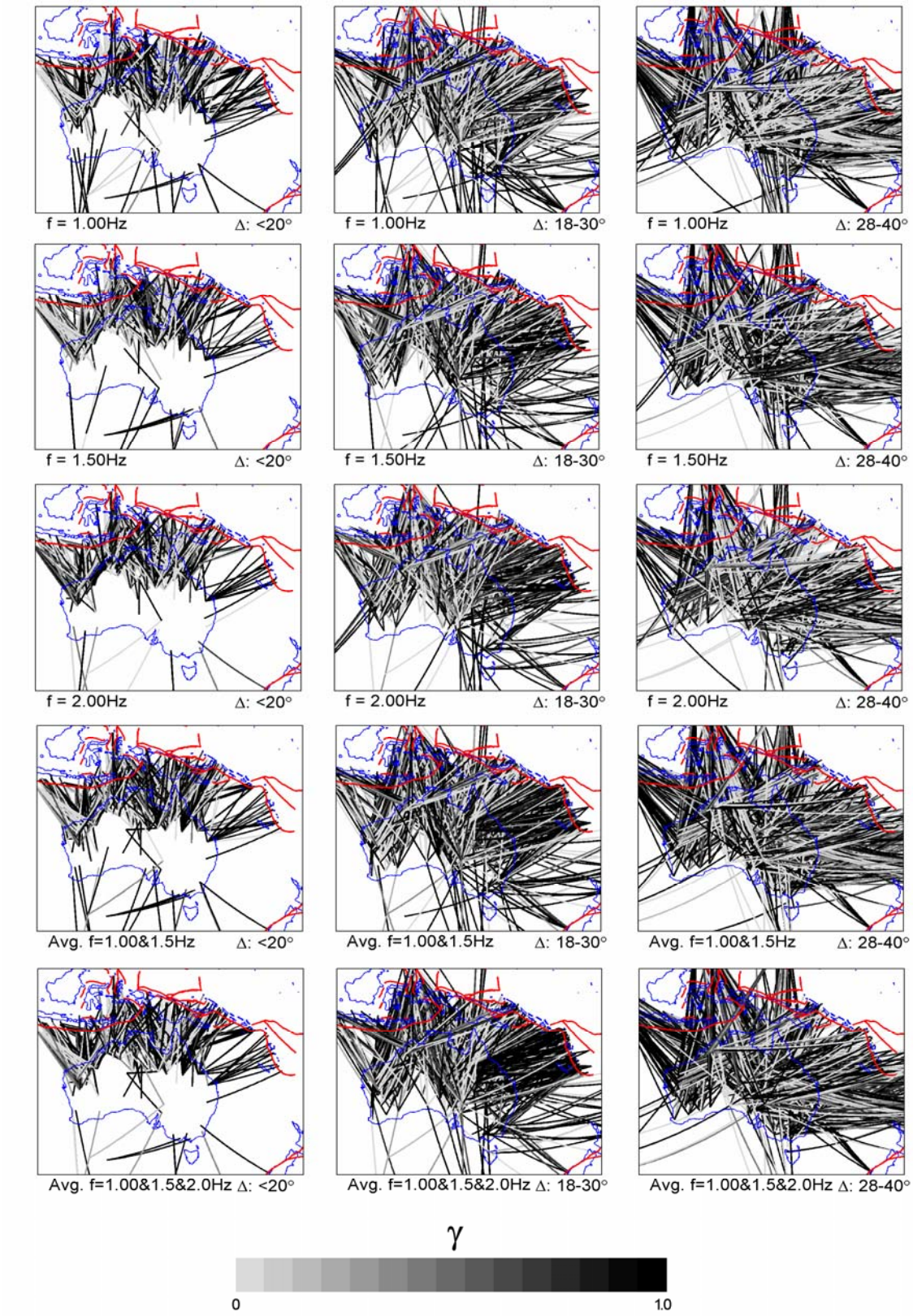

Figure 6.7: Summary of the frequency dependence of attenuation paths (γ) at center frequencies 1.00Hz, 1.50Hz, 2.00Hz, average of 1 and 1.5Hz and average of 1.0, 1.5 and 2.0 Hz with epicentral distance ranges from of 5-20º, 18-30º and 28-40º. The frequency dependence of attenuation increases with darker color.

transverse and radial component at center frequency 0.55Hz. Figure 6.8 (a) is exactly the same as Figure 5.8 that represents the attenuation beneath Australasian region with the attenuation is assumed independent of frequency.

Figure 6.8 (b) shows the attenuation images inverted from Δt^*_{SP} measurement at center frequency 1.00Hz. The images reveal that patterns of attenuation is vary from that in Figure 6.8 (a) particularly beneath the high attenuation zones in eastern part of the Australian continent, Coral Sea, Bass Strait and beneath the Great Australian Bight.

Figure 6.8 (b) shows that beneath the Coral Sea region, in particular, which is clearly pronounced as high attenuation zone in Figure 6.8 (a), seismic attenuation is slightly decreased at 1.0Hz. Moreover, the seismic attenuation is further decreased with increasing frequency (Figure 6.8 (c) and (d)). Meanwhile, the seismic attenuation anomalies beneath western part of the Australian continent show somewhat similar complexities at all center frequencies.

To produce frequency dependence of attenuation images beneath the Australian continent, the power law relationship between attenuation and frequency of equation 6.3 is employed. The attenuation images at center frequency 0.55Hz are chosen as a reference because that is where attenuation best resolved. Thus the relative frequency dependence of attenuation images at center frequency 1.00, 1.50, 2.00Hz and its average are produced.

Figure 6.9 shows the tomographic images of the frequency dependence of attenuation at 1.00, 1.50, 2.00Hz and average of 1.00, 1.50 and 2.00Hz with the attenuation at 0.55Hz used as a reference. The Figure shows that there are lateral and vertical variations in the frequency dependence of attenuation exponent γ beneath the Australasian region. The lithosphere (up to 220km) beneath the Coral Sea, Bass Strait and the Great Australian Bight is represented by a relatively high frequency dependence of attenuation γ. Meanwhile beneath the mainland of the Australian continent shows a complexity in frequency dependence of attenuation. In the deeper zone (220-320km),

the entire region is represented by low frequency dependence of attenuation. The frequency variations are discussed further in Chapter 7.

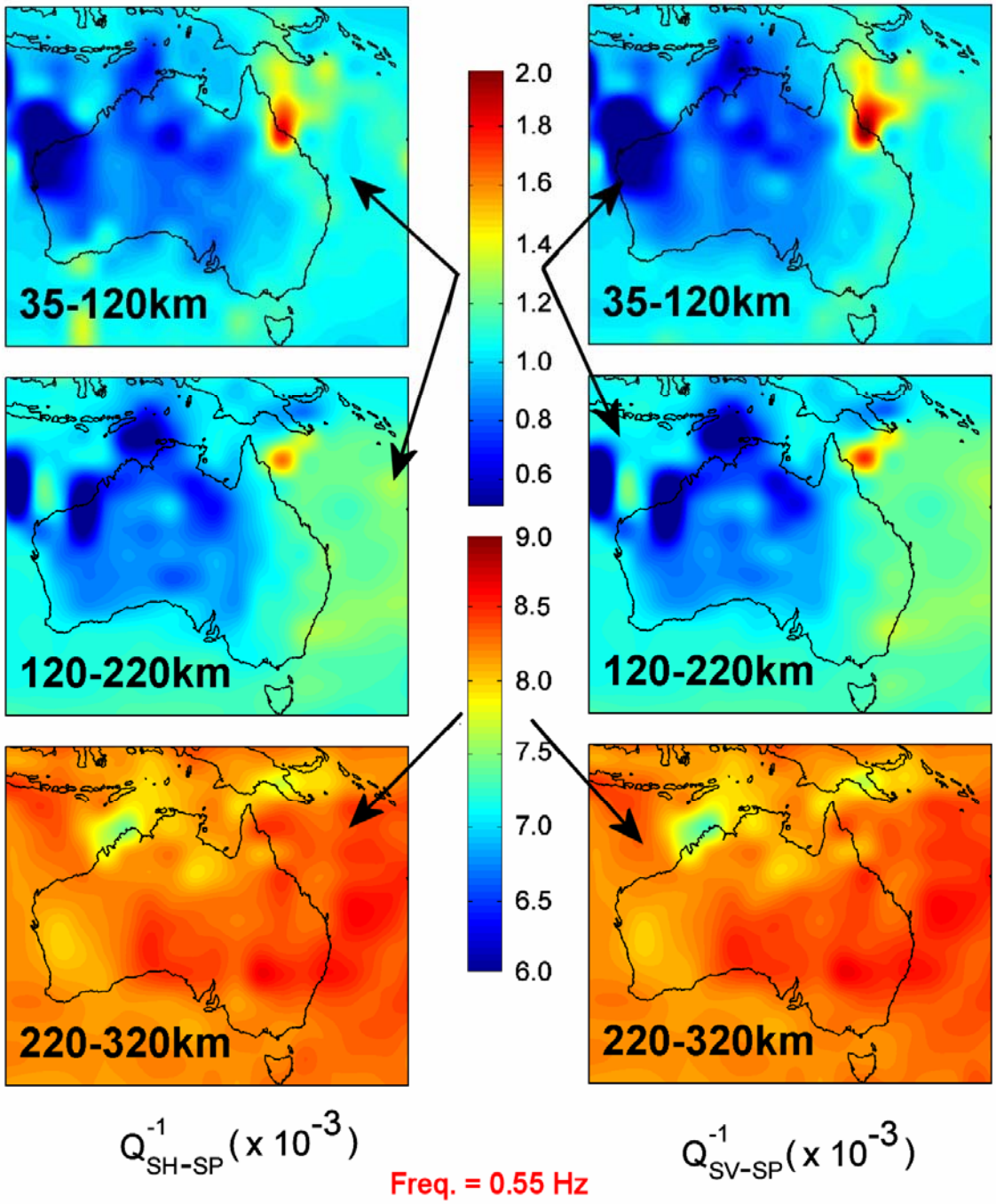

Figure 6.8 (a) continued

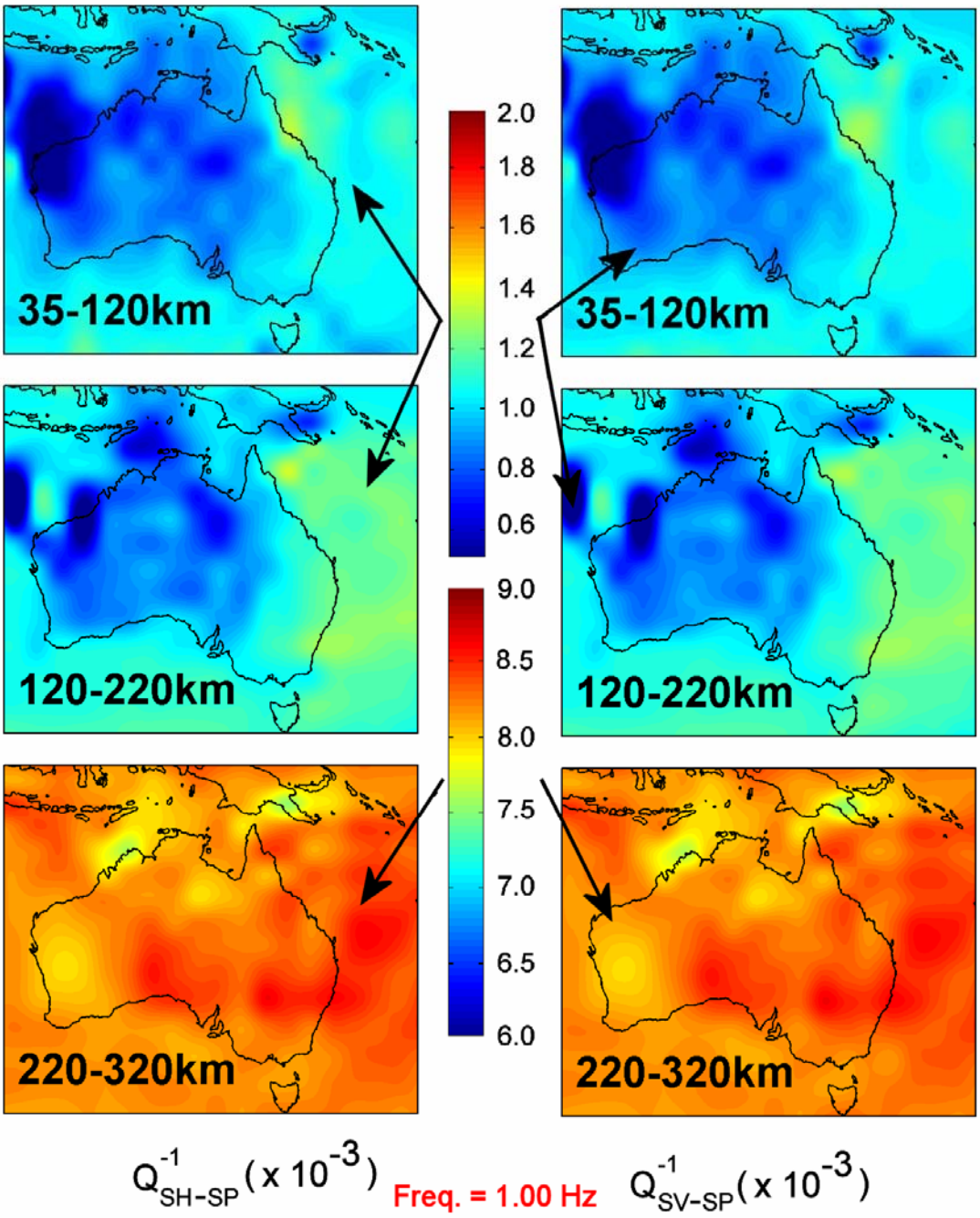

Figure 6.8 (b) continued

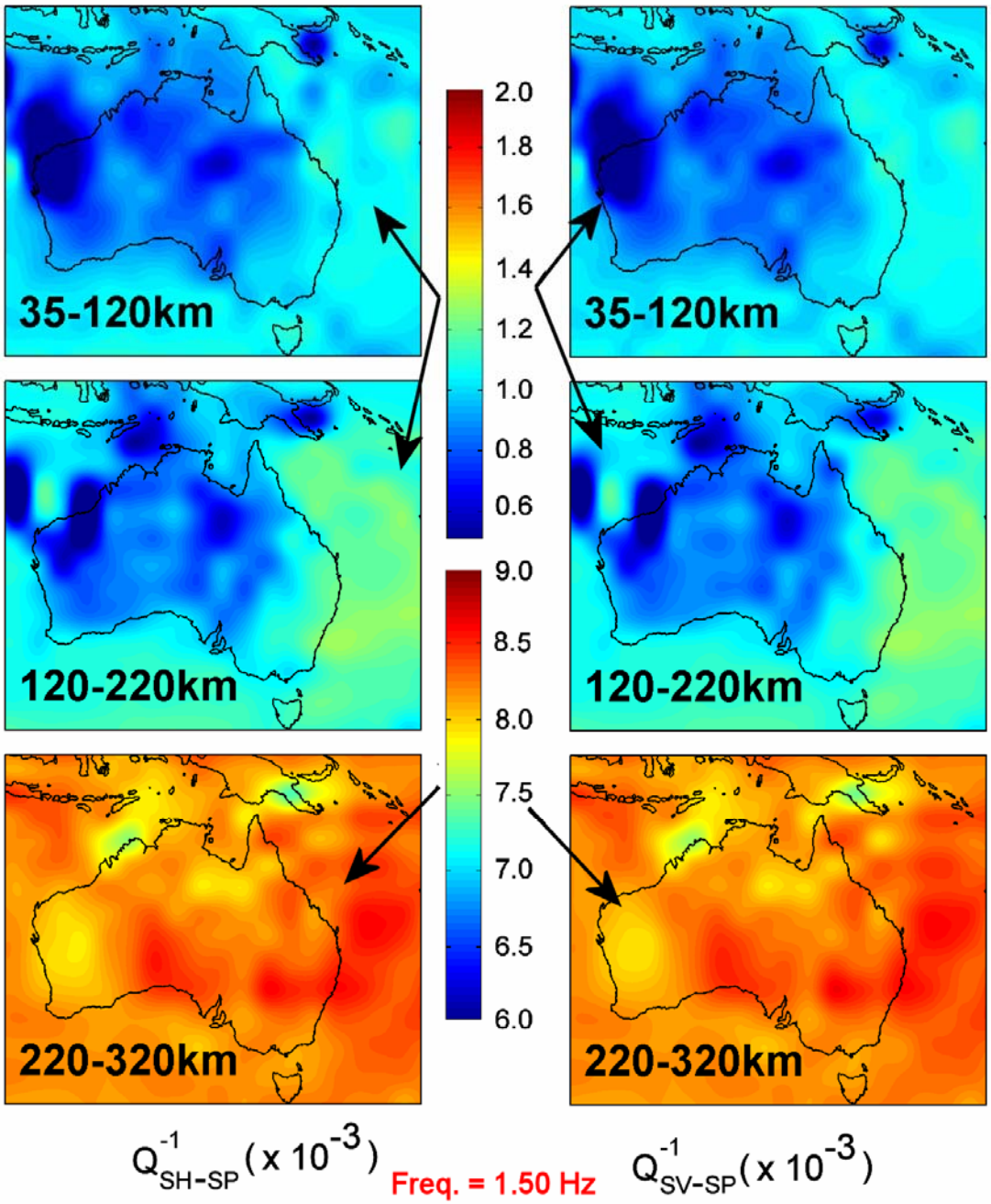

Figure 6.8 (c) continued

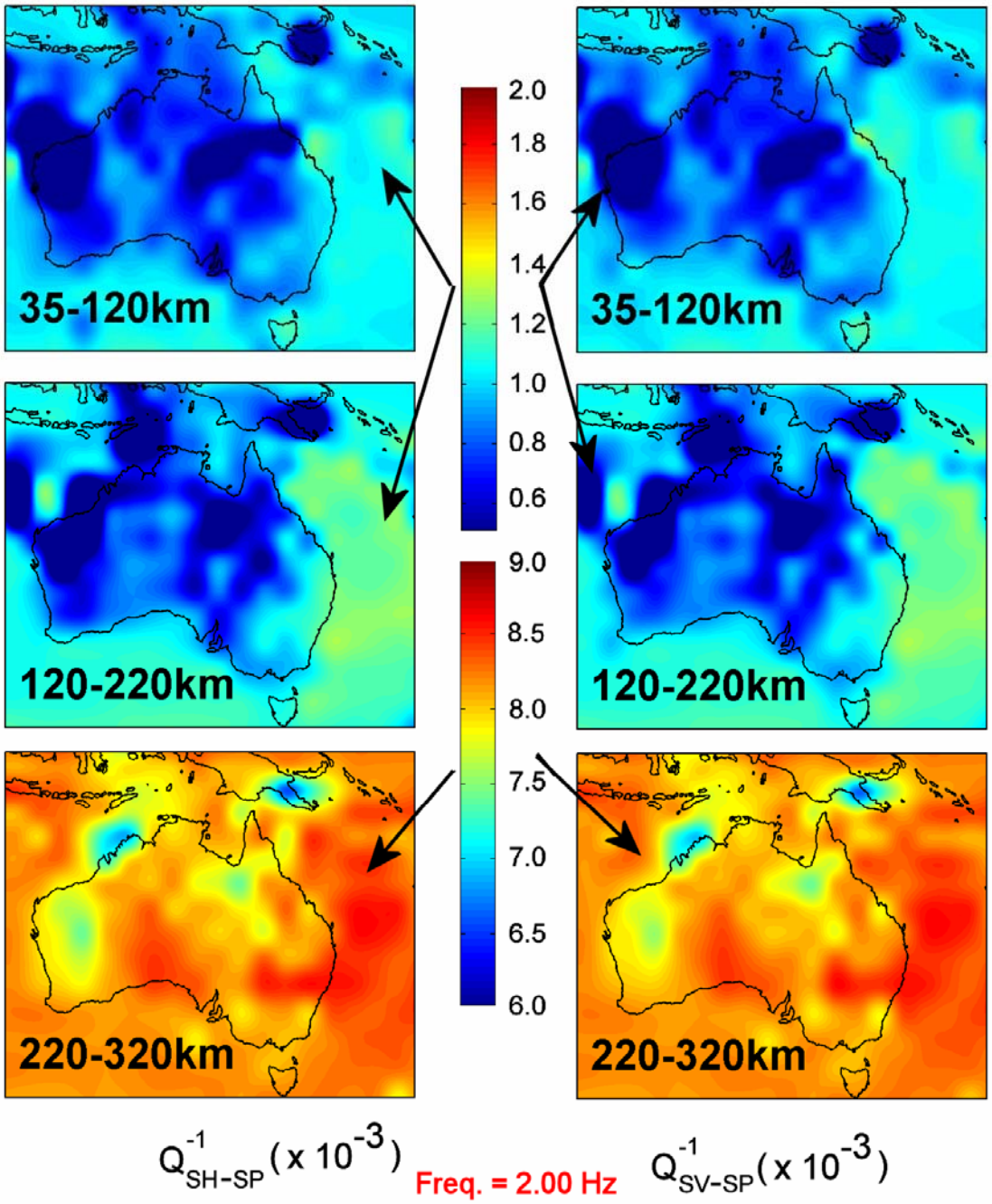

Figure 6.8 (c)

Figure 6.8: Three dimensional images of Q_s for transverse and radial components at center frequencies 0.55, 1.00, 1.50 and 2.00Hz inverted from nearly 6500 Δt^*_{SP} in Figure 6.5.

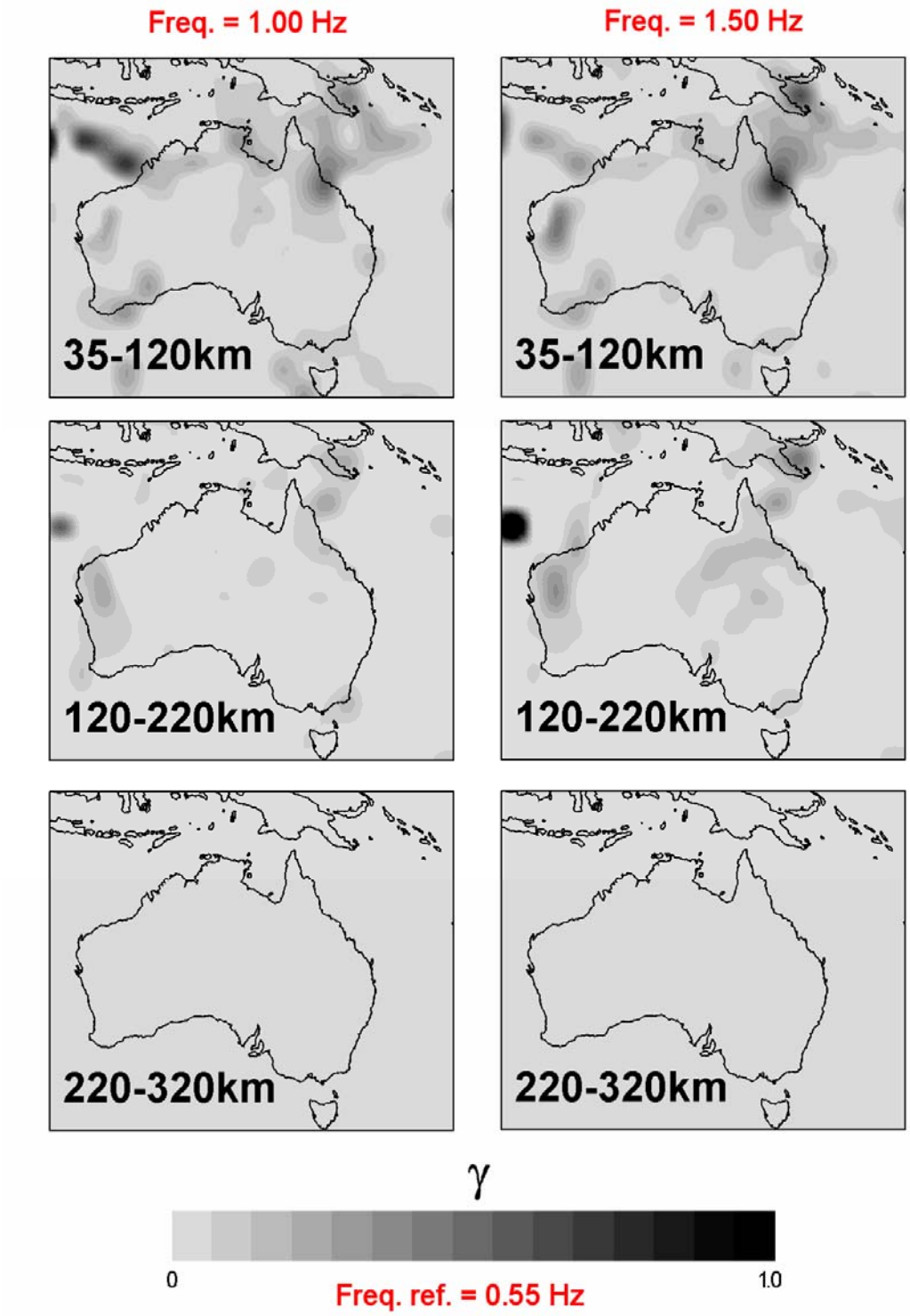

Figure 6.9 (Continued)

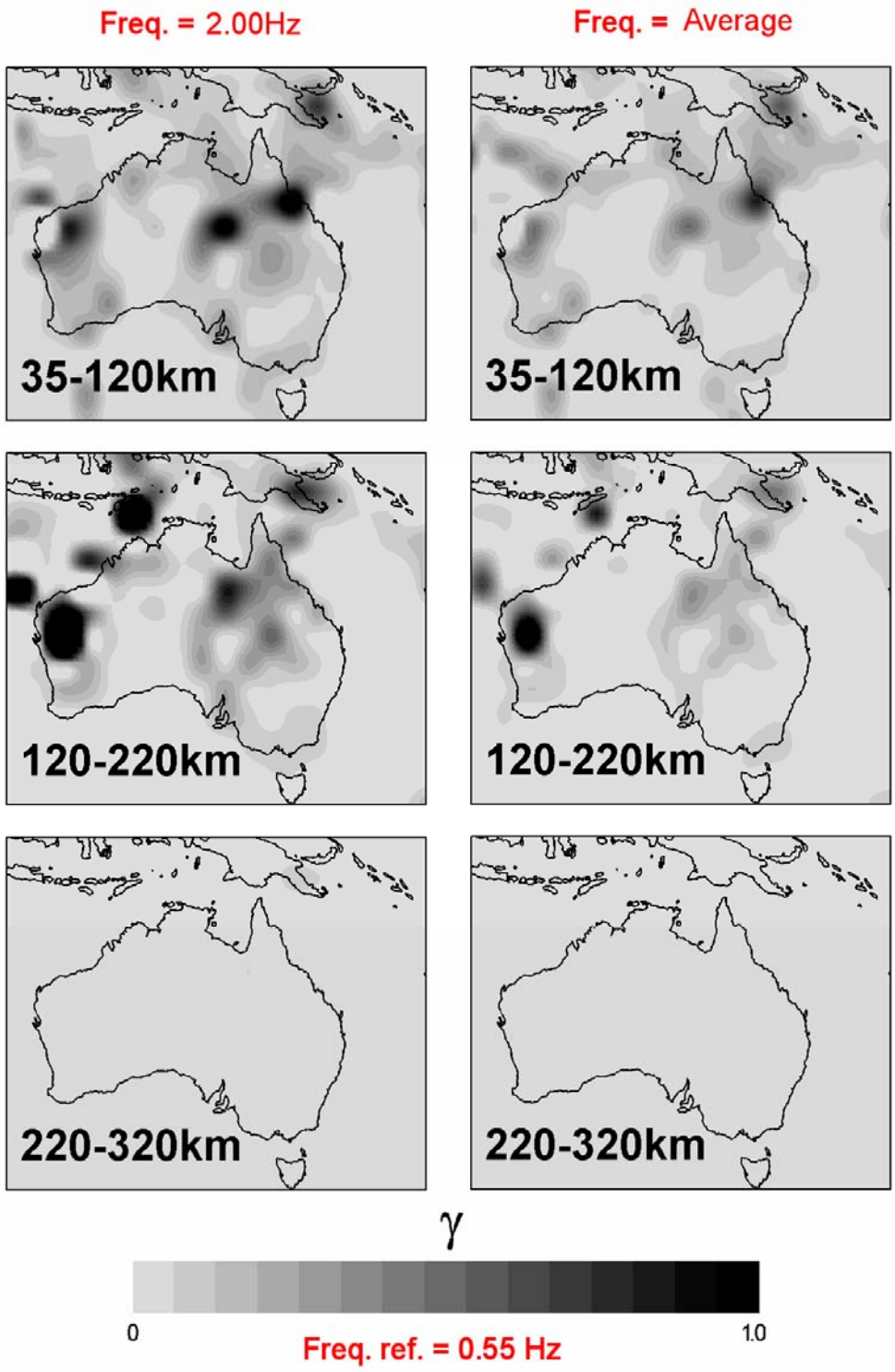

Figure 6.9: 3-D tomographic images of frequency dependence of attenuation at center frequency 1.00, 1.50, 2.00Hz, and average of 1.00, 1.50 and 2.00Hz with seismic attenuation at center frequency 0.55Hz is used as a reference.

Chapter 7

Discussion

7.1 Velocity Variations

The tomographic images (Figure 4.13 and 5.6) reveal large velocity variations beneath the Australasian region. The work in this thesis provides an independent check on the characteristics of lithospheric structure which has hitherto been largely controlled by shear wavespeed models derived from surface wave tomography [Fishwick *et al.*, 2005; Kennett 2003], and profile information for body waves.

In Figure 7.1, my results for shear wavespeed for the depth interval 120-220km are compared with the study of surface wave tomography of Fishwick [2005] at 150km depth and the body wave tomography of Kennett [2003] at 135km. Some of the differences between the images may be caused by the different approaches used to generate these images i.e. surface wave tomography versus body wave tomography, different model parameterization, resolution, etc. Despite these differences these results show similarities particularly in northern Australia where resolution is at its best (see Figure 4.9). The existence of the controversial Tasman Line is suggested by the strong contrast between seismic wavespeed beneath the oceanic and old continental region. The old continental region in the central-western part of Australia is dominated by fast seismic wavespeed, while the young eastern sea board is characterized by slow seismic

wavespeeds (anomaly 1). Other similarities also can be seen around the Indonesian subduction zone (anomaly 2) where all images demonstrate fast seismic speed. Also, beneath Papua New Guinea (anomaly 3) fast seismic wavespeed is pronounced in all images. The transition from cratonic shield to oceanic region along the coastline in the southern and western margin of Australia is suggested by the sharp change from a fast to a slow seismic wavespeed anomaly.

In a very different style of analysis to that of Kaiho and Kennett [2000] we find clear evidence for larger variation in *S* wave speed than *P* wavespeed in the lithosphere with a ratio of perturbations in the range 1.5 to 2.

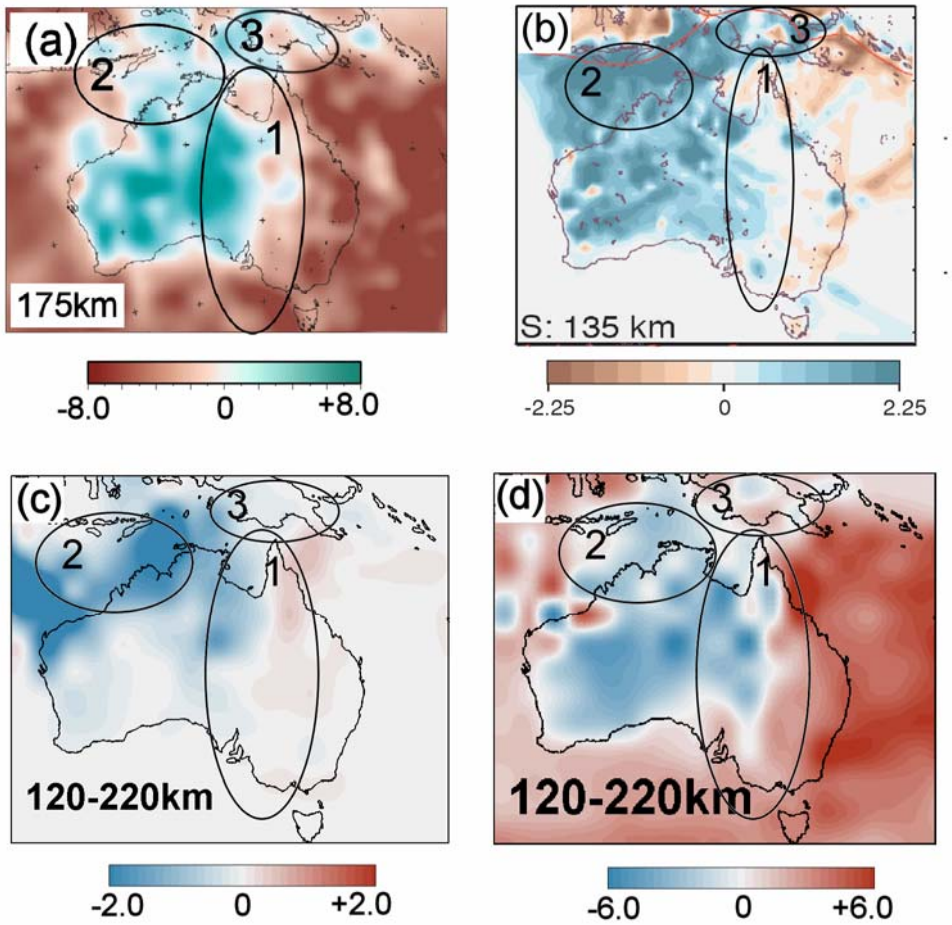

Figure 7.1: (a) Wavespeed model generated from surface wave tomography at 150km depth [Fishwick, 2005]. (b) Shear wavespeed generated from body wave tomography at 125km [from Kennett, 2003] (c) and (d) Shear wavespeed models at 120-220km from this thesis produced from *S* wave tomography using 1-D and 3-D initial models respectively. The color scales of all images are wavespeed perturbation in percent relative to the *ak135* model.

7.2 Attenuation Variations

Attenuation features beneath Australasian region can be interpreted from the *Q* behavior on the various paths. Besides, the pattern of attenuation for different paths can be used as preliminary prediction of what the final attenuation tomographic model will look like.

Figure 7.2 illustrates *Q* behavior on paths with epicentral distances less than 20º, derived from the relative frequency content of *P* and *S* waves [Kennett *et al.*, 2004] and the corresponding *S* to *P* differential attenuation (Δt^*_{SP}) results from this thesis. Kennett *et al.* [2004] estimated the spectra of *P* and *S* and measure relative frequency content by looking at the *P* and *S* wave spectra and visibly comparing the frequency contents of *P* and *S* wave. The broad dataset was classified into four classes (from high *Q* to low *Q*):

High *Q*

Low *Q*

A: similar frequency for both *P* and *S*

B: *S* slightly lower frequency than *P*

C: *S* clearly lower frequency than *P*

D: *S* low frequency compared to *P*

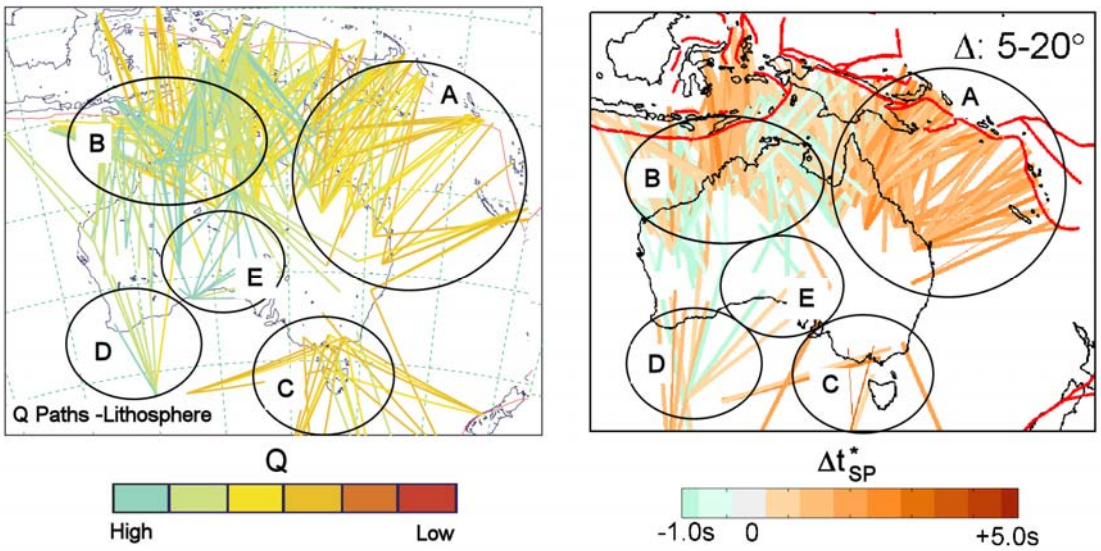

Figure 7.2: *left panel*, variations in *Q* on paths with epicentral distances less than 20º, derived from the relative frequency content of *P* and *S* [Kennett *et al.*, 2004]. *Right panel*, corresponding *S* to *P* differential attenuation (Δt^*_{SP}) paths produced in this thesis.

The Δt^*_{SP} paths displayed in Figure 7.2 are estimated quantitatively by measuring the logarithmic slope of spectral ratio between *S* and *P* waves (See Chapter 2 for more detail). The Δt^*_{SP} paths are color coded by the value of the slope of spectral ratio, i.e., orange represents low *Q* and green represents high *Q* (low *Q*=high attenuation, high *Q*=low attenuation).

Although these two plots are produced by different approach, they show similarities for most of the Australasian region: (A) Coral Sea region, both plots present a consistent pattern of low *Q* paths; (B) to the north of Australia and subduction zone, there are mixture of anomalies varying between low and high *Q*, suggesting the existence of complex structure, paths that cross the subduction zone have strong attenuation; (C) around Tasman Sea and Great Australian Bight, both sets of results show uniform low *Q*; (D) mixture between high and low *Q* in western part of Great Australian Bight; (E) a zone with high *Q* paths beneath central Australia.

Table 7.1: Attenuation variations beneath central-western and eastern Australia

Layer	***Qs***		***Qp***	
	Central-Western	Eastern	Central-Western	Eastern
Lithosphere (35-220km)	1000-1250	833-1000	2000-3000	1600-2000
Upper Mantle (220-320km)	120-140		230-250	

The tomographic attenuation images (Figure 4.15, 5.9, 5.10 and 5.11.a) provide clear evidence of attenuation variation beneath the Australasian region. The seismic wavespeed contrast between central-western Australia and eastern Australia is also pronounced in seismic attenuation. The regions of high seismic wavespeed beneath the western–central Australian cratons show very little seismic attenuation, but there is sharp change at depth structure since *S* waves that penetrate into the asthenosphere

rapidly lose high-frequency energy [Gudmundsson *et al.*, 1994]. In the east of Australia, the lower seismic wavespeed are correlated with an increase of seismic attenuation.

A summary of attenuation variation in the lithosphere and the upper mantle beneath the Australasian region is given in Table 7.1.

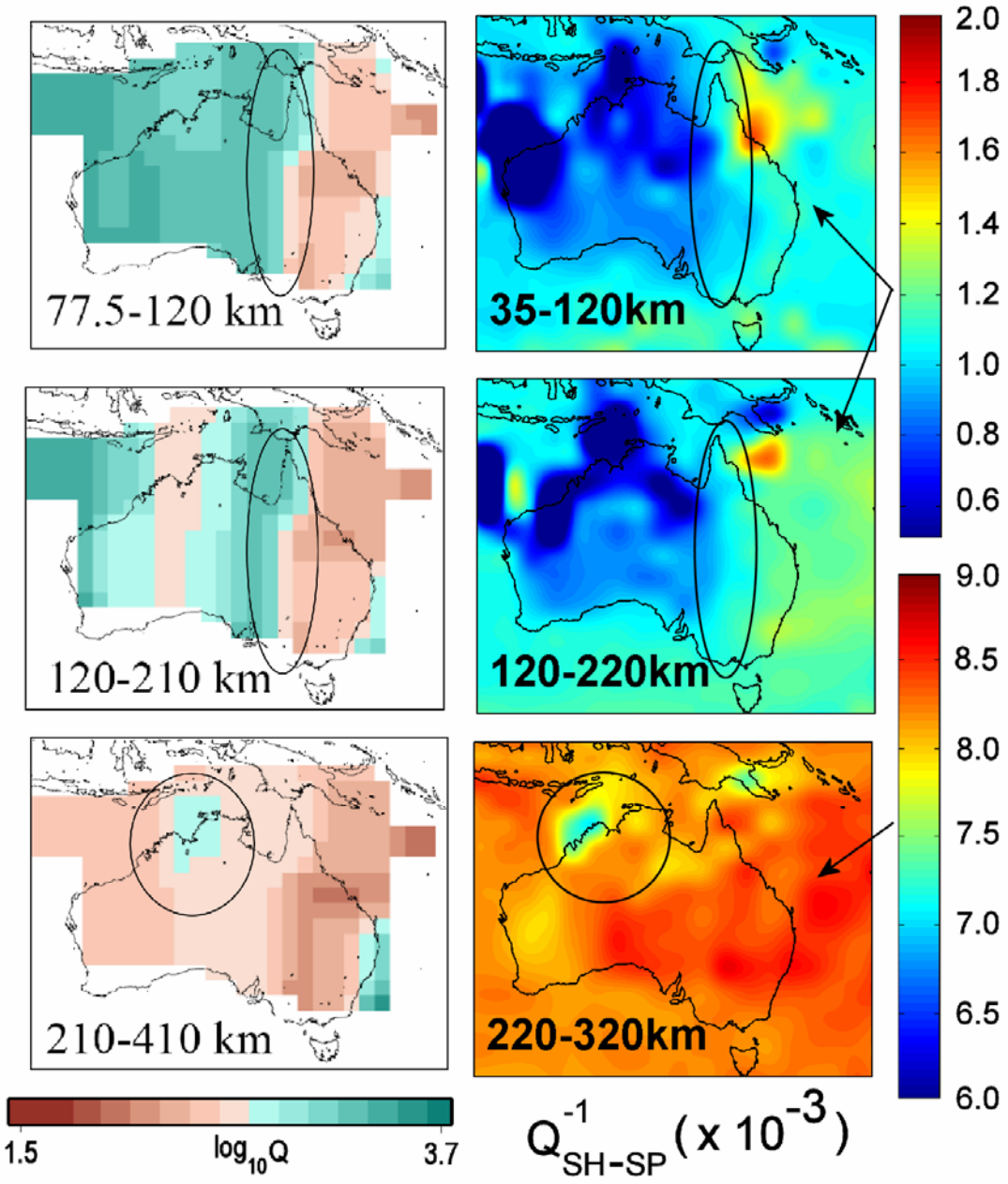

Figure 7.3: *Left panel*, pseudo 3D *Q* images beneath Australia [Cheng, 2000]. *Right panel*, corresponding 3D tomographic attenuation images produced in this thesis (color bar label is in the bottom of the images).

A comparison between the attenuation images produced in this study and the images from previous attenuation study of Australia, e.g., Cheng [2000] is shown in Figure 7.3. Although the two images are produced from different techniques (i.e. the pseudo 3-D Q model of Cheng is constructed by combining 1-D Q profiles, while the images in this thesis are produced by a direct tomography technique) and different data sets (i.e. Cheng used only 2000 paths in his data set, while I used nearly 6500 different paths), they show comparable features. In the first slice (35-120km) both images suggest a major transition from low to high attenuation in the neighborhood of the Tasman Line. In each case the contrast is dominantly north-south and significantly different from the Tasman Line as drawn from near surface information. Low attenuation features not only exist beneath central-western Australia but also extend to the north of the continent. In the second slice (120-220km), attenuation is slightly increased and the east-west transition still appears. In west Australia, a somewhat higher attenuation anomaly appears in Cheng's image, this anomaly is situated around the Great Sandy Desert where no seismic station has been deployed. My results with improved station coverage suggest that there could be some slightly increased attenuation in a similar area, but the contrasts are much less. In the third slice (220-320km), attenuation is sharply increased and there is little variation in either image. High attenuation dominates all region of Australia, except that slightly lower attenuation can be spotted in the northern part near the Kimberley region (the anomaly is marked by an ellipse).

Seismic attenuation anomalies are frequently interpreted in terms of velocity and temperature variations on the basis of laboratory experiments of elastic and anelastic properties of rock. The correlation between seismic attenuation, temperature, seismic velocity and geological age in seismology has been studied by several authors (e.g. Artemieva *et al.*, 2004; Goes *et al.*, 2005). Artemieva *et al.* [2004] evaluated the relative contributions of thermal and non thermal effects on anomalies of attenuation of shear seismic waves, Q_S^{-1}, and seismic velocity, V_S, by comparing global maps of the

thermal structure of the continental upper mantle with global Q_S^{-1} and V_S maps determined from Rayleigh waves at periods between 40 and 150s. She limits the comparison to the three continental depth (50, 100 and 150km), where model resolution is relatively high. Seismic anomalies in the upper mantle are not controlled solely by temperature variations. Continental maps have correlation coefficients of <0.56 between *Vs* and *T* and of <0.47 between *Qs* and *T* at any depth. Further, it is also suggested that not all of the *Vs* and *Qs* anomalies in the continental upper mantle can be explained by *T* variations.

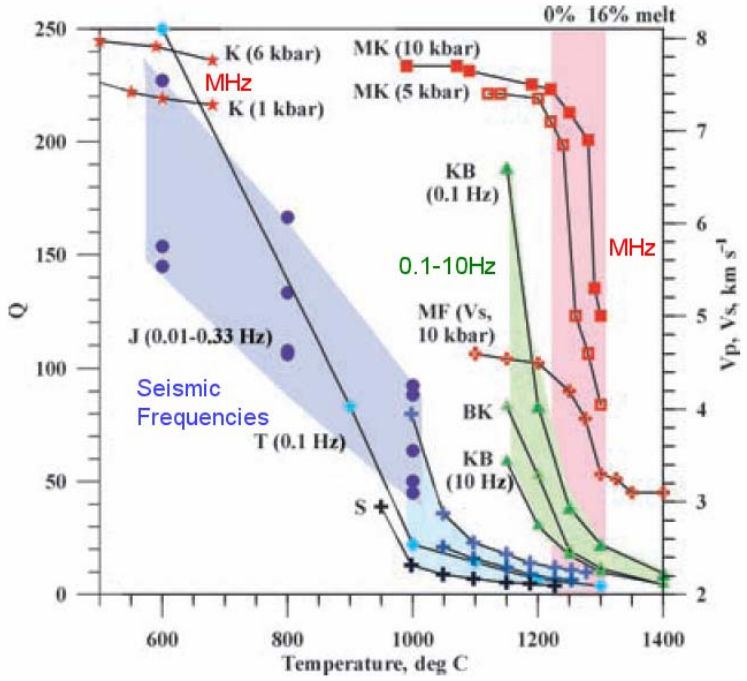

Figure 7.4: Correlation between seismic wavespeed, temperature and attenuation from various laboratory experiments: purple dots and purple shading [J]: *Q* in dunite at P=300 MPa, f=0.01-0.33 Hz (Jackson et al. 1992); blue crosses and shading [S]: *Q* in dry peridotite at P=0.20, 0.48, and 0.73 GPa measured at ultrasonic frequencies i.e. MHz (Sato et al. 1989); green triangles and shading [BK, KB]: *Q* in dunite at f=0.1 Hz and 10 Hz (Berckhemer et al. 1982; Kampfmann & Berckhemer 1985); light blue rhombs [T]: *Q* in olivine aggregate at f=0.09 Hz (Tan et al. 1997). Red symbols: seismic velocities in peridotite. Stars [K]: Vp at P=1 kbar and 6 kbar (Kern 1978); rectangles [MK]: Vp at P=5 kbar and 10 kbar (Murase & Kushiro 1979); crosses [MF]: Vs at P=10 kbar (Murase &Fukuyama 1980). Pink shaded area: the region where volume fraction of melt in peridotite increases from 0% to 16% at P=10 kbar (Murase & Fukuyama 1980). Note that this compilation covers a wide range of frequencies and condition. [Modified from Artemieva *et al.* 2004].

She argued that, V_S and Q_S^{-1} are usually inversely correlated with lithosphere temperatures: most cratonic regions show high V_S and Q_S and low T (temperature), while most active regions have seismic and thermal anomalies of the opposite sign. Her study demonstrated that the lithospheric temperature plays the dominant role in controlling *Vs* and *Qs* anomalies, but other physical parameters such as compositional variations, fluids, partial melting and scattering, may also play a significant role in determining *Vs* and *Qs* variations in the continental mantle.

Furthermore Artemieva *et al.* [2004] presented a correlation between attenuation, seismic wavespeed and temperature (Figure 7.4). Data compiled in Figure 7.4 is obtained from previous laboratory studies on mantle minerals such as: dunite, dry peridotite, and olivine aggregate at various temperature, frequency and grain size. The Figure shows that at seismic frequencies attenuation Q^{-1}, in mantle rocks at subsoliditus temperatures follow the Arrhenius law and exponentially increases with temperature.

Figure 7.5 shows a comparison between seismic wave speed and seismic attenuation images in the lithosphere beneath Australasian region. The seismic wave speed image is derived from the surface wave study of Fishwick [2005] (see Section 3.2.1 for more detail) and the seismic attenuation images (Q_P^{-1} and Q_S^{-1}) are derived in this thesis. In general, it can be observed that in the lithosphere beneath Australasian region, the Q_P^{-1} and Q_S^{-1} are inversely correlated with shear wavespeed. The Figure shows that there is an abrupt change from high shear speed to low speed for anomaly (1) is marked as a sharp change from low to high Q_P^{-1} and Q_S^{-1} (location of controversial Tasman Line). This correlation also exists in several areas: (2) low seismic speed at around 100km beneath Coral Sea is correlated with significantly increased Q_P^{-1} and Q_S^{-1}; (3) low seismic speed around Bass Strait is associated with high attenuation. To the north of Australia, (4) low seismic speed is well correlated with Q_P^{-1} and fairly well correlated with Q_S^{-1}.

The existence of hot spots beneath the Coral Sea and Bass Strait is better marked by localized high attenuation rather than by seismic wavespeed. In this sense, seismic attenuation is more sensitive to temperature than seismic wavespeed.

Based on the laboratory experiments, the sensitivity of seismic attenuation to temperatures is quite prominent. Thus, this sensitivity is used to correlate seismic attenuation anomalies in the mantle with temperature variations [Mitchell, 1995 and Romanowizc, 1995].

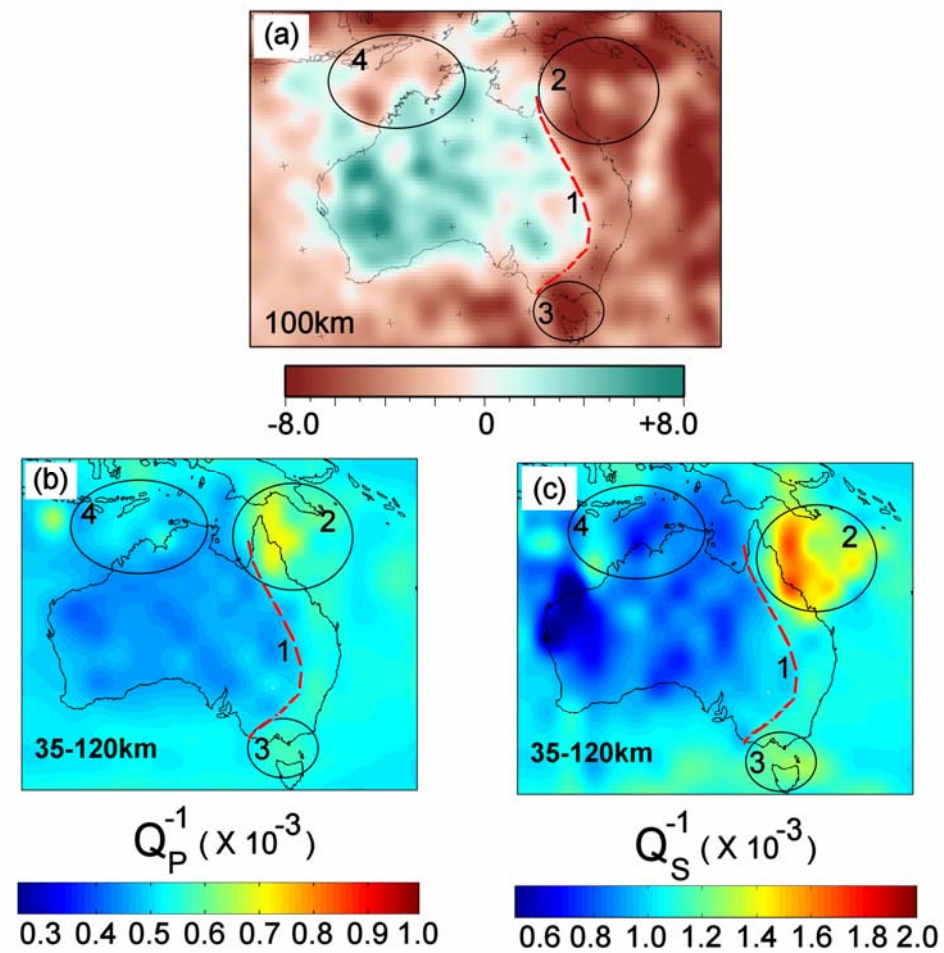

Figure 7.5: Comparison between (a) seismic speed images derived from surface wave tomography [Fishwick, 2005], (b) compressional wave attenuation Q_P^{-1} and (c) shear wave attenuation Q_S^{-1}.

In the Australian continent, the study of Goes *et al.* [2005] reveals a large-scale correlation between temperature and tectonic age. The temperature models used are

derived from the shear seismic speed models of Yoshizawa *et al.* [2004] and Simons *et al.* [2002] under assumptions about the relationship of seismic wavespeeds and temperature. The extrapolation to temperature at depth requires the assumption that heat transport is conductive and in steady-state. The wavespeed model of Simons *et al.* [2002] is built using the same method as van der Hilst *et al.* [1998] (see Chapter 3) i.e. the partitioned waveform inversion from fundamental Rayleigh waves with 40-200 s periods and higher modes with periods between 20 and 125 s along over 2200 paths sampling most of the Australian continent. To convert seismic wavespeed into temperature, Goes *et al.* [2005] invoked both elastic and anelastic effects. The elastic parameters are extrapolated linearly to high temperature and using 3rd order finite strain to high pressure. Their results show that both *S*-velocity models yield a very similar range and large-scale distribution of temperature, and temperature estimates correlate well.

A comparison between seismic attenuation results from this thesis and the estimated temperature variation in the lithosphere beneath Australia is presented in Figure 7.6. The temperature maps (c) and (d) are inferred from seismic wavespeed distributions of Yoshizawa *et al.* [2004] and Simons *et al.* [2002]. The surface heat flow information from Pollack *et al.* [1993] and geothermal location map are also presented as additional temperature information (a) and (b). In this comparison, shear wave loss factor (Q_S^{-1}) images have been constructed using both Δt^*_{SP} and Δt^*_{SS} results (e) and (f).

The comparison of the temperature and loss factor images suggests that in the lithosphere underneath Australasian region, broadly, high attenuation anomalies are associated with hot zones and vice versa. For instance, in central-western Australia, the boundary of the low attenuation anomaly with $Q_S^{-1} < 0.0008$ ($Q_S > 1250$) corresponds approximately to the 1000ºC isotherm from Goes *et al.* [2005].

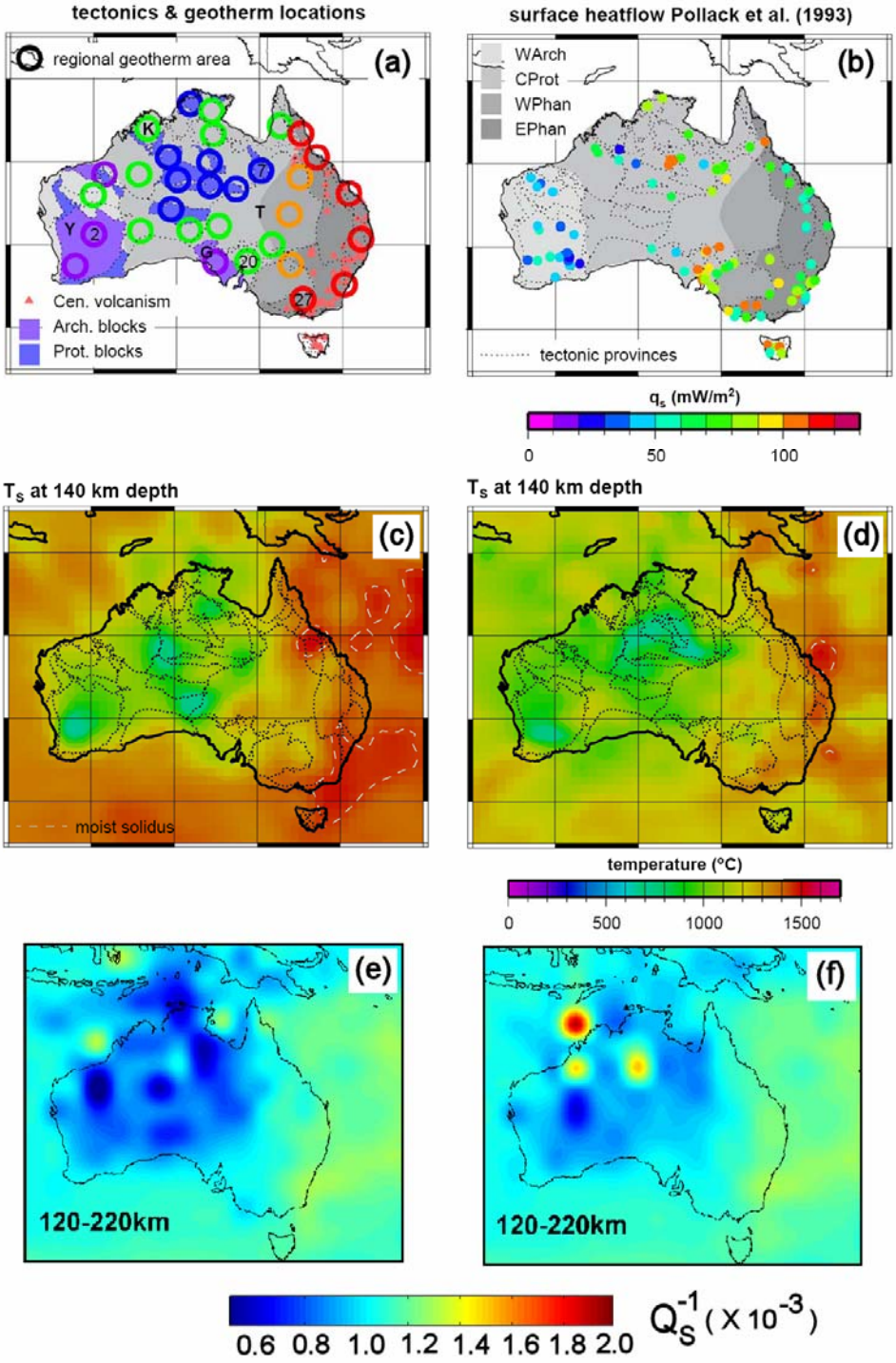

Figure 7.6: (a) Tectonic provinces of Australia (dashed lines) and locations of Cenozoic volcanism (red triangles). Color circles correspond to tectonic affiliation: purple-Archean, blue-Proterozoic, orange, red-Phanerozoic non-/volcanic.Y-Yilgarn craton, K-Kimberley, G-Gawler craton, T-Tasman Line. (b) Australian surface heat-flow data from the Pollack *et al.* [1993] (c) Map of temperature at 140 km depth, deduced from the *Vs* model of Yoshizawa *et al.* [2004], (d) Similar as (c), but inferred from the *Vs* model of Simons *at al.* [2002] (e) Shear attenuation derived from the Δt^*_{SP} and (f) Shear attenuation from the Δt^*_{SS} measurement. [(a)-(d) images from Goes *et al.*, 2005].

The higher attenuation $Q_S^{-1} = 0.0013$ ($Q_S \approx 770$) in the eastern part is similarity associated with temperature estimates around 1400ºC. The high attenuation anomalies along eastern coast of Australia correlate with the existence of recent volcanism (Figure 7.6 a) that contributes to the high surface heat flow (Figure 7.6 b). To the north of Australia, the region with low seismic Q anomalies is also correlated with high temperature. Around Coral Sea, especially Figure 7.5 (b-c) the high attenuation zone with $Q_S^{-1} = 0.0016$ ($Q_S \approx 650$) correspond to about 1500ºC.

7.3 Frequency Dependence of Attenuation

The tomographic images of the frequency dependence of attenuation through the exponent γ produced in this study are comparable with the estimates of the frequency dependence of attenuation of Cheng [2000] (Figure 7.7), even though Cheng used the oversimplified assumption that his exponent α could be treated as a path–averaged quantity.

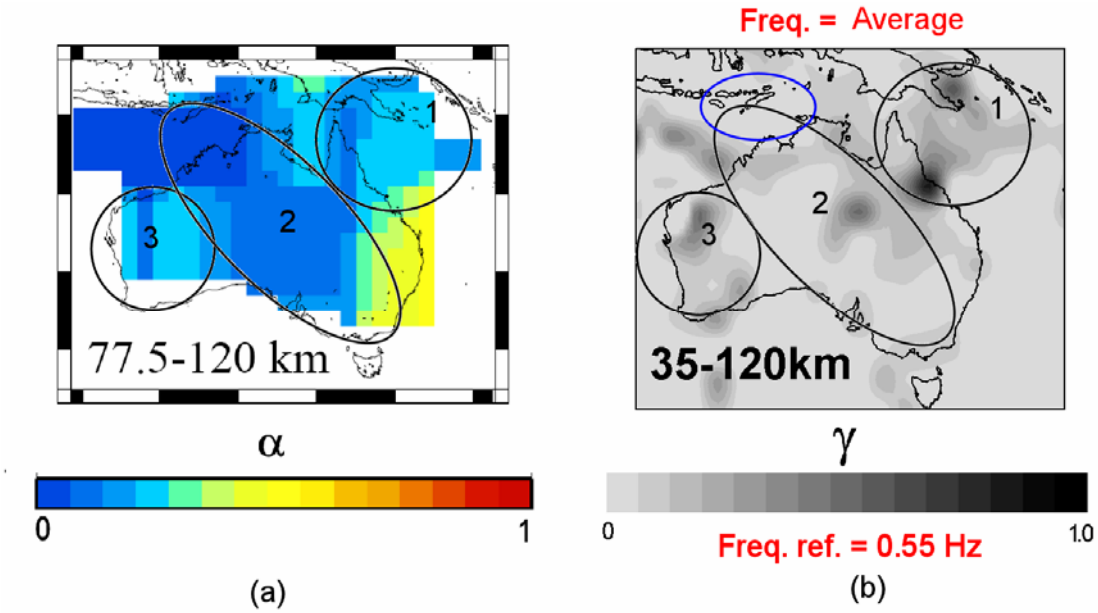

Figure 7.7: A comparison between frequency dependence of attenuation of (a) Cheng [2000] at 77.5-120km and (b) frequency dependence of attenuation produced in this study at 35-120km.

The zones beneath the Coral Sea (anomaly 1) and Western Australia (anomaly 3) are suggested as regions with a high frequency dependence of attenuation. Meanwhile, beneath central Australia (anomaly 2) both styles of images suggest somewhat lower frequency dependence of attenuation. There is generally most evidence for frequency dependence where attenuation is strong and so the curvature of differential t^* plots is easier to measure.

Studies of the frequency dependence of attenuation (exponent α) have been conducted in several regions to understand the mechanism of Q in earth's upper mantle. As explained in Chapter 2, the study of the quantity of the exponent α is frequently used as a proxy to determine the physical properties of upper mantle rocks. Jackson *et al.* [2004] and Faul *et al.* [2004] showed that partial melting results in a broad peak in attenuation in the frequency range of 0.01–1.0 Hz causing weak frequency dependence in that frequency range. The exponent α is approximately 0.15-0.30 as determined from seismic studies and laboratory measurements on the upper mantle rocks. Ulug & Berckhemer [1984] compiled the range of studies on the frequency dependence of Q up to 1982. For a model with a power-law dependence on frequency (equation 6.3), the value of exponent γ for the whole Earth is 0.2–0.4 in the frequency range 10^{-8}–10^{-2} Hz; for the mantle γ is 0.15–0.6 in the 0.001–2.0 Hz band; for the crust γ is 0.25–1.0 in the 0.025–48 Hz band.

Figure 7.7 (b) shows that in the area where seismic path density is at its best (see Figure 4.9 or Figure 7.16c) the anomalies 1, 2 and 3 show variations with moderately large exponent γ, while around the subduction zones (blue ellipse) the frequency dependence is weak, suggesting the possible presence of partial melting beneath this region.

As mentioned in Chapter 6, based on the analysis of Figure 6.8 (a), (b), (c) and (d), the seismic loss factor (Q_S^{-1}) decreases with frequency for most of the Australasian region (see Figure 7.9 (b), (c)). The seismic attenuation variation in this Figure is

represented based on the algorithm I used to present Figure 4.16, with specific 1-D profiles at different locations (See Figure 7.8).

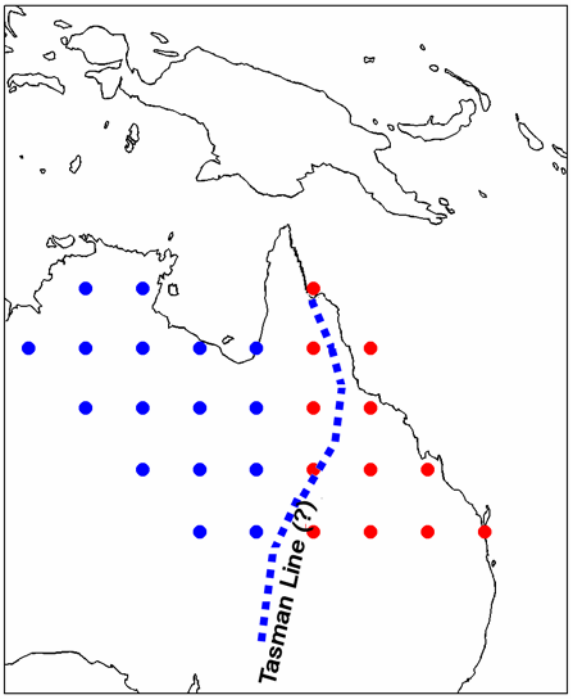

Figure 7.8: Locations of specific 1-D Q_S^{-1} profiles used to produce Figure 7.9.

The behavior of Q_S^{-1} as a function of frequency is shown in Figure 7.9 (c) and (d) as well as a summary of a relevant plot reported by Sato *et al.* [1998] for a comparison (Figure 7.9 a) and information from the laboratory experiments of Jackson [2005]. Each dot in Figure 7.9 (c) and (d) represents an average value of 16 western Australian locations (blue and green) an average of 12 eastern Australia locations (red and magenta) for a particular depth interval. Figure 7.8 shows obvious evidence that beneath the Australasian region in each of the depth intervals (35-120km, 120-220km and 220-320km), the loss factor (Q_S^{-1}) tend to decrease with frequency which is in a good agreement with the compilation by Sato *et al.* [1998] and Faul and Jackson [2005].

The information for Q_S^{-1} as a function of frequency in Figure 7.9 is then used to estimate the frequency dependence of attenuation (exponent γ) beneath the Australian

continent at various frequencies. Again, a power-law dependence on frequency as in equation 6.3 is assumed.

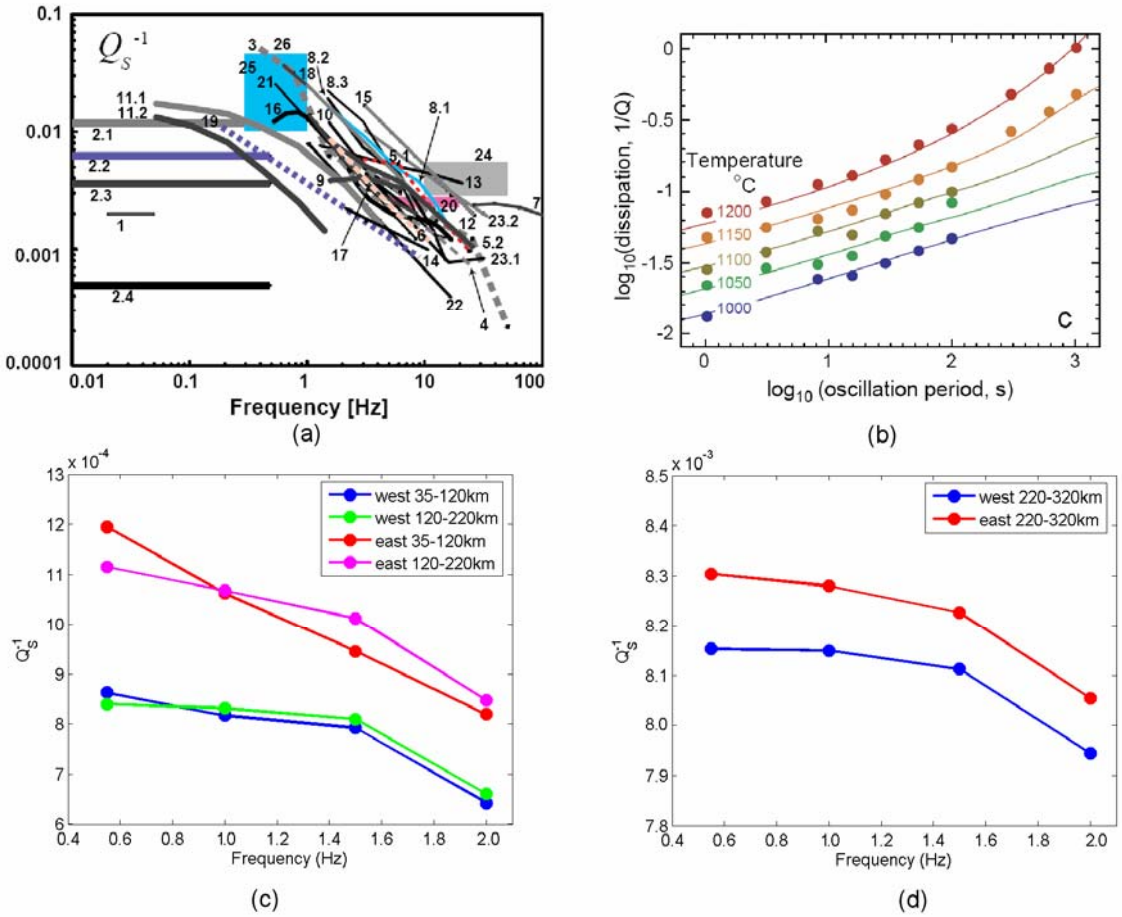

Figure 7.9: (a) Compilation of values of Q_S^{-1} as a function of frequency for the lithosphere from surface wave analysis, 1-7; multiple lapse-time window analysis, 8-12; spectral decay analysis, 11-26. [from Sato *et al.*, 1998], (b) Q_S^{-1} as a function of period from laboratory measurement of Faul and Jackson [2005] (c) plot of Q_S^{-1} as a function of frequency produced in this study at 35-120km and 120-220km for eastern and western Australia (see Figure 4.16 for location) and (d) for 220-320 km depth interval.

Table 7.2: Attenuation (Q_S^{-1}) variations beneath central-western and eastern Australia at various depth interval and frequencies (a) and the corresponding frequency dependence of attenuation γ (b).

Depth Interval (km)	Q_S^{-1} for Western Australia			
	0.55Hz	*1.00Hz*	*1.50Hz*	*2.00Hz*
35-120	0.000863	0.000817	0.000792	0.00064285
120-220	0.00084	0.000832	0.00081	0.0006607
220-320	0.008153	0.00815	0.008112	0.0079437
Depth Interval (km)	Q_S^{-1} for Eastern Australia			
	0.55Hz	*1.00Hz*	*1.50Hz*	*2.00Hz*
35-120	0.001195	0.001063	0.000946	0.00081947
120-220	0.001115	0.001068	0.001012	0.00084692
220-320	0.008304	0.008279	0.008226	0.0080536

(a)

Depth Interval (km)	γ for Western Australia		
	1.00Hz	*1.50Hz*	*2.00Hz*
35-120	0.09169	0.085003	0.22814
120-220	0.016719	0.036142	0.18587
220-320	0.000589	0.004979	0.020131
Depth Interval (km)	γ for Eastern Australia		
	1.00Hz	*1.50Hz*	*2.00Hz*
35-120	0.19692	0.23326	0.29248
120-220	0.072069	0.096227	0.21299
220-320	0.004938	0.009348	0.023696

(b)

Table 7.2 shows a summary of Q_S^{-1} and the exponent γ at 1.00Hz, 1.50Hz and 2.00Hz at various depth intervals for Western and Eastern Australia (the location refer to Figure 4.16). The corresponding plot of the exponent γ is shown in Figure 7.10. It can be seen that the frequency dependence of attenuations (exponent γ) apparently increases with frequency with $0.1 < \gamma < 0.3$ at 35-120km depth interval; $0.02 < \gamma < 0.21$ at 120-220km and $0.0006 < \gamma < 0.02$ at 220-320km for frequency 1.00 – 2.00Hz which

is in a good agreement with the compilation of Ulug & Berckhemer [1984] for the mantle. In addition, Figure 7.10 shows that the frequency dependence of attenuation for Eastern Australian region is notably higher than that for Western Australia, particularly at shallow depth.

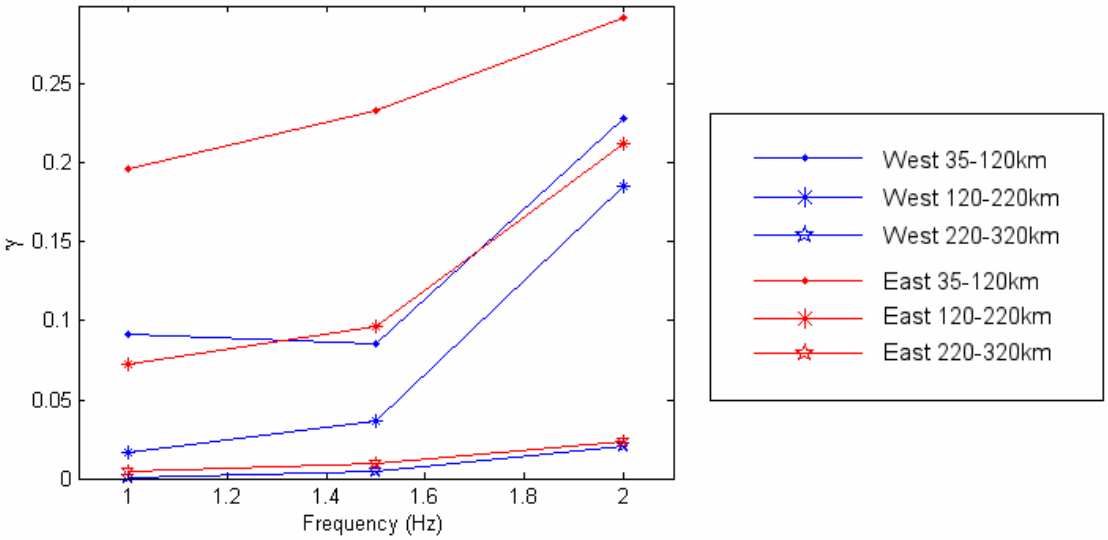

Figure 7.10: Characteristics of frequency dependence of attenuation (exponent γ) as a function of frequency for western and eastern Australia at 35-120km, 120-220km and 220-320km depth interval.

7.4 Search for Seismic Attenuation Anisotropy

If a point source is introduced into a perfectly homogeneous isotropic material, it generates a spherical seismic wavefront, that is seismic velocities do not vary with direction. Since the earth is composed of anisotropic materials whose elastic properties vary with orientation, the rays travel in straight lines out from the vicinity of the source, but the wavefront is not spherical because velocity varies as a function of ray angle. This means that the ray is not perpendicular to the wavefront [Shearer, 1999].

Figure 7.11 shows the wavefront generated by a point source (red star) in a homogenous isotropic material (a) and in a homogenous anisotropic material (b). The seismic wavefront in a homogenous isotropic material is spherical; while the wavefront

in a homogenous anisotropic material depends on the orientation of its elastic properties.

Petrophysical studies suggest that there are several factors that can affect anisotropy and it is mist likely to occur in the upper mantle. Olivine is the most rich and deformable mineral in the upper mantle; it develops a lattice preferred orientation (LPO) that might result either from active deformation of asthenospheric mantle that accommodates or causes the absolute plate motion [Bormann *et al.*, 1996 and Vinnik *et al.*, 1992] or was imposed during past deformation, and then was 'frozen' in the lithosphere during post-tectonic thermal relaxation [Silver and Chan, 1998]. Olivine has been shown to display highly anisotropic thermal diffusivity at ambient condition. Thus heat transport in the upper mantle should be anisotropic [Tommasi *et al*., 2001]. Tommasi *et al*. [2001] presented petrophysical modelling and laboratory measurements of thermal diffusivity in deformed mantle rocks between temperatures of 290 and 1,250K that demonstrate that deformation may induce a significant anisotropy of thermal diffusivity in the uppermost mantle. They found that heat transport parallel to the flow direction is up to 30 per cent faster than that normal to the flow plane. In oceans, resistive drag flow would result in lower vertical diffusivities in both the lithosphere and asthenosphere. In continents, olivine orientations frozen in the lithosphere may induce anisotropic heating above mantle plumes, favoring the reactivation of pre-existing structures.

In isotropic media, transverse *SH* (displacement only in the horizontal direction) and radial *SV* (perpendicular to the direction of the propagating ray) waves travel at the same speed. However, in anisotropic media, the two orthogonally polarized shear waves will typically travel at different speeds and arrive at slightly different times. This leads to *shear-wave splitting* in which a pulse will be split into two orthogonal components that will arrive at slightly different time [Shearer, 1999].

In a transversely isotropic medium with a vertical symmetry axis *SH* and *SV* waves have different wavespeeds that vary with inclination to the vertical. For weak

anisotropy the polarizations tend to be similar to *SH* and *SV*. But, for strong anisotropy such simple characterizations are not available.

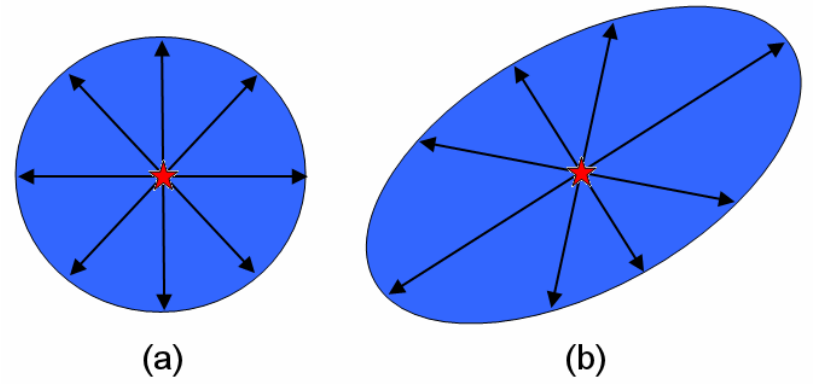

Figure 7.11: The wavefront gererated by a point of source (red star) in a homogenous isotropic material (a) and in a homogenous anisotropic material (b) [(b) is modified from Shearer (1999)].

Shear wave splitting study is valuable to study the anisotropy of the earth. Measuring shear wave splitting at a seismological station produces two parameters: the orientation of the polarization plane of the faster *S* wave and the delay between the arrival times of the fast and slow split waves. Study of shear wave splitting commonly used core *S* waves such as teleseismic *SKS* arrivals, since the polarization of the incident *S*-wave on the mantle is known to be purely *SV*, as a result of the *P* leg traveling in the fluid outer core. The delay times between the split shear waves are typically 1 to 2 second for *SKS* waves; the splitting is most likely caused primarily by azimuthal anisotropy within the upper mantle beneath the station [Shearer, 1999].

The orientation of the polarization plane of the fast *S*-wave is assumed to be a proxy for the orientation of the axis of olivine in the upper mantle [Ben-Ismail and Mainprice, 1998] and therefore provides a means of investigating upper mantle structure and its possible mechanical coupling with the crust, by studying the extent to which the measured orientations are correlated with superficial geological structures. The delay time is a function of the intrinsic anisotropy, the thickness of the anisotropic layer, the

orientation of the ray path with respect to the elastic tensor of the anisotropic medium, and the vertical coherence of the mantle fabric [Heintz and Kennett, 2005]

An investigation of seismic anisotropy underneath the Australian continent through the analysis of shear wave splitting has been conducted by Heintz and Kennett [2005]. They reported shear wave splitting observation across the entire Australian continent by analyzing seismic data recorded at 190 broadband seismic recorders. Only seismic data with good signal to noise ratio from 121 events was used in their study; the distance range was 85-150º (teleseismic core-refracted shear waves) and the magnitude of the events used was greater than 5.5. They measured the shear wave spitting using the Silver and Chan algorithm [Silver and Chan, 1991]. This algorithm consist of minimizing the energy of the *SH* component by rotating and time shifting the traces. The energy on the *SH* component is evaluated for many candidate values of the orientation of the polarization plane and delay time (with respective increments of 1º and 0.05 s) to retrieve the pair of values that best removes the influence of anisotropy. This method assumes that anisotropy is located in a single horizontal layer. The measured directions of the orientation plane and the delay time are shown in Figure 7.12.

Figure 7.12 shows that the pattern of seismic anisotropy from shear wave splitting beneath Australia is rather complex and is not correlated with the almost north-south absolute plate motion (APM). The lithospheric source of anisotropy in eastern part of the Australian continent shows no direct correlation between the orientation of the polarization and the mapped superficial structure. This may be caused by the limited amount of reliable measurements performed at each station, related to the short time span of recording, together with the sedimentary cover overlying the Palaeozoic basement almost in the entire eastern part of the continent. Meanwhile, some correlations can be seen in the north-western part of the continent (Kimberley region, region #1), Yilgarn cratonic block, and along the southern margin of the continent (see Figure 3.1 for location). In the Kimberley block, the directions of anisotropy show

various orientations. In the eastern part, directions of anisotropy are mainly oriented N 50–60º E and are sub-parallel to the structural trend of the Halls Creek orogen.

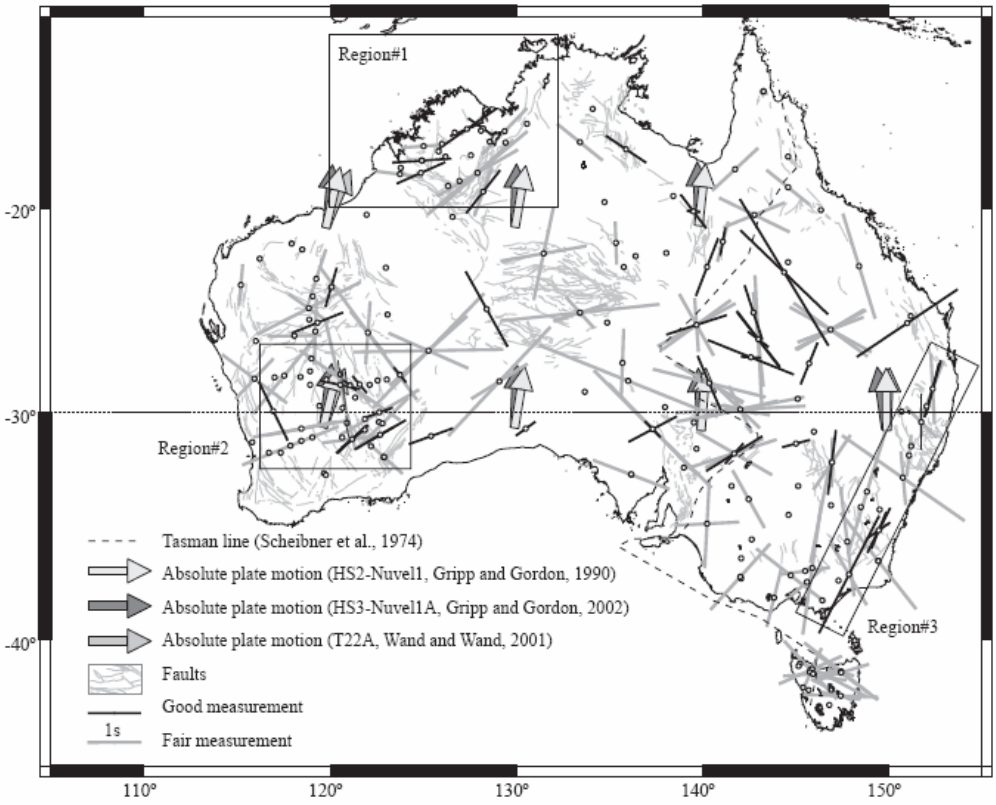

Figure 7.12: Directions of the orientation plane of the fast shear-wave. The length of each line is proportional to the delay time [from Heintz and Kennett, 2005].

In the western part however, the measured directions of anisotropy are ~N 90º E and not obviously correlated with the NW–SE structural trend. In the southern part of the Yilgarn cratonic block, two main directions of anisotropy are observed on the two sides of 30º S latitude. The N 40/50º W directions of anisotropy observed north of this line are parallel to some regional faults. In the southeast of the continent, highlight directions of anisotropy almost parallel to the structural trend of the New England and Lachlan fold belts.

The pattern of azimuthal anisotropy beneath the Australian continent has been studied through the inversion of Love and Rayleigh waveforms by Debayle and Kennett [2000]. The inversion is constrained by 1584 Love and Rayleigh wave seismograms,

each Love and Rayleigh pair corresponding to a single event. The horizontal component seismograms were rotated to produce traces oriented along the great-circle to the source (*SV*) and transverse to the path (*SH*). The inversion for structure has two steps, in the first a simultaneous inversion is made of both Love (*SH*) and Rayleigh (*SV*) waveforms to produce a path specific 1-D upper mantle model including transverse isotropy. In the second stage, the *SH* and *SV* models for the 1584 paths are inverted separately, under the assumption that they represent averages along the path, to produce representations of 3-D structure for wavespeed heterogeneities and azimuthal anisotropy (Rayleigh waves). Three slices through the *SH* and *SV* seismic wavespeed distribution along with azimuthal anisotropy are shown in Figure 7.13. Figure 7.13 shows the existence of two anisotropic layers. Down to 100km depth, the polarization varies for each location i.e. nearly north-south trending in western Australia, east-west orientation in central and east Australia. Meanwhile, the lower layer below, 150km, shows a nearly north-south component in good general agreement with the absolute plate motion (APM).

The *SH* and *SV* wavespeed heterogeneities are presented as perturbation with the same reference i.e. 4.5 km/s. Down to 200 km depth, the perturbation of *SH* wave in western and central Australia reaches 8-10%, while the *SV* wave anomaly is about 4-5%. In the eastern part of Australia, perturbation of *SH* wave is -2 to 2% and *SV* wave around -4 to -8% relative to the reference. Thus, it is revealed that down to 200km depth, for most of the continent, *SH* waves are significantly faster than *SV* waves.

The ratio of the *SH* to *SV* wavespeed is presented in terms of the parameter ξ which represent the radial anisotropy [$\xi = (V_{SH}/V_{SV})^2$]. The ξ pattern beneath the Australian continent is shown in Figure 3.5. Values of ξ up to 1.19 (9% of polarization anisotropy) have been obtained at 150km for eastern Australia. This locally large anisotropy is difficult to resolve with current mineralogical models. Figure 3.5 shows that significant polarization anisotropy with *SH* faster than *SV* for most of the continent down to 200-250km. This layer where *SH* is faster than *SV* would correspond to regions where horizontal flow dominates in the upper mantle [Debayle and Kennett, 2003].

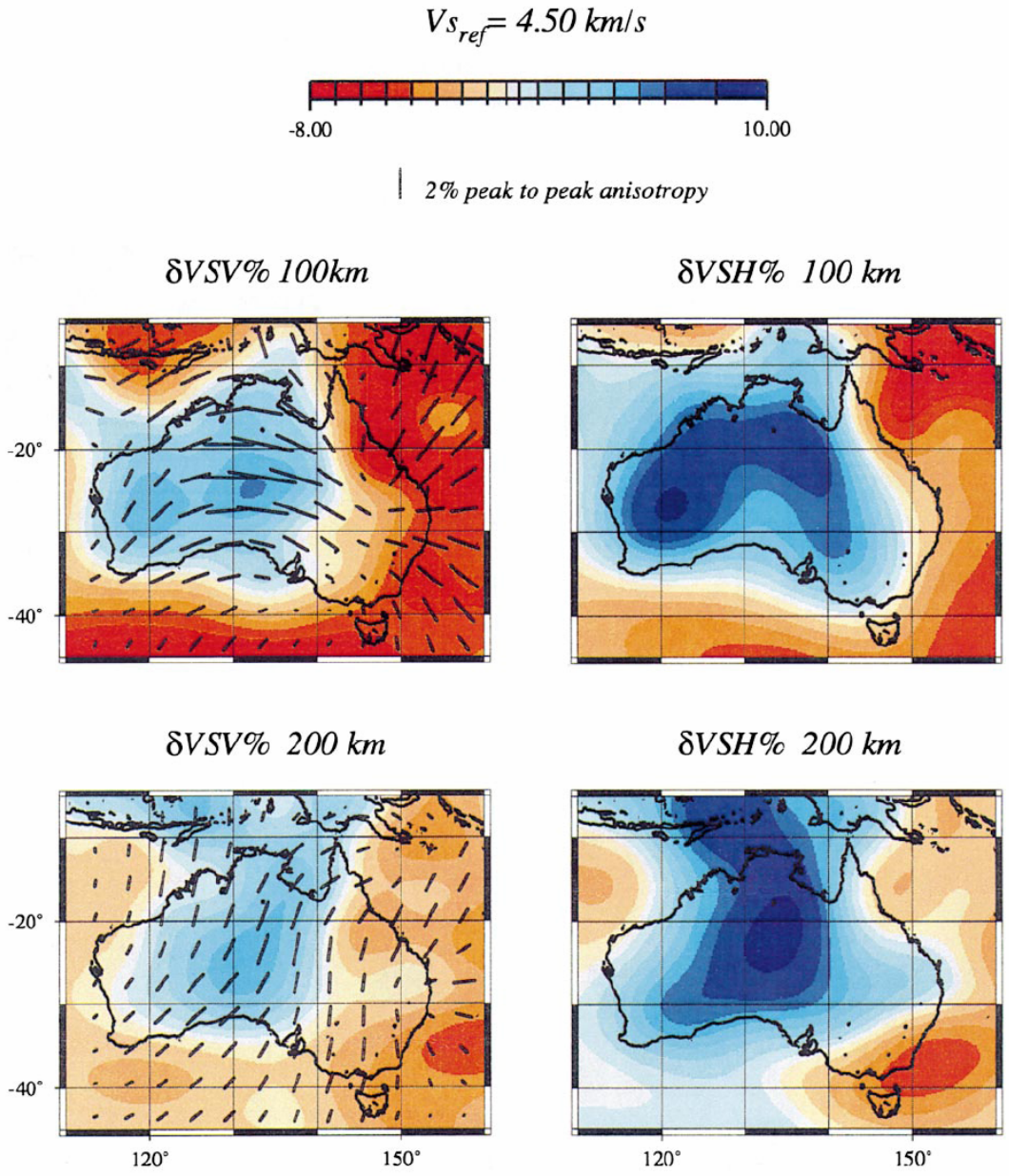

Figure 7.13: Left column: *SV* wave heterogeneities and azimuthal anisotropy (tones represent velocity contrasts and bars display azimuthal anisotropy, the length of the bars indicating the strength of anisotropy); right column : *SH* wave heterogeneities. [from Debayle and Kennett, 2000].

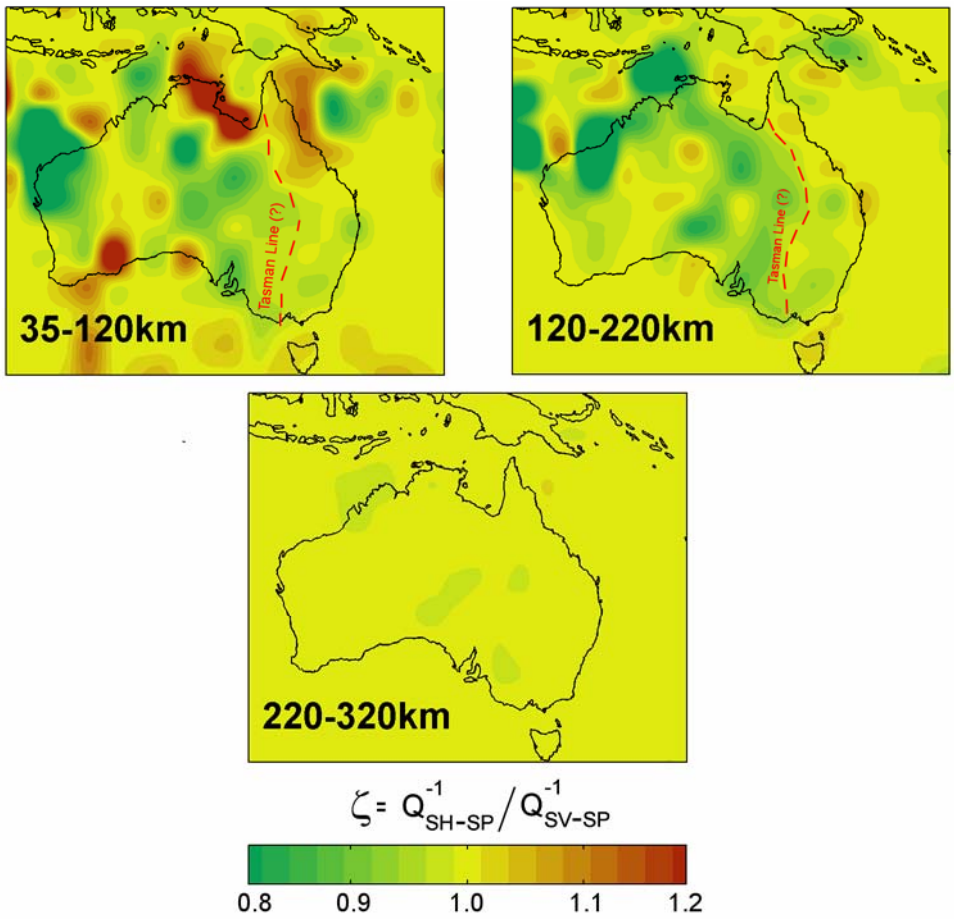

Figure 7.14: Polarisation anisotropy model for shear attenuation in terms of the ratio between *SH* and *SV* attenuation. Down to 220km depth, in the regions with good resolution, the *SH* waves have been found to propagate significantly less attenuative than *SV* waves particularly for most western, central and eastern Australia. Red dashed line in 120-220km layer is a possible location of the Tasman Line.

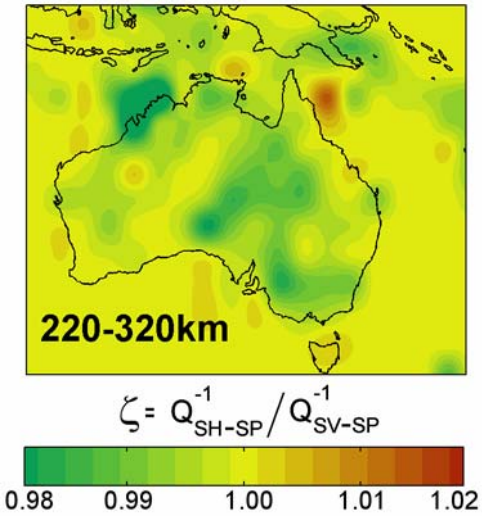

Figure 7.15: Attenuation ratio in 220-320km layer on an expanded scale relative to Figure 7.14. Although the anisotropy is not high as that of shallower layer, the *SH* wave show to propagate significantly less attenuative than *SV* for most of the continent.

Following the idea of Debayle and Kennett [2003], I introduce the radial anisotropy parameter ζ in term of the ratio between *SH* and *SV* attenuation ($\zeta = Q_{SH}^{-1} / Q_{SV}^{-1}$). The estimate of this polarization anisotropy is made from the Q_{SH}^{-1} and Q_{SV}^{-1} values that were inverted from the *S* to *P* differential attenuation measurements in Section 5.3. Both the Q_{SH}^{-1} and Q_{SV}^{-1} images are produced from exactly the same raypath coverage. The images of the parameter ζ are shown in Figure 7.14 and 7.15. Figure 7.15 is the attenuation ratio in 220-320km layer on an expanded scale relative to Figure 7.14. The Tasman Line location is also plotted along an abrupt change from low to high attenuation ratio. There is little indication of shear anisotropy in the asthenosphere (0.98 to 1.02) but in the lithosphere, ζ varies from 0.8 to 1.2.

In general, for most western-central of the Australian continent the *SH* waves are less attenuative than *SV* wave, but we have to be careful with the interpretation of the results since the most pronounced variations occur outside the regions with good resolution (particularly around the Great Sandy Desert, where there are no seismic recorders due to difficulty in transportation access).In the high attenuation zones associated with the existence of hot spots and partial melting i.e. around Indonesian subduction zone, northern Queensland, around Coral Sea and Bass Strait, the *SH* waves seems to be more attenuated than the *SV* waves. In these regions, heat transfer apparently control the seismic anisotropy, that is, heat transfer in vertical direction is most likely faster than that in horizontal direction. Lower variation in attenuation ratio to the east of the Tasman Line in 120-220km layer may be associated with the asthenosphere.

A comparison between the polarization anisotropy model of Debayle and Kennett [2003] at 125km and the polarization anisotropy produced in this study (120-220km) is shown in Figure 7.16. Ray path density and rosette diagram at 120-220km depth used in this study is also shown in the Figure.

Figure 7.16 provides a clear evidence of the existence of attenuation anisotropy in the upper mantle beneath the Australian continent. For almost the entire continent

(except for the regions where path density are poor i.e. shown by blue ellipses), where *SH* waves are generally faster than *SV* waves, the *SH* waves are generally less attenuative than *SV* waves.

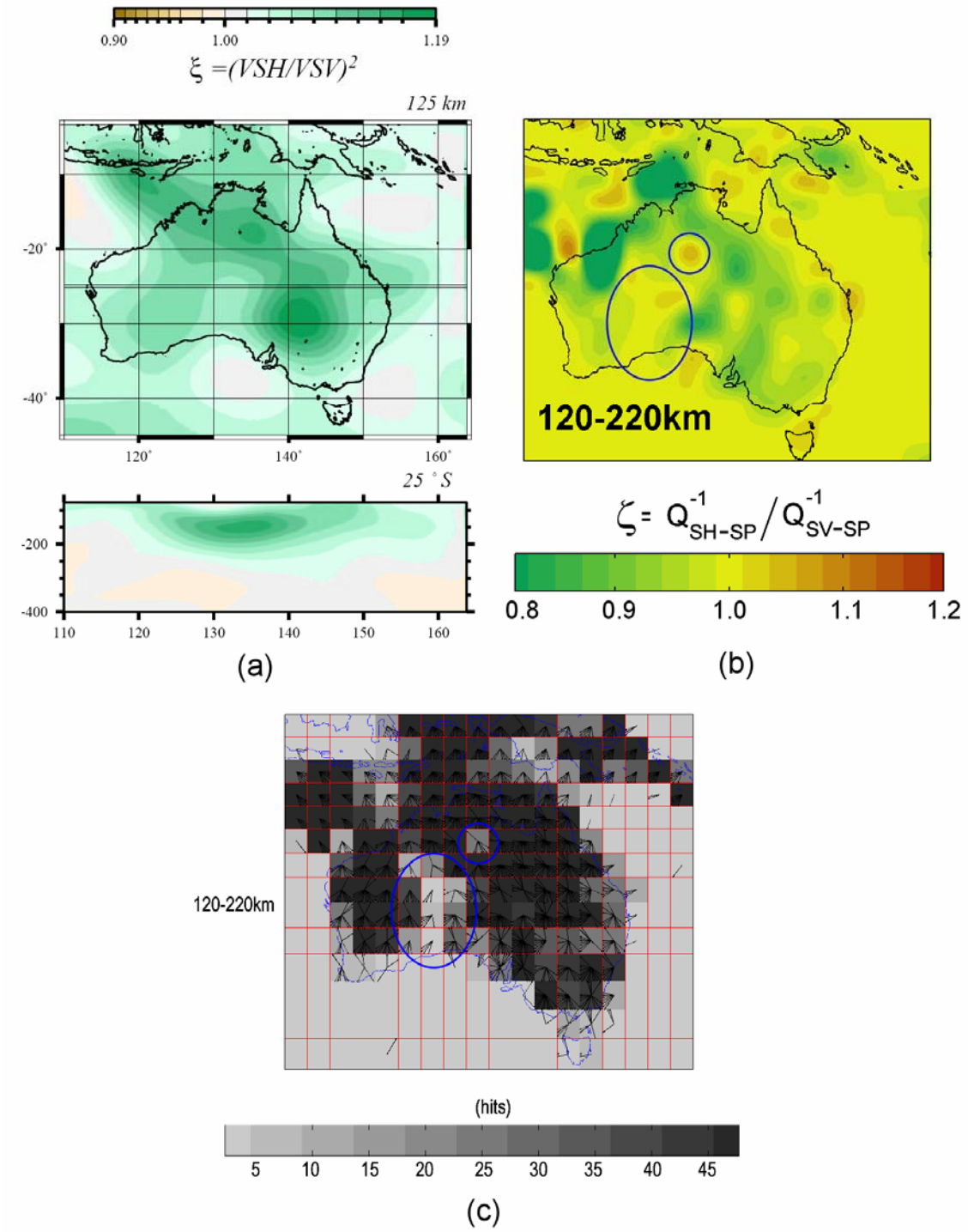

Figure 7.16: A comparison between (a) the polarisation anisotropy model for shear attenuation in terms of the ratio between *SH* and *SV* wavespeed [Debayle and Kennett, 2003] and (b) in term of the ratio between *SH* and *SV* attenuation (c) ray path density and rosette diagram at 120-220km.

In the depth interval 220-320 km (see Figure 7.14 and 7.15), the level of the level of radial anisotropy is significantly decreased compare to that at 30-120km and 120-220km intervals. Both radial anisotropic works (Debayle and Kennett [2003] and my result) show a good agreement i.e. the value of ξ or ζ is around 1.0. Suggesting the existence of 'homogenous isotropic' material in this depth interval. The more rapid flow in the asthenosphere may tend to homogenize the attenuation behaviors.

Appendix A

P-Wave Tomography of Northwestern Australia[3]

Geologically, Western Australia is characterized by three main geologic features: Pilbara, Capricorn Orogen and Yilgarn Cratons. Pilbara in the north and Yilgarn in the south are Achaean Cratons. These two cratons are separated by regions of two orogen younger sediments, they are the Bangamall 'Grenvillean' basin and the Capricorn orogen (early Proterozoic) [Betts *et al.*, 2002]. The general geological features of Western Australia have been explained in more detail in Chapter 3.1.

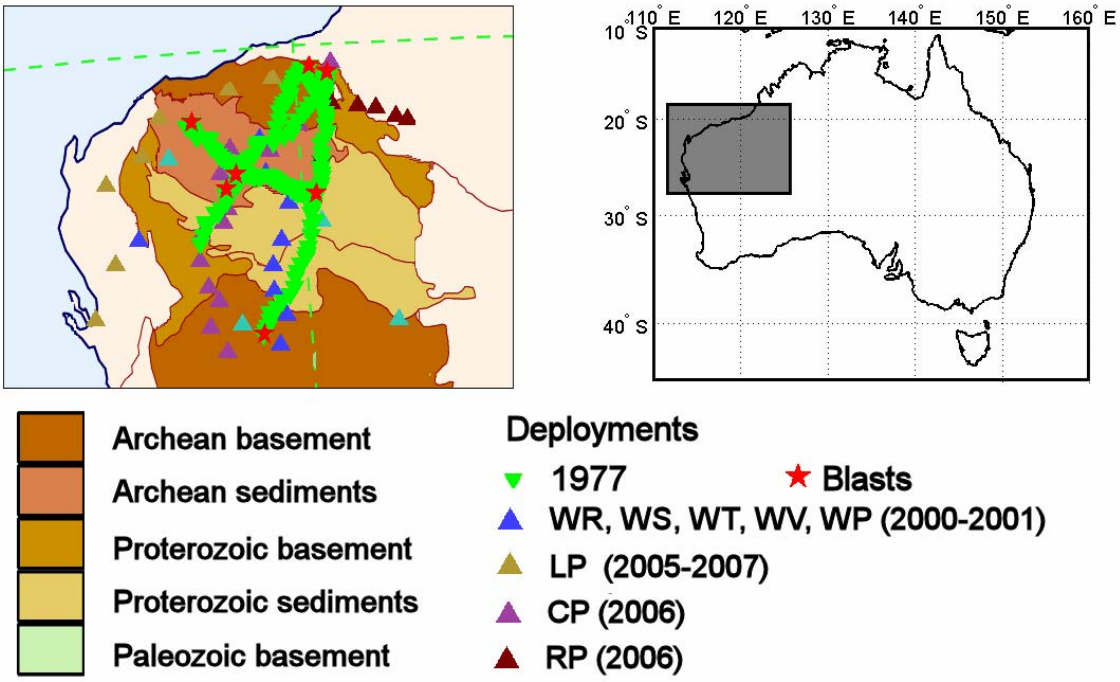

Figure A.1: Arrangement of seismic stations deployed in Western Australia that are used in this study. Seismic stations are marked by color filled triangles and 1977 mining blasts are indicated by red filled stars. Background is summary of the basement geology of the Pilbara Craton, Capricorn Orogen and Yilgarn Craton.

[3] Part of this work was presented in a poster at the European Geosciences Union meeting in Vienna 2007.

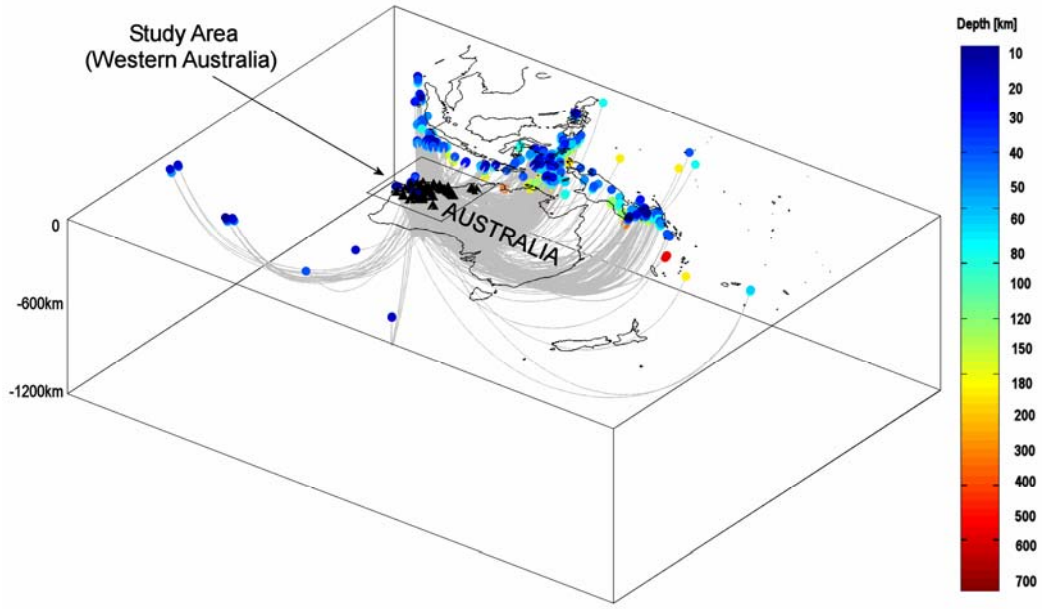

Figure A.2: Three dimensional view of seismic ray coverage of nearly 1600 *P* wave raypaths recorded by 45 seismic stations across Western Australia from local and distant events with magnitudes between 3.0 and 7.0 *mb* and depth between 1.0 and 600km. Nearly 100 *P* wave raypaths from an earlier 1977 survey in the region based on mining blasts were also included.

The main objective of this study is to image geological features beneath Western Australia by using *P*-wave tomography technique in a 3-D volume. For this purpose, seismic data during the period of 2000-2007 recorded by 45 seismic stations across Western Australia (Figure A.1) are used. The seismic data from local and distant events with magnitudes between 3.0 and 7.0mb and depth between 1.0 and 600 km are selected. Also data from an earlier 1977 survey in the region based on mining blasts were used to constrain the model. An example of local earthquake data and *P* and *S* waves traveltime picking is shown in Figure A.3.

1600 *P* wave traveltimes were hand picked and stored as data input for our tomography work. The tomography routine and the Fast Marching Method of Rawlinson *et al.* [2004] are used to trace seismic ray paths in the 1-D model *ak135*. To build a kernel matrix, the seismic ray paths are employed in the 3-D volume which was

discretised into cells of 1x1 degree grid in the area of interest and depth ranges of finer increments up to the Moho discontinuity, and 50 to 100km layers afterwards.

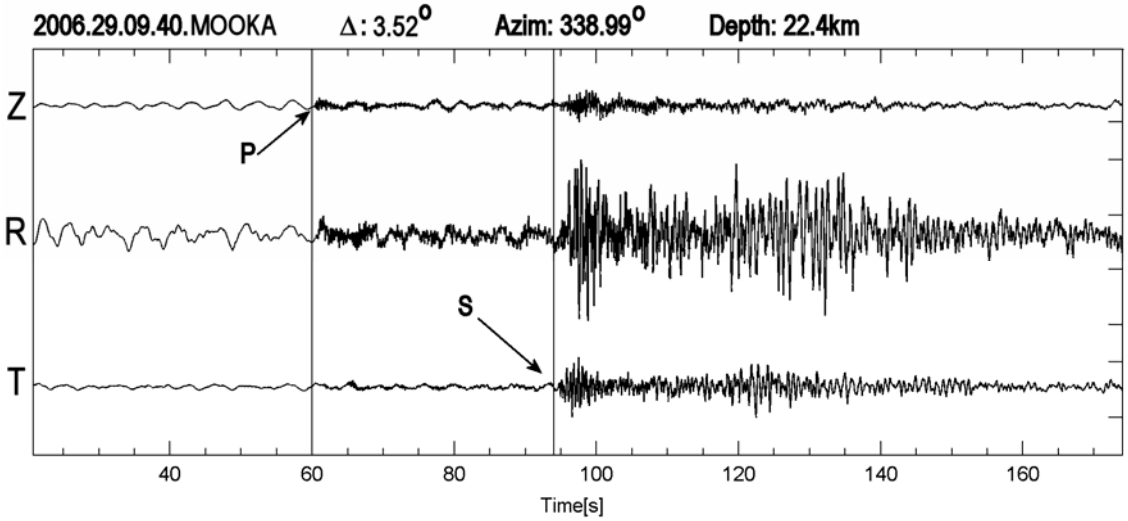

Figure A.3: An example of local earthquake data with epicentral distance 3.52° and depth 22.4km recorded by MOOKA station in Western Australia. *P* and *S* wave traveltimes picking are also shown.

The LSQR algorithm of Paige and Saunders [1982] is employed to solve the sparse matrix inversions as in equation 4.10. For this inversion a diagonal data covariance matrix with elements 0.25s, a model covariance matrix with diagonal elements 0.0001, the damping factor ε 10 and a smoothing parameter η of 5 are used. Since the LSQR algorithm is an iterative solution, several different numbers of iteration are tested.

To guide in choosing a 'suitable' number of iterations, the Root-mean Square (RMS) residual between the observed and calculated traveltimes is introduced:

$$RMS(\delta t) = \sqrt{\frac{\sum_{j}^{M}\left(t_{obs_j} - t_{cal_j}\right)^2}{M}} \qquad \text{(A.1)}$$

Here t_{obs} is the observed traveltime and t_{cal} is the calculated traveltime for the current model; M is the number of data points (rays). The root-mean square residual between the observed and calculated traveltimes is generated after each iteration and is helpful for understanding the accuracy and efficiency of the LSQR algorithm [Sinadinovski, 1994].

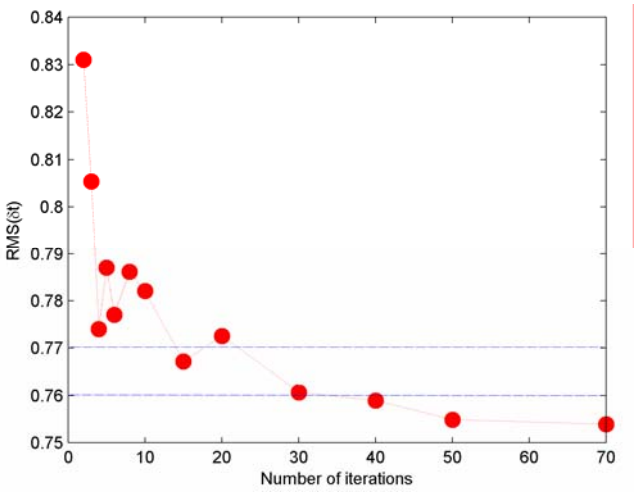

Figure A.4: Convergence curve of number of iterations as a function of the root-mean square residual between the observed and calculated traveltimes for the inversion of Western Australia seismic data. Two dashed blue horizontal lines represent the value of the RMS when the curve begins to converge.

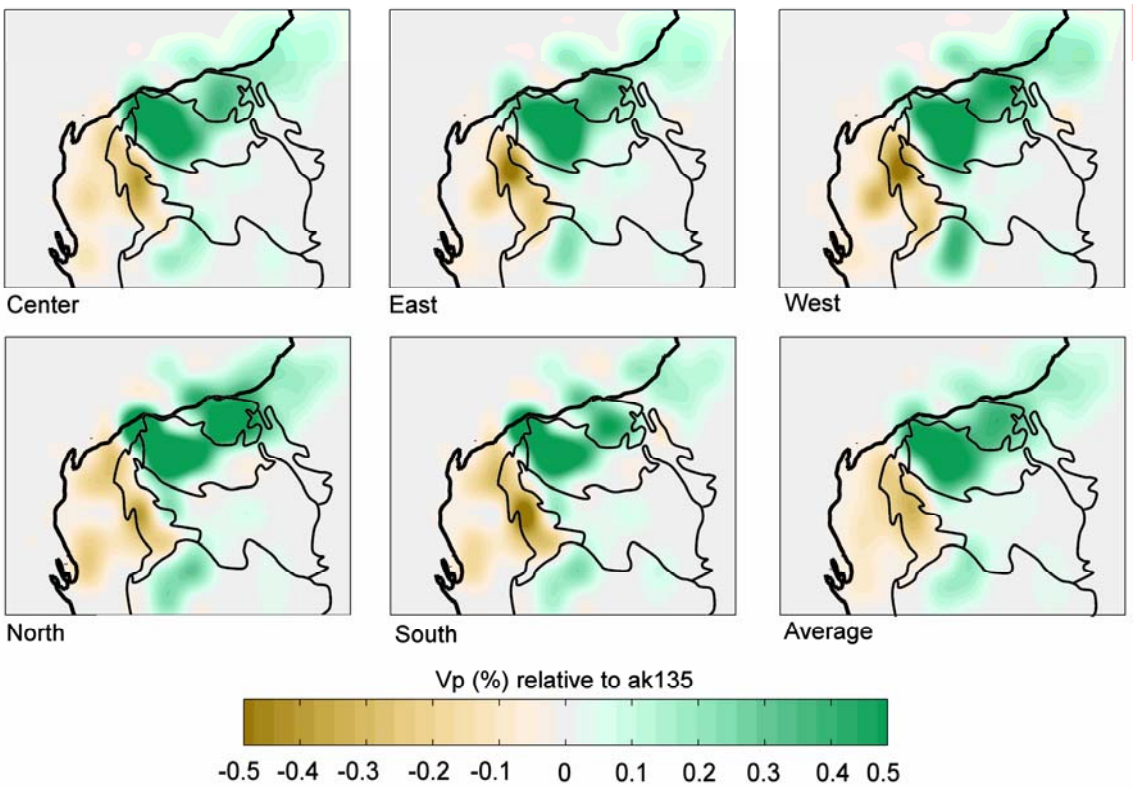

Figure A.5: *P* wave seismic perturbation images at 35km depth. The images are plotted in percent relative to the *ak135* model. Green represents fast and brown represents slow. Correlation between wavespeed anomalies and geological features is also drawn. Perturbation image produce from corresponding mesh location is shown: 'center' is the image produced from the original mesh location; 'east', 'west', 'north' and 'south' are images produced if the 'center' mesh is moved 0.5º to the east, west, north and south respectively; 'average': average of perturbation from all locations.

Figure A.4 shows the curvature of the convergence between number of iterations and the root-mean square residual between the observed and calculated traveltimes for the inversion of Western Australia seismic data. From the convergence of the curve, it is suggested that our inversion satisfies solution. Two dashed blue horizontal lines represent the value of the RMS when the curve begins to consistently converge. In this inversion, the number of iterations of 30 is chosen.

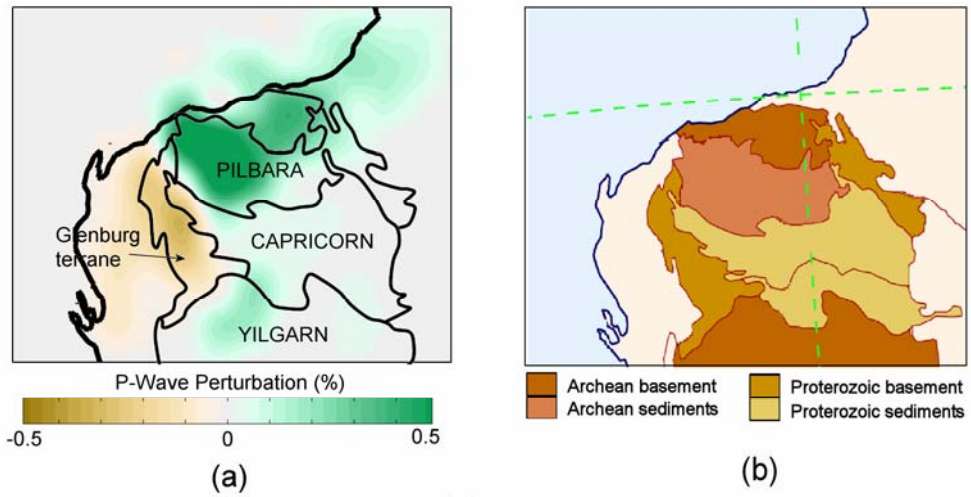

Figure A.6: A comparison between (a) *P*- wave speed perturbation produced in this thesis and (b) major surface geological features.

To avoid the influence of specific choices of cell boundaries on the inverted model, five different mesh locations are employed to build the kernel matrix with separate inversion. Thus, the first mesh is fixed in a particular location in Western Australia (let say 'center' mesh), and then the mesh is moved by 0.5º to north, south, west and east to produce a set of four meshes.

The inverted *P* wave seismic wavespeed perturbation model in the crust beneath Western Australia for center, east, west, north, south mesh locations and average of the five mesh configurations are shown in Figure A.5. The averaging has the effect of smoothing at the cellular behavior whilst retaining the intrinsic resolution.

Figure A.6 shows those three seismic images clearly delineate major geological feature beneath Western Australia. The *P*- wavespeed perturbation produced in this

thesis is clearly differentiate between the younger and older geological structures. For the areas with good ray coverage it is even possible to distinguish the provinces inside the basin. The Achaean Cratons of Pilbara in the north and Yilgarn in the south are associated with high seismic speed anomaly, while the Bangamall and Capricorn are associated with low seismic speed. Figure A.6 (c) shows the proterozoic basement of Glenburg terrane boundary is clearly distinguishable from the Pilbara, Capricorn and Yilgarn cartons.

Appendix B

Seismic Ray Theory

Seismic ray paths in the earth can be modeled using Snell's law. Snell's law describes the correlation between reflection and refraction of wavefronts at interfaces of earth velocity. To understand this law, consider a seismic ray which propagates in two layers of an earth model with seismic velocity V_1 and V_2, reflection angle θ_1 and refraction angle θ_2. By using Snell's law, we have a relation: $r_1 Sin\theta_1 / V_1 = r_2 Sin\theta_2 / V_2$, where r_1 and r_2 are earth radii from layer 1 and layer 2 respectively. In spherical coordinate, the ray parameter is a function of earth radii, inclination and seismic wavespeed:

$$\wp = \frac{r \sin\theta}{v(r)} \qquad \text{(B.1)}$$

Where $\wp$ is constant along the path. The ray parameter $\wp$ characterizes the path of the ray from the source to a receiver at the point on the surface of the earth [Kennett, 2001].

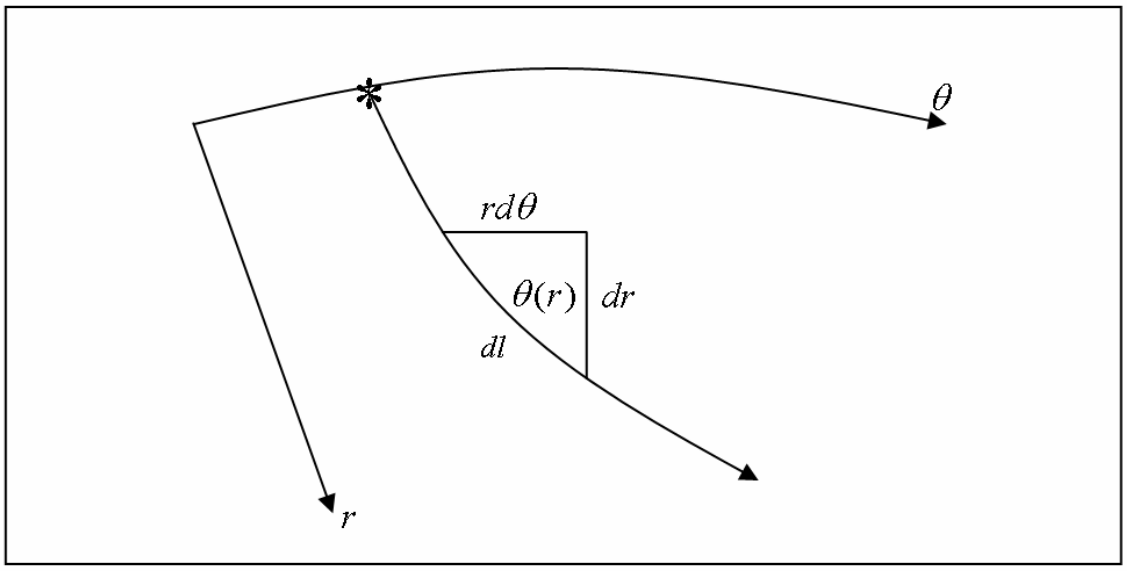

Figure B.1: Schematic diagram of a ray segment (*dl*) in Spherical coordinate.

The expressions for seismic travel time and horizontal distance traced by a particular ray in a velocity model can be easily derived. Figure B.1 shows a differential element of a ray in Spherical coordinate. From the figure, we can derive:

$$r d\theta = dr \tan\theta(r) \tag{B.2}$$

$$dt = \frac{dl}{v(r)} = \frac{dr}{v(r)\cos(\theta(r))} \tag{B.3}$$

Since the ray parameter is $\wp = \frac{r\sin\theta}{v(r)}$, we can substitute the trigonometric expressions to get:

$$d\theta = \frac{\wp\, dr}{r\sqrt{\xi^2 - \wp^2}} \tag{B.4}$$

$$dt = \frac{\xi^2 dr}{r\sqrt{\xi^2 - \wp^2}} \tag{B.5}$$

Where $\xi = r/v$. For a ray that traveling between depths r_1 and r_2, the distance and total travel time are obtained by integration of the above equations:

$$\Delta(\wp) = \int \frac{\wp\, dr}{r\sqrt{\xi^2 - \wp^2}} \tag{B.6}$$

$$\tau(\wp) = \int \frac{\xi^2 dr}{r\sqrt{\xi^2 - \wp^2}} \tag{B.7}$$

Appendix C

The Multitaper Method

The Multitaper Method (MTM) has been widely used in geophysical signal processing, including analysis of seismological data. Particularly for spectral ratio analysis, the MTM offers better results than some conventional estimators that use a single taper, e.g., the single taper of the Fast Fourier Transform (FFT) [Vernon, 1989].

Using a small set of tapers, the MTM tries to reduce the variance of spectral estimates [Percival and Walden, 1993]. The method calculates a set of independent estimates of the power spectrum. In dealing with the finite length of seismic dataset, the method also multiplies the data by orthogonal tapers which are constructed to minimize the spectral leakage.

Suppose that we have a discrete sequence $\{X_t\}$ with samples $X_0,\ldots,X_{N-1}$ and for convenience assume that $\{X_t\}$ has zero mean. A multitaper spectrum estimator uses a number (K) of orthonormal data tapers, the *k*-th member of the sequence is denoted by $\{a_{t,k} : t = 0,...,N-1\}$. The multitaper spectrum estimator $\hat{S}^{(mt)}(f) = (1/K)\sum \hat{S}_k^{(mt)}(f)$ is the average of *K* direct spectral estimators or eigen spectra:

$$\hat{S}_k^{(mt)}(f) \equiv \left| \sum_{t=0}^{N-1} a_{t,k} X_t e^{-i2\pi ft} \right|^2 \tag{C.1}$$

The eigen spectra can be approximately uncorrelated if the spectrum is not rapidly varying over the effective band-width. To solve this problem, the following approximation should be taken:

$$v(f) \equiv \frac{\hat{S}^{(mt)}(f)}{S(f)} \sim \frac{\chi^2_{2K}}{2K}, \qquad 0 < f < \frac{1}{2} \tag{C.2}$$

A random variable is defined by:

$$\eta(f) \equiv \log v(f) - \psi(K) + \log(K) \tag{C.3}$$

and variance $\sigma_\eta^2 = \psi'(K)$, where $\psi(.)$ and $\psi'(.)$ are the digamma and trigamma function respectively.

If we let

$$Y(f) \equiv \log \hat{S}^{(mt)}(f) - \psi(K) + \log(K), \tag{C.4}$$

then

$$Y(f) = \log S(f) + \eta(f). \tag{C.5}$$

For a fixed f and v such that $0 < f < 1/2$ and $0 < f + v < 1/2$, we see that

$$\begin{aligned} s_\eta(v) &\equiv \operatorname{cov}\{\eta(f), \eta(f+v)\} = \operatorname{cov}\{Y(f), \eta(f+v)\}, \\ &= \operatorname{cov}\left\{\log \hat{S}^{(mt)}(f), \log\log \hat{S}^{(mt)}(f+v)\right\} \end{aligned} \tag{C.6}$$

Provided $S(f) \approx S(f+v)$ for a small v, then $s_\eta(v) \approx \tilde{s}_\eta(v)$ with

$$\tilde{s}_\eta(v) \equiv \log\left(1 + \frac{1}{K^2}\sum_{k=0}^{K-1}\sum_{l=0}^{K-1}\left|\sum_{t=0}^{N-1} a_{t,k} a_{t,l} e^{i2\pi vt}\right|^2\right), \tag{C.7}$$

where $\tilde{s}_\eta(v)$ has unit periodicity.

A simple approximation of $s_\eta(v)$ namely $s_\eta(v) \approx \breve{s}_\eta(v)$ and

$$\breve{s}_\eta(v) = \begin{cases} \sigma_\eta^2\left(1 - \dfrac{|v|N}{K+1}\right), & \text{if } |v| \le \dfrac{(K+1)}{N} \\ 0, & \text{otherwise} \end{cases} \tag{C.8}$$

Notice that subject to the stated approximations, the covariance structure of the noise $\eta(f)$ and, hence, the covariance structure of the log multitaper spectrum estimators depends only the tapers used.

The Multitaper Method uses discrete prolate spheroidal sequences (Slepian) as data tapers [Slepian, 1987]. A representation of the five lowest-order 4π discrete prolate spheroidal sequences can be seen in Figure C.1. As can be seen from equation (C.2), the data are multiplied by several Slepian tapers which will produce a number of tapered time series from one record. Taking the DFTs of each of these time series, several 'eigenspectra' are produced which are combined to form a single spectral estimate [Vernon, 1989].

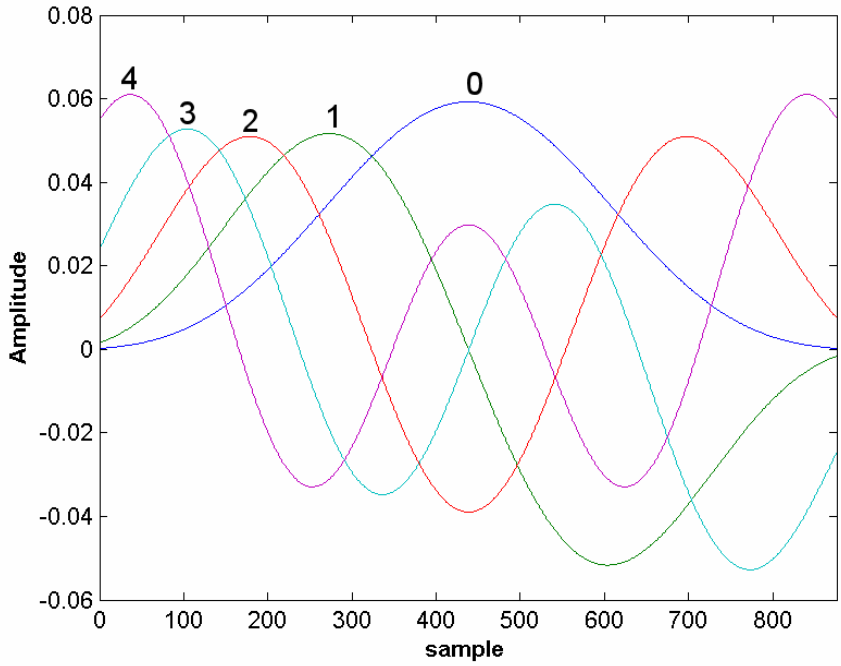

Figure C.1: Representation of the five lowest-order 4π discrete prolate spheroidal sequences. The order is shown on the top of each sequence.

A comparison between The Multitaper Method and the single taper of the Fast Fourier Transform is shown in Figure C.2. *P* wave seismic data from vertical component recorded by TL01 station is transformed into frequency domain by using these two spectral methodologies.

To measure the 'smoothness' of spectral estimates, the variance quantity is introduced:

$$Variance = \frac{1}{n}\sum_{i=1}^{n}\left(x_i - \bar{x}\right)^2 \qquad \text{(C.9)}$$

Here, x is data vector, $\bar{x}$ is data average and n is the number of elements in the sample. Table C.1 shows the variance of spectral estimation method for several different orders of taper. It can be seen that the variance decreases with increasing order of the discrete prolate spheroidal sequences (dpss). For the estimation of spectra of Australian seismic data, the 11 lowest-order 4π discrete prolate spheroidal sequence was chosen for which the variation is about 50% lower than for the single taper-Fast Fourier Transform.

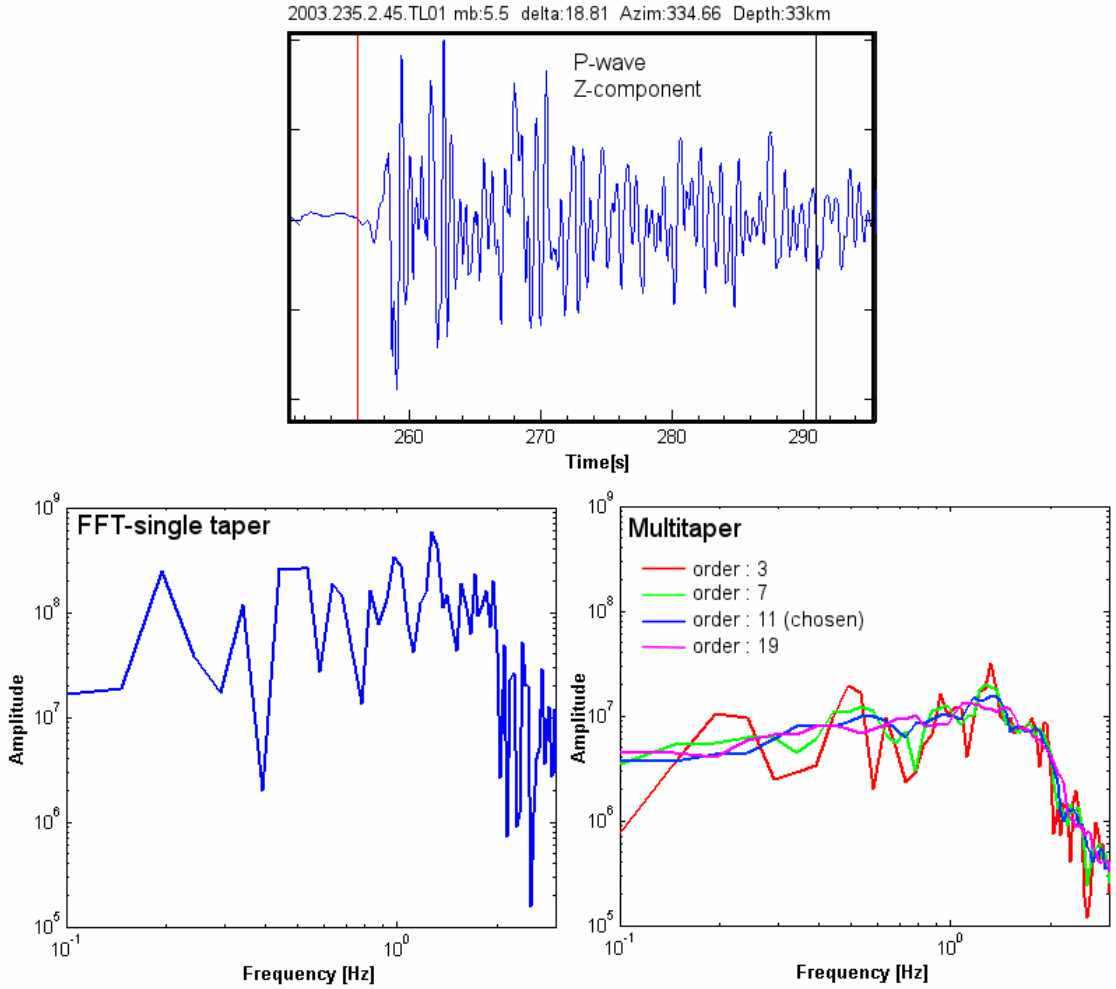

Figure C.2: A comparison between a single taper of the Fast Fourier Transform and the Multitaper method. Top panel is *P* wave seismic data of vertical component recorded by TL01 station. Estimated spectra using a single taper of the Fast Fourier Transform and the Multitaper method are shown in the bottom panel. Spectra estimated by the Multitaper method using several order of discrete prolate spheroidal sequences are also shown.

Table C.1: Variance of spectral estimation method for several orders of discrete prolate spheroidal sequence.

Method	**Variance**
FFT single taper – no. of order = 0	0.6478
Multitaper – no. of order = 3	0.3571
Multitaper – no. of order = 7	0.3258
Multitaper – no. of order = 11	0.3047
Multitaper – no. of order = 19	0.2713

Appendix D

Attenuation Measurement Software

A computer program for the attenuation measurements described in Chapter II can be found in the enclosed CD.

The CD contains:

1. attenuationSPwin.m
2. attenuationPPSSwin.m
3. attenuationSPx.m
4. attenuationPPSSx.m
5. sacread.m
6. dist.m
7. azim.m
8. CP seismic data (SAC)
9. ttimes.txt
10. Digital version of this thesis

Instructions for Unix and Windows OS:

1. Windows: Place attenuationSPwin.m, attenuationPPSSwin.m, sacread.m, dist.m, azim.m in Matlabx/work directory
   Unix: Place attenuationSPx.m, attenuationPPSSx.m, sacread.m, dist.m, azim.m in a particular directory, says: Matlabx/work
2. Place seismic data (SAC format) and ttimes.txt in a folder e.g. C:/DATA
3. Open the Matlabx application
4. Open attenuationSPwin.m for *S* to *P* differential attenuation measurements or attenuationPPSSwin.m for *P* to *P* and *S* to *S* differential attenuation measurements. In Unix environment, open attenuationSPx.m or attenuationPPSSx.m
5. Run program (e.g. press F5) to activate the GUI
6. Click 'Load Seismic' , select C:/DATA
7. Click 'Load Ttimes', select C:/DATA/ ttimes.txt
8. Click 'Execute', 'Next', 'Pick P', etc. Please see Figure 2.2 or 2.3 for more detail.

References

Aki K., 1967, *Scaling law of seismic spectrum*, Journal of Geophysical Research, **72**, 1217-1231.

Aki K., 1980, *Attenuation of shear-waves in the lithosphere for frequencies from 0.05 to 25 Hz*, Phys. Earth Planet. Inter., **21**, 50-60.

Aki K, Richards P.G., 2002, *Quantitative Seismology*, second edition, University Science Books, Sausalito, California.

Artemieva I. M., Billien M., Lévêque J.J., Mooney W. D., 2004, *Shear wave velocity, seismic attenuation, and thermal structure of the continental upper mantle*, Geophysical Journal International, **157**, 607-628.

Ben-Ismail W., Mainprice D., 1998, *An olivine fabric database: an overview of upper mantle fabrics and seismic anisotropy*, Tectonophysics, **296**, 145-157.

Betts P. G., Giles D., Lister G.S., Frick L. R., 2002, *Evolution of the Australian lithosphere*, Australian Journal of Earth Sciences, **49**, 661–695

Bormann P., Gruenthal G., Kind R., Montag H., 1996, *Upper mantle anisotropy beneath Central Europe from SKS wave splitting: effects of absolute plate motion and lithosphere–asthenosphere boundary topography?*, J. Geodyn., **22**, 11-32.

Brown A. R., 2005, *The Balance Between Geophysics and Geology in Seismic Interpretation*, Geophysical Corner, American Association of Petroleum Geologists.

Cheng H.-X., 2000, *Seismic Body Wave Attenuation in the Upper Mantle beneath the Australian Continent*, Ph.D. thesis, Research School of Earth Sciences, The Australian National University.

Coney P. J., Edwards A., Hine R., Morrison F., Windrum D., 1990, *The regional tectonics of the Tasman Orogenic system, eastern Australia*, Journal of Structural Geology, **125**, 19-43.

Dawson G.C., Krapez B., Fletcher I.R., McNaughton N.S., Rasmussen B., 2002, *Did late Paleoproterozoic assembly of proto-Australia involve collision between the Pilbara,Yilgarn and Gawler Cratons? Geochronological evidence from the Mount Barren Group in the Albany-Fraser Orogen ofWestern Australia*. Precambrian Res., **118**, 195-220.

Debayle E., Kennett B.L.N., 2000, *Anisotropy in the Australasian upper mantle from Love and Rayleigh waveform inversion*, Earth and Planetary Science Letters, **184**, 339-351

Debayle E., Kennett B.L.N., 2003, *Surface wave studies of the Australian region*, Geol. Soc. Australia Spec. Publ. **22**, and Geol. Soc. America Spec. Pap., **372**. 25-40.

Direen N.G., Allan G. C., Patrick L., Jonathan P., Teasdale, 2005, *Architecture of Proterozoic shear zones in the Christie Domain, western Gawler Craton, Australia: Geophysical appraisal of a poorly exposed orogenic terrane*, Precambrian Research, **142**, 28-44

Drummond B. J., Goleby B. R., Swanger C. P., 2000, *Crustal signature of late Archaean tectonic episodes in the Yilgarn Craton, Western Australia: evidence from deep seismic sounding*, Tectonophysics, **329**, 193-221.

Dziewonski A. M., 1979, *Elastic and anelastic structure of the earth*, Rev. Geophys. Space Phys., **17**, 303-312.

Elliot C. G., Woodward N.B., D.R. Gray, 1993, *Complex regional fault history of the Badger Head region, northern Tasmania,* Australian Journal of Earth Sciences, **40**, 155-168.

Engdahl E.R., van der Hilst R.D., Bulland R., 1998, *Global teleseismic earthquake relocation with improved travel times and procedures for depth determination*, Bull. Seismol. Soc. Am., **88**, 722–743.

Faul U.H., Fitz Gerald J. D., Jackson I., 2003, *Shear-wave attenuation and dispersion in melt-bearing olivine polycrystals II. Microstructural interpretation and seismological implications*, J. Geophys. Res, **109**, B06202, doi:10.1029/2003JB002407.

Faul U.H., Jackson I., 2005, *The seismological signature of temperature and grain size variations in the upper mantle*, Earth and Planetary Science Letters, **234**, 119-134

Fishwick S., Kennett B.L.N., Reading A.M., 2005, *Contrasts in lithospheric structure within the Australian Craton*, Earth Planet Sci. Lett., **231**, 163-176.

Fishwick S., 2005, *The Australasian Upper Mantle-Insights from Surface Wave Tomography*, PhD Thesis, Research School of Earth Sciences, Australian National University.

Flanagan M. P., Wiens D.A., 1998, *Attenuation of Broadband P and S Waves in Tonga: Observations of Frequency Dependent Q*, Pure and Applied Geoph., **153**, 345-375.

Foster D. A., Gray D.R., 2000, *The structure and evolution of the Lachlan Fold Belt (Orogen) of eastern Australia,* Annual Review of Earth and Planetary Sciences, **28**, 47-80.

Gaina C., Müller R.D., Royer J.Y., Stock J.M., Hardebeck J., Symonds P., 1998, *The tectonic history of the Tasman Sea: a puzzle with thrirteen pieces*. J.Geophys. Res., **103**, 12413-12433.

Gaina C., Müller R.D., 1999, *Evolution of the Louisiade triple junction*, J. Geophys. Res., **104**, 12927-12939.

Goes S., Simons F. J., Yoshizawa K., 2005, *Seismic constraints on temperature of the Australian uppermost mantle*, Earth and Planetary Science Letters, **236**, 227-237.

Gorbatov A., Kennett B.L.N., 2001, *P wave tomographic imaging of the southeast Pacific*, Annual Report of Research School of Earth Sciences, ANU, for 2000, 140-141.

Gray D. R., Foster D. A., 1998, *Character and kinematics of faults within the turbidite-dominated Lachlan Orogen: implications for tectonic evolution of eastern Australia*, Journal of Structural Geology, **20**, 1691-1720.

Gray D. R, Foster D. A., 2004, *Tectonic evolution of the Lachlan Orogen, southeast Australia: historical review, data synthesis and modern perspectives*, Australian Journal of Earth Sciences, **51,** 773-817

Gribb T. T., Cooper R. F., 1998, *Low-frequency shear attenuation in polycrystalline olivine: Grain boundary diffusion and the physical significance of the Andrade model for viscoelastic rheology*, J. Geophys. Res., **103**, 27267-27280.

Gudmundson O., Kennett B.L.N., Goody A., 1994, *Broadband observations of upper mantle seismic phases in northern Australia and the attenuation structure in the upper mantle*, Phys. Earth Planet. Inter., **84**, 207-226.

Gurnis M., Müller R.D., 2003, *Origin of the Australian Antarctic Discordance from an ancient slab and mantle wedge*, Geol. Soc. Australia Spec. Publ. **22** and Geol. Soc. America Spec. Pap., **372**, 417-429.

Heintz M., Kennett B.L.N., 2005, *Continental scale shear wave splitting analysis: Investigation of seismic anisotropy underneath the Australian continent*, Earth and Planetary Science Letters, **236**, 106-119.

Hickman A. H., 1983, *Geology of the Pilbara Block and its environs*, Geological Survey of Western Australia Bulletin , **127**, 268p.

Jackson D. D., Anderson D. L., 1970, *Physical mechanisms of seismic-wave attenuation*, Rev. Geophys. Space Phys., **8**, 1-63.

Jackson I., 1993, *Progress in the experimental study of seismic wave attenuation*. Ann. Rev. Earth Planet. Sci., **21**, 375-406.

Jackson I., 2000, *Laboratory Measurements of Seismic Wave dispersion and Attenuation: Recent Progress. In Earth's Deep Interior: Mineral Physics and Tomography from the Atomic to the Global Scale*, AGU Geophysical Monograph Service, vol.**117**, S. Karato et al. (eds), 265-289.

Jackson I., Fitz Gerald J. D., Faul U. H., Tan B. H., 2002, *Grain-size-sensitive seismic wave attenuation in polycrystalline olivine*, J. Geophys. Res., 107(B12), 2360, doi:10.1029/2001JB001225.

Kaiho Y., Kennett B.L.N., 2000, *Three-dimensional seismic structure beneath the Australian region from refracted wave observations*, Geophys. J. Int., **142**, 651-668.

Kawahara J., Yamashita T., 1992, *Scattering of elastic waves by a fracture zone containing randomly distributed cracks*, Pure Appl. Geophys., **139**, 121-144.

Kennett B.L.N., 2001, *The Seismic Wavefield, Vol. I: Introduction and Theoretical Development*, Cambridge University Press.

Kennett B.L.N., 2003, *Seismic structure in the mantle beneath Australia*, Geol. Soc. Australia Spec. Publ. 22, and Geol. Soc. America Spec. Pap., **372**, 7-23

Kennett B.L.N., Engdahl E. R., 1991, *Traveltimes for global earthquake location and phase identifications*, Geophys. J. Int., **105**, 429-465.

Kennett B.L.N., Engdahl E.R., Buland R., 1995, *Constraints on seismic velocities in the earth from travel times*, Geophys. J. Int., **122**, 108-124

Kennett B.L.N., Fishwick S., Heintz M., 2004, *Lithospheric structure in the Australian region - a synthesis of surface wave and body wave studies*, Exploration Geophysics, **35**, 242-250

Knopoff L. , 1964, *Q*, Rev. Geophys., **2**, 625-660.

Koketsu K., Sekine S., 1998, *Pseudo-bending method for three-dimensional seismic ray tracing in a spherical earth with discontinuities*, Geoph. Journal Int., **132**, 339-346.

Lowrie W., 2004, *Fundamentals of Geophysics*, Cambridge University Press.

Matsunami K., 1990, *Laboratory measurements of spatial fluctuation and attenuation of elastic waves by scattering due to random heterogeneities*, Pure Appl. Geophys., **132**,197-220.

Mavko G. M., Nur A., 1979, *Wave attenuation in partially saturated rocks*, Geophysics, **44**, 161-178.

Mitchell B.J., 1995, *Anelastic structure and evolution of the continental crust and upper mantle from seismic surface wave attenuation*, Rev. Geophys., **33**, 441-462.

Mitchell B. J., Baqer S., Akinci A., Cong L., 1998, *Lg coda Q in Australia and its relation to crustal structure and evolution of continents*, Pure Appl. Geophys., **153**, 655–664.

Myers J.S., Shaw R.D., Tyler I. M., 1996, *Tectonic evolution of Proterozoic Australia*, Tectonics, **15**, 1431-1446.

Nur A., 1971, *Viscous phase in rocks and the low-velocity zone*, J. Geophys. Res., **76**, 1270-1277.

Oliver N.H.S., Cawood P. A., 2001, *Early tectonic dewatering and brecciation on the overturned sequence at Marble Bar, Pilbara Craton, Western Australia: dome-related or not*, Precambrian Research, **105**, 1-15.

Paige C. C., Saunders M. A., 1982, *LSQR: An Algorithm for Sparse Linear Equations And Sparse Least Squares*, ACM Trans. Math. Soft., **8**, 43-71.

Percival D.B., Walden A.T., 1993, *Spectral Analysis for Physical Applications: Multitaper and Conventional Univariate Techniques*, Cambridge University Press.

Pollack H.N., Hurter S.J., Johnson J.R., 1993, *Heat flow from the earth's interior: analysis of the global data set*, Rev. Geophys., **31,** 267-280.

Rawlinson N., Sambridge M., 2003. *Seismic traveltime tomography of the crust and lithosphere*, Advances in Geophysics, **46,** 81-198.

Rawlinson N., Sambridge M., 2004, *Wavefront evolution in strongly heterogeneous layered media using the fast marching method*, Geophys. J. Int., **156,** 631-647.

Rawlinson N., Sambridge M., 2005, *The fast marching method: An effective tool for tomographic imaging and tracking multiple phases in complex layered media*, Explor. Geophys., **36,** 341-350.

Rawlinson N., Reading A. M., Kennett B. L. N., 2006. *Lithospheric structure of Tasmania from a novel form of teleseismic tomography*, J. Geophys. Res., **111,** B02301, doi:10.1029/2005JB003803.

Reading A. M., Kennett B.L.N., 2003, *Lithospheric structure of the Pilbara Craton, Capricorn Orogen and northern Yilgarn Craton, Western Australia, from teleseismic receiver functions*, Australian Journal of Earth Sciences, **50**, 439-445.

Rickett J., 2007, *Estimating attenuation and the relative information content of amplitude and phase spectra*, Geophysics, **72**, R19-R27.

Romanowizc B., 1995, *A global tomographic model of shear attenuation in the upper mantle*, J. Geophys. Res., **100**, 12375-12394.

Sambridge M. S., 1999, *Geophysical inversion with a neighbourhood algorithm -I. Searching a parameter space*, Geophys. J. Int., **138**, 479–494.

Sambridge M. S., 1999, *Geophysical inversion with a neighbourhood algorithm -II. Searching a parameter space*, Geophys. J. Int., **138**, 727–746.

Sato H., Fehler M., 1998, *Seismic Wave propagation and Scattering in the Heterogeneous Earth*, American Institute of Physics Press.

Shearer P.M., 1999, *Introduction to Seismology*, Cambridge University Press.

Silver P.G., Chan W.W., 1991, *Shear wave splitting and subcontinental mantle deformation*, J. Geophys. Res., **96**, 16429-16454.

Silver P.G., Chan W.W., 1998, *Implications for continental structure and evolution from seismic anisotropy*, Nature**, 335**, 34-39.

Simons F.J., Zielhuis A., van der Hilst R.D., 1999, *The deep structure of the Australian continent from surface wave tomography*, Lithos, **48**, 17-43.

Simons F.J., van der Hilst R.D., Montagner J.P., Zielhuis A., 2002, *Multimode Rayleigh wave inversion for heterogeneity and azimuthal anisotropy of the Australian upper mantle*, Geophys. J. Int., **151**, 738-754.

Sinadinovski C., 1994, *Seismic imaging with application to mine layout and development*, Ph.D. thesis, School of Earth Sciences-Geophysics, Flinders University of South Australia.

Slepian D., 1978, *Prolate spheroidal wave functions, Fourier analysis, and uncertainty, V, The discrete case*, Bell Syst. Tech. J., **57**, 1371-1429.

Tan B.H., Jackson I., Fitz Gerald J. D., 1997, *Shear wave dispersion and attenuation in fine-grained synthetic olivine aggregates: preliminary results*, Geophys. Res. Lett., **24**, 1055-1058.

Tittmann B. R., Clark V. A., Richardson J. M., 1980, *Possible mechanism for seismic attenuation in rocks containing small amount of volatiles*, J. Geophys. Res., **85**, 5199-5208.

Tommasi A., Gibert B., Seipold U., Mainprice D., 2001, *Anisotropy of thermal diffusivity in the upper mantle*, Nature, Vol. **411**.

Turner N. J., Black L.P., Kamperman M., 1998, *Dating of Neoproterozoic and Cambrian orogenesis in Tasmania*, Australian Journal of Earth Scinces, **45**, 789-806.

Ulug A., Berckhemer H., 1984. *Frequency dependence of Q for seismic body waves in the earth's mantle*, J. Geophys., **56,** 9–19.

van der Hilst R. D., Kennett B.L.N., Christie D., Grant J., 1994, *Project SKIPPY explores the mantle and lithosphere beneath Auatralia*, EOS, **75**, 177-181.

van der Hilst R. D., Kennett B.L.N., Shibutani T., 1998, *Upper mantle structure beneath Australia from portable array deployments* in *Structure and Evolution of the Australian Continent*, J. Braun, J. Dooley, B. Goleby, R. van der Hilst and C. Klootwijk (eds.), AGU Geodynamics Monographs, **26**, 39-58.

Vernon F.L., 1989, *Analysis of Data Recorded on the ANZA Seismic Network*, PhD thesis, University of California, San Diego.

Vinnik L.P., Makeyeva L.I., Milev A., Usenko A.Y., 1992, *Global patterns of azimuthal anisotropy and deformations in the continental mantle*, Geophys. J. Int., **111,** 433-447.

Walsh J. B., 1966, *Seismic wave attenuation in rock due to friction*, J. Geophys. Res., **71**, 2591-2599.

Webb S.L., Jackson I., Fitz Gerald J. D., 1999, *Viscoelasticity of the titanate perovskites CaTiO3 and SrTiO3 at high temperature*, Phys. Earth Planet. Interiors, **115**, 259-291.

Weissel J.K., Hayes D.E., 1974, *The Australian Antarctic Discordance: new results and implications*, J. Geophys. Res., **79**, 2579-2587.

Widiyantoro S., 1997, *Studies of Seismic Tomograpy on Regional and Global Scale*, Ph.D. thesis, Research School of Earth Sciences, The Australian National University.

Widiyantoro S., van der Hilst R. D., 1996, *Structure and evolution of lithospheric slab beneath the Sunda arc, Indonesia*, Science, **271**, 1566-1570.

Yoshizawa K., Kennett B.L.N., 2004, *Multimode surface wave tomography for the Australian region using a three-stage approach incorporating finite frequency effects*, Journal of Geophys. Res., **109**, 1-19.

Zielhuis A., van der Hilst R.D., 1996, *Upper mantle shear velocity beneath eastern Australia from inversion of waveforms from Skippy portable arrays*, Geophys. J. Int., **127**, 1-16.